Titanate-based paraelectric glass-ceramics for applications in GHz electronics

Dissertation
zur Erlangung des Grades
"Doktor der Naturwissenschaften"
am Fachbereich Physik, Mathematik und Informatik
der Johannes Gutenberg-Universität in Mainz

Hubertus Braun

geb. in Mainz
Mainz, 2015

Datum der mündlichen Prüfung: 08.05.2015

Meinem Großvater

Abstract

The area of wireless communication applications is in an ongoing development process (mobile phone standards: GSM/UMTS/LTE/5G, global navigation satellite systems (GNSS): GPS, GLONASS, Galileo, Beidou) towards higher data rates and miniaturization which results in a high demand for new optimized microwave materials. This trend becomes especially apparent considering the increasing development and number of smart phones in the recent years, combining the use of multiple technologies of different operating microwave frequencies on a limited spatial area (data: 1G-4G, GPS, WLAN, Bluetooth). The required performance increase for future technologies (e.g. 5G) can be achieved by the use of MIMO-based antenna systems (multiple-input & multiple-output, controlled combination of multiple antennas) for which dielectric loading-based technologies are one of the most promising implementation solutions.

The aim of this work was the development of a suitable paraelectric glass-ceramic (ε_r > 20, Qf > 5000 GHz, $|\tau_f|$ < 20 ppm/K; at GHz frequencies) of the La_2O_3-TiO_2-SiO_2-B_2O_3-system for dielectric loading-based mobile communication technologies as an alternative to existing, commercially used sintered ceramic materials. The focus laid on the question, how the macroscopic dielectric properties of the glass-ceramic material could be correlated and respectively modified by the control of its microstructure. In this work, it was shown that the given dielectric requirements could be fulfilled by the investigated system and that glass-ceramic-based dielectrics showed superior nonelectronic properties to sintered ceramics (homogeneity, low porosity, metal adhesion) proving that glass-ceramic materials are a suitable alternative.

A stable basic glass with a minimum glass former content has been developed and the chemical composition has been optimized against unwanted devitrification and redox instabilities (prevention of Ti^{4+} reduction to Ti^{3+}). Suitable oxidizing agents for low dielectric loss TiO_2-based glass-ceramics were identified by the use of EPR and optical spectroscopy. The influence of the melting conditions on the nucleation mechanisms (surface, Pt, Ti^{3+}) was investigated and the ceramization process was adapted for a maximum amount of the desired crystalline phases to achieve optimum dielectric properties. The microstructure of the glass-ceramic was analyzed by SEM/TEM and XRD measurements and correlated with the macroscopic dielectric properties which were characterized by GHz resonance methods. The dielectric high frequency loss mechanisms were investigated by the use of impedance spectroscopy methods and THz ellipsometry. Two prototype antenna series were analyzed to prove the suitability of glass-ceramic-based dielectrics for the use in dielectric loaded applications.

Kurzdarstellung

Das Gebiet der drahtlosen Kommunikationsanwendungen befindet sich in einem permanenten Entwicklungsprozess (Mobilfunkstandards: GSM/UMTS/LTE/5G, globale Navigationssatellitensysteme (GNSS): GPS, GLONASS, Galileo, Beidou) zu immer höheren Datenraten und zunehmender Miniaturisierung, woraus ein hoher Bedarf für neue, optimierte Hochfrequenzmaterialien resultiert. Diese Entwicklung zeigt sich besonders in den letzten Jahren in der zunehmenden Entwicklung und Anzahl von Smartphones, welche verschiedene Technologien mit unterschiedlichen Arbeitsfrequenzen innerhalb eines Geräts kombinieren (data: 1G-4G, GPS, WLAN, Bluetooth). Die für zukünftige Technologien (z.B. 5G) benötigte Performancesteigerung kann durch die Verwendung von auf MIMO basierenden Antennensystemen realisiert werden (multiple-input & multiple-output, gesteuerte Kombination von mehreren Antennen) für welche auf dielectric Loading basierende Technologien als eine der vielversprechendsten Implementierungslösungen angesehen werden.
Das Ziel dieser Arbeit war die Entwicklung einer geeigneten paraelektrischen Glaskeramik (ε_r > 20, Qf > 5000 GHz, $|\tau_f|$ < 20 ppm/K; im GHz Frequenzbereich) im La_2O_3-TiO_2-SiO_2-B_2O_3-System für auf dielectric Loading basierende Mobilfunkkommunikationstechnologien als Alternative zu existierenden kommerziell genutzten Sinterkeramiken. Der Fokus lag hierbei auf der Frage, wie die makroskopischen dielektrischen Eigenschaften der Glaskeramik mit ihrer Mikrostruktur korreliert bzw. modifiziert werden können. Es konnte gezeigt werden, dass die dielektrischen Materialanforderungen durch das untersuchte System erfüllt werden und dass auf Glaskeramik basierende Dielektrika weitere vorteilhafte nichtelektronische Eigenschaften gegenüber gesinterten Keramiken besitzen, womit dielektrische Glaskeramiken durchaus als geeignete Alternative angesehen werden können.
Ein stabiles Grünglas mit minimalen Glasbildneranteil wurde entwickelt und die chemische Zusammensetzung bezüglich Entglasung und Redoxinstabilitäten optimiert. Geeignete Dotierungen für dielektrisch verlustarme TiO_2-haltige Glaskeramiken wurden identifiziert. Der Einfluss der Schmelzbedingungen auf die Keimbildung wurde untersucht und der Keramisierungsprozess auf einen maximalen Anteil der gewünschten Kristallphasen optimiert um optimale dielektrische Eigenschaften zu erhalten. Die mikroskopische Struktur der Glaskeramiken wurde analysiert und ihr Einfluss auf die makroskopischen dielektrischen Eigenschaften bestimmt. Die Hochfrequenzverlustmechanismen wurden untersucht und Antennen-Prototypenserien wurden analysiert um die Eignung von auf Glaskeramik basierenden Dielektrika für die Verwendung in dielectric Loading Anwendungen zu zeigen.

Contents

1 Introduction

In mobile phone networks the communication from cell to cell is enabled by a dense network of antennas located on masts and associated base stations. The average base station coverage is around 18 resp. 35 km at operating frequencies of 1800 resp. 900 MHz [RI06]. Each of these base stations houses microwave resonators that are necessary to carry signals of specific frequencies and filter out spurious signals and sidebands. For these types of narrow bandwidth applications, where frequency selectivity is paramount, low dielectric loss and temperature-stable dielectric resonators are superior to metal cavity resonators. Dielectric oxide ceramics have revolutionized the microwave wireless communication industry by reducing size and cost of filter, resonator and antenna components in various applications ranging from cellular phones to global positioning systems [Seb08]. Especially paraelectric microwave materials play a key role in a wide range of present and future high frequency applications (0.1-100 GHz). In particular the area of terrestrial and satellite communication (Radio, GNSS, WLAN, DBS TV) is in an ongoing development process which results in a high demand for new optimized microwave materials.

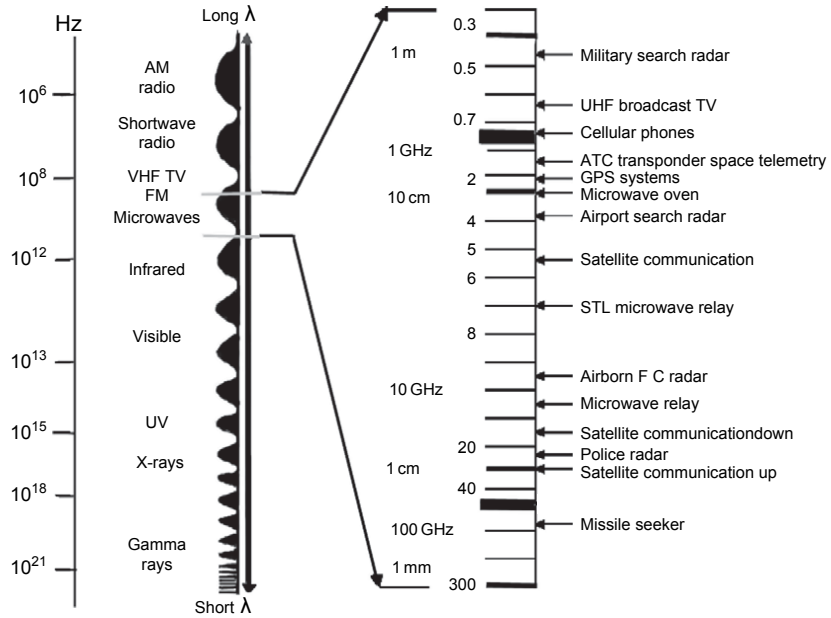

Figure 1.1: Frequency spectrum and for several microwave applications [Seb08]

This trend becomes especially apparent considering the increasing number of smart phones combining the use of multiple microelectronic components of different operating microwave frequencies on a limited spatial area (GSM/UMTS/LTE, GPS, WLAN, Bluetooth). Miniaturization is a critical factor for hand-held devices and can be directly observed in the decrease of size and weight of the devices in recent years. The required performance increase for future technologies (e.g. 5G) can be achieved by the use of MIMO-based antenna systems. Miniaturization and MIMO can be realized by the use of dielectric loading-based implementation solutions.

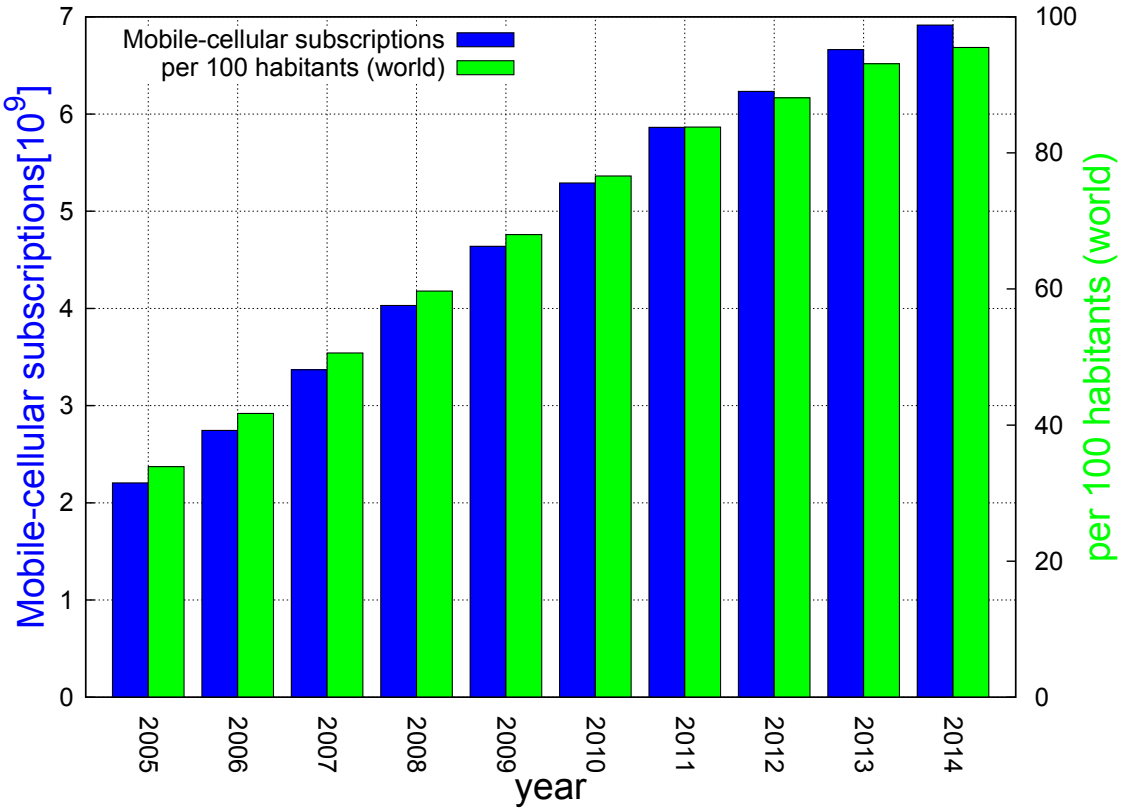

Figure 1.2: The growth of mobile communications in the world since 2005 [ITU14]

The concept of using solid dielectrics as resonators to replace the traditional air-filled metal cavities was first described by Richtmyer in 1939 [Ric39], showing in a theoretical work that ring shaped dielectrics could be used as resonators (DR). In the 1960s many researchers investigated the microwave properties of various dielectrics [RBS61, SMKH62a] and a characterization method for the dielectric properties was introduced by Hakki and Coleman [HC60]. Cohn [Coh68] designed a TiO_2-based microwave filter which was not suitable for practical use due to the high temperature coefficient of the ceramic resulting in a poor temperature stability of resonant frequency (TiO_2: ε_r = 104, Qf = 42000 GHz at 3 GHz, τ_f = +427 ppm/K [WMT84]). In the 1970s substantial research for temperature stable dielectric resonator materials

was performed [RWU+01, Wak89] and the first low τ_f, low dielectric loss BaO-TiO_2-based ceramics were developed ($BaTi_4O_9$: ε_r = 37, Qf = 23000 GHz, τ_f = +15 ppm/K and $Ba_2Ti_9O_{20}$: ε_r = 39, Qf = 32000 GHz, τ_f = +2 ppm/K [Seb08]). The breakthrough to commercialization was achieved by Murata Manufacturing [WMT84] with the development of τ_f-adjustable ceramics in the ZrO_2-SnO_2-TiO_2 system ($Zr_{0.8}Sn_{0.2}TiO_4$: ε_r = 39, Qf = 52000 GHz, τ_f = (0 $\pm$ δ) ppm/K [Seb08]) or CaO-MgO-TiO_2 system ($Ca_{0.05}Mg_{0.95}TiO_3$: ε_r = 21, Qf = 56000 at 7 GHz, τ_f = (0 $\pm$ δ) ppm/K [Seb08]) in the early 1980s. The growth of the mobile communications market in the 90s (see fig. 1.2) motivated further research interest in microwave dielectrics. High permittivity materials (ε_r > 75) were required to achieve a maximum miniaturization for the use in handset applications and also very high Q materials (Qf > 100000 GHz) for base station applications became necessary [FA08]. The former are mostly dominated by ceramics from the BaO-RE_2O_3-TiO_2 (RE: Rare earth elements) system with ε_r of 80-90 while $Ba(Mg_{1/3}Ta_{2/3})O_3$ provides the highest Qf values up to 300000 GHz [RI06].
The increasing interest of science and industry also becomes obvious when looking at the amount of 2300 investigated so-called *low loss dielectric materials*, resulting in more than 5000 publications and 1000 patents in the area of dielectric resonator materials and their related application areas ([Seb08], published 2008).

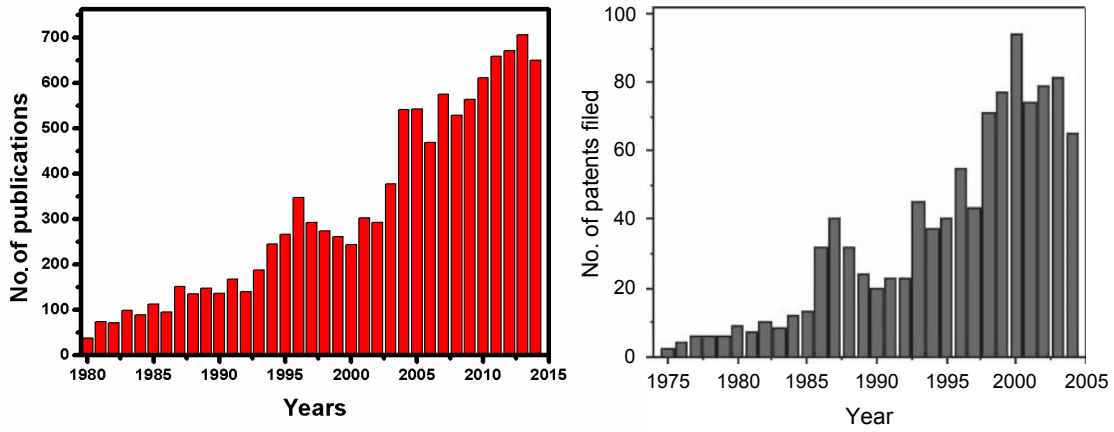

Figure 1.3: Number of publications of dielectric resonator materials [Seb15] (left) and number of filed patents for relevant technologies [Seb08] (right)

The focus of this work lies on the development of a suitable dielectric glass-ceramic material for dielectric loading-based wireless communication technologies (MIMO, GPS, multiresonant DR antennas) which show superior performance advantages in comparison to conventional metal-based technologies in terms of miniaturization, frequency stability and antenna efficiency at operation in proximity to the human body. These advantages will be explained in more detail in the following.

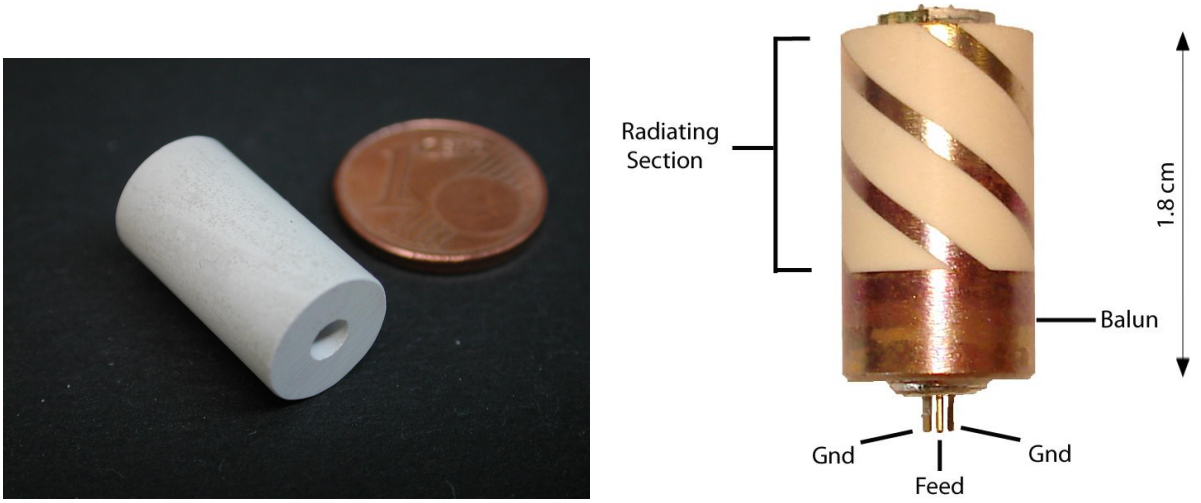

(a) Glass-ceramic blank as dielectric (b) Commercial DLA with helix design [MLZ08]

Figure 1.4

One main source of external losses for an antenna are losses caused by the presence of external objects located in close proximity respectively in the antenna near-field ($r_{\text{near}} \approx 3\ \lambda$, approx. 45 cm at f = 2 GHz). This effect is known as body-loading [MLZ08]. Body loading by objects such as human body tissue (ε_r(GHz) $\approx$ 40-50, $\tan(\delta) \approx$ 0.1-1.0; [Lei11]) leads to a reduced antenna performance (see fig. 1.5):

- detuning (shift of frequency)
- rapid decrease of antenna efficiency due to additional dielectric losses

Conventional pure metal-based antennas are designed for an operation in such lossy body loaded environments (e.g. mobile phone antenna operating close to the human body) and are optimized for a consistent performance in talk positions as well as in free space. The antenna match (impedance match between antenna and voltage source) improves with increasing amount of body loading to partially compensate the efficiency reduction (efficiency: ratio of emitted radiation to input energy). Additionally the frequency is tuned to lower frequencies (detuning) with increasing body loading by the associated increase of the overall permittivity of the system. Such antennas only reach efficiencies of approx. 3-5 $\%$ [Lei11] and the low performance is counteracted by an increased radiation power and a higher number density of base stations. In fig. 1.5 the same antenna in different environments is shown. In practice the most commonly quoted parameter to describe the antenna performance is the S_{11} parameter in dependence of frequency (reflection coefficient or return loss) which is a measure for the amount of power which is reflected back from the antenna to the energy source due to the impedance mismatch and is normally given in dB.

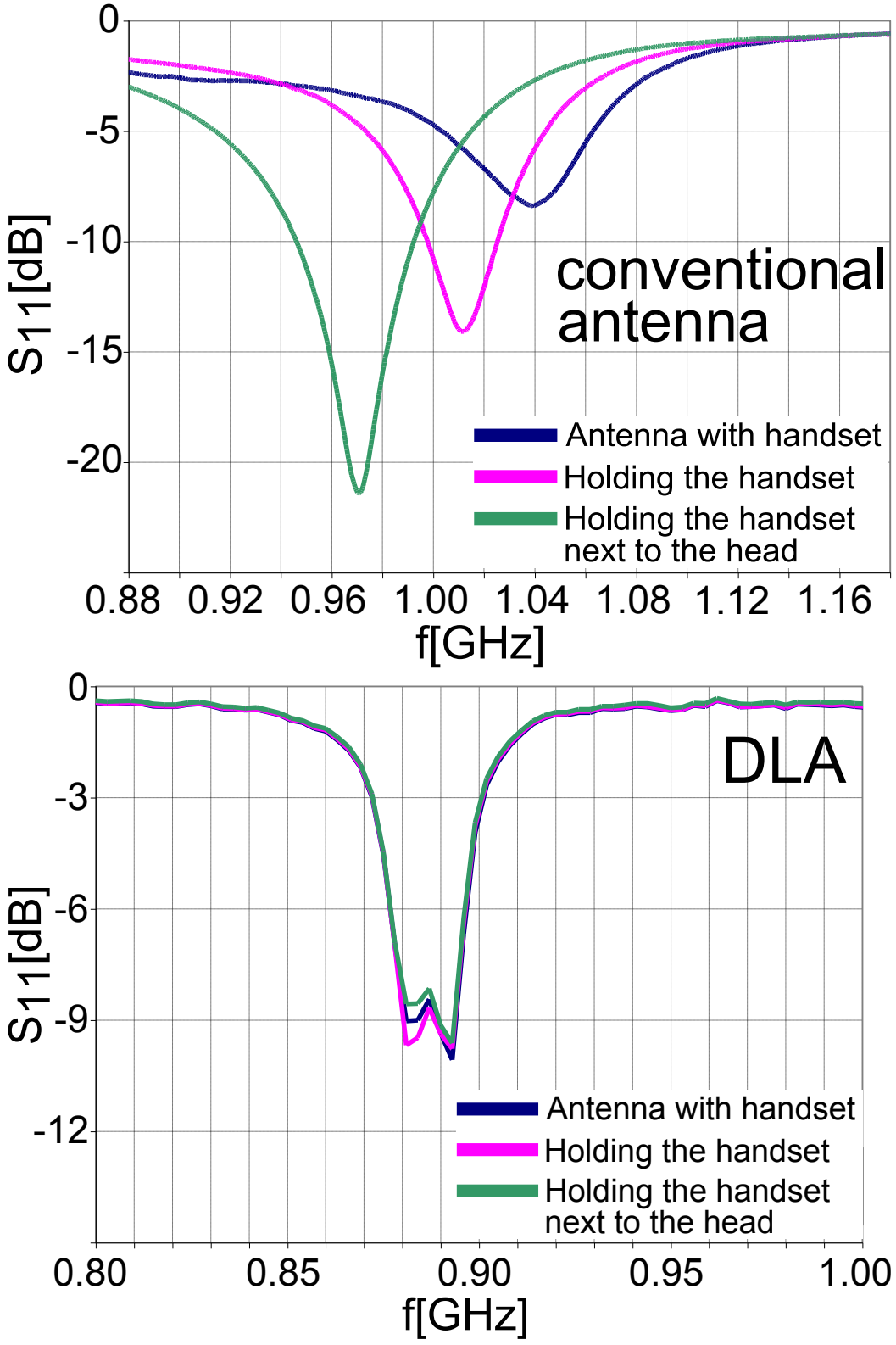

Figure 1.5: Comparison of a conventional metal-based antenna (top) with a dielectric loaded antenna by a frequency dependent measurement of S_{11}[dB] in different environments [Mir10]

For the metal-based antenna a frequency shift of up to 10 $\%$ occurs in comparison to the antenna operating in free space (blue curve) and the reflected power at resonance decreases by 6 dB and even 13 dB ($\approx$ factor 20) due to the improving impedance match. The remainder of the power is either absorbed as internal losses or transformed to radiation. A more elegant solution to prevent body loading is provided by dielectric loading. For this technique ceramic bodies with high permittivity and low dielectric loss are used. The higher permittivity (in comparison to air) leads to a reduction of the size and near-field volume of the antenna and thereby indirectly minimizes the negative influence of external objects resp. body loading effects on the antenna performance. In fig. 1.5 a comparison between the properties of a so-called dielectric loaded antenna (DLA) and a conventional metal-based antenna is shown. For the DLA the influence of body loading is rather neglectable. Due to their comparatively smaller size dielectric loaded antennas are suitable to take part in the ongoing miniaturization trend of mobile communication devices. The resonator length (R_L) respectively antenna size is proportional to the effective resonator wavelength and therefore reduces with the root of the permittivity of the used dielectric.

$$R_L \sim \lambda_{\text{eff}} = \lambda_{\text{vac}} \cdot \frac{1}{\sqrt{\varepsilon_r}} \tag{1.1}$$

The key material parameters to express the suitability of a material are therefore:

- high permittivity (ε_r > 20)
- low dielectric loss $\tan(\delta)$ resp. high quality factor Q (Qf > 5000 GHz)
- low temperature coefficient of resonance frequency ($|\tau_f| \leq 20$ ppm/K)

The requirements on the frequency stability of a GPS antenna are quite strict, the frequency tolerance Δf is around $\pm$1.5 MHz at $f_{\text{GPS}} \approx$ 1.5 GHz [Lei11] (equivalent to τ_f = 20 ppm/K for a temperature difference of $\Delta T = \pm$50 K).

Material	Abbreviation	ε_r	Qf[GHz]
$BaMg_{1/3}Ta_{2/3}O_3$	BMT	24	250000
$BaZn_{1/3}Ta_{2/3}O_3$	BZT	29	150000
$Ba(Co, Zn)_{1/3}Nb_{2/3}O_3$	BCZN	34	90000
$SrTiO_3$–$LaAlO_3$	STLA	39	60000
$CaTiO_3$–$NdAlO_3$	CTNA	45	48000
$ZrTiO_4$–$ZnNb_2O_6$	ZTZN	44	48000
$Ba_4Nd_{9.333}Ti_{18}O_{54}$	BNT	80	10000

Table 1.1: Commercially used ceramics for microwave applications (all τ_f = 0) [RI06]

A quite large number of commercially available conventional sintered ceramics with excellent dielectric properties (see tab. 1.1) already exists, but due to their production process (sintering) they have some disadvantageous non-electronic properties which cause problems for their use in dielectric loaded applications:

- porosity (problematic for metallization processes)
- blank inhomogeneity/non-uniformity (performance deterioration)
- batch-to-batch variation of the dielectric properties ($\Delta\varepsilon/\varepsilon \approx$ 1-2 %, necessity of adaption of the production process due to the lack of reproducibility)

At low frequency ranges dielectric resonators become larger which intensifies the production-related problems mentioned above. Especially for the frequency range below 2 GHz, which is important for mobile communications (approx. 800 to 1800 MHz) large blank geometries are necessary [PA99]. Glass-ceramic-based dielectrics tend to have comparatively higher dielectric losses but provide other essential advantages over sintered ceramics. As glass-ceramics are initially produced from a homogeneous liquid glass melt, they are intrinsically pore-free and provide a better material homogeneity and reproducibility. For example for commercial optical glasses, homogeneities of $\Delta\varepsilon/\varepsilon < 5 \cdot 10^{-5}$ over lenses of 20 cm diameter are standard in industrial production.
The aim of this work is the development of a suitable dielectric glass-ceramic material with sufficiently good dielectric properties (according to the requirements for ε_r, Qf, τ_f mentioned above) to provide an alternative to the already existing sintered ceramics. Furthermore the connection between the macroscopic dielectric properties and the microscopic microstructure of the material will be investigated in detail and especially the contributions of different physical mechanisms on the dielectric loss are investigated.

2 Theory

2.1 Glasses

A basic definition for glass is given by Scholze [Sch88]: „In the physicochemical sense, glass is an undercooled liquid“. It is helpful to observe the solidification process to understand this definition in more detail, for example, looking at the volume change with temperature, beginning with a melt at high temperature above the melting point. In general, the volume decreases during the cooling process and at sufficiently slow heating rate the crystallization starts at the melting temperature T_m leading to a more densely packed crystal structure with a lower thermal expansion coefficient [CN07] (discontinuous first order phase transition, represented by the solid line in fig. 2.1).

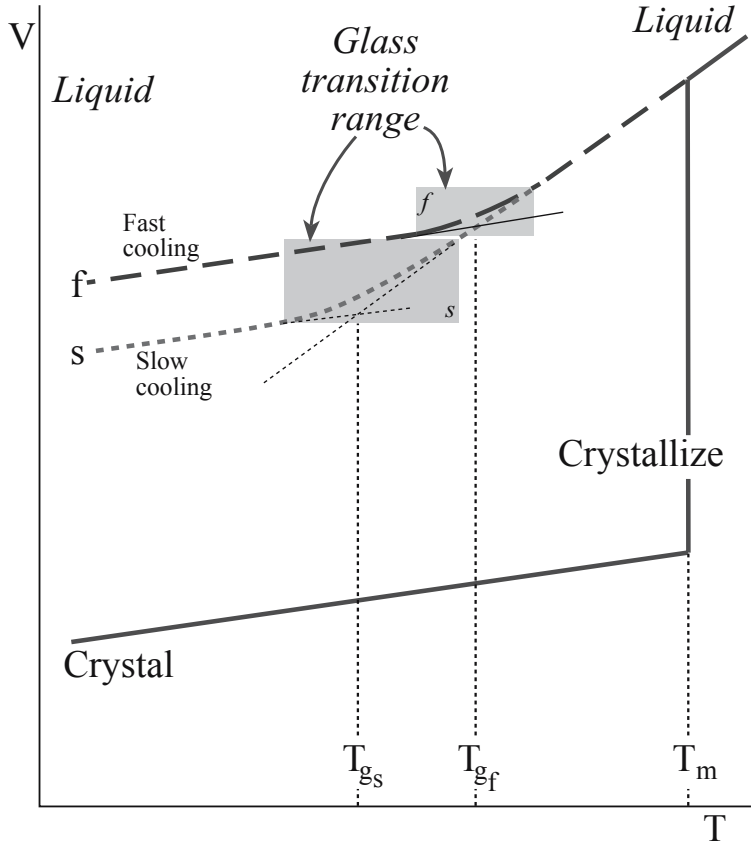

Figure 2.1: V(T) plot for a glass-forming and crystal-forming liquid [CN07]

At higher cooling rates the volume continues to decrease below T_m (dashed curves in fig. 2.1) and in the temperature range between T_m and T_g the material state is considered as undercooled melt, which is still in a (metastable) thermodynamical equilibrium. The viscosity of the undercooled liquid continuously increases with decreasing temperature which kinetically slows down the adjustment to a more dense liquid structure. This process continues until a cooling rate dependent temperature T_g is reached, which is defined as glass transition temperature. At high cooling rates, T_g is shifted to higher temperatures leading to lower density glasses. The glass transition is a continuous transition and therefore a more correct wording is glass transformation/transition range. At T_g the viscosity of the melt is so high that due to the low particle mobility no further equilibration in experimentally accessible timescales is possible. This transition is neither thermodynamic nor dynamic transition. Its definition is arbitrarily but narrowly specified by the available measurement techniques at $\eta(T{=}T_g) := 10^{12}$ Pa s [TKNV05]. Below T_g the material is in a solid metastable state in form of an amorphous solid, which is not in the thermodynamical equilibrium. The glass has a disordered microscopic structure comparable to a liquid, which distinguishes itself by the lack of an atomic long-range order (characteristic for crystals). The change in the static structure of the system at T_g is barely observable while the dynamic correlations e.g. viscosity change by orders of magnitude (structural relaxation).

This slowing down of the atomic dynamics when approaching the glass transition from the high temperature side, is well described by Götze's mode-coupling theory (MCT) [Göt08, SG91, Göt99]. For supercooled liquids at temperatures below the melting point the nonlinear feedback mechanisms in the microscopic dynamics of the particles lead to a dynamical arrest of the system. This can be understood as trapping of atoms in cages built up by their nearest neighbors, leading to a freezing in of the liquid-like atomic motion at a critical temperature T_c (cage effect) [BRMF10]. This process takes place well above the caloric glass transition ($T_g < T_c$). Fundamental aspects of the glass transition can be obtained from the MCT via the evolution equations derived from the Mori-Zwanzig projection formalism. Hereby, the observables are classified in relevant and irrelevant quantities and an exact, strongly nonlinear differential equation for the relevant observable $G_n(t)$ is obtained:

$$\frac{\partial G_n(t)}{\partial t} = \sum_m \left\{ \Xi_{nm} G_m(t) - \int_0^t K_{nm}(t') G_m(t-t') \mathrm{d}t' \right\} + f_n(t) \quad . \tag{2.1}$$

The frequency matrix Ξ is dependent on the mean values of the relevant observ-

ables in thermal equilibrium. The forces f_n and the memory kernel $K_{nm}(t) = F(G_n, G_m, G_nG_m, G_nG_n, ...)$, which is a complex nonlinear function of the observables, are still dependent on the irrelevant observables. The Mori equations (eq. (2.1)) can be used to derive equations of motion of the correlation functions of relevant observables. The evolution of the density autocorrelation $\Phi(t) = \langle\rho(t)\rho(0)\rangle$ can be described by

$$\left[\frac{\partial^2}{\partial t^2} + \gamma_R\frac{\partial}{\partial t} + \Xi^2\right]\Phi(t) + \int_0^t K(t-t')\frac{\partial\Phi(t')}{\partial t'}\mathrm{d}t' = 0 \quad . \tag{2.2}$$

In eq. (2.2) the residual forces f_n are implicitly incorporated in the memory kernel $K(t)$. A reasonable approximation for $K(t)$ via the correlation function $\Phi(t)$ can be made to achieve a self-consistent equation. A simple model system for K which preserves the underlying bifurcation scenario is $K = v_1\Phi + v_2\Phi^2$. For adequately chosen coupling parameters (v_1, v_2) Φ does not converge to the equilibrium value ($\Phi_\infty = 0$) but instead reaches a finite value of $\Phi_\infty > 0$. The transition to a non-ergodic glass phase appears as a result of a bifurcation scenario of the nonlinear differential equation. The temperature dependence of the coupling parameters is responsible for the existence of a critical temperature T_c at which the system undergoes the glass transition from ergodic to non-ergodic.

Goldschmidt [Gol26] published in 1926 first hypotheses about the conditions of glass formation. In analogy to the packing density in crystals, the ratio of the ionic radii is hereby of key importance. Oxides or compounds with cation to anion ratios of 0.3 ± 0.1 showed strong tendency of glass formation. This is the case for the main glass-forming oxides: SiO_2, B_2O_3, P_2O_5, GeO_2 and others. These glass formers can also be used as admixture to increase glass formation tendency of compounds which normally tend to crystallize [SD08, BDT+00]. In 1932, Zachariasen [Zac32] postulated the network hypothesis based on the fact that the bonding energies in materials of equivalent chemical composition are very similar in the glassy and crystalline state. He concluded that the chemical bonding resp. near-range order is similar in both states, as for example in silicates the typical SiO_4-tetrahedra (see fig. 2.2). The cations which participate in the formation of the glass structure are classified into 3 groups:

- network-former (Si, B, P, Ge, As, etc. mainly present in the glass with coordination numbers of 3 or 4
- network-modifier (alkali and alkaline earth metals), coordination numbers of 6
- intermediate oxides (Al, Ti, Zn, Pb, Nb, Ta) coordination numbers of 4 to 6

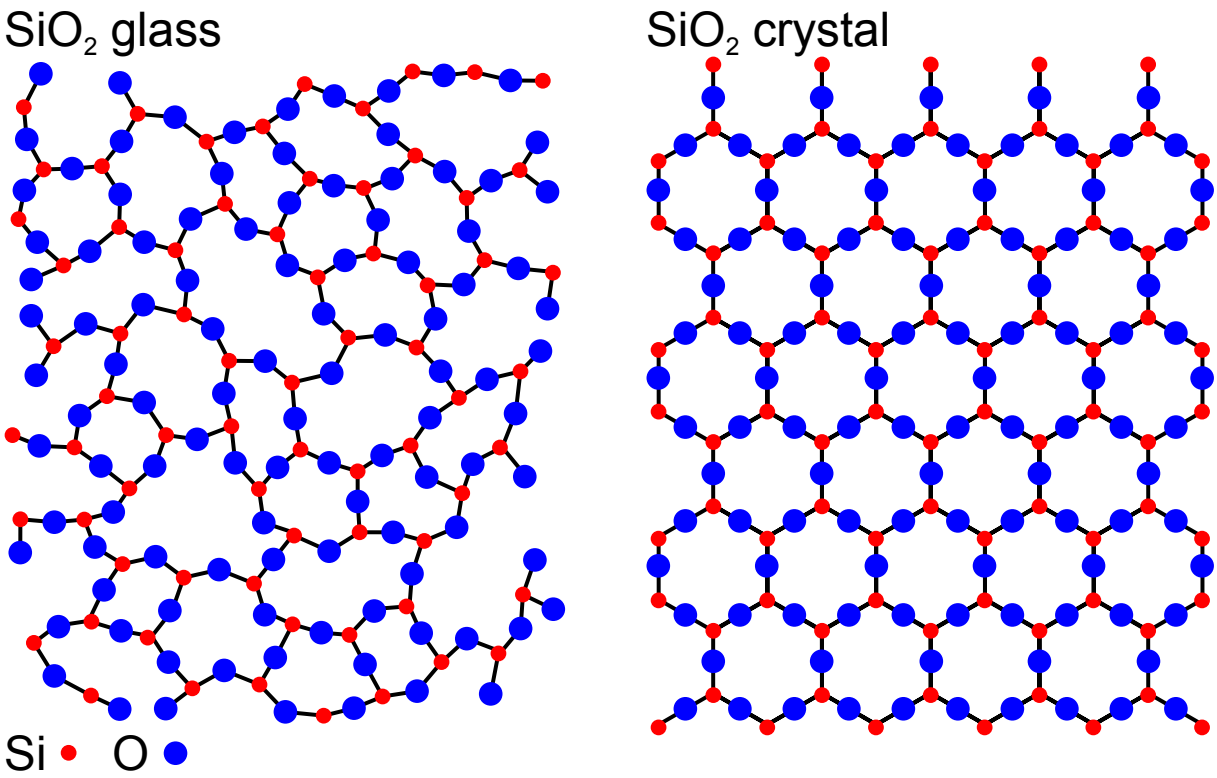

Figure 2.2: Comparison of the microscopic structure of a quartz glass (left) and quartz crystal (right) (modified from [Zac32])

A major weakness of the structural approaches is that the nature of bonding which should determine the structure in principle, is not taken in consideration. Rawson stated that the glass forming tendency would increase for higher bond strengths ($B_{\mathrm{M-O}}$, M: cation) and lower melting temperature (Rawson criterium: glass formation $\sim B_{\mathrm{M-O}}/T_m$). An important prediction of this approach is that mixtures of various oxides show an enhanced glass formation in regions of low melting temperature, respectively in composition regions close to eutectic points [Rao02, Li00].
An important concept to stabilize glass formation in multicomponent systems is the principle of glass frustration [KKZ+95]. The increase of the number of different cations/components leads to a "geometrical frustration" respectively increased disorder of the system and thereby retards the formation of an ordered crystalline state [Zar91], respectively stabilizes the disordered amorphous glassy phase. For a more detailed view on the glass formation and structure, reference is made on standard text books like [Sch88, Vog92, Göt08].

2.2 Glass-ceramics

As glasses are metastable, under appropriate treatment a transformation to the thermodynamically more stable crystalline state can occur. The conversion into a partially crystalline material can give the material superior properties than those of the original glass. Glass-ceramics are melted and formed by a conventional glass production process followed by a subsequent heat treatment of the glass which leads to a controlled partial crystallization („ceramization“) of the basic glass („green glass“). The crystallization process is a two phase process [Tam33]. The first step consists of the formation of stable crystallization nuclei inside the glassy matrix and during the second phase crystals start to grow on these nucleation sites (see fig. 2.3(a)). Both processes are strongly temperature dependent and therefore can be directly controlled by the application of defined heating rates and holding times (see fig. 2.3(b)). As optimum nucleation temperature normally values between T_g and T_g + 50 K are found [McM79a].

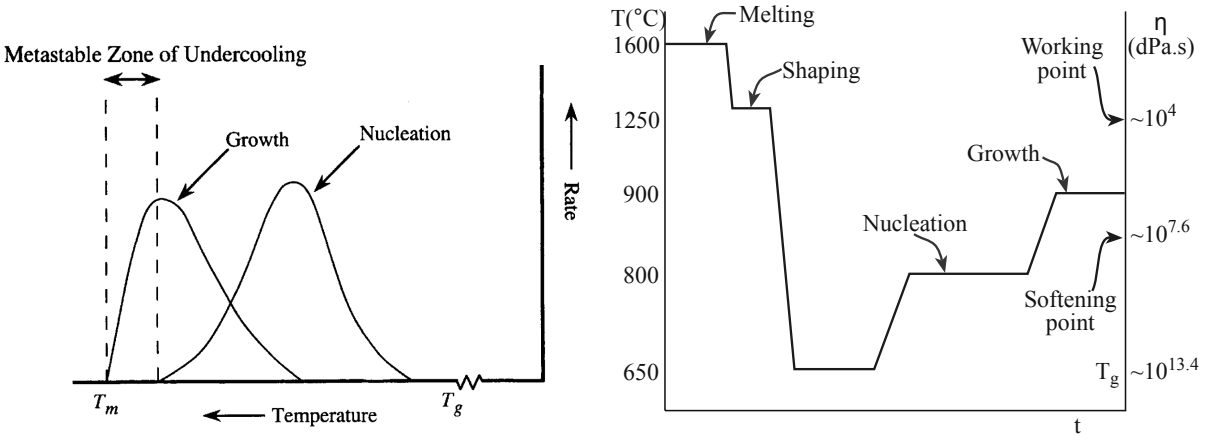

(a) Schematic representation of the nucleation and crystallization growth rates in dependence of temperature [She05b]

(b) Typical ceramization program for a commercial glass-ceramic [CN07]

Figure 2.3

The smaller the overlapping area between nucleation and crystallization range the more stable the glass becomes against crystallization. The nucleation process can occur either by homogeneous or heterogeneous nucleation. Homogeneous nuclei are formed directly from the melt and have similar chemical composition as the amorphous matrix around them. Heterogeneous nuclei are not necessarily of similar composition as the melt or crystal and can be additives to the melt. They build the initial surface for a further epitaxial growth of a crystal. A possibility to enhance nucleation rates is the addition of nucleation agents to the melt (e.g. TiO_2 or ZrO_2)

which form heterogeneous nuclei. The temperature dependence of the homogeneous nucleation rate R_N can be described by an Arrhenius type behavior and the activation energy depends on the activation energy of the nucleation process ($\Delta G^*(T)$: critical free nucleation enthalpy) and the diffusion $\Delta G_D(T)$ which are both temperature dependent [Vog92]:

$$R_N(T) = A \exp\left(-\frac{\Delta G^* + \Delta G_D}{RT}\right) \quad , \tag{2.3}$$

$\Delta G = \Delta G_S + \Delta G_V$ corresponds to the energy which is necessary to form a nucleus and consists of two contributions. The first part is associated with the formation of a new surface causing an enthalpy increase of $\Delta G_S = 4\pi r^2 \sigma > 0$ and the second contribution is related to the energy which is released during the phase transition to the lower energy crystalline state $\Delta G_V = \frac{4\pi}{3} r^3 \Delta g_V < 0$ for $T < T_m$ (r: nucleus radius, σ: surface tension, g_V: change of free volume enthalpy at phase transition). In this estimation the size of the nucleus is assumed to be spherical. In fig. 2.4 it can be seen that the sum of both contributions has a maximum (ΔG^*) at a critical radius r^*. If a thermal fluctuation provides sufficient energy to overcome the critical value ΔG^*, the formed nucleus of critical size will continue to grow on its own [Vog92].

$$\Delta G = \Delta G_S + \Delta G_V = 4\pi r^2 \sigma + \frac{4\pi}{3} r^3 \Delta g_V \quad , \tag{2.4}$$

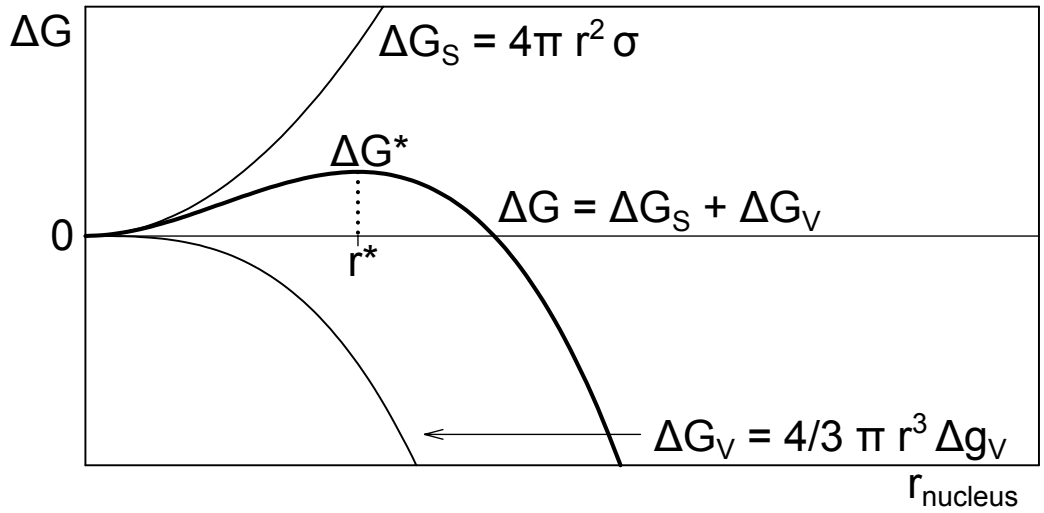

Figure 2.4: Homogeneous nucleation: Enthalpy contributions related to the formation of the nucleus (modified from [Vog92])

r^* and ΔG^* depend on the degree of undercooling. With lower temperatures the tendency to form a nucleus increases (due to ΔG_V) but also the diffusion slows down due to the increase in viscosity. The nucleation rate can be assumed to be proportional the diffusion coefficient [Car07] and therefore inversely proportional to the viscosity,

according to the Stokes-Einstein-equation [ADP06]:

$$D = \frac{k_B T}{6\pi\eta r} \quad . \tag{2.5}$$

A local change of viscosity can lead to an induced nucleation/crystallization. Keding et al. [KR97, KR00] and Carl [Car07] investigated the effect of electrochemically induced nucleation due to the reduction of Ti^{4+} to Ti^{3+}. Ti^{4+} can act as network-former (mostly tetragonal/four-fold coordinated, see chapter 2.8) or network-modifier (mostly octahedral/six-fold coordinated), whereby Ti^{3+} only occurs in six-fold coordination as network-modifier inside the glass matrix and thereby leads to a decrease of the viscosity. Therefore the change of coordination number by reduction can cause an enhanced nucleation. Unwanted nucleation (and consequent devitrification) due to the reduction of Ti^{4+} can occur during the manufacturing process (flame hydrolysis deposition) of TiO_2 containing ultra low expansion glass (containing approx. 10 wt% of TiO_2, see fig. 2.5(a)).

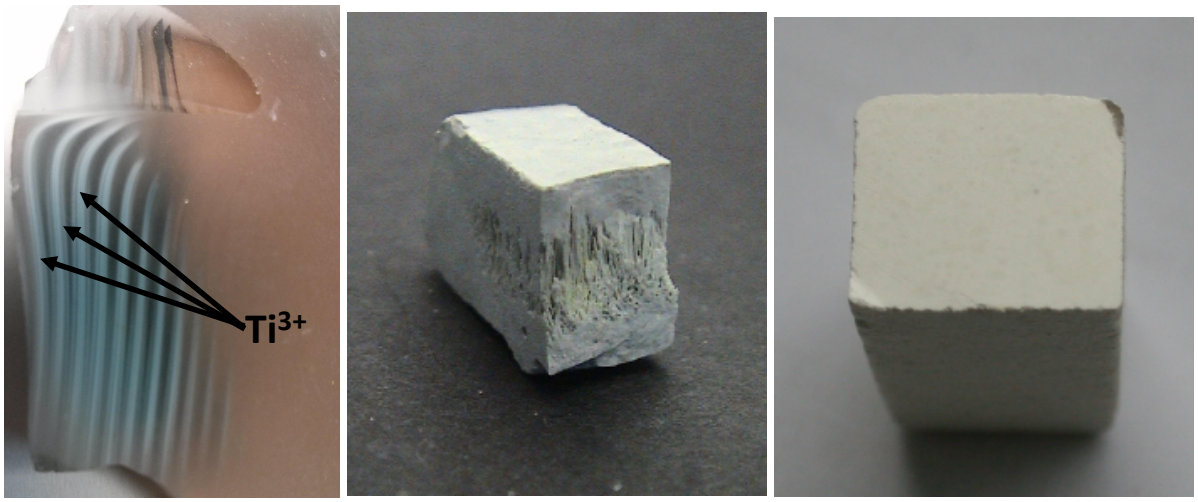

(a) Locally reduced ULE glass (blue Ti^{3+} striae) showing devitrification

(b) Devitrified glass

(c) Ceramized glass

Figure 2.5

Ceramized glasses (see fig. 2.5(c)) distinguish themselves from devitrified ones by the following characteristics [McM79a]:

- high nucleation rates
- homogeneous distribution of crystallites
- uniform crystallite size

Furthermore a differentiation has to be made between an unwanted crystallization (devitrification, see fig. 2.5(b)) which already happens during the casting of the melt and the controlled crystallization growth process during the ceramization (see fig. 2.5(c)). During the crystallization process the surrounding area depletes in compounds of the crystalline composition, the crystal growth then becomes dominated by diffusion processes [BDT+00]. The crystal growth rate increases until shortly before the melting temperature is reached (see fig. 2.3(a)). An alternative nucleation/crystallization process is given by Stookey [Sto59]. He pointed out that glass compositions exist which form homogeneous liquids in their molten state but which separate on (slow) cooling or reheating into two liquid/glass phases. This phase separation process can shift the chemical composition closer to the stoichiometry of the nucleus and thereby enhance the nucleation process. For a more detailed view on the crystallization process of glasses, reference is made on standard text books like [Tam33, McM79a, Vog92, She05b]. One aim of this work is to optimize the glass composition in a way that the glass is stable against devitrification with a minimum amount of glass former oxides (here: SiO_2, B_2O_3, Al_2O_3) to obtain a glass-ceramic with maximum amount of crystalline phase content.

2.3 Redox behavior of glasses

When glasses containing redox active oxides (e.g. $Ti^{3+/4+}$, $Ce^{3+/4+}$, $Sb^{3+/5+}$, $As^{3+/5+}$, $Fe^{2+/3+}$ etc.) are melted at high temperatures (1400-1650 °C for most of glasses in this work), after sufficient time of melting an equilibrium of the partial oxygen pressure in the ambient atmosphere and the glass melt (physically dissolved oxygen) is achieved and the relative concentrations of the different oxidation states reach equilibrium values [PD96]. This can be understand in the following way: With increasing temperature of the melt, the redox equilibrium of the oxides shifts to its reduced state (see eq. (2.6)) and thereby released oxygen dissolves in the glass and increases the partial oxygen pressure of the melt. This leads to $p_{O_2,\text{melt}} > p_{O_2,\text{air}}$ ($p_{O_2,\text{air}}$ is temperature independent). The general process will be explained exemplarily on the most relevant redox species in this work TiO_2:

$$2TiO_2 \underset{T\downarrow}{\overset{T\uparrow}{\rightleftharpoons}} Ti_2O_3 + \frac{1}{2}O_2 \uparrow \quad . \tag{2.6}$$

To equilibrate the p_{O_2} of melt and atmosphere, oxygen diffuses out of the melt with increasing temperature and the oxygen loss (respectively degree of reduction) reaches a maximum value at the highest temperature (melting temperature of the glass T_m). Decreasing the temperature during the casting would cause a reversion and oxygen normally would diffuse back and reoxidize the polyvalent ions according to eq. (2.6). But as the cooling process during the casting occurs in seconds, the oxygen diffusion "freezes in" at some fictive temperature below the melting temperature (oxygen diffusion rate is strongly temperature dependent, see eq. (2.18)), causing also a fixation of the redox state of the polyvalent ions [Pau85, SMR03]. The process of oxygen exchange between melt and atmosphere for such reducing conditions can be expressed in the following way [Eic11] using Kröger-Vink notation [KV56, MH03]:

$$O_O^{\times} \rightleftharpoons V_O^{\times} + \frac{1}{2}O_2 \uparrow \longrightarrow V_O^{\bullet\bullet} + 2e^{'} + \frac{1}{2}O_2 \uparrow \quad . \tag{2.7}$$

The electrons released during this oxygen vacancy formation (see eq. (2.7)) will be trapped by the redox ions according to the following mechanism:

$$Ti_{Ti}^{\times} + e^{'} \longrightarrow Ti_{Ti}^{'} \quad . \tag{2.8}$$

The Ti^{3+} ions are hereby strongly polarized [XLYY12, WF50] and can be understood as Ti^{4+} ions with a delocalized electron, providing a hole-type hopping conduction mechanism (see chapter 2.7.1), which is a well known source of additional dielectric loss for example in reduced $BaTiO_3$ crystals [IH78, KP03]:

$$\mathrm{Ti}_{\mathrm{Ti}}^{\times} + \mathrm{Ti}_{\mathrm{Ti}}^{'} \rightleftharpoons \mathrm{Ti}_{\mathrm{Ti}}^{'} + \mathrm{Ti}_{\mathrm{Ti}}^{\times} \quad . \tag{2.9}$$

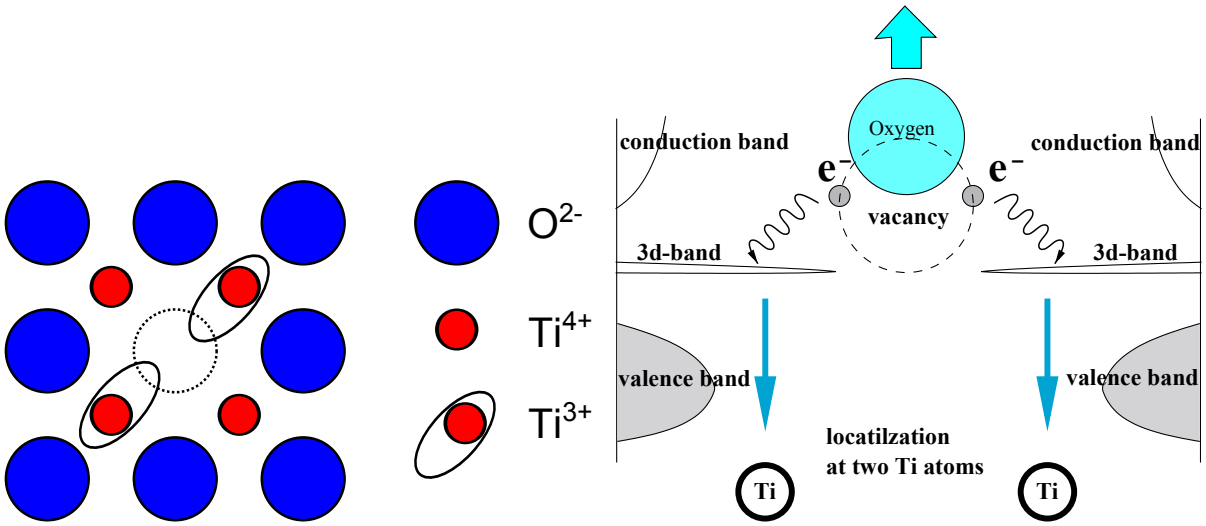

(a) Schematic picture of an oxygen vacancy in TiO_2 (modified from [XLYY12])

(b) Oxygen atom leaving behind two electrons into 3d defect bands (modified from [SSL+02])

Figure 2.6: Ti^{3+}-$V_O^{\bullet\bullet}$-Ti^{3+} formation

This can also be understood as creation of defect bands in the band gap leading to an enhanced electrical conductivity, exemplary explained for a rutile (TiO_2) crystal. The electron density of states for an oxygen vacancy containing TiO_2 crystal was calculated using the software MedeA (VASP5.2 code). Due to the oxygen vacancy a defect band below the conduction band edge is formed, leading to an enhanced conductivity. The valence band consists of the filled O 2p states, whereby the empty conduction band is made up by the Ti 3d states (see fig. 2.6 (b) and fig. 2.7).
Additionally to the polaron hopping mechanism, the diffusion of oxygen vacancies inside the material would provide an ionic conductivity contribution, which is neglectable at room temperature [Eic11, PKN+07]:

$$\mathrm{O}_{\mathrm{O}}^{\times} + \mathrm{V}_{\mathrm{O}}^{\bullet\bullet} \rightleftharpoons \mathrm{V}_{\mathrm{O}}^{\bullet\bullet} + \mathrm{O}_{\mathrm{O}}^{\times} \quad . \tag{2.10}$$

If only a single redox oxide is present, the equilibrium may be represented by a general expression (A^{m+}: reduced ion/reductant, $A^{(m+n)+}$: oxidized ion/oxidant) [Pau82]:

$$\mathrm{A}^{\mathrm{m+}} + \frac{n}{4}\mathrm{O}_2 \underset{T\downarrow}{\overset{T\uparrow}{\rightleftharpoons}} \mathrm{A}^{(\mathrm{m+n})+} + \frac{n}{2}\mathrm{O}^{2-} \quad . \tag{2.11}$$

As the activity of the redox and oxygen ions in the glass are composition and temperature dependent, the equilibration constant $K_A(T)$ (eq. (2.13)) is normally

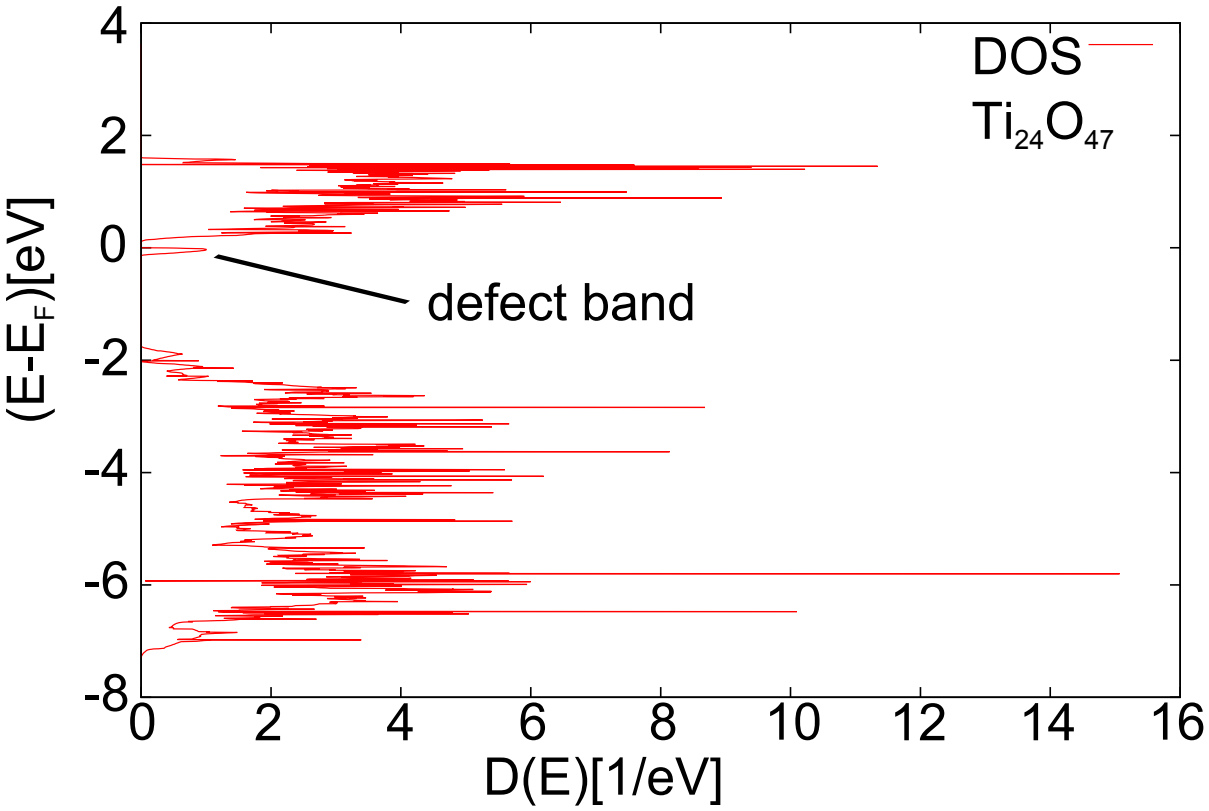

Figure 2.7: Density of states for $Ti_{24}O_{47}$

unknown. As the activity of the redox and oxygen ions in the glass are composition and temperature dependent, the equilibration constant $K_A(T)$ (eq. (2.13)) is normally unknown.
The degree of reduction depends on multiple factors [PD65, Par12]:

- Furnace atmosphere: air, O_2 bubbling, vacuum, raw materials (e.g. carbonates, hydrates, nitrates)
- Melting temperature
- Chemical composition of the melt (optical basicity [DI76]) and therefore indirect to the total concentration of the polyvalent ion [PD65]
- Equilibrium value independent of valence state of the raw materials
- Melting time (if equilibrium value is not stabilized yet, $t_{\text{equi}} \approx$ 10-100 h [Par12])
- Mutual redox interaction between different polyvalent ions (takes place during cooling from melting temperature to cooling temperature around T_g when oxygen diffusion process is already frozen in)

2.3.1 Furnace atmosphere and melting temperature

The oxidation-reduction equilibrium in glass usually moves towards the reduced side with increasing temperature. This can be explained by the following consideration (exemplary shown for the equilibrium of $\mathrm{Ti}^{3+/4+}$): The redox reaction eq. (2.6) may be written in the term of the ionic species present in the glass melt at high temperatures [SMR03, MMR10, KMAR11] (see eq. (2.11)):

$$\mathrm{Ti}^{3+} + \frac{1}{4}\mathrm{O}_2 \overset{K(T)}{\rightleftharpoons} \mathrm{Ti}^{4+} + \frac{1}{2}\mathrm{O}^{2-} \quad . \tag{2.12}$$

Then the equilibrium constant $K(T)$ is given by :

$$K(T) = \frac{a_{\mathrm{Ti}^{4+}} \cdot (a_{\mathrm{O}^{2-}})^{\frac{1}{2}}}{a_{\mathrm{Ti}^{3+}} \cdot (a_{\mathrm{O}_2})^{\frac{1}{4}}} \overset{!}{=} \exp\left(-\frac{\Delta G_0}{RT}\right) \quad , \tag{2.13}$$

as $\Delta G \overset{!}{=} 0 = \Delta G_0 + RT\ln(K)$ in the equilibrated state (ΔG_0: standard Gibbs free energy). The activities ($a_{\mathrm{Ti}^{4+}}$, $a_{\mathrm{Ti}^{3+}}$, $a_{\mathrm{O}^{2-}}$) of the different ions generally cannot be determined [Pau82] and therefore the equilibrium constant (as well as the standard free Gibbs energy ΔG_0) is usually unknown. But if a glass of constant chemical composition, under unchanged atmospheric conditions (constant p_{O_2}) is melted at different temperatures, the temperature dependence of the equilibrium constant can be expressed by the Van´t Hoff isochore [Pau82]

$$K(T) = C\exp\left(-\frac{\Delta H_0}{RT}\right) \quad , C \text{ temperature independent constant} \tag{2.14}$$

and the following assumptions for the activities can be made: Over a limited temperature range $a_{\mathrm{O}^{2-}}$ remains approximately constant (for a melt of constant chemical composition [Pau85, PD65, Brü85, Joh65]). The temperature dependence of the cation activities can be written as $a_i(T) \approx \gamma_i(T) \cdot c_i$, with $\gamma_{\mathrm{Ti}^{3+}}(T) \approx \gamma_{\mathrm{Ti}^{4+}}(T)$ [Pau82] (c_i: cation concentrations) and therefore the ratio $a_{\mathrm{Ti}^{4+}}/a_{\mathrm{Ti}^{3+}} = c_{\mathrm{Ti}^{4+}}/c_{\mathrm{Ti}^{3+}} \cdot \underbrace{\gamma_{\mathrm{Ti}^{4+}}(T)/\gamma_{\mathrm{Ti}^{3+}}(T)}_{\approx 1}$.

With $a_{\mathrm{O}_2} = p_{\mathrm{O}_2}$ it follows then from eq. (2.13)/(2.14):

$$K(T) \sim \frac{c_{\mathrm{Ti}^{4+}}}{c_{\mathrm{Ti}^{3+}}} \sim \exp\left(-\frac{\Delta H_0}{RT}\right) \quad . \tag{2.15}$$

For all oxides this reaction shows an exothermic behavior ($\Delta H_0 < 0$) and therefore the redox equilibrium shifts to the reduced site with increasing temperature (see fig. 2.8).

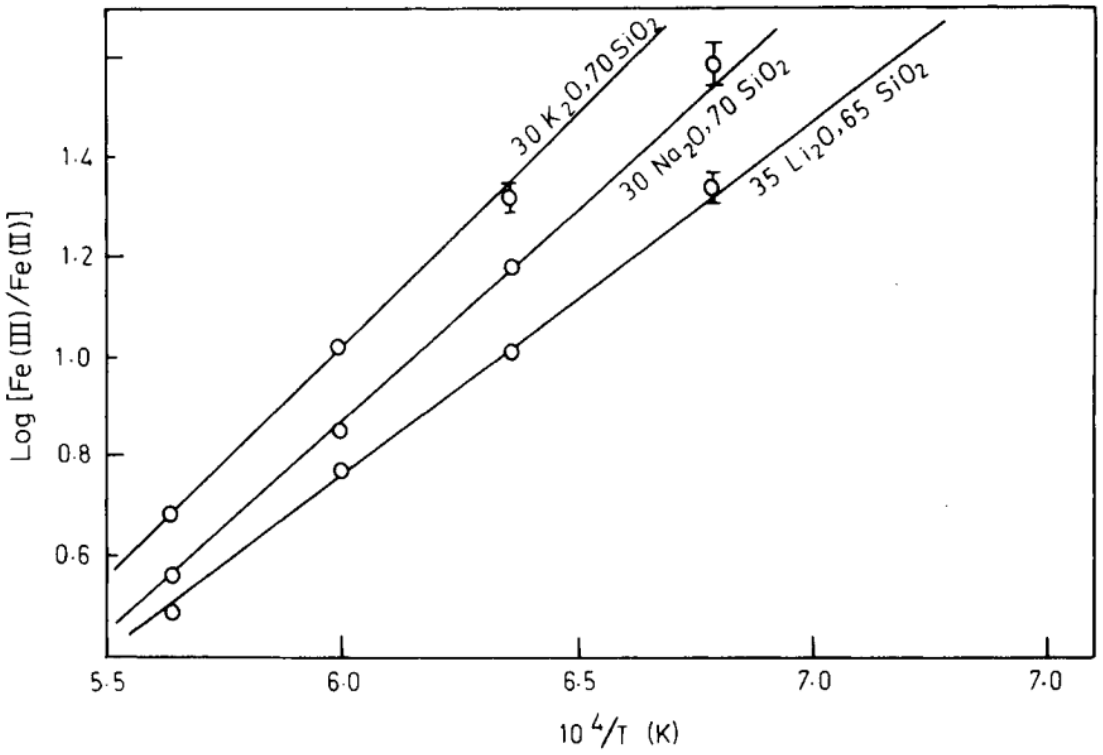

Figure 2.8: Fe^{3+}/Fe^{2+} ratio temperature variation in alkali-silicate melts [Pau82]

2.3.2 Chemical composition

To understand the influence of different chemical glass compositions on the redox behavior of polyvalent ions in the glass, Duffy et al. [DI71, DI75] introduced the term of an optical basicity Λ based on the concept of the Lewis basicity. The optical basicity is hereby related to the ability of the oxygen ion to donate negative charge. Its "electron donor power" depends on the strength of the covalent bonding (basically related to the electronegativity) to the cations in the melt [Duf89]. The higher the negative charge concentration close to the oxygen ion, the higher is its polarization effect on neighboring polyvalent ions, shifting their valency to the upper oxidation state. Increasing optical basicity therefore favors the upper oxidation state [Duf96].
Optical basicity contributions can hereby be determined in various ways [DI76, DS96] from the electronic polarizability and refractive index, band gap energies or electronegativity of the different oxides. The optical basicity of a glass can then be calculated by [Duf93]:

$$\Lambda_{\text{glass}} = X_{\text{AO}}\Lambda(\text{AO}) + X_{\text{BO}}\Lambda(\text{BO}) + \ldots \quad , \tag{2.16}$$

whereby $\Lambda(\text{AO})$, $\Lambda(\text{BO})$ are the optical basicities of the oxides and X_{AO}, X_{AO} the equivalent fractions of oxygen atoms they contribute.

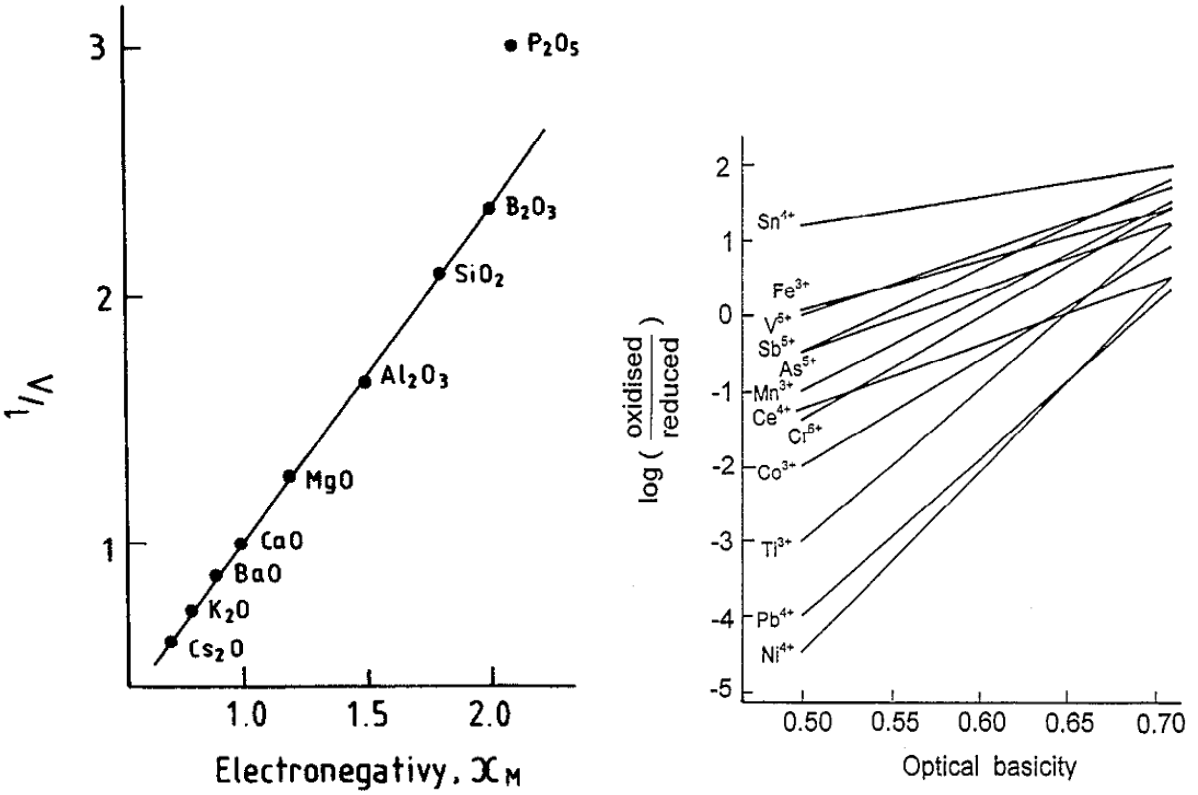

(a) Relationship between optical "acidity" of oxides (corresponds to inverse basicity $1/\Lambda$) and electronegativity χ_M shows a linear relationship: $1/\Lambda = a\chi_M + b$ (transition metals excl.) [Duf93]

(b) Linear relationship between $\ln(c_{\mathrm{A}^{(m+n)+}}/c_{\mathrm{A}^{m+}})$ of redox ion couples and the optical basicity, measured in silicate glass systems at 1400 °C in air atmosphere by Duffy et al. [Duf96]

Figure 2.9

Oxide	P_2O_5	B_2O_3	SiO_2	Al_2O_3	TiO_2	ZrO_2	La_2O_3	CeO_2
Λ	1.00	1.15	1.40	0.78	1.00	1.10	1.15	1.14

Oxide	Li_2O	Na_2O	K_2O	MgO	CaO	SrO	BaO	Sb_2O_3
Λ	0.33	0.42	0.48	0.60	1.00	0.90	1.07	1.01

Table 2.1: Optical basicity values for various oxides [Duf93, Duf89, DS96, HBF+02]

For glasses melted at similar conditions (atmosphere, melting temperature, etc.) the redox ratio depends on Λ in the following way [Duf93, Duf96] (see fig. 2.9(b)):

$$\ln\left(\frac{c_{\mathrm{A}^{(m+n)+}}}{c_{\mathrm{A}^{m+}}}\right) = a_0 + b_0 \cdot \Lambda \quad , b_0 > 0 \quad \text{(except for } \mathrm{Cu}^{1+/2+}\text{)} \quad . \tag{2.17}$$

Morinaga et al. [MYT94] showed the effect of Ti^{3+} formation in dependency of different optical basicity values by varying the glass compositions at constant melting conditions (see fig. 2.10).

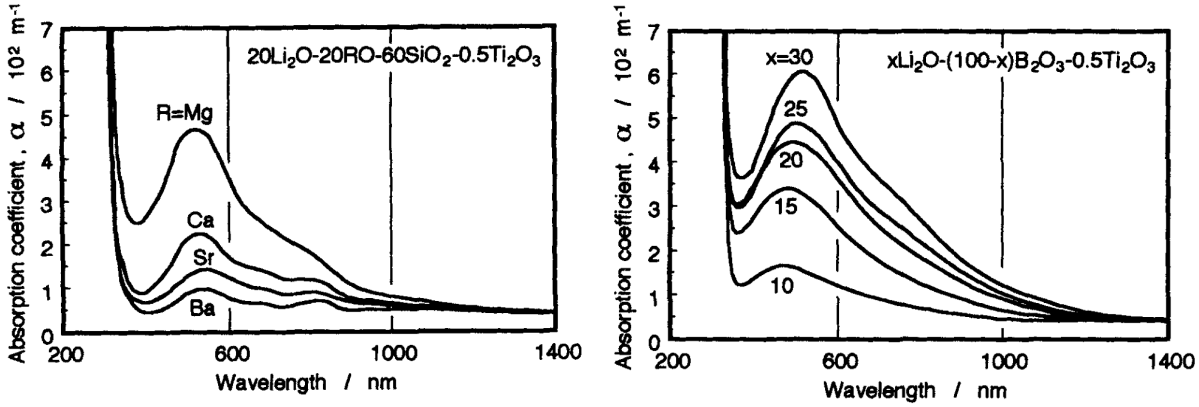

(a) Lithium alkaline earth silicate glasses (b) Lithium borate glasses

Figure 2.10: Investigation of the Ti^{3+} formation on basis of optical absorption measurements ($\alpha_{Ti^{3+}} \approx 550$ nm) for varying glass composition respectively basicity [MYT94]

2.3.3 Melting time

For a standard glass melted at 1450 °C in air, the oxygen diffusion constant can be roughly estimated to $D \approx 10^{-4}$ cm^2/s [Par12] ($\Delta x = \sqrt{2Dt}$: Einstein-Smoluchowski relation). Assuming a necessary diffusion length of Δx = 10 cm through the melt, we can estimate an equilibration time of $t_{\text{equi}} \approx 140$ h. In addition to the diffusion process, the contribution of thermal heat flow will also lead to a faster equilibration. Therefore it seems rather difficult to estimate the equilibration time in general as t_{equi}. Also the temperature dependence of the diffusion constant for glass melts follows an Arrhenius-type behavior [Dun82]:

$$D(T) \sim \exp\left(-\frac{\Delta E}{RT}\right) \quad . \tag{2.18}$$

Paul et al. [PD65] found equilibration times around 10-60 h for Ce containing silicate glass melts (see fig. 2.11), while Johnston [Johnston] found 20 h for Fe containing glasses.

It is important to mention, that the reduction velocity (increase in concentration per time) is not uniform (faster at the begin, followed by a slow saturation behavior). Which means that even melts which were melted shorter than the equilibration time can also contain a considerable amount of reduced species [GPT].

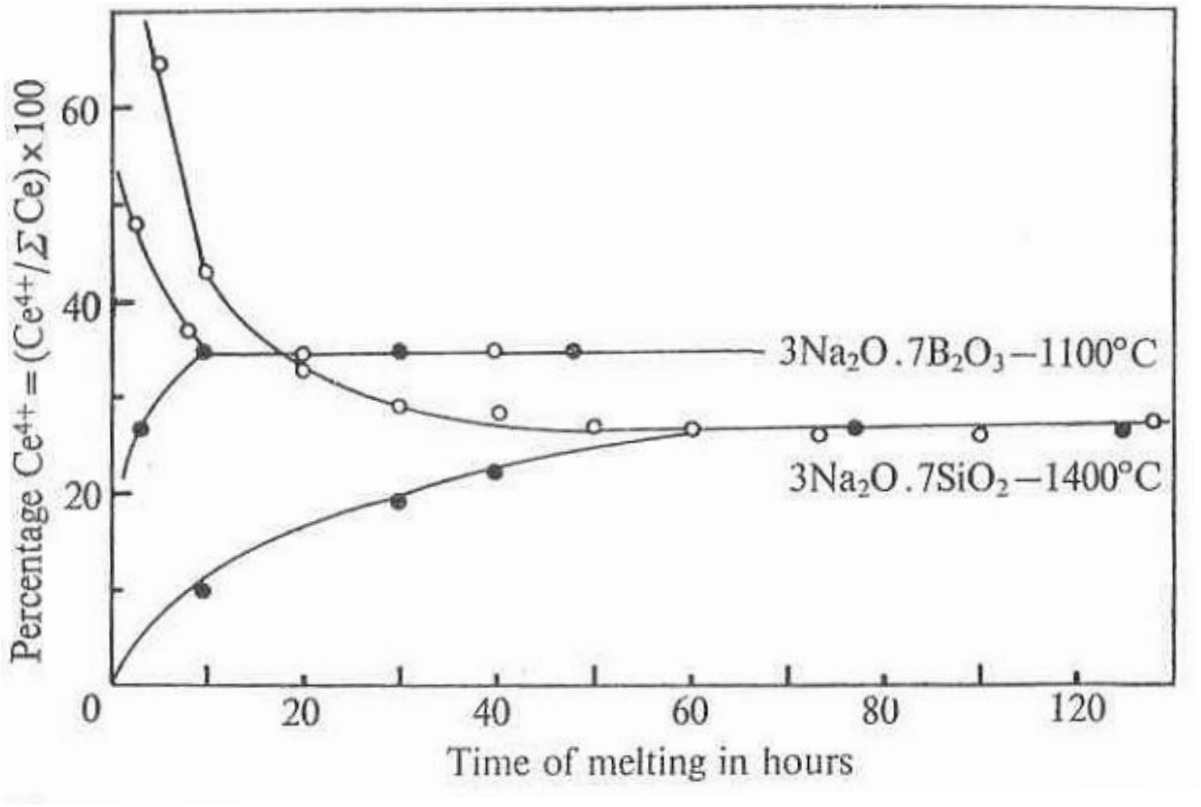

Figure 2.11: Redox equilibration times for different glass compositions and starting raw materials (•: $CeO_2(Ce^{4+})$, ○: cerous oxalate (Ce^{3+})) [PD65]

2.3.4 Mutual redox interaction between different polyvalent ions

In the case of more than one redox oxide present in the glass melt, the equilibration process becomes more complex due to reciprocal interaction between different polyvalent ions during the cooling process, when temperatures are too low for oxygen diffusion between melt and atmosphere. At the melting temperature, the mutual interaction can be neglected and all redox oxides (here represented by A and B) interact independently with the furnace atmosphere [Pau82, Brü85] corresponding to eq. (2.11):

$$\mathrm{A}^{\mathrm{m}+} + \frac{n}{4}\mathrm{O}_2 \rightleftharpoons \mathrm{A}^{(\mathrm{m}+\mathrm{n})+} + \frac{n}{2}\mathrm{O}^{2-} \tag{2.19}$$

$$\mathrm{B}^{\mathrm{p}+} + \frac{q}{4}\mathrm{O}_2 \rightleftharpoons \mathrm{B}^{(\mathrm{p}+\mathrm{q})+} + \frac{q}{2}\mathrm{O}^{2-} \quad . \tag{2.20}$$

During the casting of the melt, the temperature decreases in seconds to the cooling temperature T_C ($T_C \approx T_g$). The oxygen exchange with the atmosphere freezes in at a fictive temperature between T_m and T_C. During this period the only exchange of

oxygen can be realized between the polyvalent ions in the glass melt, which happens on time scales which are much shorter than the diffusion driven oxygen exchange process. The mutual interaction times at 1400 °C in a glass melt are approximately of the order of 10^{-9} s [Par12], if we consider these to change in proportion to diffusion/viscosity (about a factor 10^{12} from 1400 °C to T_g) we can estimate a freezing in of these processes at around T_g (corresponding to $t_{\text{int}} \approx 10^3$ s). If the redox potentials of R_{A} and R_{B} are different (i.e. the free energy change of reactions eq. (2.19)-(2.20) are different in the glass at a particular temperature), the redox pairs will interact and shift each of the above equilibria in a way that the redox pair with a higher redox potential will be oxidized by the redox pair with the lower redox potential [Pau82, KRW38]. The redox potential R can hereby be related to the ease of reduction in the melt, the lower R the easier the ion gets reduced:

$$q\text{A}^{\text{m}+} + n\text{B}^{(\text{p}+\text{q})+} \underset{R_{\text{B}}>R_{\text{A}}}{\overset{R_{\text{A}}>R_{\text{B}}}{\rightleftharpoons}} q\text{A}^{(\text{m}+\text{n})+} + n\text{B}^{\text{p}+} \quad . \tag{2.21}$$

As these interactions proceed at much smaller length scales ($\approx$ nm) and time scales ($\approx$ ns [Par12]), they can proceed to completion as the reaction times are much shorter than the cooling process. Schreiber et al. [SPBS96a] showed this exemplary for the redox interaction of Fe and Cr ($R_{\text{Fe}} > R_{\text{Cr}}$). 3 melts were melted at 1400 °C and 1100 °C containing single dopants and the combination of both. The determination of the redox species was performed by chemical analysis at room temperature. The results are shown in tab. 2.2 and are consistent with eq. (2.22):

$$3\text{Fe}^{2+} + 1\text{Cr}^{6+} \overset{R_{\text{Fe}}>R_{\text{Cr}}}{\longrightarrow} 3\text{Fe}^{3+} + 1\text{Cr}^{3+} \quad . \tag{2.22}$$

T_m=1400°C	Fe^{2+}	Fe^{3+}	Cr^{3+}	Cr^{6+}
+ Fe	0.130	0.850	-	-
+ Cr	-	-	0.049	0.006
+ Fe&Cr	0.112 (Δ=-3 · 0.006)	0.868(Δ=+3 · 0.006)	0.055(Δ=+0.006)	0(Δ=-0.006)

T_m=1100°C	Fe^{2+}	Fe^{3+}	Cr^{3+}	Cr^{6+}
+ Fe	0.024	0.956	-	-
+ Cr	-	-	0.039	0.016
+ Fe&Cr	0 (Δ=-3 · 0.008)	0.980(Δ=+3 · 0.008)	0.047(Δ=+0.008)	0.008(Δ=-0.008)

Table 2.2: Determination of redox species for 3 different doping compositions: 0.980 wt% Fe-oxide, 0.055 wt% Cr-oxide, 0.980 wt% Fe-oxide + 0.055 wt% Cr-oxde for two melting temperatures 1400 °C (upper table) and 1100 °C (lower table)

The redox potentials of different species are strongly dependent on melting conditions

(T_m, p_{O_2}) and chemical composition and therefore also the equilibration constant (eq. (2.21)) is unknown [LB86, PD96]. Although the value of the redox potential for a particular redox ion pair is quite sensitive to the melting conditions and glass composition, the order of the different species appears to be relatively independent [Sch87]. Therefore the character of different redox oxides as either oxidizing or reducing agent can still be predicted. Redox series from different authors for different glass systems and melting conditions are listed in tab. 2.3:

Ref.	glass system	redox potential series
[LB86]	$10Na_2O$-$90B_2O_3$	$Ti^{43} > Cu^{21} > Fe^{32} > V^{54} > Cr^{63} > Mn^{32} > Co^{32}$
	50 Na_2O - 50 B_2O_3	$Ti^{43} > Fe^{32} > V^{54} > Cu^{21} > Cr^{63} > Mn^{32} > Co^{32}$
[Par12]		$Sn^{42} > Fe^{32} > Sb^{53} > As^{53} > V^{54} > Ce^{43} > Mn^{32} > Cr^{63}$
[Tre60]		$Sn^{42} > Fe^{32} > Sb^{53} > As^{53} > Ce^{43} > Mn^{32} > Cr^{63}$
[Joh65]	Na_2O-$2SiO_2$	$Ti^{43} > Sn^{42} > Fe^{32} > Sb^{53} > Ce^{43} > Mn^{32} > Co^{32} > Ni^{32}$
[SJT80a]	CaO-MgO-Al_2O_3-SiO_2	Ti^{43} » $Eu^{32} > Cr^{32} > Fe^{32} > Ce^{43}$
[KRW38]		$Ti^{43} > Sn^{42} > Fe^{32} > As^{53} > Cu^{21} > Ce^{43} > Mn^{32} > Cr^{63}$
[Bam77]		$Ti^{43} > Sn^{42} > Fe^{32} > Sb^{53} > As^{53} > Cu^{21} > V^{53} > Ce^{43} > Mn^{32} > Cr^{63} > Co^{32} > Ni^{32}$

Table 2.3: Redox potential series determined by different authors for different glass systems

$Ti^{3+/4+}$ always has a very high redox potential which means, that the oxidized state is comparatively stable, whereby $Sb^{3+/5+}$, $As^{3+/5+}$ and $Ce^{3+/4+}$ already show a dominant presence of the reduced species at already low melting temperatures and can therefore be used as oxidizing agents for ions with higher redox potential as for example $Ti^{3+/4+}$ [Bam77, HJ27]. This type of redox behavior also makes these oxides suitable as refining agents [She05b]. If Sb_2O_5 is added to the glass batch (usually additions of 0.1-1.0 wt% for commercial glasses), it liberates oxygen gas during the melting which sweeps out dissolved gases (for example from carbonate or nitrate-based raw materials). During the cooling the situation is reversed, the mainly as Sb^{3+} present antimony now absorbs oxygen from remained bubbles in the glass which were not swept out during the initial heating:

$$Sb_2O_5 \underset{T\downarrow}{\overset{T\uparrow}{\rightleftharpoons}} Sb_2O_3 + O_2 \uparrow \quad . \tag{2.23}$$

Usually Sb_2O_3 resp. As_2O_3 is used as raw material which transforms already at low temperatures (before the melting process) to Sb_2O_5, therefore antimony oxide additives will be written as Sb_2O_5 throughout this work. These refining agents are necessary to cast bubble free glasses, as the cooling process is too fast to ensure a long enough diffusion time for the oxygen to equilibrate with the furnace atmosphere.

Refining agents are important additives to ensure bubble free glasses [Noe97]. For this glass-ceramic system, they are further essential in their function as oxidizing agent to prevent the reduction of Ti^{4+}. During the melting additional oxygen is provided, so less Ti^{3+} is formed (if the redox equilibrium is not reached) and during the cooling the refining agent reoxidizes the Ti^{3+} via eq. (2.21). Using eq. (2.14) the degree of reduction χ_{red} can be expressed as:

$$\chi_{red} = \frac{c_{red}}{c_{red} + c_{ox}} \overset{(2.14)}{=} \frac{1}{1 + C_0 \exp\left(-\frac{\Delta H_0}{RT}\right)} \quad . \tag{2.24}$$

With the use of experimental data from Johnston [Joh65] (for $Sb^{3+/5+}$) and Paul et al. [PD65] (for $Ce^{3+/4+}$), typical values for C_0, ΔH_0 for different glass systems could be evaluated by fitting eq. (2.24). It can be seen in fig. 2.12 that with decreasing basicity Λ the melting conditions become more reducing as expected.

Ref.	Ion	glass system	Λ	C_0	ΔH_0[kcal]	$T_{10\%}$	$T_{50\%}$	$T_{90\%}$	$T_{95\%}$
[Joh65]	Sb	Na_2O-2SiO_2	0.61	$1.89 \cdot 10^{-8}$	-52.4	1050	1210	1420	1500
[PD65]	Ce	3Na_2O-7SiO_2	0.60	$3.42 \cdot 10^{-4}$	-23.8	900	1230	1800	2110
	Ce	3K_2O-7B_2O_3	0.56	$1.58 \cdot 10^{-3}$	-18.3	790	1160	1890	2360
	Ce	3Li_2O-7B_2O_3	0.49	$1.12 \cdot 10^{-2}$	-7.3	290	560	1390	2240

Table 2.4: Fit results for the temperature dependence of χ_{red} (temperatures in °C)

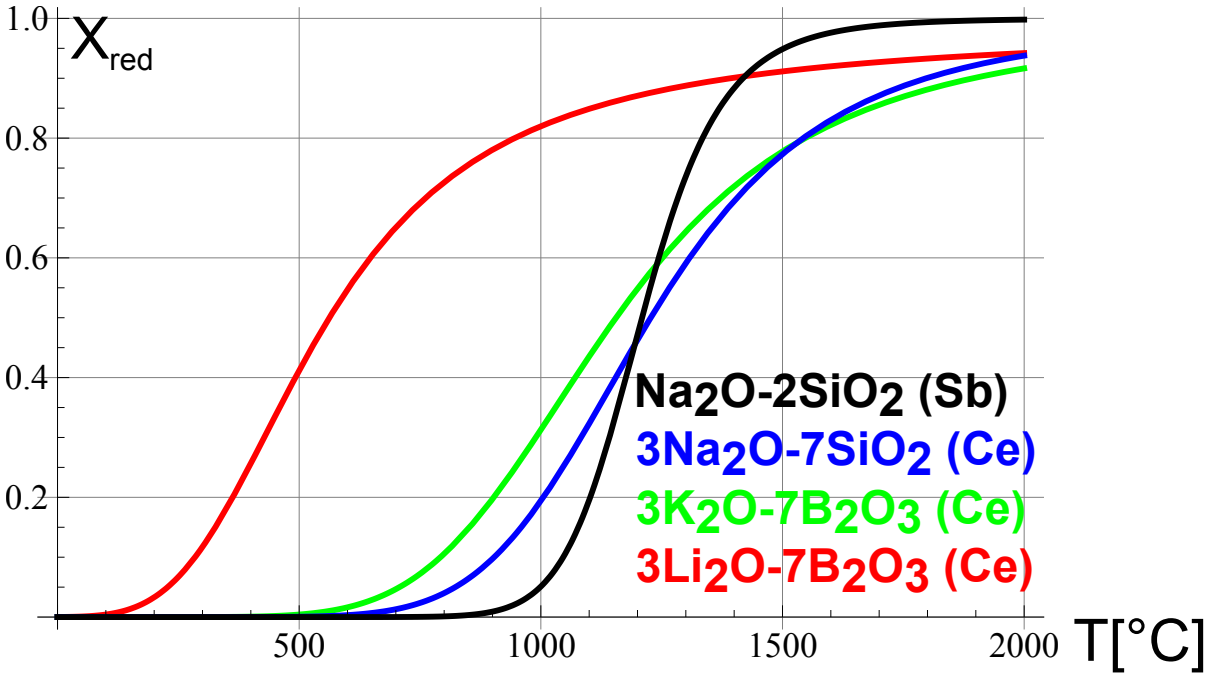

Figure 2.12: Temperature dependence of χ_{red} for Sb and Ce in different chemical environment

The comparison between CeO_2 and Sb_2O_5 shows why Sb_2O_5 is a stronger refining agent. It releases/absorbs twice more oxygen per ion and works in a much narrower temperature range. Even though in both cases it can be seen that the curves saturate at higher temperatures and that even at high melting temperatures (1500-1600 °C) considerable amounts of the oxidized ion are still present, which then are able to reoxidize for example Ti^{3+} during the cooling via eq. (2.21):

$$Ti^{3+} + Ce^{4+} \overset{R_{Ti} \gg R_{Ce}}{\longrightarrow} Ti^{4+} + Ce^{3+} \quad . \tag{2.25}$$

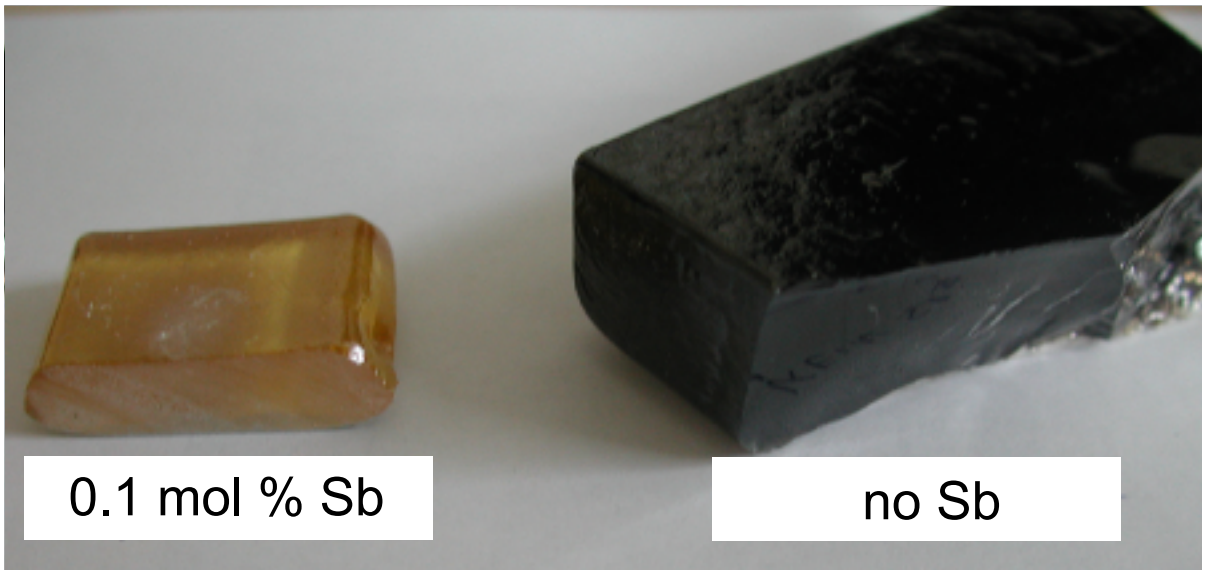

Figure 2.13: La_2O_3-TiO_2-SiO_2-B_2O_3 glass 37778 with and without Sb_2O_5 (0.1 mol%)

Optimal experimental methods to investigate the concentration changes of the redox ions are EPR and optical transmission methods as they show comparatively good detection limits and also for optical transmission measurements quantitative results can be obtained. Other possible methods like XANES, EXAFS or chemical methods were not investigated due to their comparatively lower resolution limit.

2.4 Permittivity

2.4.1 Macroscopic and microscopic polarization

The interaction between electromagnetic fields and solids can be described in a microscopic or macroscopic way. Under the influence of an electric field $\mathbf{E}$ positive and negative charges are displaced in opposite direction and thereby create dipoles which contribute to a macroscopic polarization $\mathbf{P}$. In a linear dielectric the polarization can be described in dependence of the applied external electric field by:

$$\mathbf{P} = \varepsilon_0 \chi_e \mathbf{E} \quad , \tag{2.26}$$

with vacuum permittivity ε_0 = $8.854 \cdot 10^{-12} \frac{\mathrm{A\,s}}{\mathrm{V\,m}}$ and the material specific dielectric susceptibility χ_e.
For cubic crystals or amorphous solids χ_e is a scalar quantity (isotropic), but in general a symmetric 2nd-order tensor (for the sake of simplicity χ_e will be treated as scalar in the following). The definition of the electric displacement field $\mathbf{D}$ follows from eq. (2.26):

$$\mathbf{D} = \varepsilon_0 \mathbf{E} + \mathbf{P} = \varepsilon_0 (\underbrace{1 + \chi_e}_{=\varepsilon_r}) \mathbf{E} = \varepsilon \mathbf{E} \quad , \tag{2.27}$$

with the permittivity $\varepsilon = \varepsilon_0 \varepsilon_r$.
The simple expression for the polarization in eq. (2.26) is only valid for time-independent fields in the frequency domain, as the displacement of charges by the external field can not take place instantaneously. In the time domain the dependence is given by:

$$\mathbf{P}(t) = \varepsilon_0 \int_{-\infty}^{t} \chi_e(t - t') \mathbf{E}(t') \, \mathrm{d}t' \quad . \tag{2.28}$$

Using Fourier transformation with the use of the convolution theorem leads to:

$$\mathbf{P}(\omega) = \varepsilon_0 \chi_e(\omega) \mathbf{E}(\omega) \quad \Leftrightarrow \quad \mathbf{D}(\omega) = \varepsilon(\omega) \mathbf{E}(\omega) \quad . \tag{2.29}$$

Assuming a harmonic time dependence ($\mathbf{E}(\mathbf{r}, t) = \mathbf{E}(\mathbf{r}) e^{-i\omega t}$) the generalized Ampère law can be written as:

$$\nabla \times \mathbf{H} = \mathbf{j}_L \underbrace{- i\omega \mathbf{D}}_{=\mathbf{j_V}} \quad . \tag{2.30}$$

A non-vanishing electric current density $\mathbf{j}_L = \sigma\mathbf{E}$ (Ohm's law) leads to ohmic losses in the material:

$$\nabla \times \mathbf{H} = \sigma\mathbf{E} - i\omega\mathbf{D} = -i\omega \underbrace{\left(\varepsilon + i\frac{\sigma}{\omega}\right)}_{:=\varepsilon^*} \mathbf{E} = -i\omega\varepsilon^*\mathbf{E} \quad . \tag{2.31}$$

The complex relative permittivity of a material is then defined as [Hun09]:

$$\varepsilon_r^* = \frac{\varepsilon^*}{\varepsilon_0} = \frac{1}{\varepsilon_0}\left(\varepsilon + i\frac{\sigma}{\omega}\right) = \varepsilon_r' + i\varepsilon_r'' = \varepsilon_r'(1 + i \underbrace{\tan(\delta)}_{=\frac{\varepsilon_r''}{\varepsilon_r'}=\frac{|\mathbf{j_L}|}{|\mathbf{j_V}|}}) \quad . \tag{2.32}$$

$\tan(\delta)$ equals the ratio of imaginary part to real part, respectively the ratio of electric current density to displacement current density and therefore represents a direct measure of the existing losses.
Furthermore it should be mentioned, that real and imaginary part are not independent functions (see [Pap62]). This dependence is generally valid for complex functions $f(z)$ with $z = \omega + i\epsilon$, which are analytic in the range $\mathrm{Im}(z) \geq 0$ and approach zero for $|z| \to \infty$ ($\lim_{|z|\to\infty} |f(z)| = 0$). This properties are valid for the complex permittivity. The so-called Kramers-Kronig relation describes the relation between $\varepsilon_r'(\omega)$ and $\varepsilon_r''(\omega)$:

$$\varepsilon_r'(\omega) = 1 + \frac{2}{\pi}\int_0^\infty \frac{\omega'\varepsilon_r''(\omega')}{\omega'^2 - \omega^2}\,\mathrm{d}\omega' \tag{2.33}$$

$$\varepsilon_r''(\omega) = \frac{2\omega}{\pi}\int_0^\infty \frac{\varepsilon_r'(\omega')}{\omega'^2 - \omega^2}\,\mathrm{d}\omega' \quad . \tag{2.34}$$

It is obvious, that in each case either the real or imaginary part has to be known for a large frequency range to determine the other unknown part.
After having considered the macroscopic description, the microscopic explanation for the polarization mechanism inside a dielectric will be briefly summarized. In fig. 2.14(a) $\varepsilon_r'(\omega)$ for an ionic crystal is shown. The overall polarization consists of 3 parts which only contribute in special frequency ranges. Dipolar polarization only exists for materials which contain permanent dipoles and contributes only until the microwave frequency range. Ionic polarization describes the displacement of charged ions from their equilibrium lattice position by the external electric field and contributes only until the infrared range. The third part is the electronic polarization which represents the contributions of electronic excitations (e.g. displacement of the electron density against the atomic core, excitations of electron-hole pairs) and contributes until the UV range.

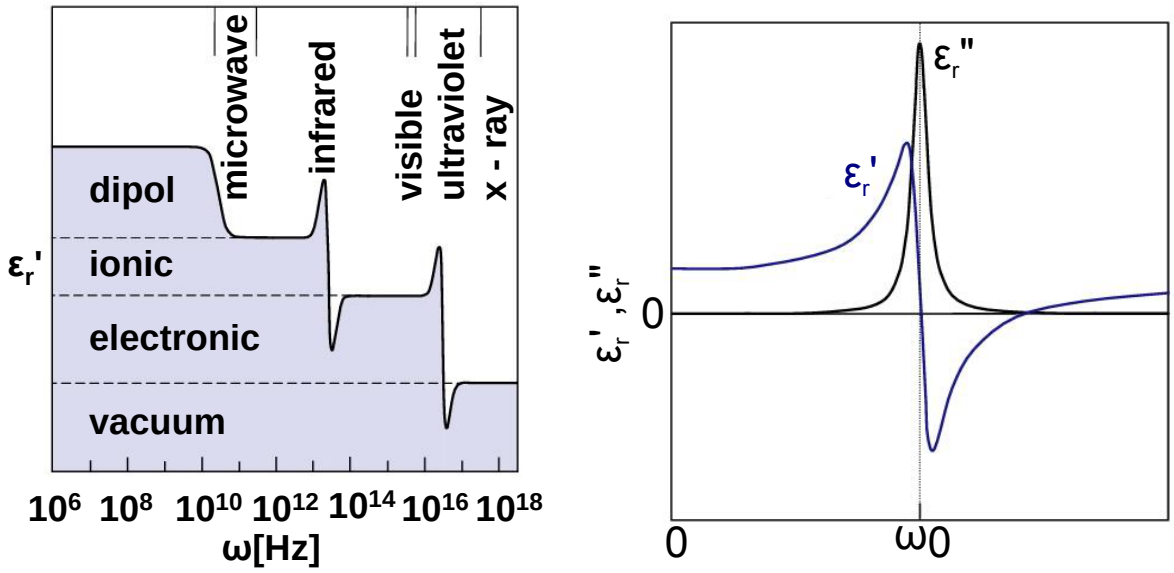

(a) Schematic representation of the contributions of $\varepsilon_r'(\omega)$ for an ionic crystal (modified [Hun09])

(b) Frequency dependence of $\varepsilon_r'(\omega)$ and $\varepsilon_r''(\omega)$ for the oscillator model (modified [Hun09])

Figure 2.14

The electronic polarization can be described comparatively accurate with a simple damped harmonic oscillator model (first mentioned by H. Lorentz). The idea for this model is the following, bound electrons around the core are excited to forced vibrations by an electromagnetic wave. The real and imaginary part of the permittivity are then given by eq. (2.35)-(2.36), which are shown in fig. 2.14(b):

$$\varepsilon'(\omega) = 1 + \frac{n_e e^2}{\varepsilon_0 m_e} \frac{\omega_1^2 - \omega^2}{(\omega_1^2 - \omega^2)^2 + \gamma^2\omega^2} \tag{2.35}$$

$$\varepsilon''(\omega) = \frac{n_e e^2}{\varepsilon_0 m_e} \frac{\gamma\omega}{(\omega_1^2 - \omega^2)^2 + \gamma^2\omega^2} \quad , \tag{2.36}$$

m_e is the electron rest mass, n_e the electron density, ω_1 the resonance frequency and γ the damping. It can be seen in fig. 2.14(b), that the losses are mainly confined to a narrow range around the resonance frequency ω_1. The ionic polarization contribution can be described with a similar ansatz and leads to a similar dependence for $\varepsilon_r^*(\omega)$:

$$\varepsilon'(\omega) = \varepsilon'(\infty) + \sum_i \frac{4\pi\rho_i \cdot \omega_i^2(\omega_i^2 - \omega^2)}{(\omega_i^2 - \omega^2)^2 + \gamma_i^2\omega^2} \tag{2.37}$$

$$\varepsilon''(\omega) = \sum_i \frac{4\pi\rho_i \cdot \omega_i^2(\gamma_i\omega)}{(\omega_i^2 - \omega^2)^2 + \gamma_i^2\omega^2} \quad , \tag{2.38}$$

ω_i, γ_i, ρ_i are resonance frequency, damping and oscillator strength of the i-th IR active

optical phonon mode. $\varepsilon'(\infty)$ is the permittivity at high frequencies (for example in the optical frequency range), at which only the electronic polarization contributes. Measurements of the refractive index at optical frequencies ($\approx$ 400 THz) for the investigated glass of this work resulted in values of n_r = 1.95-2.00 resp. ε_r = 3.8-4.2 (with $\varepsilon_r = n_r^2$). For the here investigated glasses and glass-ceramics the dominant amount is obviously contributed by the ionic polarization (ε_r(10 GHz) $\approx$ 20). For the GHz frequency range the following assumption can be made: $\omega, \gamma_i \ll \omega_i$ (see fig. 2.14, $\omega_i \approx$ THz), which leads to the following proportionality for the ratio of real to imaginary part of the permittivity:

$$\underbrace{\frac{\varepsilon''}{\varepsilon'}}_{:=Q^{-1}} = \frac{\sum_i 4\pi\rho_i \cdot \gamma_i/\omega_i^2}{\varepsilon'(\infty) + \sum_i 4\pi\rho_i} \cdot \omega \tag{2.39}$$

$$\Rightarrow Q \cdot f = \text{const.} \quad . \tag{2.40}$$

The product $Q \cdot f$ is often used in literature as material specific parameter to characterize the dielectric loss. If only intrinsic losses (as described by eq. (2.40)) are present Qf should be frequency independent, but mostly other extrinsic contributions are present and therefore the Qf value in combination with a frequency value is stated.

2.4.2 Mixtures of dielectrics with different permittivity

For multiphase systems (e.g. glass-ceramics) different models exist to determine the overall permittivity from the permittivities of the individual phases. With the help of these models an estimation for the permittivity of the residual glass phase in the investigated glass-ceramic systems can be made. Maxwell derived a relation for the total permittivity ε_{tot} of a system of randomly located spheres with permittivity ε_K and volume fraction V_K inside a matrix of permittivity ε_G ([MH03]):

$$\varepsilon_{\text{tot}} = \varepsilon_G \left(1 + \frac{3V_K(\varepsilon_K - \varepsilon_G)}{\varepsilon_K + 2\varepsilon_G - V_K(\varepsilon_K - \varepsilon_G)}\right) \quad . \tag{2.41}$$

This model is suitable for small crystal phase contents (< 10 %: isolated crystals). For higher crystal phase contents a more suitable choice is the Lichtenecker model [MH03]. It describes the system as randomly distributed and oriented capacitances (serial or parallel) of different permittivity. The capacitance of a capacitor which incorporates these dielectrics of different permittivity, depends on their spatial distribution. For parallel positioning it follows $\varepsilon_{\text{tot}} = \sum_i V_i\varepsilon_i$ and at serial positioning $\varepsilon_{\text{tot}}^{-1} = \sum_i V_i\varepsilon_i^{-1}$.

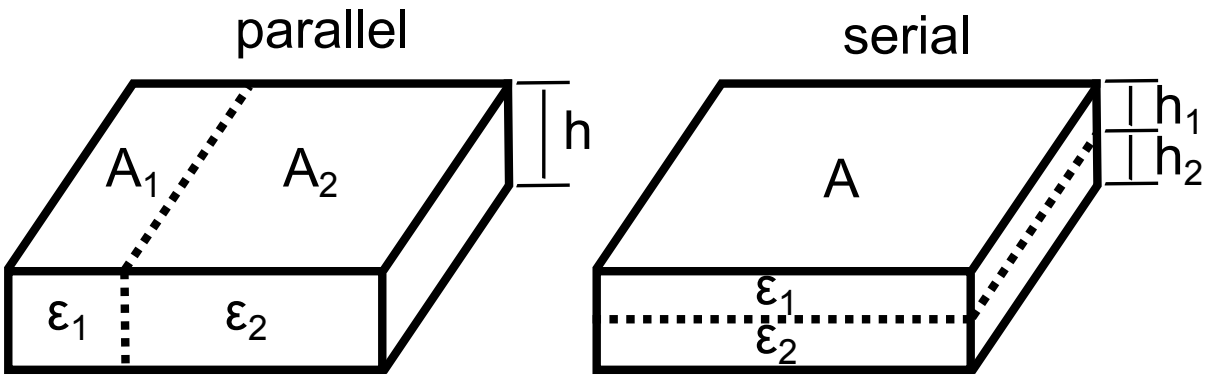

Figure 2.15: Different positioning of phases in a capacitor (modifield from[MH03])

These expressions can be generalized to eq. (2.42) with n = -1 (serial) or n = +1 (parallel). For an unknown random distribution we choose an $\bar{n} = 0$ resp. n approaches zero. The total permittivity is then calculated with the use of the approximation $x^n = 1 + n\ln(x)$ (for small n):

$$\varepsilon_{\text{tot}}^n = \sum_i V_i \varepsilon_i^n \quad \overset{\lim n \to 0}{\Longrightarrow} \quad \ln(\varepsilon_{\text{tot}}) = \sum_i V_i \ln(\varepsilon_i) \quad . \tag{2.42}$$

Even if the derivation of this relation is questionable from a theoretical point of view, it shows in comparison with other theoretical models [PP07] the best consistency with experimental results ($\Delta\varepsilon/\varepsilon < 5\%$).

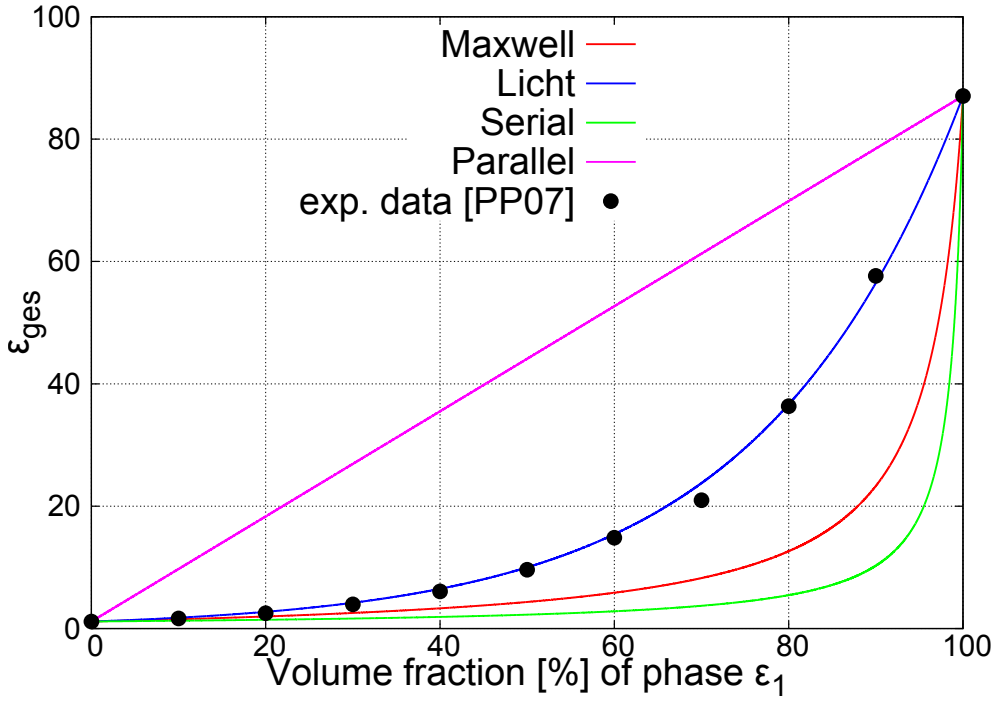

Figure 2.16: Comparison of different models using the experimental data of [PP07] for ε_1 = 87.05 and ε_2 = 1.15

2.5 Q factor and losses

In chapter 3.9.1 it will be shown, that the electromagnetic modes show discrete resonance frequencies under assumption of ideal/loss-free materials. This would correspond to a frequency dependence equivalent to a Dirac delta function $\delta(\omega)$. In reality, this delta function is broadened in a narrow frequency range around the resonance due to the existing losses. Main contributions are ohmic losses in the metal walls and dielectric losses in the materials depending on the used experimental setup. A measure for the broadening of a resonance mode is the so-called Q factor. From a measurement of the resonance excitation spectrum, Q can be determined and with the help of theoretical models of the different loss contributions (ohmic, radiation, dielectric, etc.) the relevant dielectric loss of the material can be extracted.
Q is defined as 2π times the ratio of the time averaged stored electromagnetic field energy inside the resonator (here: U) to the energy dissipation per frequency cycle. From the conservation of energy it follows that the negative rate of change of the stored field energy with time has to equal the dissipation energy. Therefore it follows ([Jac99]):

$$Q = 2\pi \frac{U}{(-\dot{U}) \cdot T} = -\omega_0 \frac{U}{\dot{U}} \quad . \tag{2.43}$$

Solving of eq. (2.43) leads to an exponentially decreasing solution $U(t)$ with decay constant inversely proportional to Q.

$$\dot{U} = -\frac{\omega_0}{Q} \cdot U \quad \Longrightarrow U(t) = U_0 e^{-\frac{\omega_0}{Q} t} \tag{2.44}$$

As $U(t) \sim |\mathbf{E}(t)|^2$, a damped oscillation follows for the fields:

$$E(t) = E_0 e^{-\frac{\omega_0}{2Q} t} e^{-i(\omega_0 + \Delta\omega)t} \quad . \tag{2.45}$$

Due to the damping ($\gamma = \omega_0/2Q$) the undamped resonance frequency ω_0 shifts to $\omega = \sqrt{w_0^2 - \gamma^2} = \omega_0 + \Delta\omega$, which leads for $Q \gg 1$ to $\Delta\omega \approx -\omega_0 \cdot \frac{1}{8Q^2}$.
From eq. (2.45) it follows via Fourier transformation, that the frequency dependence of a damped oscillator does not consist of a singular frequency but a superposition of frequencies around $\omega = \omega_0 + \Delta\omega$:

$$E(\omega) = \frac{1}{\sqrt{2\pi}} \int_0^\infty E_0 e^{-\frac{\omega_0}{2Q} t} e^{-i(\omega_0 + \Delta\omega)t} e^{+i\omega t} \, \mathrm{d}t \quad . \tag{2.46}$$

The Fourier transformation can be calculated analytically and leads to a Lorentz shaped frequency distribution for the energy ($U(\omega) \sim |\mathbf{E}(w)|^2$):

$$U(\omega) \sim \frac{1}{(\omega - \omega_0 - \Delta\omega)^2 + (\omega_0/(2Q))^2} \quad . \tag{2.47}$$

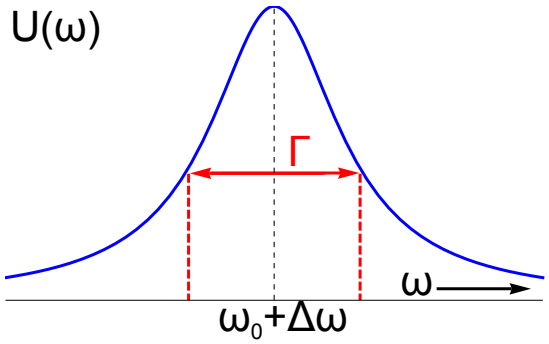

Figure 2.17: Resonance curve with FWHM Γ

From the FWHM Γ the Q factor can be determined via $Q = \frac{\omega_0}{\Gamma}$ (follows from eq. (2.47)). From the measured overall Q, the different loss contributions can be determined for systems with known field geometries. In chapter 3.9.1 the corresponding mathematical expressions for the Hakki-Coleman (eq. (3.32)) and the cavity resonance method (eq. (3.70)) are given.

Losses in metallic conductors

An EM wave with wave vector k, which hits a conducting surface, enters the material in case of a non-ideal conductor (finite conductivity σ, permeability μ). The fields inside the conductor lead to electric surface currents $\mathbf{J_S}$ and therefore to Joule losses. Solving Maxwell's equations in proximity of a conducting half space ($z > 0$) leads to the following EM fields inside the conductor [Jac99]:

$$\mathbf{E}(z) \sim e^{ikz} e^{-z/\delta_0} \quad \text{, with} \quad \delta_0 = \sqrt{\frac{2}{\omega\mu\sigma}} \quad . \tag{2.48}$$

The characteristic distance $\delta_0 = \sqrt{\frac{2}{\omega\mu\sigma}}$ is termed as skin depth. For GHz frequencies δ_0 is in the µm range: δ(1 GHz, σ_{copper}) = 0.3 µm. It can be shown that the Joule loss P_{loss} depends on the surface current density $\mathbf{J_S}$ in the following way [Jac99]:

$$\frac{\mathrm{d}P_{\text{loss}}}{\mathrm{d}A} = \frac{1}{2} \underbrace{\frac{1}{\sigma\delta_0}}_{=R_S} \cdot |\mathbf{J_S}|^2 \quad . \tag{2.49}$$

The surface resistivity $R_S = \sqrt{\pi\mu f/\sigma}$ plays an important role for the determination of the Q values with the GHz characterization methods (see chapter 3.9.1).

2.6 Temperature coefficient τ_f

The temperature dependent shift of the resonance frequency can be described by the temperature coefficient of resonance frequency τ_f. Antennas which are used in mobile applications are used under different temperature conditions and should therefore have a small temperature dependence to achieve a stable working frequency during operation. For a DR antenna, τ_f is a composite parameter related to the temperature coefficient of the permittivity τ_ε and the linear thermal expansion coefficient of the dielectric α_L:

$$\tau_f(\tau_\varepsilon, \alpha_L) = \frac{1}{f_0}\frac{\partial f_0}{\partial T} = -\frac{1}{2}\tau_\varepsilon - \alpha_L = -\frac{1}{2}\frac{1}{\varepsilon_r}\frac{\partial \varepsilon_r}{\partial T} - \frac{1}{D}\frac{\partial D}{\partial T} \quad . \tag{2.50}$$

This relation is valid exactly for a one-dimensional resonator of length D and permittivity ε_r. As for example an infinitely extended dielectric slab with metallic boundary conditions and thickness $D \ll H_i$ and lengths $H_i \to \infty$. In this system resonances occur if the thickness D is a multiple of the half effective wavelength λ_{eff}:

$$p \cdot \frac{\lambda_{\text{eff}}}{2} = p \cdot \frac{\lambda_0}{2\sqrt{\varepsilon_r}} \stackrel{!}{=} D \quad , p \in \mathbb{N}. \tag{2.51}$$

The resonance frequency is then given via $f_0 = \frac{c}{\lambda_0}$:

$$f_0 = \frac{p \cdot c}{2} \cdot \frac{1}{D\sqrt{\varepsilon_r}} \quad . \tag{2.52}$$

To determine the relation (2.50) from eq. (2.52) the temperature dependence of f_0 is required:

$$f(T + \mathrm{d}T) = f(\varepsilon_r(T), D(T), H_i(T)) + \frac{\partial f}{\partial \varepsilon_r}\frac{\partial \varepsilon_r}{\partial T}\mathrm{d}T + \frac{\partial f}{\partial D}\frac{\partial D}{\partial T}\mathrm{d}T + \sum_{i=1}^{2}\frac{\partial f}{\partial H_i}\frac{\partial H_i}{\partial T}\mathrm{d}T \tag{2.53}$$

$$\Rightarrow \quad \frac{1}{f}\frac{\partial f}{\partial T} = \underbrace{\left[\frac{\varepsilon_r}{f}\frac{\partial f}{\partial \varepsilon_r}\right]}_{:=a_\varepsilon}\underbrace{\frac{1}{\varepsilon_r}\frac{\partial \varepsilon_r}{\partial T}}_{=\tau_\varepsilon} + \underbrace{\left[\frac{D}{f}\frac{\partial f}{\partial D}\right]}_{:=a_D}\underbrace{\frac{1}{D}\frac{\partial D}{\partial T}}_{=\alpha_L} + \sum_{i=1}^{2}\underbrace{\left[\frac{H_i}{f}\frac{\partial f}{\partial H_i}\right]}_{:=a_{H_i}}\underbrace{\frac{1}{H_i}\frac{\partial H_i}{\partial T}}_{=\alpha_L} \quad . \tag{2.54}$$

We can derive a general expression for τ_f and the coefficients a_ε, a_D und a_{H_i} (assumption of an isotropic solid):

$$\tau_f = a_\varepsilon \cdot \tau_\varepsilon + (a_D + a_{H_1} + a_{H_2}) \cdot \alpha_L \quad . \tag{2.55}$$

For the special case of the infinitely extended dielectric slab with metallic boundary conditions we can confirm the coefficients of eq. (2.50) with the use of eq. (2.52):

$$\frac{\partial f_0}{\partial \varepsilon_r} = \left(-\frac{1}{2}\right)\frac{f_0}{\varepsilon_r} \qquad \Longleftrightarrow \qquad a_\varepsilon = -\frac{1}{2} \tag{2.56}$$

$$\frac{\partial f_0}{\partial D} = (-1)\frac{f_0}{D} \qquad \Longleftrightarrow \qquad a_D = -1 \tag{2.57}$$

$$\frac{\partial f_0}{\partial H_i} = 0 \qquad \Longleftrightarrow \qquad a_{H_i} = 0 \quad . \tag{2.58}$$

f_0 of the Hakki-Coleman method can be expressed implicitly (see eq. (3.26)) as:

$$f_0 = \frac{c}{2\pi}\sqrt{\frac{x^2(f_0, \varepsilon_r, a, h, p)}{a^2} + \frac{(p\pi)^2}{h^2}} \cdot \frac{1}{\sqrt{\varepsilon_r}} \quad , \tag{2.59}$$

with a as cylinder radius, h cylinder height, p number of nodes and $x = x_{mnp}(f_0, \varepsilon_r, a, h, p)$ the eigenvalue of the eigenmode characterized by the mode numbers m and n. The calculation of the coefficients a_a, a_h and a_ε is analog to eq. (2.54), but can not be performed analytically anymore. By writing eq. (2.59) in form of the eigenvalue equation $F_2 = F_2(f_0, \varepsilon_r, a, h, p) = 0$ (eq. (3.22), for the case of the TE_{0np} resonance), the following relation can be used to determine the partial derivatives (see [BSMM05]):

$$\frac{\partial f_0}{\partial q}(\varepsilon_r, a, h, p) = -\frac{\frac{\partial F_2}{\partial q}}{\frac{\partial F_2}{\partial f_0}} \quad , q = \varepsilon_r, a, h \quad . \tag{2.60}$$

The temperature coefficient τ_f for the Hakki-Coleman method can be determined to (complete derivation can be found in [Bra11]):

$$\tau_f = \left(-\frac{1}{2} + \Delta a_\varepsilon\right)\tau_\varepsilon - \alpha_L \quad , \tag{2.61}$$

with Δa_ε given by:

$$\frac{\partial f_0}{\partial \varepsilon_r}\frac{\varepsilon_r}{f_0} = a_\varepsilon = -\frac{1}{2} + \underbrace{\left(\frac{\partial x}{\partial \varepsilon_r}\right) \cdot \frac{\frac{x\varepsilon_r}{a^2}}{\frac{x^2}{a^2} + \frac{(p\pi)^2}{h^2}}}_{=\Delta a_\varepsilon} \quad . \tag{2.62}$$

For the permittivity range $\varepsilon_r > 10$, it can be shown that $|\Delta a_\varepsilon| < 0.010$ which leads to a relative deviation of less than 2% in relation to the coefficient -$\frac{1}{2}$. For this permittivity range, the eigenvalue $x(\varepsilon_r)$ can be assumed in good approximation as independent of the permittivity ($\Leftrightarrow \Delta a_\varepsilon = 0$). This approximation leads to a similar frequency dependence as in the case of the dielectric slab ($\Leftrightarrow f_0 \sim \frac{1}{\sqrt{\varepsilon_r}}$).

2.7 High frequency dielectric loss

Stevels [Ste85a, Ste57, Ste85b] gives a schematic picture over the frequency dependence of the dielectric loss for glasses at different temperatures. He classifies the different contributions in 3 types of relaxation phenomena:

- Conduction/migration losses (conductivity due to hopping processes of electrons or ions, with (1): σ_{DC}, dominant for $f < 1$ Hz and (2): σ_{AC}, dominant for $f > 1$ Hz)
- Deformation losses (3) (only detectable at low temperatures, understood as local motions of atoms in their own interstices separated by low potential barriers of ≈ 0.1 eV and therefore comparatively strong temperature dependence)
- Network losses (4) (vibrational losses due to interaction with the phonon modes in the IR)

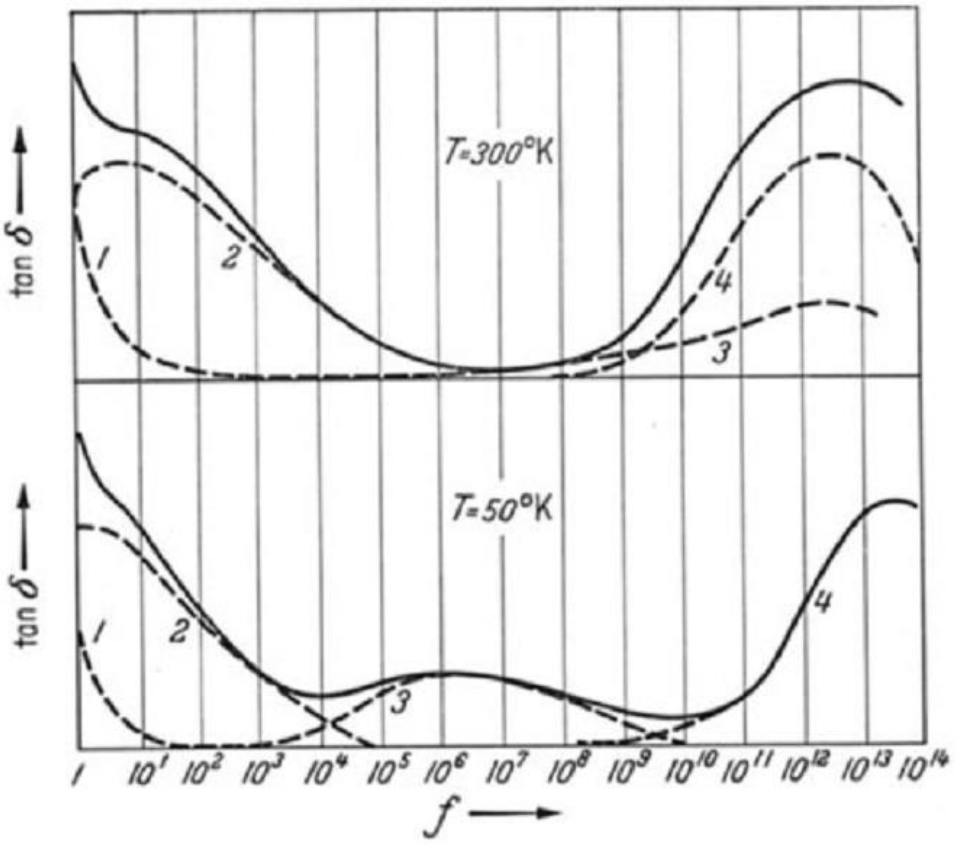

Figure 2.18: Schematic representation of the frequency spectrum of dielectric losses in glass at different temperatures (50 and 300 K) [Ste57]

The $\tan(\delta)$ hereby shows a minimum in the region around 10^{-5} to 10^{-9} Hz and increasing values for higher and lower frequencies [Isa62].

2.7.1 Electrical conductivity

The electrical conductivity of a wide class of conducting materials (including amorphous semiconductors, defect containing single crystals, polymers, ionic conductors and glasses, see fig. 2.19) shows a universal frequency dependence which is given by the phenomenological UDR model (universal dielectric response) proposed by Jonscher [Jon99, Jon81, Jon77]:

$$\sigma(f) = \sigma_{DC} + \sigma_0 f^s \quad . \tag{2.63}$$

The exponent s varies in the range 0.4 to 1 for different materials and the temperature dependence of σ_{DC} and σ_0 follows a thermally activated Arrhenius type behavior. s has a comparatively weak temperature dependence and decreases with increasing temperature. Jonscher [Jon77] states that this model is valid up to GHz frequencies until the low frequency flank of the phonon mode interaction starts to show contributions of the form $\sigma_{\text{pho}} \sim \omega^2 \Leftrightarrow Qf =$ constant (see eq. (2.40)).
The universal physical mechanisms to explain this behavior are still discussed in literature and not fully understood until today [Jon81]. But it is proven empirically as "universal law" independent of

- Physical structure (single-crystal, polycrystalline, amorphous)
- Chemistry (organic, inorganic, biological)
- Mechanism (dipoles, polarons, charge carrier hopping)
- Geometry (bulk/surface, continuous/granular)

and will be used in this work to model the frequency behavior of glass and glass-ceramics materials.
Ionic conductivity contributions in glass are mainly dependent on the amount of alkali or earth-alkali ions [Ste57] which are only present as impurities in the ppm level in the investigated glass systems and therefore are not considered to give any relevant contributions to the dielectric loss especially in the GHz frequency regime.

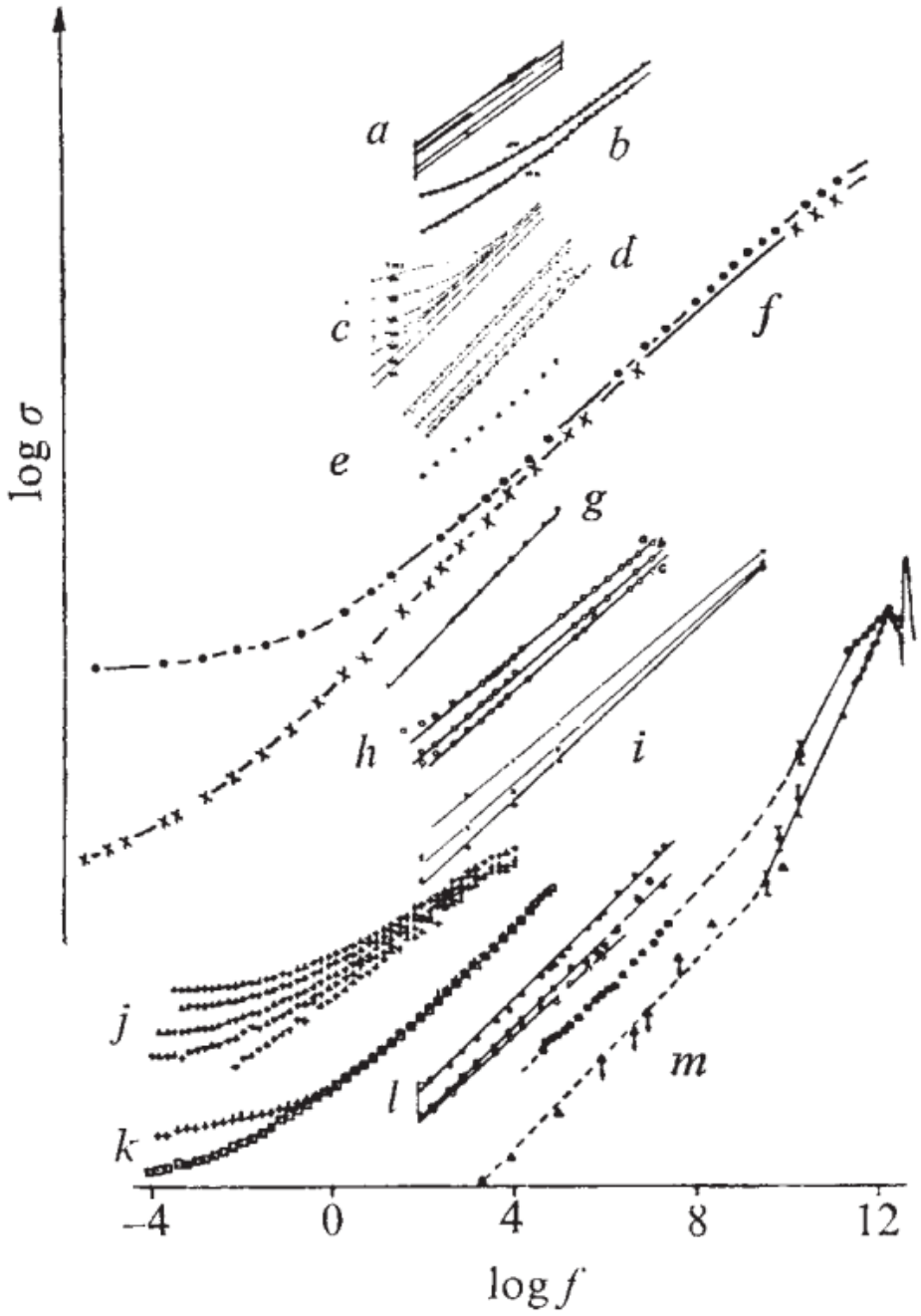

Figure 2.19: Compilation of AC conductivity data for a range of materials [Jon77] (displaced vertically). Curve h shows glasses containing high amounts of transition metals ($50P_2O_5$-(25-x)CaO-(x+25)FeO). a: doped single crystal silicon at T = 3/4/8/12 K, b: Na^+-doped single crystal alumina, c: amorphous silica at T = 84-295 K, d: chalcogenide glasses ($Sb_xAs_{(1-x)}S_{60}$) at 293 K, e: single crystal anthracene, f: single crystal anthracene with evaporated β carotene at 294 K, g: trinitrofluorine-polyvinyl carbazole, i: $4V_2O_5$-P_2O_5 glass at 3 temperatures, j: amorphous SiO at T = 211-297 K, k: stearic acid film between Al/Au electrodes, l: amorphous As_2Se_3, Se, As_2S_3 at 300 K, m: As_2Se_3

Transition metal containing conductive glasses

Most relevant for this work, is the contribution to the electrical conductivity in glasses due to the presence of transition metal ions and in particular the presence of Ti^{3+}, which is well known in literature to influence the conductivity [Pau75, RM78]. Depending on the glass type and concentration of transition metals, conductivity values between 10^{-4} and 10^{-12} S/cm (at 300 K) are observed [MCM79b], classifying these glasses as amorphous semiconductors. The electrical conductivity hereby occurs due to electron hopping processes from an ion of lower valency state to an ion of higher valency [MCM79b] (see eq. (2.9)). As the resulting mobility values are comparatively low ($< 10^{-4}$cm^2/(Vs)), the electron moves so slowly through the lattice that the ligand environment around its host ion has time to adept to the new charge distribution, wherefore the mechanism is described often in literature as small polaron hopping [Sch69, Sch68, Mur82]. The polaron as quasi particle is hereby understood as the electron including the distortion of the lattice near its occupied ion site (see fig. 2.20). The presence of the electron leads to a displacement of neighboring ions (nearest neighbors are mostly negatively charged oxygen anions) due to the electric repulsion. Thereby the electron energy decreases by an amount E_S resulting in an increase of the activation energy ΔE of the hopping process to $W = \Delta E + E_S$, leading to a self-trapping effect.

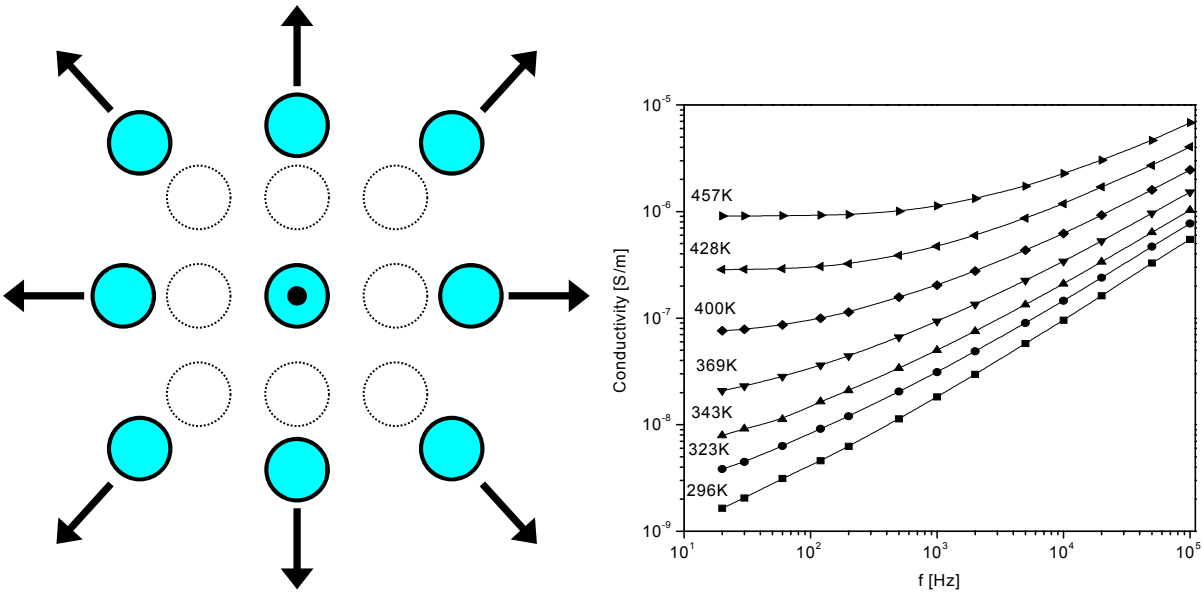

(a) Polaron formation due to displaced lattice atoms/ions by an excess electron (modified from [MB03])

(b) Typical frequency dependence of a small polaron hopping process (P_2O_5-FeO glass) [MB03]

Figure 2.20: Transition metals in glasses leading to small polaron conductivity

The frequency dependence follows the UDR model (eq. (2.63)), whereby the σ_{DC} contribution is described by Mott [Mot68] with a modified Arrhenius law which is closely related to conduction in doped semiconductors:

$$\sigma_{DC} = c(1-c)\frac{A}{T}e^{-\frac{W}{k_B T}} \quad , \tag{2.64}$$

with c as ratio of ion concentration in the reduced state to the total concentration of transition metal ions, A a material specific constant and W the activation energy for the hopping process [SM72].

Ti^{3+} formation in crystals due to donor doping

The formation of Ti^{3+} in crystals by donor doping can be understood in the following way (exemplary for the substitution of Sb^{5+} for Ti^{4+} in the $La_4Ti_9O_{24}$ (= $La_{0.44}Ti_1O_{2.67}$) phase). The ionic radius of Sb^{5+} is with 60 pm (at coordination number 6) very similar to that of Ti^{4+} (60.5 pm). The amount of the reduced Sb^{3+} stays in the residual glass as the ionic radius of Sb^{3+} is with 76 pm (all ionic radii mentioned in this work, are referring to [Sha76]) too large to substitute in the crystal, which was shown by Bechstein et al. [BKS+09] for TiO_2 crystals. The resulting formation of $V_O^{\bullet\bullet}$-Ti^{3+} pairs (see eq. (2.7)) is considered by subtracting a $\frac{\delta}{2}O_2$ - term ($\delta > 0$):

$$0.22La_2O_3 + (1-x)TiO_2 + 0.5xSb_2O_5 - \frac{\delta}{2}O_2 \uparrow \xrightarrow{T_{Cer}} La^{3+}_{0.44}Ti^{4+}_{1-x-2\delta}Ti^{3+}_{2\delta}Sb^{5+}_{x}O^{2-}_{2.67+0.5x-\delta} \quad . \tag{2.65}$$

Due to the excess oxygen of the donor ion Sb_2O_5 and also the vacancy formation causing a deficiency of oxygen, the intermediate compound does not correspond to the right stoichiometry of the undoped crystal and therefore could stabilize by different theoretically possible processes:
a) In case of reducing conditions resp. high content of oxygen vacancies ($0.5x < \delta$), the excess oxygen from the Sb_2O_5 will partially reduce the amount of oxygen vacancies ($\delta' = \delta - 0.5x < \delta$) but will not affect a reoxidation of the Ti^{3+} in the crystalline phase:

$$La^{3+}_{0.44}Ti^{4+}_{1-x-2\delta}Ti^{3+}_{2\delta}Sb^{5+}_{x}O^{2-}_{2.67+0.5x-\delta} \longrightarrow La^{3+}_{0.44}Ti^{4+}_{1-x-2\delta}Ti^{3+}_{2\delta}Sb^{5+}_{x}O^{2-}_{2.67-\delta'} \quad . \tag{2.66}$$

In Kröger-Vink notation this can be simplified:

$$Sb_2O_5 + V_O^{\bullet\bullet} \xrightarrow{T_{Cer}} 2Sb_{Ti}^{\bullet} + 5O_O^{\times} \quad . \tag{2.67}$$

b) In case of oxidizing melting conditions resp. high amount of donor doping (0.5x > δ), the excess oxygen will be placed on interstitial lattice positions or theoretically also could lead to the formation of defects on the La (see eq. (2.68)) or Ti (see eq. (2.69)) site of the crystal (for simplification oxygen vacancies were excluded):

$$2\mathrm{Sb_2O_5} \xrightarrow{T_{\mathrm{Cer}}} 4\mathrm{Sb}^{\bullet}_{\mathrm{Ti}} + 10\mathrm{O}^{\times}_{\mathrm{O}} + 1\mathrm{V}^{''''}_{\mathrm{Ti}} \tag{2.68}$$

$$3\mathrm{Sb_2O_5} \xrightarrow{T_{\mathrm{Cer}}} 6\mathrm{Sb}^{\bullet}_{\mathrm{Ti}} + 15\mathrm{O}^{\times}_{\mathrm{O}} + 2\mathrm{V}^{'''}_{\mathrm{La}} \quad . \tag{2.69}$$

A more energetically favorable process than eq. (2.68) and eq. (2.69) would be the loss of oxygen from the intermediate compound and the associated partial reduction of one of the existing cations [Smy00]. As La^{3+} is comparatively stable, the Ti^{4+} ion will be dominantly reduced. We define $\varepsilon := x - 2\delta$, whereby ε represents the amount of excess oxygen which remains after the oxygen vacancies (represented by δ) are already completely filled up, eq. (2.66) then becomes:

$$\mathrm{La}^{3+}_{0.44}\mathrm{Ti}^{4+}_{1-\mathrm{x}-2\delta}\mathrm{Ti}^{3+}_{2\delta}\mathrm{Sb}^{5+}_{\mathrm{x}}\mathrm{O}^{2-}_{2.67+0.5\varepsilon} \tag{2.70}$$

$$\rightarrow \mathrm{La}^{3+}_{0.44}\mathrm{Ti}^{4+}_{1-\mathrm{x}-\underbrace{(2\delta+\varepsilon)}_{=\mathrm{x}}}\mathrm{Ti}^{3+}_{\underbrace{2\delta+\varepsilon}_{=\mathrm{x}}}\mathrm{Sb}^{5+}_{\mathrm{x}}\mathrm{O}^{2-}_{2.67} + \frac{\varepsilon}{4}\mathrm{O}_2 \uparrow \tag{2.71}$$

$$= \mathrm{La}^{3+}_{0.44}\mathrm{Ti}^{4+}_{1-2\mathrm{x}}(\mathrm{Ti}^{3+}\mathrm{Sb}^{5+})_{\mathrm{x}}\mathrm{O}^{2-}_{2.67} + \frac{\varepsilon}{4}\mathrm{O}_2 \uparrow \quad . \tag{2.72}$$

For this case of oxygen overcompensation, we see from eq. (2.72) that the amount of Ti^{3+} in the crystalline phase equals the amount x of the doped donor ion, independent of the amount of oxygen vacancies δ. Basically this process can also be understood as a charge compensation effect due to the incorporation of a higher charged donor ion Sb^{5+} on the Ti^{4+}-site by formation of Ti^{3+} [MH03]:

$$\mathrm{Sb_2O_5} \xrightarrow{T_{\mathrm{Cer}}} 2\mathrm{Sb}^{\bullet}_{\mathrm{Ti}} + 4\mathrm{O}^{\times}_{\mathrm{O}} + \frac{1}{2}\mathrm{O}_2 + 2\mathrm{e}^{'} \quad . \tag{2.73}$$

Case b) is the relevant situation for the here investigated Sb-doped glass-ceramics, as Sb acts as oxidizing agent during the melting and therefore $\delta \ll x$. But during the ceramization process, the reduction of Ti^{4+} to Ti^{3+} is caused by the substitution of a donor ion Sb^{5+} leading to a semiconductive behavior (see fig. 2.21).

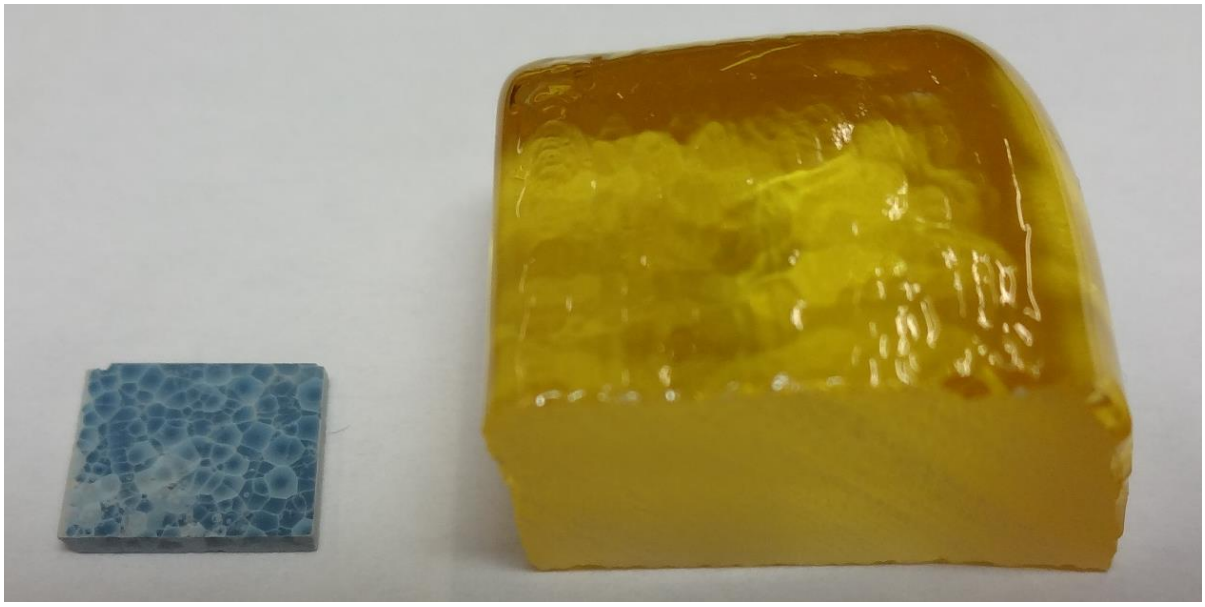

Figure 2.21: Right: clear Sb-doped glass (43722: 0.1 mol% Sb_2O_5) without any traces of Ti^{3+} (proven by EPR and optical transmission), left: ceramized sample 43722DEH366 (900 °C, 15 h) showing dark blue color from Ti^{3+}

The Ti^{3+} created in this doping process, is not coupled to an oxygen vacancy as in the case of fig. 2.6. Scharfschwerdt et al. [SMS+96] show that these different types of Ti^{3+} environments lead to a deformation of the original crystal structure and can be distinguished by EPR analysis (see fig. 2.22 for the case of a $BaTiO_3$ crystal).

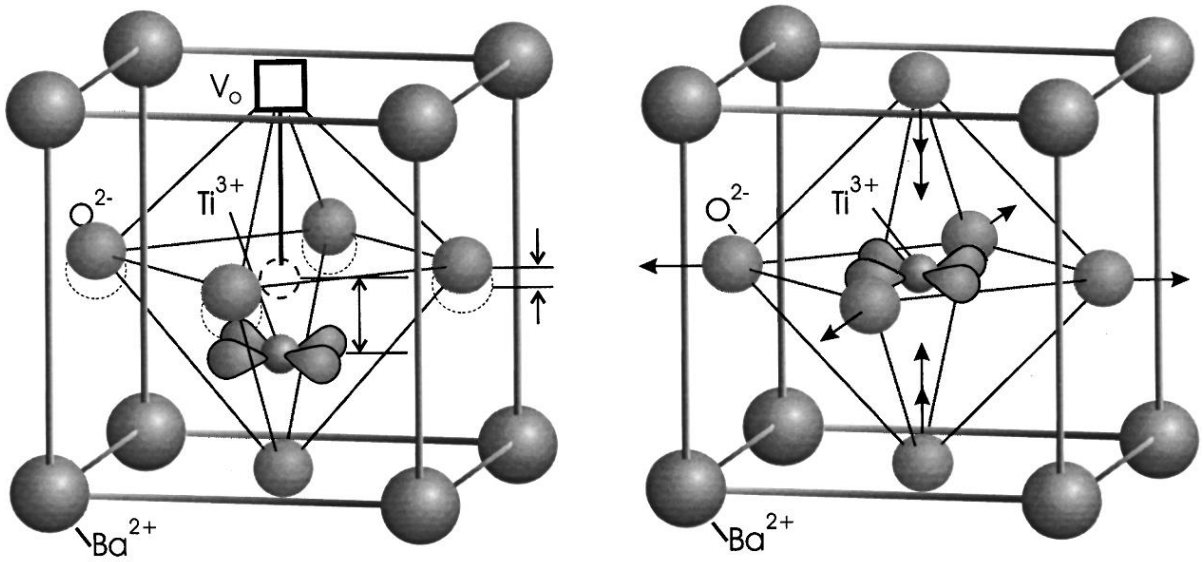

Figure 2.22: Left: Ti^{3+} formation due to oxygen vacancy, right: Ti^{3+} formation due to donor doping [SMS+96]

This also means that Ti^{3+} defects caused by donor doping can not be reoxidized during the ceramization process, whereby the Ti^{3+} defects caused by oxygen vacancies can be removed by reoxidation/annealing [WF50]. Andrade et al. [ALN+08] showed on Ti^{3+} containing calcium aluminosilicate glasses using EPR spectroscopy that a significant reoxidation already takes place at 850 °C (for 24 h).

Isovalent doping (Ce)

The substitution of Ce^{3+} on the La^{3+} A-site also causes a 4f defect band in the band gap, whereby its conductivity contribution should be comparatively lower as from Ti^{3+} defects, as these 4f defect states are much more localized. Ce^{3+} and La^{3+} have very similar ionic radii (114 pm and 116 pm at coordination number of 8) the substitution should not cause big deformations of the crystalline structure and therefore also cause less additional losses due to anharmonicity of the phonon modes (in comparison to the incorporation of Ti^{3+} on the B-site). The small amounts of present Ce^{4+} (ionic radius of 87 pm at coord. number of 6) are probably not able to substitute on the Ti^{4+} B-site (60.5 pm), as investigated by Fang et al. [FBS+07] for various cerium titanates. For Ce-doped $BaTiO_3$ a substitution of Ce^{4+} on the Ti^{4+} B-site is observed [HH01], but this is only possible due to the significantly large size of the TiO_6-octahedron in comparison to other titanate-based perovskites like $CaTiO_3$ or $SrTiO_3$ (see [YYM04]).

2.7.2 Phonon contribution

The search for suitable low loss materials for microwave applications has been mainly empirical until today. One key problem is the minimization of the dielectric loss as the loss contributions (intrinsic and extrinsic) are rather unknown and difficult to determine [PKKV96]. The most promising approach to understand the dielectric properties in the GHz range (which is far below the usual resonances of optical phonons) is the investigation of the frequency range up to the IR (1-10 THz) where the polar phonon modes are located [PK03]. Early work on far infrared dielectric dispersion of titanate-based perovskites was done by Spitzer et al. [SMKH62b]. Room temperature measurements of the reflectivity R from 70-5000 cm^{-1} were made to investigate the phonon resonance frequencies and their damping and correlate these with the losses in the microwave frequency range. The underlying idea was to extrapolate the dielectric loss from the THz range down to the GHz range. To obtain the complex permittivity ε_r from the reflectivity $R = I_r/I_0$, the complex reflection coefficient of the wave amplitudes $\rho = E_r/E_0 = \varrho e^{i\phi}$ has been determined via eq. (2.74) using Kramers-Kronig relation [MR71]:

$$\phi(\omega) = \frac{2\omega}{\pi} \int_0^\infty \frac{\ln(\varrho(\omega'))}{\omega'^2 - \omega^2} \, \mathrm{d}\omega' \tag{2.74}$$

$$\varrho = \sqrt{R} \quad . \tag{2.75}$$

With known ϱ and ϕ, the complex permittivity $\varepsilon_r(\varrho, \phi) = \varepsilon_r' + i\varepsilon_r''$ or refractive index $\tilde{n}(\varrho, \phi) = n + ik$ can be calculated by solving eq. (2.76) [DG02]:

$$\varrho e^{i\Phi} = \frac{(n-1) - ik}{(n+1) - ik} \quad . \tag{2.76}$$

The complex permittivity is then given by:

$$\varepsilon_r' = n^2 - k^2 \tag{2.77}$$

$$\varepsilon_r'' = 2nk \quad . \tag{2.78}$$

The obtained real and imaginary part of the permittivity are then fitted by the classical dispersion formula (see eq. (2.37)/(2.38)) using $3j$+1 parameters for j IR active modes (ω_j: resonance frequency, γ_j: damping coefficient, ρ_j: oscillator strength of the j-th phonon mode and ε_∞) and compared with the experimental data via eq. (2.79):

$$R = \left| \frac{\sqrt{\varepsilon} - 1}{\sqrt{\varepsilon} + 1} \right|^2 \quad \text{, for reflection in air.} \tag{2.79}$$

This method has the disadvantage that assumptions for the unknown frequency regions have to be made ($\varepsilon'(\infty)$ is estimated from the refractive index at optical frequencies far above the phonon resonances) to calculate the K-K relation (see eq. (2.74)) and also the fitting of a complex function with a high number of parameters can make the analysis difficult. Another possibility to analyze the reflectivity data, also proposed by Spitzer et al. [SMKH62b, SK61], is to fit the measured R directly via eq. (2.79) with ε given by eq. (2.37)/(2.38) to avoid K-K analysis but therefore requires a complicated fitting function with $3n$+1 parameters. Similar work was performed by other authors [WMT86, STL$^+$07, Shi04, Shi03]. The extrapolation of the obtained THz results to the GHz region normally leads to an underestimation of the GHz $\tan(\delta)$ values (factor 2-3 smaller in investigations of [SMKH62b]), as it just includes the contribution of a direct one-phonon absorption but not other loss mechanisms like conductivity [SMKH62b] or multiple-phonon processes [PKKV96]. Tagantsev et al. clarifies that the extrapolation of one-phonon absorption losses down to the GHz range seems to give a loss estimation in the right order of magnitude but is not the dominant physical mechanism correlated with the dielectric loss in the microwave region [TPS93, Tag93]. For the microwave frequency range no phonons exist whose energy and wave vector can be equal to those of the microwave photons. Apart from that the prediction of ε' gives a reasonable estimation for the GHz range. First theoretical attempts concerning a possible multiple-phonon process were presented by Stolen et al. and Bilz et al. for simple alkali halide crystals [BGH60, SD65]. Gurevich and Tagantsev [GT91] developed a rigorous theoretical description of intrinsic dielectric losses in perfect crystalline materials caused by anharmonic interaction between electromagnetic waves and phonons, with main loss contributions given by two or three-phonon processes. They showed that depending on the crystal symmetry, temperature and frequency interval the loss is given by a wide variety of possibilities: $\varepsilon''(\omega, T) \sim \omega^m T^n$ ($m \in$ [1,5], $n \in$ [1,9]) (for the classical damped oscillator model, see eq. (2.37), a linear dependence is expected $\varepsilon'' \sim \omega T$ as $\gamma_{pho} \sim T$ [KNP$^+$06]). In the microwave frequency range far below the optical phonon resonances ($\omega_\gamma \ll \omega_{\text{pho}}$) the dominant intrinsic contribution is given by two-phonon difference processes in the vicinity of the degeneracy lines of the phonon spectrum [TPS93]. Sparks et al. describes three possible processes (see fig. 2.23 a)):

- (E): Photon energy close to the phonon resonance frequencies (more important at higher frequencies (infrared) than in the microwave range)
- (D): Creation of a new phonon with energy $\hbar\omega_j = \hbar\omega_i + \hbar\omega$ by annihilation of a photon with energy $\hbar\omega$ and a phonon with $\hbar\omega_i$ (here exemplarily for a transition from an acoustic to an optical phonon branch)
- (S): Creation of new phonon on same branch (only possible for nonzero phonon damping), similar to D except that annihilated and created phonon are on same branch

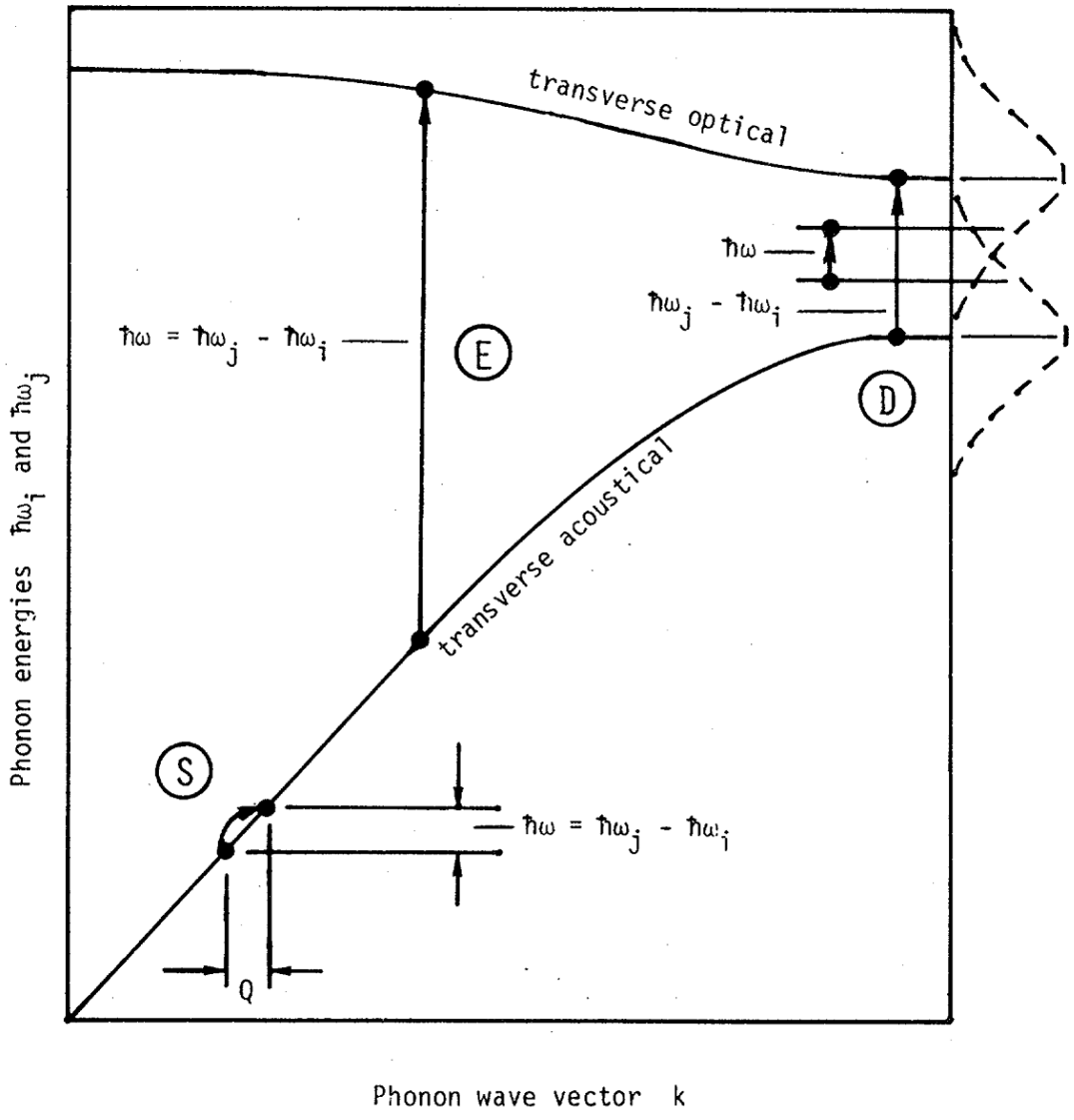

Figure 2.23: Schematic representation of three important two-phonon absorption processes [SKM82]

The frequency difference between the two phonon branches generally exceeds the frequency of the microwave photon by far even for adjacent branches of the phonon dispersion ($\Delta\omega_{\text{pho}} \approx$ THz $\ll \omega_\gamma \approx$ GHz). Nonetheless due to the finite phonon damping (schematically shown in fig. 2.23) energy and momentum conservation can still be fulfilled even for processes involving GHz photons. Although the two-phonon difference process is an intrinsic type of loss, the phonon damping mainly depends on extrinsic defect contributions [ZWKU97]. For medium to high temperatures (inc. room temperature) and frequencies below the damping of thermal phonons γ_T ($\omega \ll \gamma_T \approx 10^{11-12}$ Hz at room temperature) the two-phonon loss contribution should be proportional to the frequency: $\varepsilon''(\omega, T) \sim \omega T^2$ [PKKV96, KNP+06]. The linear frequency behavior also was observed experimentally in the work of Petzelt et al. [PS93] for optimized high Qf ceramics but temperature dependent measurements mostly were not consistent with the theoretical predictions [PKKV96] and also differ strongly for various ceramics (see fig. 2.24).

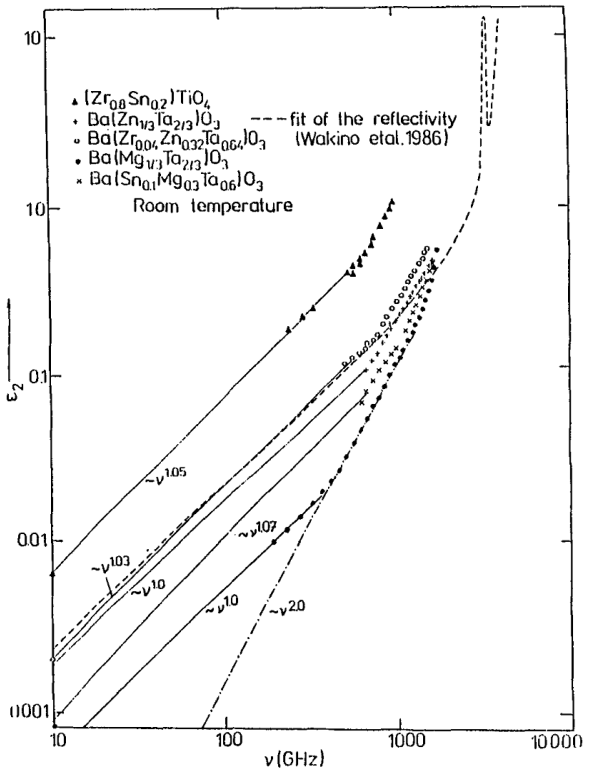

(a) Losses from SMM transmission measurements on several high Qf ceramics, full lines interpolate between the MW and SMM region [PS93]

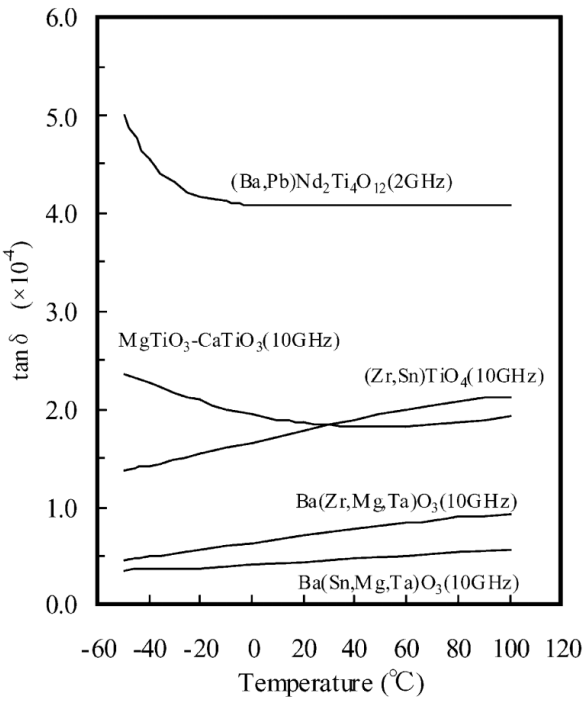

(b) Various temperature dependencies of $\tan(\delta)$ for optimized high Qf ceramics [HT03]

Figure 2.24

Petzelt et al. focused on frequencies in the submillimeter (SMM) range below the phonon resonances but above the microwave (MW) region and investigated numerous commercial microwave materials via Fourier transmission methods (15-100 cm^{-1}) and backward-wave-oscillator spectroscopy (5-30 cm^{-1}) [PKKV96]. His results show that the first deviation from the linear frequency dependence is found at around 500 GHz (15-25 cm^{-1}) indicating the increasing contribution of the low frequency flank of the lower polar phonon modes. In addition to the mentioned intrinsic multiple-phonon contribution extrinsic losses also can be present. Extrinsic losses are caused by various types of defects or impurities like dopant atoms, vacancies, structural disorder, grain boundaries [BPMA09], multiple phases and porosity [PAT+97]. Petzelt et al. classified the extrinsic contributions into four groups [PS93]:

- Defect or (static) disorder induced one-phonon absorption ($\varepsilon'' \sim \omega^m$ ($m \in$ [1,3], temperature independent)
- Localized defect vibrations or defect dipole relaxations ($\tan(\delta) \sim \frac{\omega\tau}{1+\omega^2\tau^2}$ with $\tau(T)$ as relaxation time showing Arrhenius-type behavior; shown by [ZWKU97, SIM+10, BPMA09] that only small contributions for T < 150 K in ultra low-loss materials exist)
- Motion/diffusion of charged defects/charge carriers as for example conductive losses (normally dominating below the microwave frequency range)
- Phonon scattering on defects leading to reduced phonon lifetime respectively increased damping of phonons (temperature independent)

Despite the existing theoretical work for mainly ideal single crystal materials of the mentioned authors above, in conclusion it may be stated that there are currently no satisfactory models that can explain extrinsic loss contributions due to microstructure and processing conditions of polycrystalline ceramics [PA99]. For the here investigated glass-ceramic system containing a mixture of multiple phases of amorphous and crystalline structure, the latter contribution is probably the most dominant and can be understood as extrinsically defect-broadened two-phonon difference process [SKM82]. Even though the identification via temperature and frequency dependence of the dielectric loss seems to be rather difficult. The additional phonon broadening in the IR range as external contribution can be measured by reflectivity measurements or ellipsometry in the lower THz regime.

Influence of oxygen vacancies on the dielectric loss

One special type of defect, the formation of oxygen vacancies, shall be discussed more detailed as it seems to be one of the dominant contributions to the dielectric loss of the investigated materials. Typically in titanate-based sintered ceramics an effect described as coring is well known in literature [FA08, PPW$^+$09, TWP$^+$00, PA99]. During high temperature sintering in air atmosphere, oxygen diffuses out of the ceramic and causes a partial reduction of Ti^{4+} to Ti^{3+}. During the comparatively fast cooling process afterwards, an incomplete reoxidation (oxidation only possible in the surface area which is in contact with the air atmosphere) leads to a dark core in the interior of the sintered pellet (dark color due to optical absorption of Ti^{3+}). This coring effect only occurs in ceramics with dense structure, for higher porosity levels the oxygen exchange with the core enhances which leads to an interesting porosity dependence of the dielectric loss (see fig. 2.25). With increasing porosity the Q reduces as expected, but at porosity levels lower than 8 % the Q drastically increases due to the reoxidation of the core which is enhanced by the less dense/more porous structure [PA99]. The 92 % density corresponds to the percolation limit of open interconnected porosity.

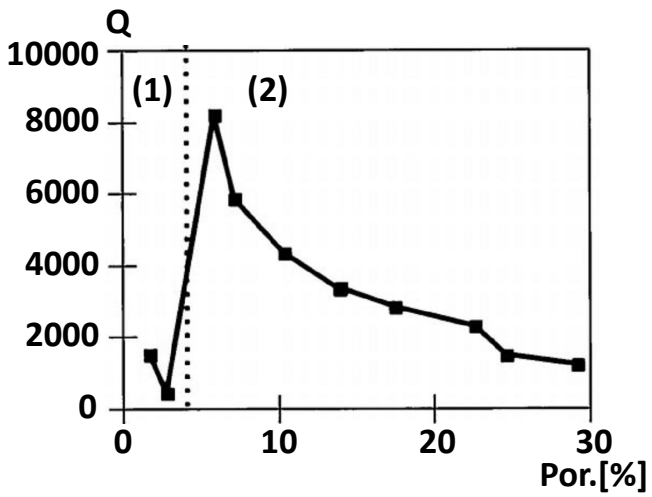

(a) Q(at 3 GHz) of sintered TiO_2 in dependence of porosity level ((1): coring regime, (2): no coring) [TWP$^+$00]

(b) Coring of sintered TiO_2 (1 h at 1500 °C) [PPW$^+$09]

Figure 2.25: The effect of coring on the dielectric loss

The presence of oxygen vacancies in the lattice is known to degrade the Q value but the physical mechanism is not clearly understood. Templeton et al. [TWP+00] and Negas et al. [NYB+93] showed that only very limited amounts of reduction led to a severe deterioration of Q. Freer et al. [FA08] relates the Q reduction to an increase of the phonon damping induced by structural disordering as for example the formation of oxygen vacancies. Pullar et al. [PPW+09] observed via TEM that the grains in the dark core contained planar defects attributed to the concentration of oxygen vacancies onto specific crystallographic planes, in a manner similar to that observed in Magnelli phases [RM91, BH72].
Iddles et al. [IBM92] showed that doping of $ZrO_2 - TiO_2 - SnO_2$ ceramics with small amounts of donor ions like Nb_2O_5 led to an increase of Q. He explained this by a compensation of oxygen defects (see eq. (2.81)) which are caused by common acceptor type impurities like Fe_2O_3 or Al_2O_3 (see eq. (2.80)):

$$Fe_2O_3 \longrightarrow 2Fe'_{Ti} + 3O^{\times}_{O} + V^{\bullet\bullet}_{O} \tag{2.80}$$

$$Fe_2O_3 + Nb_2O_5 \longrightarrow 2Fe'_{Ti} + 2Nb^{\bullet}_{Ti} + 8O^{\times}_{O} \quad . \tag{2.81}$$

A complete removal of oxygen vacancies by exact compensation of acceptors and donors resulted in Q values similar to reoxidized oxygen vacancy-free undoped ceramics, from which can be concluded that the oxygen vacancy itself is a more severe defect for the Q deterioration than the substitution of a dopant ion on the Ti^{4+} lattice site. Too high amounts of Nb_2O_5 lead to an overcompensation of the acceptor ions and the Q factor decreased again accompanied by a dark coloration and increase in conductivity which can obviously be attributed to the formation of Ti^{3+} according to eq. (2.73).

2.8 The La_2O_3-TiO_2-SiO_2 system

In this chapter the positive and negative material properties of the used oxidic compounds will be summarized and reasons for the choice of this system will be given. The key requirements for a suitable system are at first determined by the dielectric properties of the existing crystalline phases, which are investigated in literature (as for example the comprehensive work of Sebastian [Seb08]) under consideration of the requirements for the application ($\varepsilon_r > 20$, Qf > 5000 GHz and $|\tau_f| \leq 20$ ppm/K).
The final decision to chose the La_2O_3-TiO_2-SiO_2 system was made in a preliminary fundamental work [Bra11] in which it was shown that the desired phases (see yellow phases in tab. 2.5) could be crystallized in a glass-ceramic during the ceramization. In [Bra11] the glass-forming range of this system was investigated and determined. In this work, a further stabilization of the glass via substitution of dopants (prevent surface devitrification or redox instabilities) and a further investigation/optimization of the nucleation/ceramization process is performed. In tab. 2.5 the known crystalline phases of the systems are listed:

Phase	ε_r	Qf [GHz]	τ_f [ppm/K]	Source
$La_4Ti_9O_{24}$	37	24800(8.1 GHz)	+15	[LL05, TKK93]
$La_2Ti_2SiO_9$	28	29500(5.0 GHz)	+23	[TSS11]
TiO_2(Rutil)	104	44000(4.0 GHz)	+450	[MYI87, Seb08]
$LaBO_3$	12.5	53000(11.5 GHz)	N/A	[TK05, TYK03]
$La_2Ti_2O_7$	47	8050(7.8 GHz)	-10	[TKK93]
$La_2Ti_3O_9$	130	5100(3.0 GHz)	+320	[LL06, LL05]
SiO_2(glass)	3.8	67000(8.7 GHz)	N/A	[Jan03]

Table 2.5: Relevant crystal phases in the La_2O_3-TiO_2-SiO_2 system

The phases marked in yellow color show optimal dielectric properties for the given requirements and could also be crystallized during the ceramization process. ε_r and Qf are sufficiently high to fulfill the requirements. The τ_f values are optimal for the use in glass-ceramic materials, as the residual glassy phase generally has a negative τ_f [Seb08, WH99] and both phases can thereby compensate to an overall τ_f close to zero. The phases marked gray are minor phases (< 20 wt%) for some glass compositions. TiO_2 (rutile) has excellent dielectric properties [Coh68] but also an extremely high τ_f. $LaBO_3$ crystallizes from the excess B_2O_3 and La_2O_3 which are not used in the major crystalline phases. The aim is always a single-phase material with main content of $La_4Ti_9O_{24}$ or $La_2Ti_2SiO_9$, as multiple-phase materials always tend to have a higher losses [TKK93] (see fig. 2.26). The mixing rules for multiple-phase materials are usually predicted by the empirical relations (2.82)-(2.84) [Seb08] (V_i: volume fraction):

$$\ln(\varepsilon_{\text{tot}}) = \sum_i V_i \cdot \ln(\varepsilon_i) \tag{2.82}$$

$$\frac{1}{Q_{\text{tot}}} \geq \sum_i V_i \cdot \frac{1}{Q_i} \tag{2.83}$$

$$\tau_{f_{\text{tot}}} = \sum_i V_i \cdot \tau_{f_i} \quad . \tag{2.84}$$

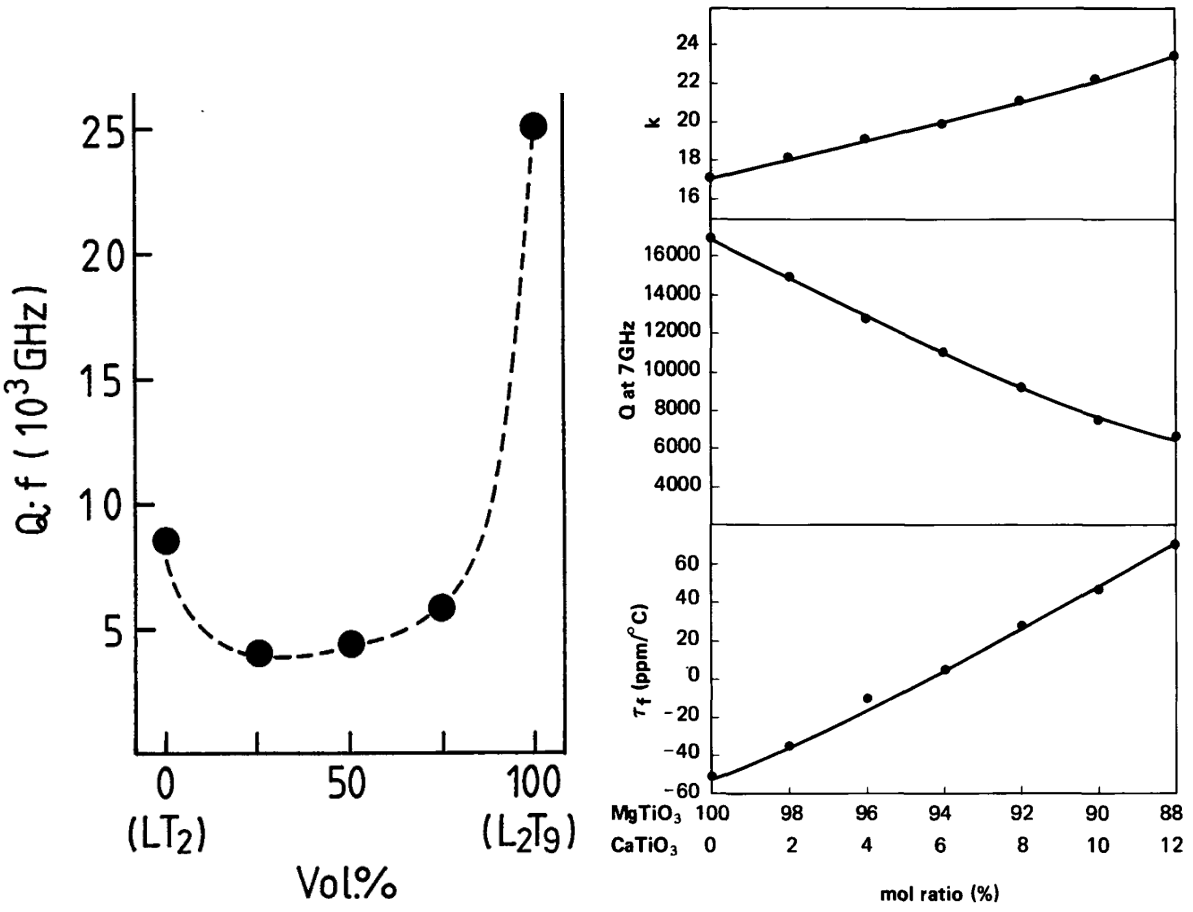

(a) Decrease of Qf for multiple-phase materials, here mixture of $La_2Ti_2O_7$ with $La_4Ti_9O_{24}$ [TKK93]

(b) Mixing of $MgTiO_3$ (ε_r = 17, Qf = 120000 GHz, τ_f = -50 ppm/K) and $CaTiO_3$ (ε_r = 160, Qf = 7000 GHz, τ_f = +850 ppm/K) [Wak89]

Figure 2.26: Mixing of multiple crystalline phases

The $La_2Ti_2O_7$ phase only appeared in compositions of low SiO_2 content ($La_2Ti_2O_7 + SiO_2 \leftrightarrows La_2Ti_2SiO_9$). The $La_2Ti_3O_9$ phase could not be found. $La_2Ti_2O_7$ and $La_2Ti_3O_9$ show comparatively unsuitable dielectric properties and therefore no attempts were made to stabilize their formation in the glass-ceramic.

A further reason for the use of the mentioned oxides inside a glass-ceramic material are their positive properties concerning glass formation. The large ionic radius of the La^{3+} cation leads to a small mobility in the glass network and an increase of the electric resistance by blocking ionic hopping processes (as for example from alkali impurities). La_2O_3 glasses are known for their high refractive index due to their high electronic polarizability [Vol84]. Volf [Vol84] and Scholze [Sch88] rank TiO_2 as oxide with the largest permittivity (ε_r(1 GHz) = 25.5) of all oxidic glass components. Titanium oxide in its pure form as rutile (TiO_2), but also as major constituent of several microwave ceramics (see tab. 1.1) is known for excellent dielectric properties (see tab. 2.5). The advantageous properties of this system, are also reflected in their utilization as microwave dielectric materials. From the 2300 in literature known "low loss dielectric resonator materials", 46 % contain TiO_2 and 40 % rare earth metal oxides [Seb08]. These exceptional properties result from the small size of the Ti^{4+} ion (0.61 Å, six-fold coordination in TiO_6 octahedron; [Seb08]) and its high charge, which lead to a high ionic polarizability. Under application of an electric field, the Ti^{4+} ion can easily be displaced against the O^{2-} ions and form an electric dipole [MYI87, XXHQ07]. According to the network theory of Zachariasen (see chapter 2.1) tetrahedral coordination is essential for the glass formation. The ratio Ti^{4+}/O^{2-} is much greater than 0.414 and therefore exceeds the maximum limit permissible for tetrahedral coordination [Rao64]. The Ti^{4+} ion normally favors six-fold coordination, which would prevent the capability to work as glass former in the three-dimensional random-network picture. Ti^{4+} is therefore considered as intermediate glass former. Nevertheless Rao [Rao64] found that binary compositions of TiO_2-A_2O (A = K, Rb, Cs) formed stable glasses. He also proved the six-fold coordination and thereby disproved the predictions of the classical network theory, similar results were also obtained by Zarzycki [Zar71]. Yang et al. [YDES08] and Farges et al. [Far96, Far97, FJN+96, FJR96] showed via XANES and EXAFS measurements for various TiO_2 containing glasses that the coordination number of the Ti^{4+} ion seems to be dominantly 5 (60 %), but also 4 (20 %) and 6 (20 %) were detected. The 5 coordinated Ti^{4+} can act simultaneously as network former and network modifier [FJN+96]. Schneider et al. [SRKR98] obtained similar results via XPS measurements. All authors concluded that TiO_2 is able to stabilize the glass network even despite its partially non-tetragonal coordination. Similar results were found also during this work, when the TiO_2 was completely removed from the glass, strong devitrification occurred. In addition to the advantageous physical properties, TiO_2 is also a commonly available, non-toxic and cost-efficient raw material making it ideal for the use in commercial applications.

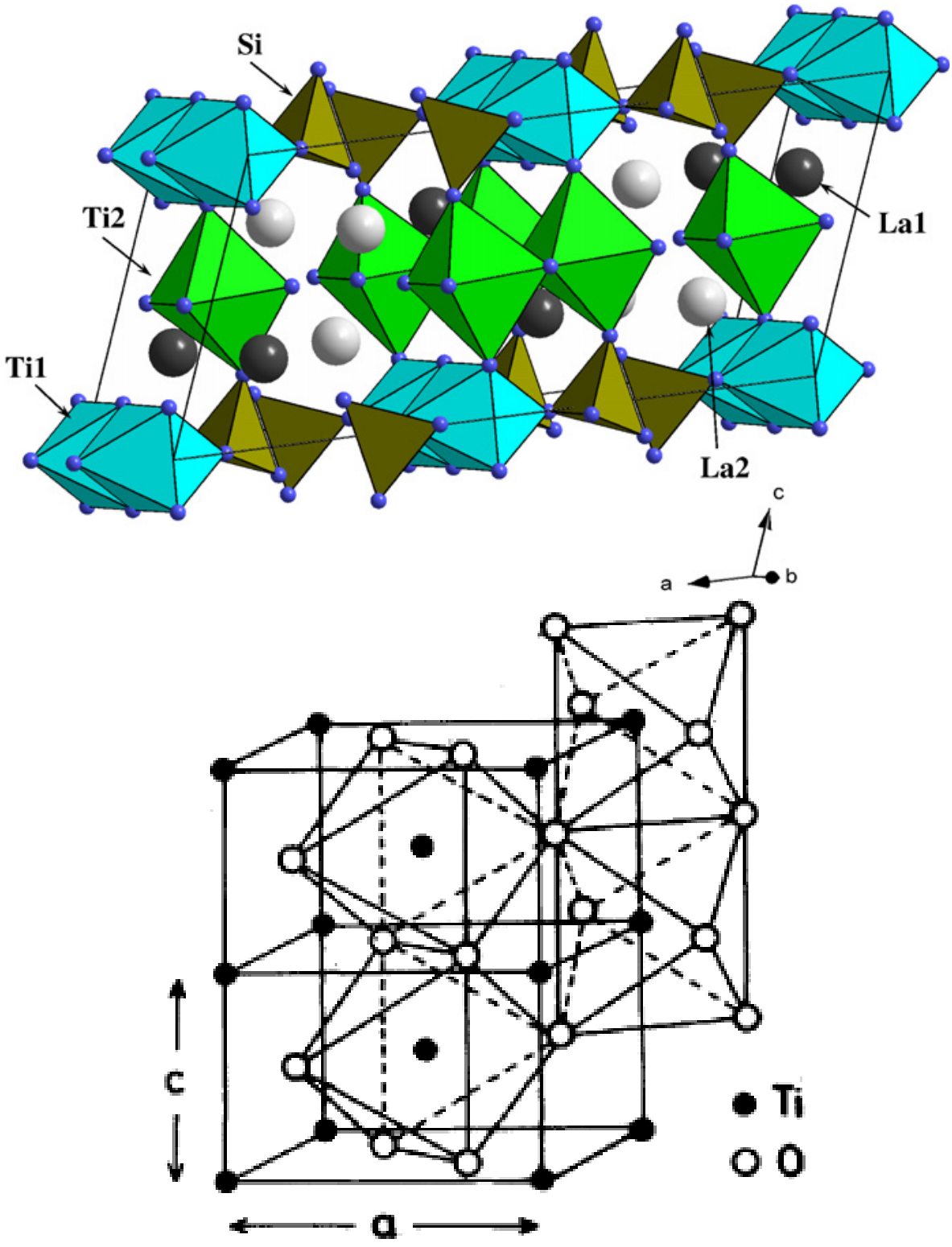

Figure 2.27: Top: $La_2Ti_2SiO_9$ structure: network of isolated SiO_4 tetrahedra, connected by TiO_6 octahedra, which are embedded between La^{3+} cations [PKN+07]; bottom: rutile (TiO_2) structure: Ti^{4+} ion embedded between 6 O^{2-} ions [MYI87]

To enhance the glass forming ability of the system mainly the well known network former oxides SiO_2 and B_2O_3 were used. Successful attempts with additional Al_2O_3 were made in the previous work [Bra11], but the best combination was found to be the La_2O_3-TiO_2-SiO_2-B_2O_3 system. Unfortunately SiO_2 and B_2O_3 only have a low ionic polarizability (and therefore permittivity) due to their strong covalent bonds, but also they have a comparatively low dielectric loss [NG46, Seb08]. Besides SiO_2 is needed to stabilize the formation of $La_2Ti_2SiO_9$ instead of $La_2Ti_2O_7$ and B_2O_3 is necessary to reduce the melting temperature of the system. Based on the phase diagram of the La_2O_3-TiO_2 system (fig. 2.28) it can be seen that close to the stoichiometry of the $La_4Ti_9O_{24}$ phase a eutectic of the binary system exists [MS62]. Compositional regions close to eutectic points are known to have increased tendency of glass formation (see rawson criterium in chapter 2.1). For this reason, the first compositional attempts were made for La:Ti ratios close to this eutectic composition. Unfortunately these glasses showed a strong devitrification tendency and the composition was changed closer to the stoichiometry of the $La_2Ti_2SiO_9$ phase. The determination of the optimum glass composition will be presented in detail in chapter 4.1.

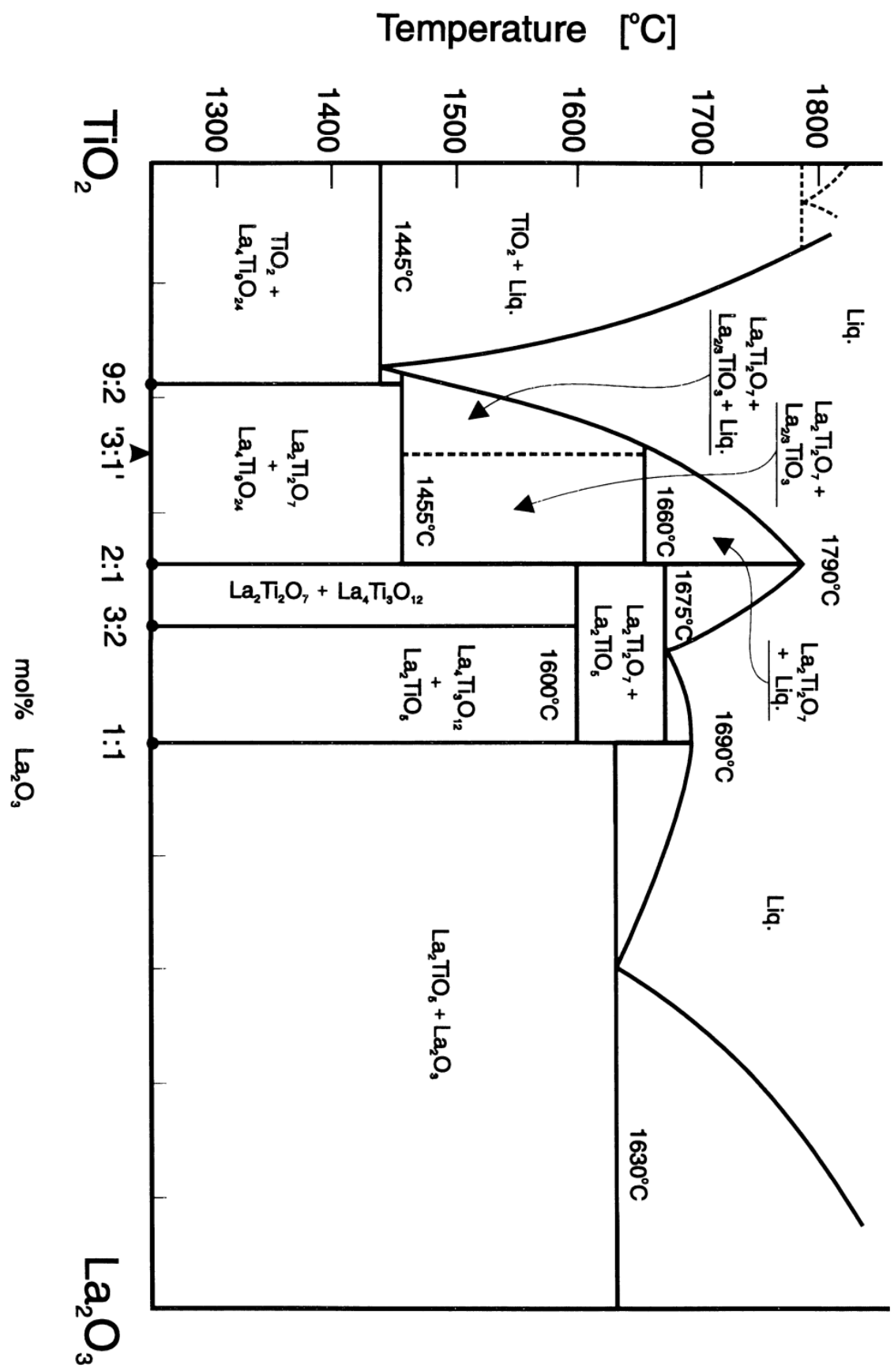

Figure 2.28: Phase diagram of the La_2O_3-TiO_2 system [SKS99] (phase content in mol%)

3 Experimental methods

3.1 Glass production

The glass samples were melted from milled dry powders according to the batch composition in a Pt-Ir alloy crucible. In this work two different crucible volumes were used, the first type were the so-called screening-melts (glass volume of 30 cm^3) which were mainly used to investigate („screen“) the glass forming area in the system (glass stability and crystalline phases after ceramization) and thereby find the optimum chemical composition. Disadvantage of these melts is the small volume, which can not be stirred/homogenized. The second type were the so-called liter melts (glass volume around 1 liter), which are casted into size-adjustable steel molds. From each liter melt 4 glass bars of 2 $\times$ 5 $\times$ 23 cm size could be made (see fig. 3.1), which were then cut into suitable geometries for subsequent measurements. The higher volume and the possibility to stir the melt ensured more homogeneous samples. The melting temperature T_m varied between 1450 °C to 1650 °C. A typical melting procedure for a liter melt can be summarized as:

- Insertion of raw materials in 5 g steps at T_m - 100 °C (typically 1500 °C), until batch is melted
- Oxygen bubbling and stirring (to achieve oxidizing melting conditions) with 27 l/h for 30 min at T_m - 50 °C (typically 1550 °C)
- Keeping time at the HTF (high temperature chamber furnace) for t_k = 30 min at T_m (typically 1550 °C)
- Casting into steel mold (on room temperature)
- Cooling in the cooling furnace to prevent crack formation (preheated at T_g - 20 °C) with 20 K/h until room temperature

The glass samples were produced at the glass melting facilities of SCHOTT in Mainz and were labeled using 5-digit numbers.

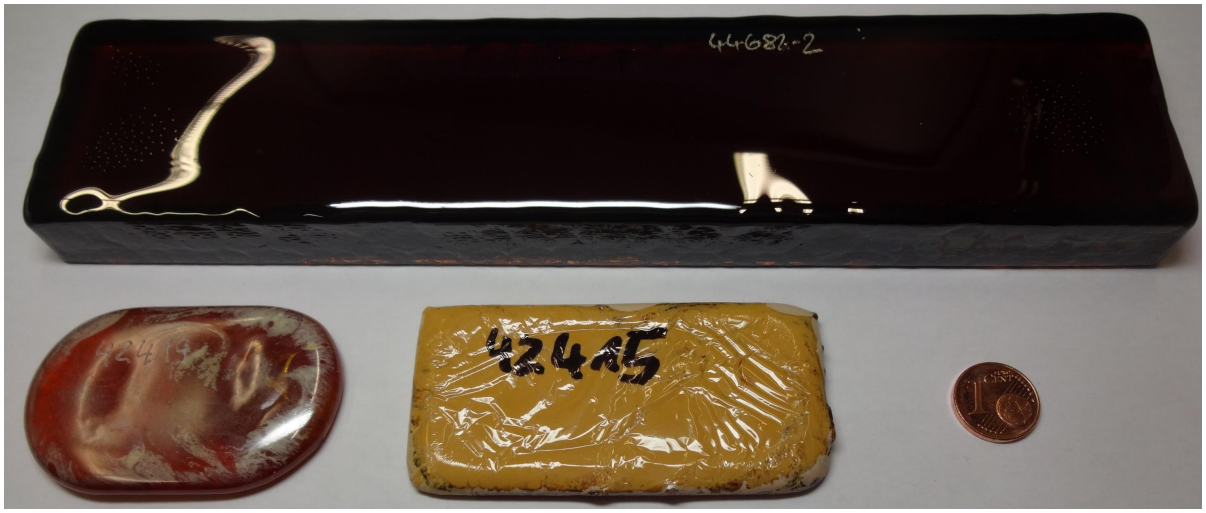

Figure 3.1: Example of two screening melts (bottom) and one liter melt bar (top)

3.2 Differential thermal analysis (DTA)

DTA is a thermal analysis method for materials, which uses the fact that during first order phase transitions (e.g. melting, crystallization) a characteristic amount of energy (latent heat) is released/absorbed. The sample temperature is measured relative to a reference sample while both are heated up with a predefined (mostly constant) heating rate. The temperature profile contains information about the type and temperature of the phase transition. The temperatures of the reference and the investigated sample are measured by using thermocouples. Their difference $\Delta T = T_{\text{sample}} - T_{\text{ref}}$ is proportional to an electric signal given in µV/mg. As reference sample, inert materials were used, meaning materials without phase transitions in the investigated range. Endothermic reactions, like the melting of a crystalline phase, cause a decrease of the signal at the melting temperature. Exothermic reactions, like the crystallization of an amorphous phase, cause an increase of the signal intensity. DTA measurements were mainly necessary to identify the crystallization temperatures of the glass to allow a better control of the ceramization process. In fig. 3.2 a DTA of glass 42732 is shown exemplarily. The glass transition can be determined at the point of inflection at T_g (768 °C). The exothermic peaks at 963 °C, 1045 °C and 1055 °C belong to the crystallization of three phases, which melt at the endothermic peaks at 1103 °C, 1167 °C and 1305 °C. The mass of sample and reference (Al_2O_3) was 250 mg. All DTA measurements were made with a Netzsch STA 409 PC/PG using a Pt-Ir alloy crucible.

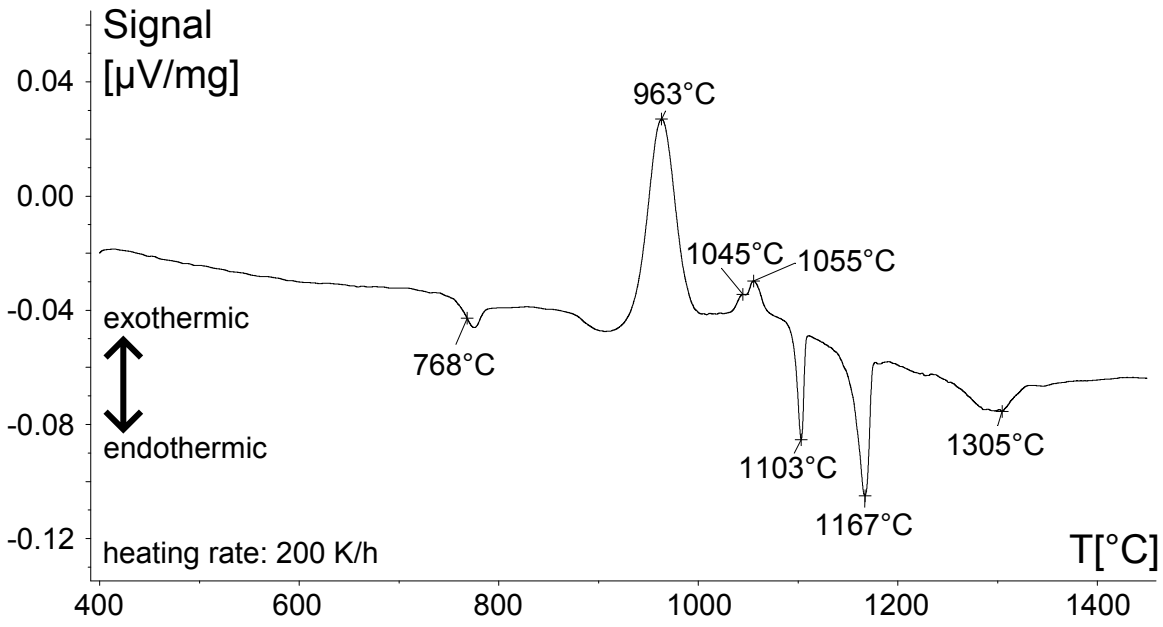

Figure 3.2: DTA of glass 42732

3.3 Ceramization - controlled crystallization

During the ceramization process an amorphous sample partially crystallizes. The glasses were embedded into quartz sand to stabilize the glass mechanically against temperature related changes of shape at temperatures above T_g. The ceramization temperatures for the investigated system were around 800 °C to 1100 °C. A typical ceramization program as it was used for most samples is shown in tab. 3.1.

R1	Z1	H1	R2	Z2	H2	R3	Z3	H3	R4	Z4
200	900	5	40	750	0	20	550	0	40	20

Table 3.1: Typical ceramization program (Abbr.: R: Rate [K/h], Z: holding temperature [°C], H: holding time [h])

The ceramized glasses were labeled with a DEH number, for example the glass 36436 becomes 36436DEH001 after the ceramization process DEH001.

3.4 X-ray diffraction (XRD)

XRD analysis enables the possibility to determine crystalline structures, in special cases also temperature dependent. The characteristic X-ray radiation of a copper anode (45 kV, 40 mA) with λ_{K_α} = 0.154 nm was used to provide a monochromatic source (wavelengths of the order of magnitude of the lattice planes). The adjacent λ_{K_β}radiation (0.139 nm) is removed by a nickel filter. For known wavelength $\lambda =$

$\lambda_{K_\alpha,\mathrm{Cu}}$ and diffraction angle θ for constructive interference, the lattice parameters d_{hkl} can be determined via the Bragg equation:

$$n \cdot \lambda = 2d_{hkl} \cdot \sin(\theta),\ n \in \mathbb{N}. \tag{3.1}$$

The bulk samples were milled in a tungsten carbide cylinder to a fine powder and measured in Bragg-Brentano geometry (θ-2θ). To identify the crystalline phases inside the glass-ceramic, the diffraction spectra $I(2\theta)$ are compared with XRD databases (JCPDS of ICDD). To quantify the crystalline phase content the Rietveld method [Rie68] was used. For a known crystalline structure a theoretical intensity distribution is calculated and then the measured data is fitted (see fig. 3.3) under variation of numerous parameters (offset and curve parameters, wavelength, background, lattice parameter, etc.). The amount of amorphous phase can be determined by using a fully crystalline reference material. The reference material is mixed with the sample by a 1:1 ratio. The determination of the amorphous content is comparatively inaccurate and the error should be at least estimated to 10 wt%. The X-ray absorption of the reference material and the sample should be similar and the purity & crystallinity should be close to 100 %. In this work ZnO was dominantly used as reference material.

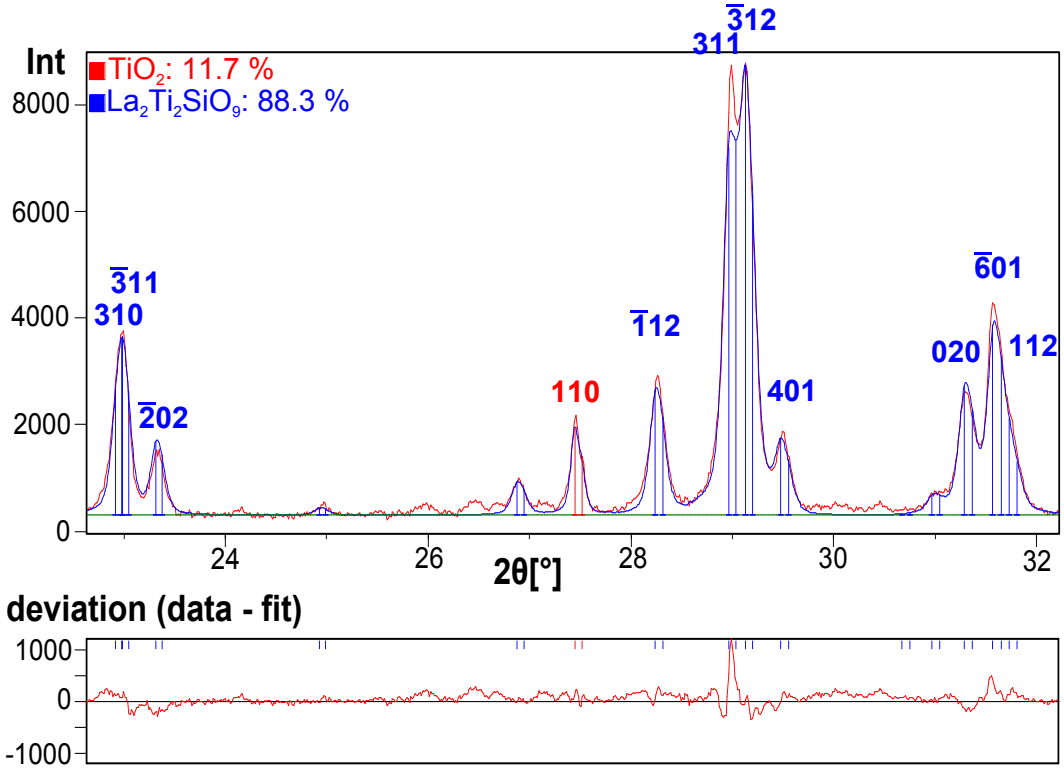

Figure 3.3: Rietveld analysis example with identified crystalline phases: $La_2Ti_2SiO_9$, TiO_2. The measured spectrum is shown in red, the blue curve is the Rietveld fit (bottom: deviation between data and fit)

Additionally, XRD offers the possibility to observe the temperature ranges of the growing crystalline phases (HT-XRD). A similar analysis as the DTA, but with the possibility of phase identification. For temperature dependent measurements bulk samples had to be used. This caused a problem, as the investigated systems showed surface crystallization with oriented crystal growth leading to modification of the measured spectra (intensity ratios changed due to preferred orientation of crystals at the surface in comparison to the spectra of randomly oriented crystals in powder spectra). Also the HT-XRD signal was dominated by the surface signal making the HT-XRD not suitable for the investigations of the for this work relevant bulk crystalline phases.

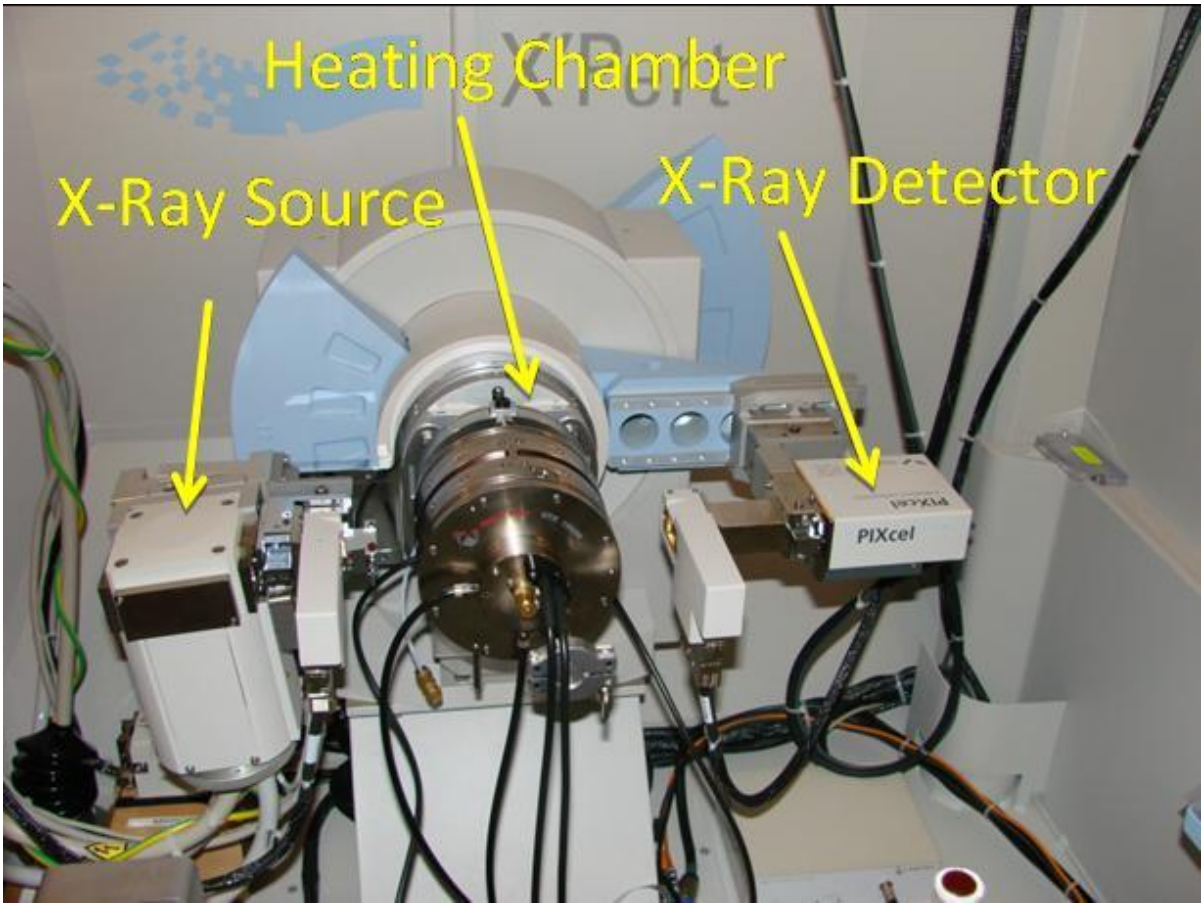

Figure 3.4: Experimental XRD setup with heating chamber

All measurements were performed with a X-ray diffractometer Siemens D5000 and for the evaluation the software X´Pert Highscore Plus was used.

3.5 Scanning/transmission electron microscopy (SEM/TEM) and energy-dispersive X-ray spectroscopy (EDX)

SEM enables the possibility to investigate structures microscopically down to the nm scale and in combination with an element specific analysis of the investigated surface area via EDX. A monoenergetic (0.1-30 keV) electron beam systematically scans over the surface under vacuum conditions and the backscattered electrons are detected and represented in a monochrome grayscale image. The samples are coated with carbon to avoid the accumulation of electrons on the surface.
TEM is a similar technique where the electron beam is transmitted through a thin specimen. The TEM sample preparation is comparatively complex, as bulk samples have to be polished to around 30 µm thickness. The specimen is glued on a copper ring sample holder and a hole with a flat gradient is made using an ion mill. The thin area close to the edge of the hole which is thin enough to allow a transmission of electrons is investigated. The possible resolution for available microscopes are in the range of 1-10 nm for SEM and around 0.1-1 nm for TEM.
The keV electrons will kick out electrons of the inner atomic shells and thereby excite the emission of characteristic X-ray which can be used for quantitative material specific analysis of the sample (EDX). With this method elements with atomic number $Z > 5 = Z_{\mathrm{Bor}}$ can be detected with a detection limit of approx. 0.5 wt%. The lateral spatial resolution of EDX is limited by the size of the excited volume. The electrons are scattered inside the material and excite a pear-shaped volume below the entry surface of approx. 1 µm for SEM/EDX and 1-10 nm for TEM/EDX. The microscopes used in this work were a LEO Gemini 1530 SEM and a JEOL 2010F TEM.

3.6 Dielectric/impedance spectroscopy

Impedance analyzers are a common measurement technique for the determination of dielectric properties ($\varepsilon_r(\omega)$, $\sigma(\omega)$) in the mHz to MHz frequency range. The specimens are placed between two electrodes of known capacity $C_0 = \varepsilon_0 \frac{A}{d}$ and a sinusoidal AC voltage U of amplitude U_0 = 1 V is applied. This results in a current I with a phase of $\phi(\omega) = +\pi/2 - \delta(\omega)$ between the voltage and the current. For an ideal loss-free capacitor the phase difference would be 90°, but real capacitors show an additional contribution $\delta(\omega)$ due to extrinsic losses as ohmic losses or the dielectric loss of the sample. The current can be decomposed in 2 components (I_{0_1}: loss current amplitude

in phase with voltage and I_{0_2}: displacive current amplitude with phase difference of $\pi/2$). The complex conductivity $\sigma^* = \sigma_1 - i\sigma_2$ can then be determined via [MH03]:

$$\sigma_i = \frac{I_{0_i}}{U_0}\frac{\varepsilon_0}{C_0} \quad . \tag{3.2}$$

The complex permittivity follows from the conductivity via $\varepsilon_r^* = \varepsilon_r^{'} + i\varepsilon_r^{''} = i\frac{\omega}{\varepsilon_0}\sigma^*$ (see eq. (2.31)).
The measured samples had a sample thickness of below 1 mm and were metallized on the contact surfaces by sputtering with $\mathrm{Cr/Ag}$. The measurements could be performed temperature dependent between -100 °C and +300 °C. The measurement setup is shown in fig. 3.5.

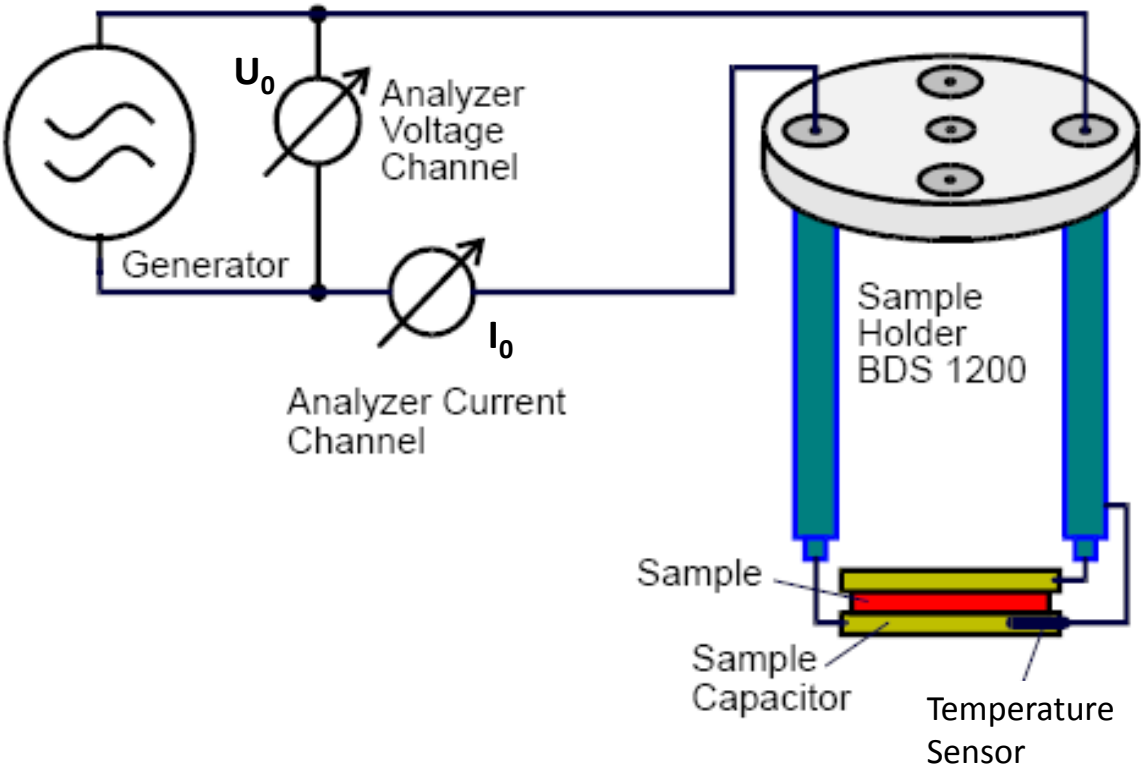

Figure 3.5: Schematic description of the measurement setup [Bra11]

All measurements were made using a Novocontrol Alpha-AHPF Analyzer.

3.7 Electron paramagnetic resonance (EPR)

Electron paramagnetic/spin resonance (EPR/ESR) spectroscopy offers the possibility to investigate materials with unpaired electrons by using the Zeeman effect [HS95]. If we consider the simple case of a free electron in the absence of an external magnetic field, we find that the two spin states (m_s = $\pm\frac{1}{2}$) are degenerated. Application of an external magnetic field $\mathbf{B}_0$ leads to a parallel (m_s = -$\frac{1}{2}$) or antiparallel (m_s = +$\frac{1}{2}$) orientation of the electrons magnetic moment relative to the field ($E_{\text{mag}} = -\boldsymbol{\mu}_\mathbf{e}\mathbf{B_0}$) with different energy Zeeman levels $E(m_s) = m_s g_e \mu_\text{B} B_0$. This leads to an energy difference between ground and excited state of $\Delta E = g_e \mu_\text{B} B_0$ ($g_e \approx 2.0023$: free electron g factor, μ_B: Bohr magneton). Transitions between these states can be excited by absorption of microwave radiation with photon energies corresponding to the energy state difference ($E_{\text{pho}} = \Delta E$):

$$h\nu = g_e \mu_\text{B} B_0 \quad . \tag{3.3}$$

For practical reasons, the microwave absorption intensity is measured in dependence of a variable magnetic field at a fixed resonance frequency inside a microwave cavity resonator. The g factor of the electron in atomic environments can differ from the free electron value due to spin-orbit coupling which is a dominant effect especially for transition metals and lanthanides. The atomic environment (crystal field) of the electron can cause additional local magnetic fields contributions which are added to the externally applied field to an effective field $B_{\text{eff}} = B_0 + B_{\text{loc}}$ and therefore: $h\nu = g_e \mu_\text{B} B_{\text{eff}} = g_{\text{eff}} \mu_\text{B} B_0$. The effective g-factor (from now on written as g) thereby incorporates material characteristic information:

$$g = \frac{h\nu}{\mu_\text{B} B_0} \quad . \tag{3.4}$$

For single-crystalline samples it is represented by a three-dimensional tensor, but for the here investigated isotropic materials, the g-tensor simplifies to a scalar. The signal intensity can be increased significantly by measuring at lower temperatures as the population of spin states is strongly temperature dependent and described by a Maxwell distribution:

$$\frac{n_\uparrow}{n_\downarrow} = e^{-\frac{\Delta E}{k_\text{B} T}} \quad . \tag{3.5}$$

All measurements of this work were carried out at the boiling point of liquid nitrogen (77 K).

The EPR signal intensity is understood as the integrated intensity under the measured absorption curve which is proportional to the number of unpaired electrons inside the sample. For experimental reasons (mainly to achieve a higher signal-to-noise ratio) the derivative of the absorption curve is normally measured instead of the absorption itself [EEWW10]. Therefore a double integration of the measured signal is necessary to evaluate the amount of unpaired electrons in the sample (see fig. 3.6).

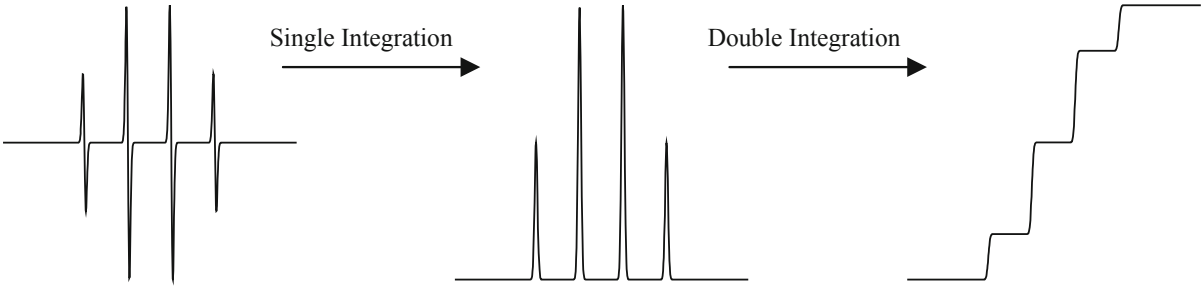

Figure 3.6: Signal evaluation via numerical double integration [EEWW10]

Measurements are nondestructive and only small amounts of material are necessary (< 100 mg). A major advantage in comparison to other spectroscopic techniques is the high material specifity, as ordinary solvents, and especially important for this work, basic glass matrix components (SiO_2, B_2O_3, Al_2O_3, P_2O_5) consist of oxides with paired electrons which do not contribute to the EPR signal. The sensitivity of EPR is much higher than for the optical transmission methods and can be estimated to less than 100 ppm of Ti^{3+} concentration [BB70]. The measurements were made using a MiniScope MS100 (Magnettech) EPR spectrometer.

Quantitative EPR

The influence of the experimental parameters (e.g. linearity of the receiver gain) on the signal intensity was investigated to ensure a reliable comparison of different sample measurements. The sample holders are quartz glass tubes of 25 cm length and 4 mm diameter (wall thickness 0.5 mm), which are placed into the rectangular microwave cavity resonator operating at the TE_{102} mode which provides an optimal spatial distribution of the electromagnetic field density (homogeneous and maximum magnetic field and minimum electric field in the center at the location of the sample, see fig. 3.7).

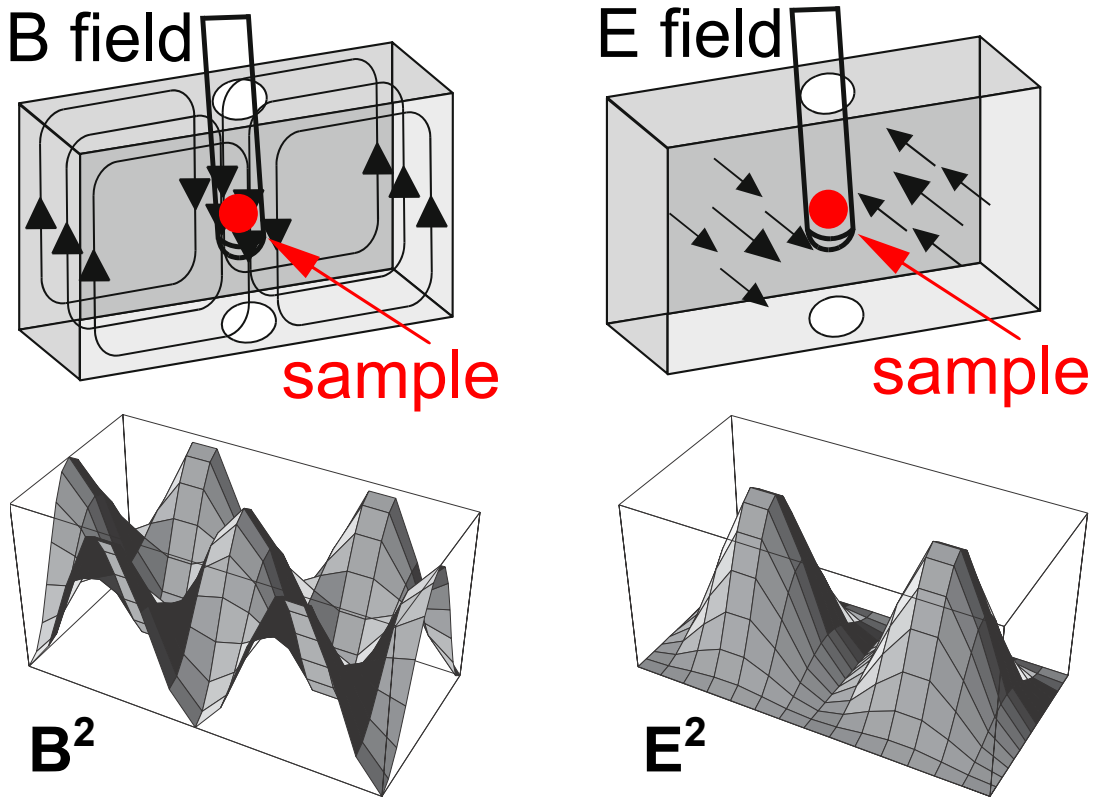

Figure 3.7: Top: schematic electromagnetic field distribution for the TE_{102} cavity mode, bottom: field intensities in the horizontal plane at the sample height [EEWW10]

The position of the sample holder in the cavity was optimized for the location of maximum magnetic field to achieve an optimal signal-to-noise ratio. The maximum of the magnetic field was determined by measuring different heights of the resonator with a point source of DPPH (a high intensity radical often used as EPR reference material). This calibration was necessary as the magnetic field along the vertical central axes shows a quite strong spatial dependence (see fig. 3.8).

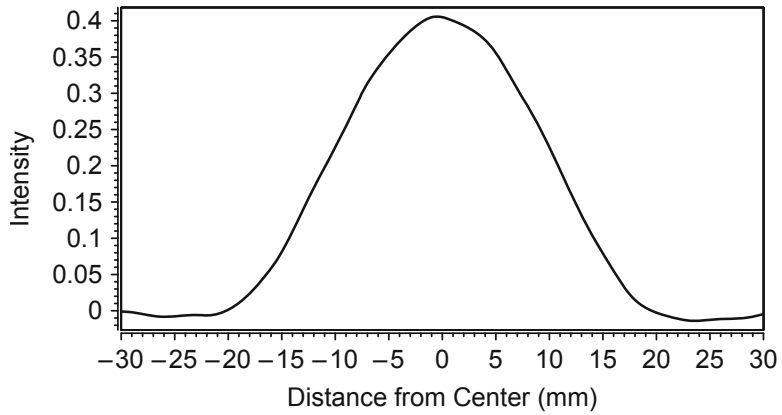

Figure 3.8: Spatial dependence of TE_{102} fields [EEWW10]

The sample size should be kept as small as possible to achieve a homogeneous field distribution across the sample volume. The intensity of the microwave radiation could be controlled via the intensity gain (linear signal to intensity correlation) and the microwave attenuation coefficient (logarithmic signal intensity correlation). Calibration measurements were performed to ensure that no saturation effects occurred. Quantitative analysis of sample concentrations is practically not possible without a characterized and suitable standard sample. The standard and the investigated material should be as similar (volume, chemical composition, electric and magnetic properties) as possible for various reasons. If materials with different dielectric and magnetic properties are used, the electromagnetic field distribution of the microwave radiation in the sample can be different (high permittivity materials lead to deviations of the field and different dielectric or magnetic loss values lead to different reductions of signal intensities). Also the resonator Q and modulation amplitude can be different, which effect the signal intensity as well. Different publications exist in literature, using $\mathrm{CuSO_4 \cdot xH_2O}$ as standard sample [LSSR71, ELM01, Car07]. Eaton [EEWW10] mentions a list of problems concerning its suitability, including the instability in air due to its high hygroscopy. For this work, pure $\mathrm{Ti_2O_3}$ powder was tried as standard to determine the amount of $\mathrm{Ti^{3+}}$ ions inside the glass (see chapter 4.2). The measured intensity was around two orders of magnitude lower than expected, therefore a quantitative analysis could not be achieved. The reason is probably the quite high permittivity in comparison to the investigated glass samples [Rie07], leading to distorted field geometry of the cavity mode. An additional problem could be the antiferromagnetic behavior of $\mathrm{Ti_2O_3}$ at the investigated temperature range which would lead to an increased microwave absorption respectively a lower signal intensity per ion [Abr63]. Even though a suitable standard could not be found, a suitable reference standard for relative intensity measurements could be identified. Different transition metals were investigated with g values not to close to the $\mathrm{Ti^{3+}}$ signal around g = 1.95 $\pm$ 0.15 (see fig. 3.9). The use of a reliable reference standard will allow to cancel out uncertainties of the experimental setup parameters by measuring the investigated sample always simultaneously with the same reference standard, which needs to be reproducibly mounted due to the variations of the magnetic field. In tab. 3.3 $\mathrm{Ti^{3+}}$ g values from different authors are summarized. The values vary due to the different chemical environments. Ti has two stable isotopes with a nuclear magnetic moment, $^{47}_{22}\mathrm{Ti}$ with I = 5/2 (7.5 % natural abundance) and $^{49}_{22}\mathrm{Ti}$ with I = 7/2 (5.4% natural abundance). The EPR spectra of Ti is therefore mainly dominated by isotopes without hyperfine structure. In spectra with enriched amount of the two mentioned isotopes, the hyperfine structure can be resolved even in glassy environment [PK72].

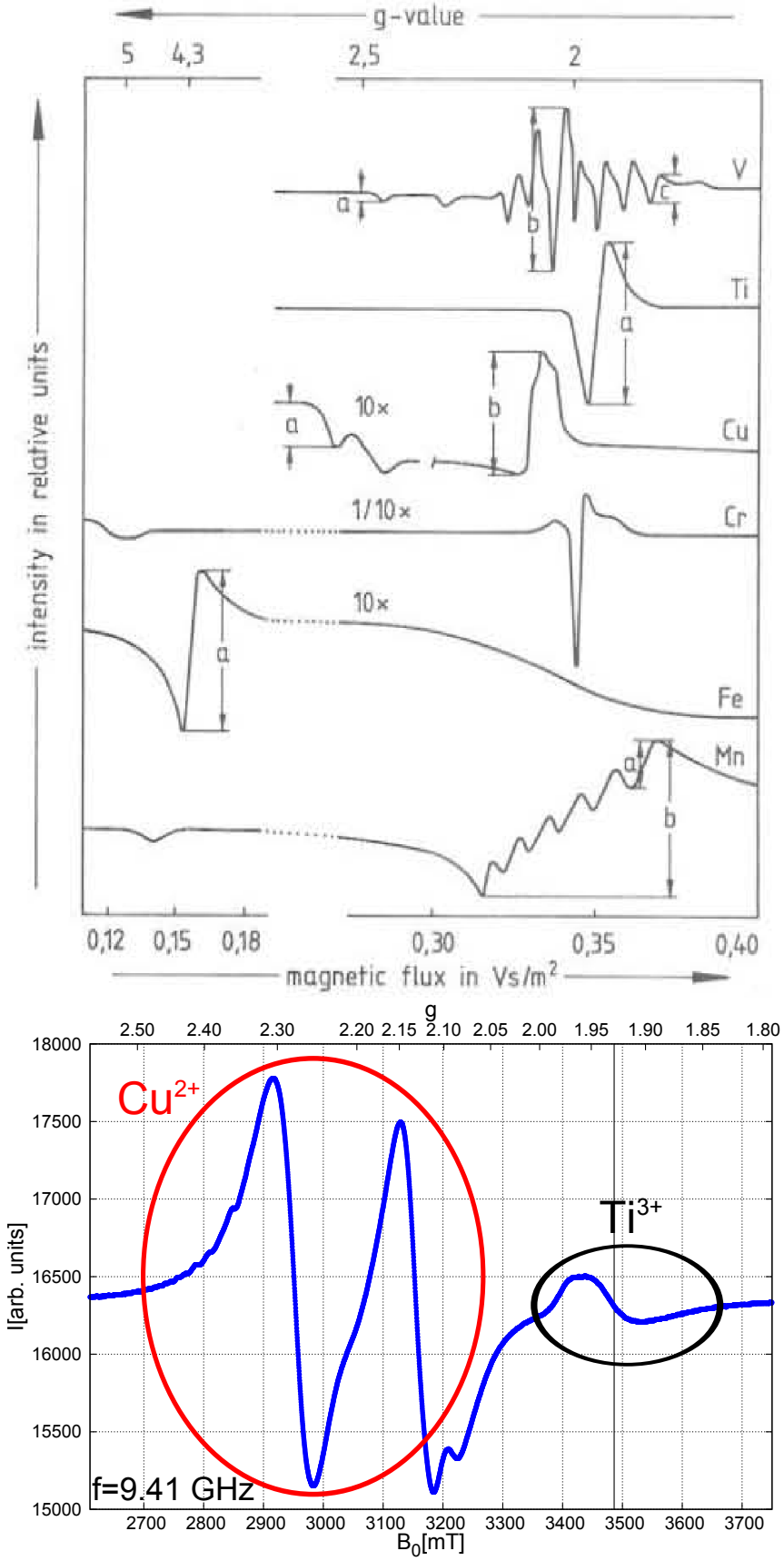

Figure 3.9: Top: representative X-Band ESR spectra of 3d transition metal ions in sodium borate glasses [LB86], bottom: measurement of Ti^{3+} containing glass with $Cu(NO_3)_2$ reference standard

3.8 Optical methods

3.8.1 UV-VIS-IR spectroscopy

UV(ultraviolet)-VIS(visible)-IR(infrared) spectroscopy is an absorption or reflectance method which uses electromagnetic radiation from the near-UV to the near-IR range (0.2-20 µm). Transmission methods can only be used for transparent samples like glasses while reflectance methods can also be used for non-transparent samples. The surfaces of the samples need to be very smooth which can be achieved by optical polishing (mostly using CeO_2 which is a common polishing material in the glass industry) and need to be parallel to each other. The sample thicknesses are around 0.1-1.0 mm. In this work, mainly transmission methods were used, as they showed a higher accuracy in comparison to reflectance methods. In transmission measurements, the light hits the sample under normal incidence, whereby for reflectance methods a neglectable angle of smaller than 10° can be tolerated. The absorption of an electromagnetic wave inside a material can be described by the Beer-Lambert law:

$$I_T(d) = I_0 e^{-\alpha d} \quad , \tag{3.6}$$

with $I_T(d)$ transmitted intensity after distance d, I_0 intensity of the wave before entering the medium, α absorption coefficient.
The complex refractive index $\tilde{n}$ of a glass is dependent on the wavelength:

$$\tilde{n}(\lambda) = n(\lambda) + ik(\lambda) \ , \tag{3.7}$$

whereby the imaginary part is related to the absorption coefficient by $k = \lambda\alpha/(4\pi)$.
The reflectivity $r = I_r/I_0$ on a surface between two media with refractive indices $\tilde{n}$ and $\tilde{n}_0$ is determined by:

$$r = \left|\frac{\tilde{n} - \tilde{n}_0}{\tilde{n} + \tilde{n}_0}\right|^2 \approx \left(\frac{n-1}{n+1}\right)^2 \text{, for } \ k \ll n \ \text{ and } \ n_0 = 1 \ . \tag{3.8}$$

By measuring a sample of finite thickness, also contributions from multiple reflections have to be considered. Using a geometric series expansion we obtain the total reflectivity R_t and transmission T_t (neglecting interference effects [DG02]):

$$R_t = r + r(1-r)^2 \cdot \frac{e^{-2\alpha d}}{1 - r^2 e^{-2\alpha d}} \tag{3.9}$$

$$T_t = (1-r)^2 \cdot \frac{e^{-\alpha d}}{1 - r^2 e^{-2\alpha d}} \overset{[2.O]}{\approx} (1-r)^2 e^{-\alpha d} \quad . \tag{3.10}$$

As n and α are unknown, two independent measurements have to be performed, either a transmission and a reflectivity measurement (T_t, R_t) or a combination of two transmission measurements of different thickness (T_1, T_2). The absorption coefficient can then be determined by:

$$\alpha(T_t, R_t) = \frac{1}{d} \cdot \ln\left(\frac{(1-R_t)^2 - T_t^2 + \sqrt{4T_t^2 + (T_t^2 - (1-R_t)^2)^2}}{2T_t}\right) \tag{3.11}$$

$$\alpha(T_1, T_2)_{[2.O]} = \frac{1}{d_2 - d_1} \cdot \ln\left(\frac{T_1}{T_2}\right) \quad . \tag{3.12}$$

For the combination of two transmission methods no analytical solution exists, but the second order approximation (neglecting all multiple reflections > 2) is accurate enough for this work ($n \approx 2 \Leftrightarrow r^2 = 0.012$). A combination of two transmission measurements turned out to be more suitable, as reflectivity measurements always have a worse signal-to-noise ratio and therefore a comparatively higher error respectively lower resolution. An important criteria for transmission measurement is the sample homogeneity (meaning no striae inside the two samples).

3.8.2 Optical transitions

Absorption bands in glasses are mostly located at both edges of the visible spectrum. Absorptions in the shorter wavelength regime are caused by interatomic electronic transitions/excitations and in the longer wavelengths by vibrational modes of ions [BK99]. Former lie in the UV and the latter in the IR region of the spectrum for most of glasses, causing an absorption-free respectively transparent region in the visible spectrum [Gan92]. In materials containing polyvalent ions, excitations of electrons between adjacent ions and within individual cations (intra-ionic) are possible [WA76]. Transitions between neighboring ions are called charge transfer transitions (CT) including anion-cation and cation-cation transitions. Several oxygen-cation CT transitions lie in the UV range, but absorption edges also can extend in the visible region [Nol80]. All investigated glasses in this work have a high content of TiO_2 (> 40 mol%) and show a yellowish hue which can be attributed to the extension of the

$Ti^{4+} \leftarrow O^{2-}$ CT absorption edge in the visible range [BSDN91] (ν = 49800 cm^{-1} (201 nm) [EE03]). The oscillator strength P (eq. (3.13)) of the electronic transitions [WEBA89] strongly depends on the restraints given by the transition selection rules (see tab. 3.2):

$$P = \left(\frac{1}{\pi r_0}\right) \frac{1}{\varrho_T} \int_{\text{peak}} \alpha(\nu)\, \mathrm{d}\nu \quad , \tag{3.13}$$

with $r_0 = e^2/(m_0 c^2) \approx 2.818 \cdot 10^{-15}$ (classical electron radius) and ϱ_T as particle density.

- Russel-Sounder selection rule: $\Delta S = 0$
- Laporte selection rule: $\Delta L = \pm 1$

Violations of these rules are called forbidden transitions and are of comparatively weaker intensity. The Russel-Sounder rule can be partially circumvented by the influence of spin-orbit coupling (e.g. enables 4f-4f transitions) and Laporte forbidden transitions due to vibronic coupling (e.g. enables 3d-3d transitions in octahedral environment) or ligand field interaction causing a lower symmetric environment (e.g. enables 3d-3d transitions in tetragonal environment) [Gan92].

Type of transition	approx. P
Spin-forbidden, Laporte-forbidden	10^{-7}
Spin-allowed, Laporte-forbidden	10^{-2} to 10^{-5}
Spin-allowed, Laporte-allowed (e.g. CT)	10^{-1}

Table 3.2: Oscillator strengths for various types of transitions [Pau82]

Numerous mechanisms exist for the creation of colors in glasses. Most of commercial glasses are colored by intra-ionic transitions between the 3d or 4f energy levels of dissolved transition-metal or lanthanide ions [Bam77, Bur81, She05b]. The two relevant species for this work are the ion redox pairs of $Ti^{3+/4+}$ and $Ce^{3+/4+}$. The oxidized ions do not show any intra-ionic transitions, whereby the presence of the reduced species leads to optical absorptions in the visible and infra-red range.

Optical transitions of Ti^{3+}

The electron configuration of Ti^{3+} is given by [Ar]3d^{1}4s^2. The ground state of the free ion $^2D_{3/2}$ is five fold degenerated, but in a ligand field the different 3d energy states split up and 3d-3d optical transitions become possible (in accordance with the selection rules). An octahedral environment would only allow one possible transition ($^2T_{2g} \rightarrow {}^2E_g$), but in literature mostly a combination of one main peak ($\nu_1(^2B_{2g} \rightarrow {}^2B_{1g})$ $\approx$ 20000 cm^{-1}) and one smaller peak ($\nu_2(^2B_{2g} \rightarrow {}^2A_{1g}) \approx$ 14000 cm^{-1}) are described.

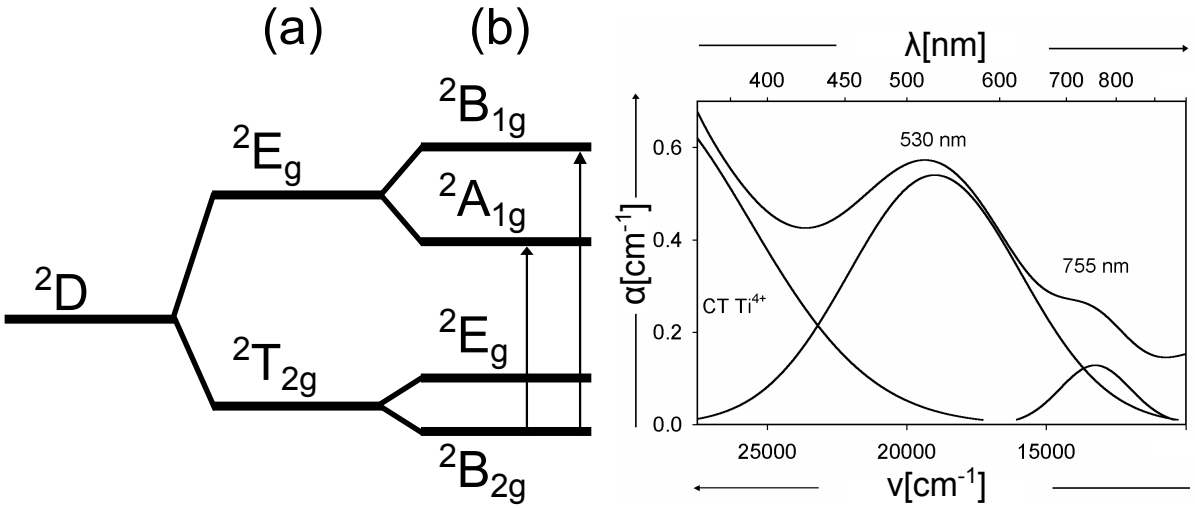

(a) Ti^{3+} energy levels in an octahedral environment (a) tetragonally distorted (b) by the Jahn-Teller effect [Pau75]

(b) Absorption spectrum with Ti^{3+}/Ti^{4+} absorptions in TiO_2-doped $74SiO_2$-$16Na_2O$-$10B_2O_3$ glass (modified from [Sch04])

Figure 3.10: Optical transitions in TiO_2 containing glasses

Ref.	Material	ν_1[cm^{-1}]	ν_2[cm^{-1}]	g
[BSDN91]	P-Na-Al-Ti-O	17700	13800	1.925
[SPBS96b]	Si-Na-B-Ti-O	18900	13250	1.93
[RW79]	Ba-B-Si-Ti-O	20000	13400	1.938
[Pau75]	B/P-Na-Ti-O	17000-21800	12300-14400	1.914-1.94
[ELM01]	various glass types	17000-19050	14000-14900	1.908-1.93
[LB86]	B-Na-Ti-O	22200		1.95
[BB70]	Si-Na-Ti-O	20000		1.925-1.94
[Pau82]	P-Na-Ti-O	18000	14000	
	B-Na-Ti-O	21000	14000	
[MYT94]	Si-A-E-Ti-O	18530-19240	12500	
	B-A-E-Ti-O	19430-25020	12500	
	P-Al-A-E-Ti-O	17020-18130	12500	
[Gan92]	silicate glasses	18100	14300	
[Nol80]	Si-Mg-Ca-Al-Fe-Ti-O	17700		
[ALN$^+$08]	Al-Ca-Si-Mg-Ti-O			1.96
[Car07]	various glass types			1.951
[PK72]	B-Ca-Ti-O			1.95
[AB70]	B-Ca-Ti-O			1.942
[KP03]	$BaTiO_3$			1.932
[XLYY12]	TiO_2			1.978

Table 3.3: Overview about literature data of Ti^{3+} containing materials concerning their optical and EPR properties (data given in wavelength units was transformed in cm^{-1}, *: A = alkali, E = earth alkali)

This additional minor absorption is caused by a tetragonal distortion of the octahedral environment by stretching the octahedra along one axis. Thereby the octahedral symmetry is broken and the degeneration of the lowest energy state $^2T_{2g}$ is removed (see fig. 3.10), leading to a lower energy state. This effect is known as Jahn-Teller effect [Pau82, WA76]. In tab. 3.3 results of different authors are summarized.

Optical transitions of Ce^{3+}

The electron configuration of Ce^{3+} is given by [Xe]4f^1, having one unpaired 4f valence electron. The 4f valence electrons of the lanthanides are located at inner atomic shells and are therefore more screened from interaction with the ligand field as the 3d valence electrons of the transition metals. As a consequence lanthanide compound spectra are similar to the free ion spectra as they interact very weakly with the ligands. This leads to comparatively narrow absorption peaks. The ^2F ground state of the free ion is split by spin-orbit coupling into a $^2F_{5/2}$ and a $^2F_{7/2}$ state by 2200-2250 cm^{-1} [BRC66, Lan36, DKPK04, WBC$^+$89, WEBA89] (see fig. 3.11(b)). In glasses, only one comparatively broader peak is found, Zheng et al. [ZZY$^+$13] located this absorption at 2150 cm^{-1} in Ce-doped TeO_2-ZnO-Na_2O glasses. Additional splitting into Stark levels can occur due to interaction of a crystalline environment (e.g. for CeF_3, see fig. 3.11(a)). The first excited state (5d) lies around 38000 cm^{-1} above the ground state [Web73]. The absorptions of Ce^{3+} therefore only consists of the one mentioned 4f-4f transitions in the near-IR and 4f-5d transitions in the UV.

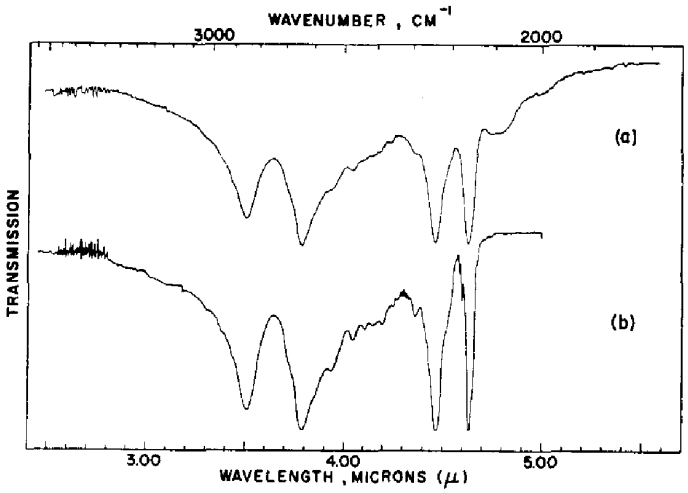

(a) Absorption spectra of a 0.125 mm thick CeF_3 crystal (cooled by liq. a: N, b: He) showing the four major transitions from the $^2F_{5/2}$ ground state to the four Stark levels $^2F_{7/2}$ of the state [BRC66]

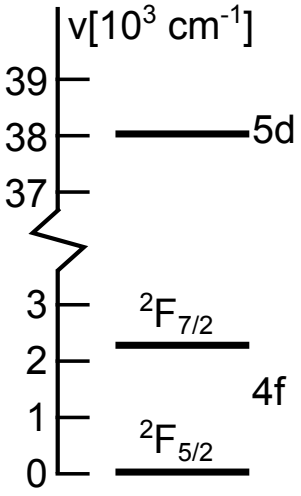

(b) Energy level diagram of Ce^{3+} (mod. from [PMZ76])

Figure 3.11: Ce^{3+} absorptions

3.8.3 Ellipsometry

Ellipsometry is an optical characterization technique using light from the IR to the UV range for the direct determination of the frequency dependence of the dielectric properties of a material. The incident light beam is linearly polarized (using a wire grid polarizer) and the change of polarization is measured upon reflection by an optically polished sample surface under a known angle of incidence (AOI). The AOI is chosen close to the brewster angle to achieve a maximum difference in r_s and r_p.

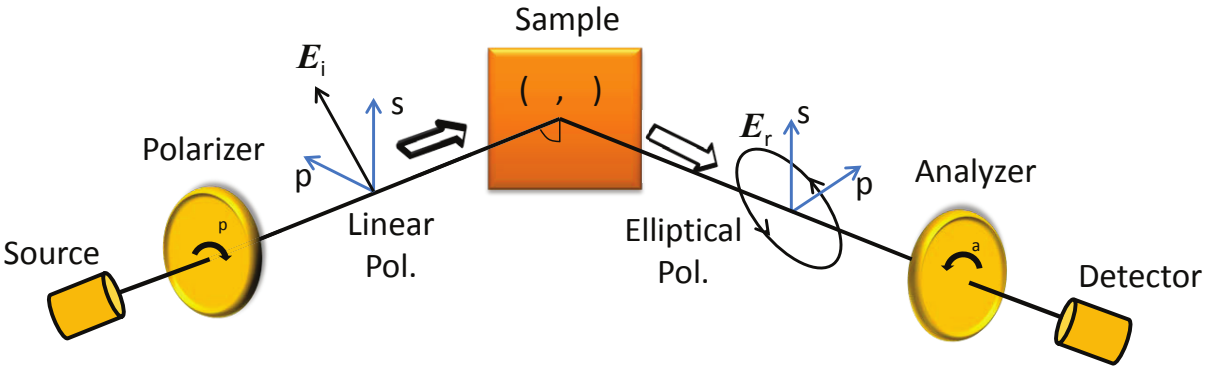

Figure 3.12: Ellipsometry schematic experimental setup [NA13]

The plane of incidence is determined by the incident and reflected beam and the polarization state is expressed according to the s and p direction (see fig. 3.12). The ratio of the electric field components before and after reflection are expressed by the complex reflection coefficient r_s and r_p and their ratio is defined as ρ which is parameterized by the angles Ψ ($\tan(\Psi) = |r_p|/|r_s|$ depending on the amplitude ratio) and Δ (phase shift: $\delta_p - \delta_s$) [NA13]:

$$\rho(\Psi, \Delta) = \tan(\Psi)e^{i\Delta} = \frac{r_p}{r_s} = \frac{E_{r_p}}{E_{i_p}} / \frac{E_{r_s}}{E_{i_s}} \quad . \tag{3.14}$$

For bulk samples the angles Ψ and Δ can be directly extracted from the experimental data for every measured frequency. For a given AOI α the complex permittivity is then given by eq. (3.15) which can be derived from the Fresnel equations [Kuz98]:

$$\varepsilon_r(\alpha; \Psi, \Delta) = \sin^2(\alpha) \left(1 + \tan^2(\alpha) \left(\frac{1-\rho}{1+\rho} \right)^2 \right) \quad . \tag{3.15}$$

The experimental setup is described in fig. 3.13/3.14. The position of the light source (synchrotron) was fixed and for a minimum of one polarizer angle (normally the data was averaged over 2 to 4 different angles) the intensity was measured for rotating

analyzer position (RAE: rotating analyzer ellipsometry, here: 20 analyzer positions equally distributed along 360°). The AOI could be varied between 65° and 85° and the covered spectral range was between 50 to 700 cm^{-1}.

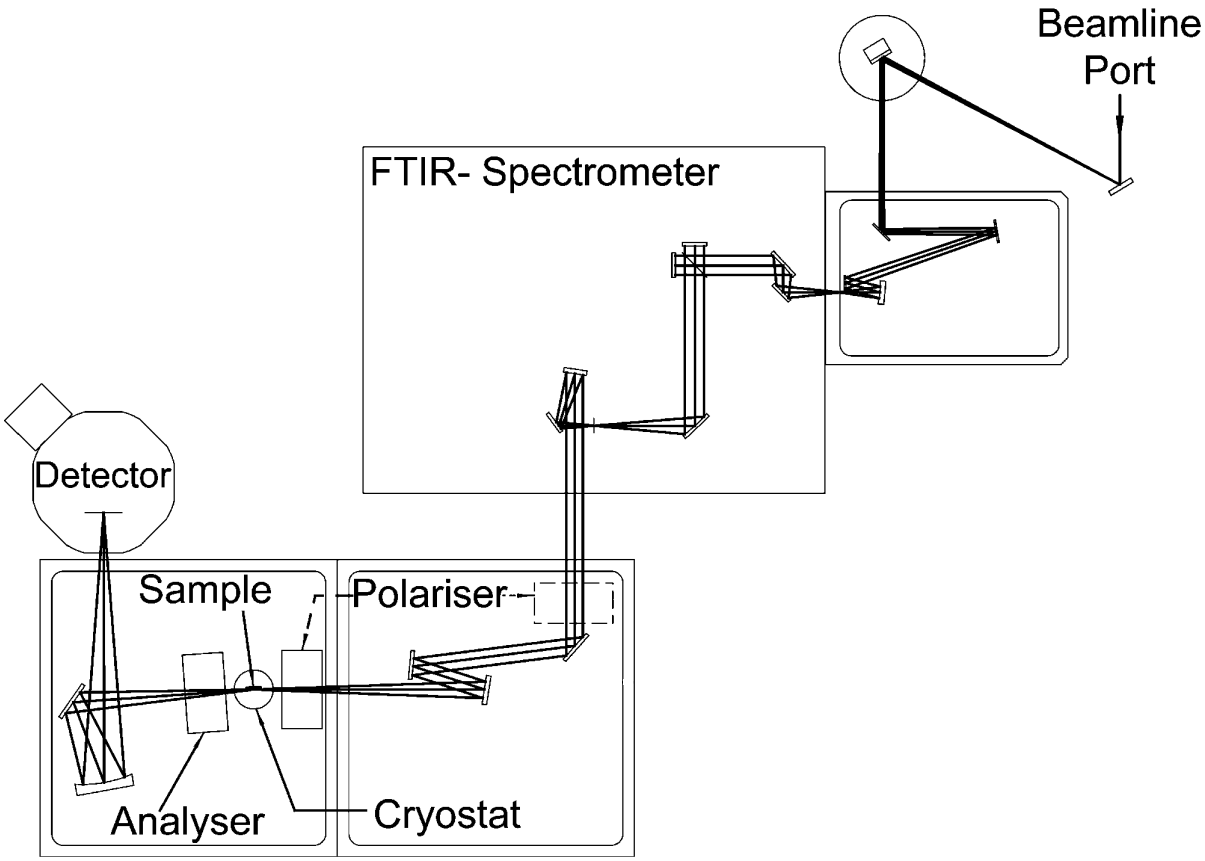

Figure 3.13: Sketch of the ellipsometer setup at the IR-beamline of the ANKA synchrotron light source at KIT (dotted arrow indicates variable possibilities for the polarizer position) [BHK04]

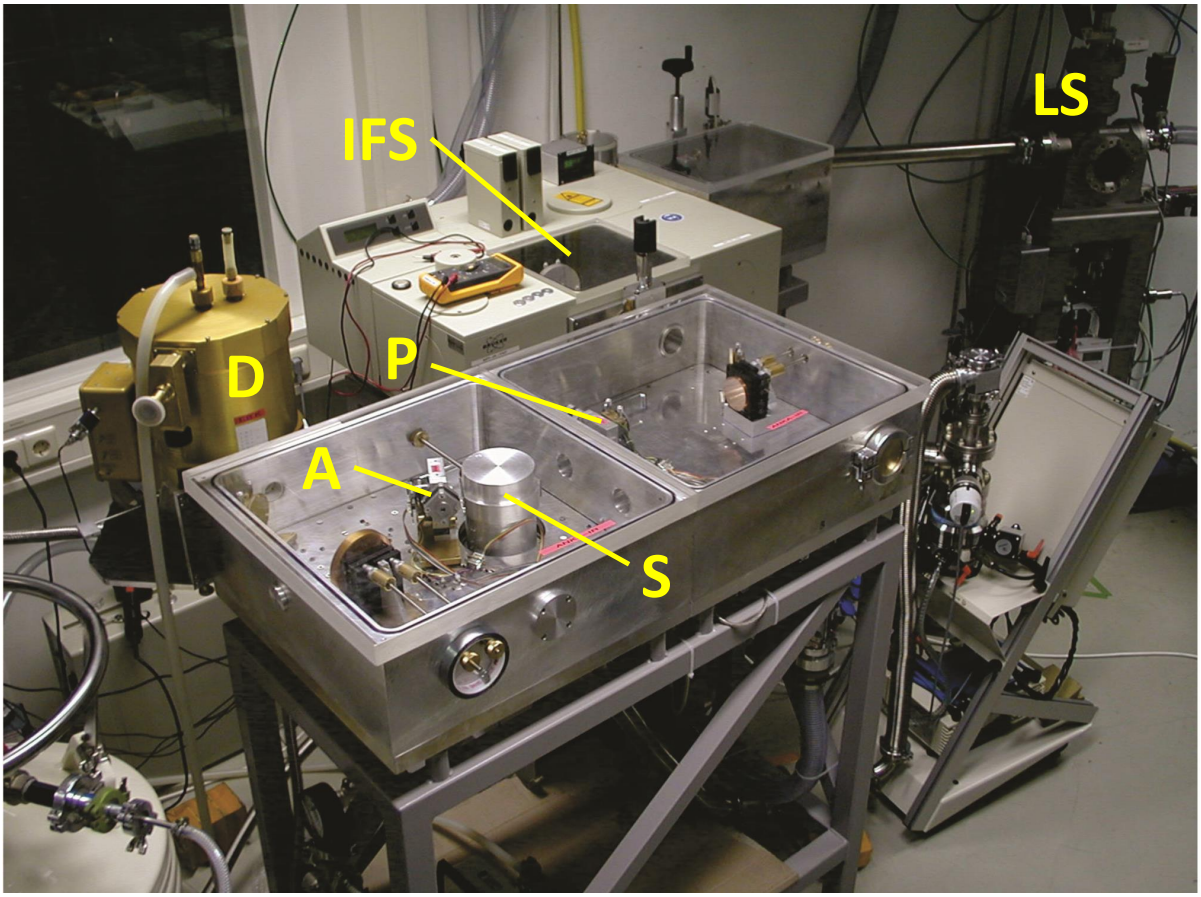

Figure 3.14: Experimental setup at the synchrotron facility ANKA at the KIT (LS: synchrotron light source, IFS: Bruker IFS 66 v/S spectrophotometer, P: polarizer, A: analyzer, S: sample, D: He cooled bolometer detector) [Prö14]

The advantages of ellipsometry in comparison to other reflection techniques are:

- the complex permittivity can be extracted directly without the use of complex fitting models or the use of Kramers-Kronig analysis (see chapter 2.7.2)
- no reference measurement (absolute intensity values) necessary as only intensity ratios are measured, resulting in less susceptibility against intensity instabilities of the source

The sources of error mainly are determined by imprecisions in the positioning of the optical elements and leakage in the polarizers [NA13, AB77]. The measurements were performed at room temperature and under vacuum conditions to avoid absorption from water and other gases with IR-active bands.

3.9 Dielectric characterization in the GHz range

In comparison to other GHz characterization methods (transmission, reflection, perturbation methods) resonance methods offer the best resolution for dielectric losses, but also the highest experimental requirements concerning equipment and sample preparation [She05a, She09, SML07, BJJR+02]. All measurements were made in collaboration with the group of Prof. Rolf Jakoby (TU Darmstadt, Institute for Microwave Engineering and Photonics) using an Anritsu 37397C vector network analyser. Comparative measurements were made at the group of Prof. Michael Lanagan (Penn State University, Department of Materials Science and Engineering) and at the group of Prof. Ian Reaney (Sheffield University, Department of Materials Science and Engineering). The samples were prepared from bulk pieces by mechanical preparation, the top and bottom surfaces were optically polished. Special care was taken during the preparation process as the accuracy of the measurement depends crucially on the cylinder symmetry. The determination of ε_r and $\tan(\delta)$ from the measured data was done numerically using a Mathematica8.0 script (see chapter A.2) for each of the 3 used methods.

3.9.1 Hakki-Coleman method

The main GHz characterization method of this work is the Hakki-Coleman method. The sample is placed between two conductive metal plates (polished copper) and then a GHz signal is transmitted through the sample which excites an electromagnetic resonance. The sample can thereby be understood as dielectric resonator. The coupling loops at the end of the coaxial cables are oriented parallel to the sample, to generate a field distribution inside the sample which corresponds to the TE_{011} eigenmode. The inner conductor of the coaxial cable is slightly longer than the outer conductor and is bent backwards and soldered to the outer conductor to form a loop. By measuring the resonance frequency and the width (FWHM) of the resonance peak (see chapter 2.5), the permittivity and the dielectric loss of the material can be determined at one frequency point (resonance frequency of the mode). Different frequencies can be measured by varying the size of the sample, approximately between 5-15 GHz for the investigated materials.

The derivation of the theoretical basics will be shortly summarized. A detailed consideration can be found in [KG86]. Starting with Maxwell's equations for the cylindrical dielectric waveguide (see fig. 3.17, with relative permittivity ε_r, relative

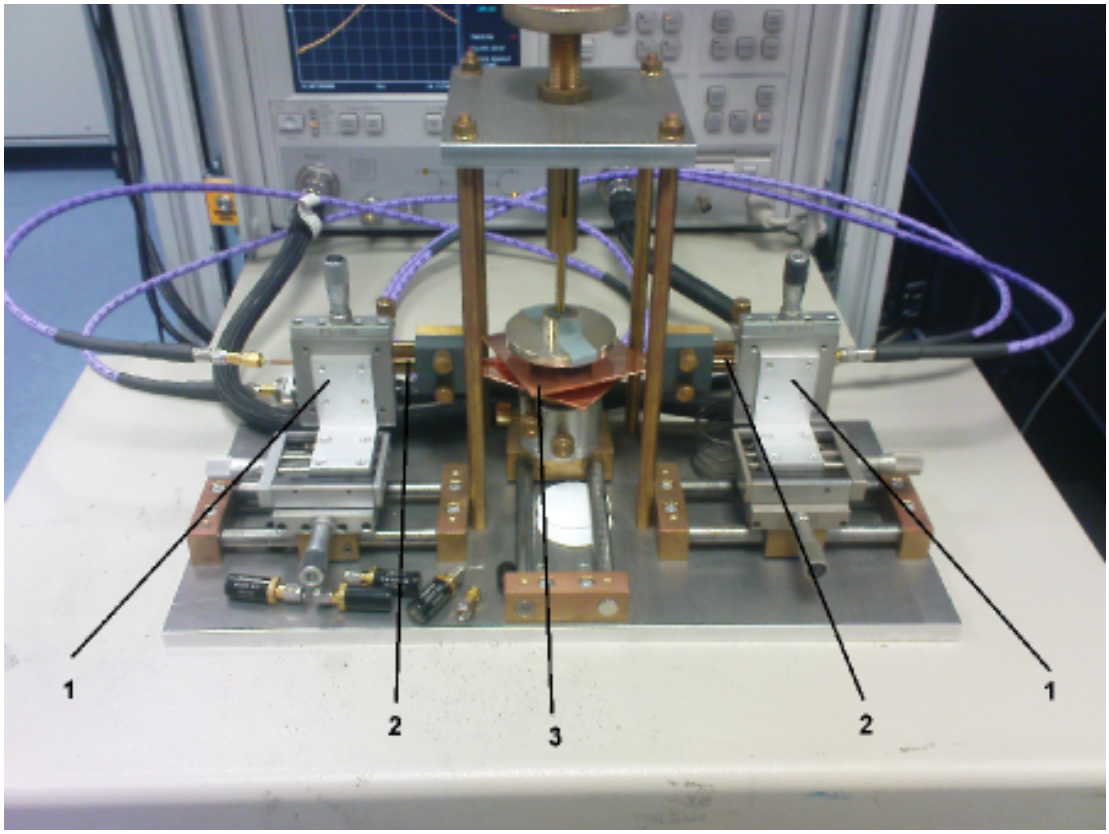

Figure 3.15: Experimental setup of the Hakki-Coleman method at the TU Darmstadt. The coupling loops and copper cables (2) can be adjusted using the setting screws (1). The polished copper plates (3) are adjustable in height to avoid air gaps between the sample and the metal [Bra11]

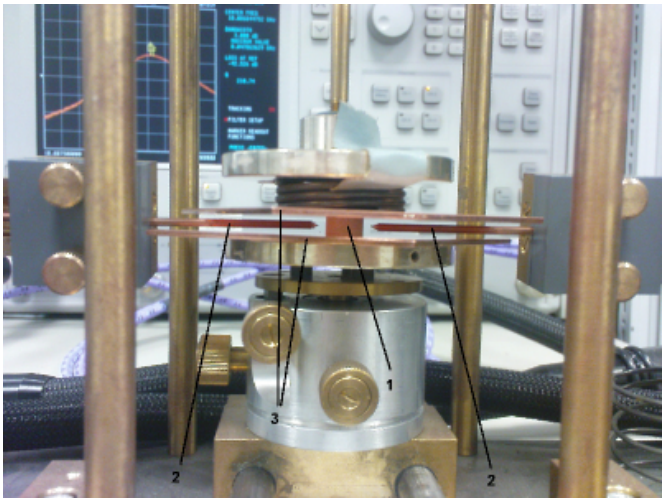

(a) Close-up view of the measurement setup, including sample (1), copper cables (2) and copper plates (3) [Bra11]

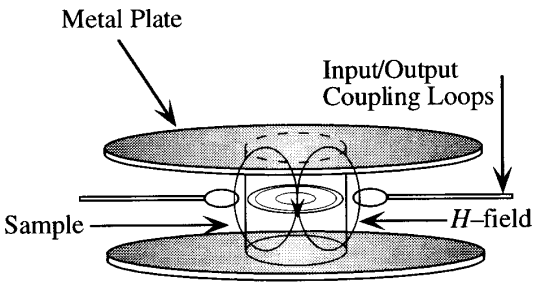

(b) Schematic description of the coupling, inc. the generated H field distribution [MJN98]

Figure 3.16: Hakki-Coleman measurement setup

permeability μ_r = 1 and radius a) using a harmonic time dependence leads to:

$$\nabla \times \mathbf{H} = i\omega\mathbf{D} + \mathbf{j} \tag{3.16}$$

$$\nabla \times \mathbf{E} = -i\omega\mathbf{B} \tag{3.17}$$

$$\nabla \cdot \mathbf{D} = \rho \tag{3.18}$$

$$\nabla \cdot \mathbf{B} = 0 \quad . \tag{3.19}$$

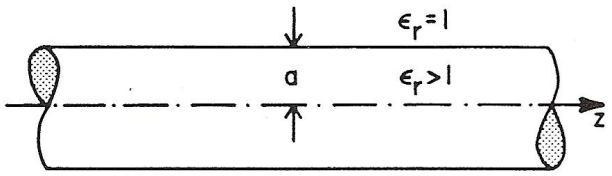

Figure 3.17: Dielectric waveguide [KG86]

The source-free wave equations are solved for $\mathbf{E}$ and $\mathbf{H}$ in cylindrical coordinates under assumption of a loss-free material ($\varepsilon_r'' = 0$). Using the boundary conditions for the fields (tangential components of $\mathbf{E}$ and $\mathbf{H}$ continuous at the boundary dielectric to air ($r = a$)) leads to the eigenvalue equation of the waveguide:

$$F_1(x)F_2(x) - F_3^2(x) = 0 \quad , \tag{3.20}$$

with

$$F_1(x) = \frac{J_m'(x)}{x} + \frac{K_m'(y)J_m(x)}{\varepsilon_r y K_m(y)} \quad \text{, TM}_{0n} \text{ modes for } \; m = 0 \tag{3.21}$$

$$F_2(x) = \frac{J_m'(x)}{x} + \frac{K_m'(y)J_m(x)}{y K_m(y)} \quad \text{, TE}_{0n} \text{ modes for } \; m = 0 \tag{3.22}$$

$$F_3(x) = \frac{\beta a m}{k_0 a\sqrt{\varepsilon_r}} J_m(x)\left(\frac{1}{x^2} + \frac{1}{y^2}\right) \quad \text{, HEM}_{mn} \text{ modes for } \; m \neq 0, \tag{3.23}$$

with eigenvalue $x_{mn}(f_0, \varepsilon_r, a)$ and:

$$y = \sqrt{(k_0 a)^2(\varepsilon_r - 1) - x^2} \tag{3.24}$$

$$\beta a = \sqrt{(k_0 a)^2 \varepsilon_r - x^2} \quad . \tag{3.25}$$

$J_m(x)$ and $K_m(x)$ are the Bessel functions resp. modified Bessel functions of the second kind and $k_0 = \omega_0/c$. β can be interpreted as wave number in z-direction. Inserting two ideal conducting plates perpendicular to the cylinder axis in the distance h, leads to the Hakki-Coleman geometry and creates a dielectric resonator with the usual resonator condition (length is an integral multiple of half the wavelength, eq. (2.51):

$\beta \stackrel{!}{=} p \cdot \frac{\pi}{h}/$, with $p \in \mathbb{N}$). The eigenvalue then becomes (see eq. (3.25)):

$$x_{mnp} = \sqrt{(k_0 a)^2 \varepsilon_r - \left(\frac{a}{h} p\pi\right)^2} \quad . \tag{3.26}$$

Eq. (3.26) substituted in (3.20) results in an implicit equation of the form:

$$g(f_0, \varepsilon_r; a, h, m, p) = 0 \quad . \tag{3.27}$$

For known resonator geometry (diameter d = $2a$, height: h) and resonance mode EM_{mnp} the permittivity ε_r can be determined numerically from the measured resonance frequency. The dielectric loss of the sample $\tan(\delta) = 1/Q_d$ is only one contribution of the measured loss $1/Q_l$ (Q_l: loaded Q). To understand the different contributions of the measured loaded Q we need to introduce some basic terms from network theory. An experimental setup like the Hakki-Coleman setup is considered as a two-port network [ZB65] (see fig. 3.18).

Figure 3.18: Two-gate network (modified from [ZB65])

A signal a_1 (proportional to the voltage) is emitted from the network analyzer and transmitted through the resonator. The transmitted signal $b_2 < a_1$ is detected while a_2 is set to zero. The S parameters are now defined via the scattering matrix $\mathbf{S}_{2\times2}$:

$$\begin{pmatrix} b_1 \\ b_2 \end{pmatrix} = \begin{pmatrix} S_{11} & S_{12} \\ S_{21} & S_{22} \end{pmatrix} \begin{pmatrix} a_1 \\ a_2 \end{pmatrix} \quad . \tag{3.28}$$

The scattering matrix represents the relation between the incoming (a_i) and outgoing (b_i) signals. The transmission factor S_{21}=$(\mathrm{b}_2/\mathrm{a}_1)\,|_{a_2=0}$ is a measure of the ratio of incoming to outgoing signal amplitude and describes the amount of signal which is transmitted through the resonator. The S parameters can be measured directly with the network analyzer and mostly are expressed logarithmically. For a passive two-gate network S_{21} is called insertion loss S_{21}[dB] =10 lg $|S_{21}|^2$ = 20 lg $|S_{21}|$ [KH84] (remark: S_{21}[dB] describes a power ratio, sometimes also written as α[dB], whereby the S_{21} itself describes a voltage ratio). The insertion loss can be interpreted as additional loss contribution to the overall loss, describing the amount of energy which is not

available for the excitation of the resonator. The measured loss $1/Q_l = 1/Q_u + 1/Q_i$ is the sum of intrinsic/unloaded losses $1/Q_u$ of the resonator (representing the contributions of the dielectric loss, ohmic loss in the metals and the radiation loss) and the insertion (extrinsic) loss $1/Q_i = 1/Q_l \cdot |S_{21}|$ [Kaj84].

$$\frac{1}{Q_{\text{loaded}}} = \frac{1}{Q_{\text{unloaded}}} + \frac{1}{Q_{\text{i}}} \quad \Leftrightarrow \quad \frac{1}{Q_{\text{loaded}}} = \frac{1}{Q_{\text{unloaded}}} \cdot \frac{1}{1 - |S_{21}|} \quad . \tag{3.29}$$

The $Q_l = f_0/\Delta f_{3\text{dB}}$ value can be directly determined via eq. (2.47) by measuring the peak resonance frequency (f_0) and the FWHM ($\approx \Delta f_{3\text{dB}}$). With the measured Q_l and S_{21} we can then calculate Q_u with eq. (3.29):

$$Q_u = \frac{f_0}{\Delta f_{3\text{dB}}} \frac{1}{1 - 10^{\frac{S_{21}[\text{dB}]}{20}}} \quad . \tag{3.30}$$

The unloaded Q (Q_u) can then be expressed as sum of the intrinsic contribution [HC60, KDA+99]:

$$\frac{1}{Q_u} = \frac{1}{Q_d} + \frac{1}{Q_R} + \frac{1}{Q_C} \quad , \tag{3.31}$$

with

- $1/Q_d = p_d \cdot \tan(\delta)$: dielectric loss of the sample
- $1/Q_R$: radiation Losses, neglectable for closed resonator systems or if metal plates are much bigger than the sample diameter
- $1/Q_C = P_C/(\omega_0 U_0)$: ohmic losses in metal plates ($P_C \sim R_S$)
- p_d: filling factor $p_d = U_d/U_0$, ratio of (time averaged) stored field energy inside the sample to the field energy in the complete resonator

The dielectric loss of the material $\tan(\delta)$ can then be calculated from Q_u via:

$$\tan(\delta) = \frac{1}{p_d}\left(\frac{1}{Q_u} - \frac{1}{Q_C}\right) = \frac{U_d + U_a}{U_d}\left(\frac{1}{Q_u} - \frac{1}{Q_C}\right) = \frac{A}{Q_u} - B \quad , \tag{3.32}$$

with $A = 1 + U_a/U_d$ ($U_{a,d}$: stored energy in air, dielectric) and $B = P_C/(\omega_0 U_d)$. A and B can be determined from the electromagnetic fields of the TE_{011} mode (see [KG86, HC60]) using eq. (3.33)-(3.35):

$$U_d = \frac{1}{2}\varepsilon_r \varepsilon_0 \int_V |E_{\phi,d}|^2 \, \mathrm{d}V \tag{3.33}$$

$$U_a = \frac{1}{2}\varepsilon_0 \int_V |E_{\phi,a}|^2 \, \mathrm{d}V \quad . \tag{3.34}$$

The stored field energy is calculated using $U_{EM} = \frac{1}{4}(\varepsilon \int \mathbf{E}^2 + \mu \int \mathbf{H}^2)\ \mathrm{d}V = \frac{1}{2}\varepsilon \int \mathbf{E}^2\ \mathrm{d}V$ [WEM05], considering that the field components E_r and E_z are zero for the TE_{011} mode and the fact that the magnetic and electric field energy are identical at resonance [Poz04] (factor 1/4 due to time averaging). The ohmic losses in the metal plates P_C can be determined in first order approximation from the surface resistivity and the tangential components of the H field (H_r and H_ϕ, whereby H_ϕ = 0 for the TE_{011} mode) via eq. (2.49) [LL67]:

$$P_C = \frac{1}{2}R_S \int_S |J_S|^2\ \mathrm{d}S = \frac{1}{2}R_S \int_S |H_{r,i}|^2\ \mathrm{d}S \quad . \tag{3.35}$$

A and B can then be expressed as:

$$A = 1 + \frac{J_1^2(x)}{\varepsilon_r K_1^2(y)} \left[\frac{K_0(y)K_2(y) - K_1^2(y)}{J_1^2(x) - J_0(x)J_2(x)} \right] \tag{3.36}$$

$$B = \frac{p^2 R_S}{2\pi f^3 \mu_0^2 \varepsilon_r \varepsilon_0 h^3} \left[1 + \frac{J_1^2(x)}{K_1^2(y)} \left[\frac{K_0(y)K_2(y) - K_1^2(y)}{J_1^2(x) - J_0(x)J_2(x)} \right] \right] \quad . \tag{3.37}$$

The determination of ε_r and $\tan(\delta)$ is made in the following way:

1. For unknown materials, measurement of the permittivity in the MHz range, as ε(MHz) $\approx \varepsilon$(GHz) (see fig. 2.14), otherwise rough estimation for the permittivity
2. Calculation of the resonance frequencies of the TE_{011} mode and adjacent modes (HEM_{111}, HEM_{211}, TM_{011}) using the estimated permittivity and eq. (3.27)
3. Measurement of the GHz spectrum in the frequency range of the four modes mentioned above and identification of the resonance peaks to the modes
4. Measurement of $f_{TE_{011}}$ ($\Rightarrow$ ε_r with eq. (3.27)), insertion loss S_{21}[dB] and $Q_{\text{loaded,TE}_{011}}$ ($\Rightarrow \tan(\delta)$ with eq. (3.30) and (3.32))

Exemplary the resonance frequencies for a standard sample geometry and permittivity are calculated:

EM_{mnp}	HEM_{111}	TE_{011}	HEM_{211}	TM_{011}	HEM_{121}	HEM_{131}	HEM_{221}	TE_{021}
f[GHz]	9.623	10.736	11.383	11.632	12.588	14.118	14.532	15.292

Table 3.4: Lowest modes of the Hakki-Coleman method, exemplary for ε_r = 20, d = 10 mm, h = 4 mm

Eq. (3.27) is plotted in fig. 3.19(a), showing the permittivity dependence of resonance frequency for the Hakki-Coleman modes. In fig. 3.19(b) a frequency spectrum (S_{21}[dB] in dependence of frequency) of the lowest modes is shown exemplarily.

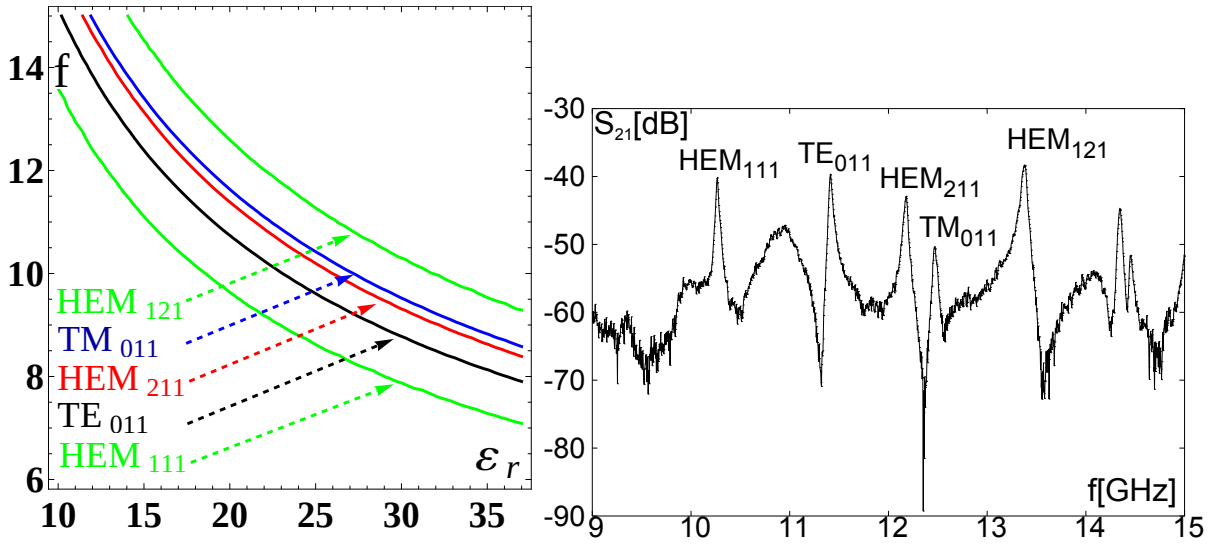

(a) Lowest Hakki-Coleman modes (HEM_{111}, TE_{011}, HEM_{211}, TM_{011}, HEM_{121}), exemplarily for d = 10 mm, h = 4 mm

(b) Frequency spectrum $S_{21}(f)$ of a sample with d = 9.87 mm, h = 3.97 mm, ε = 18 und $Q_{l,TE_{011}}$ = 378

Figure 3.19: Resonance modes of the Hakki-Coleman method

To avoid an overlap of the resonance peaks an optimized diameter to height ratio for the sample is usually used. It can be shown with eq. (3.27) that for a ratio of approximately d/h = 2.5 the difference between the resonance frequencies of adjacent modes to $f_{TE_{011}}$ is maximal [Seb08]. For samples of unknown permittivity it can be difficult to identify the different modes. The TE_{011} resonance can be identified by lifting up the upper metal plate which leads to a small shift of the resonance frequency to lower frequencies whereby the adjacent modes shift to higher frequencies [KWW86]. This frequency shift is related to the fact that the E field amplitude for the TE_{011} resonance is going to zero at the top/bottom of the sample (E field has only a tangential component which needs to approach zero for metallic boundary conditions) whereby the adjacent modes have non-vanishing orthogonal E field components. There are several reasons to use the TE_{011} mode (lowest transverse electric mode) to determine the dielectric properties. In principle it would be possible to use all existing modes but the TE_{011} mode has a relative simple field geometry (radial symmetric E field, see fig. 3.20) which can be excited comparatively easy using two coupling loop rings. Additionally the calculation of the Q value can become comparatively complex for non-radial symmetric modes.

From the field geometry of the TE_{011} resonance it can be seen, that the coupling loops should be oriented parallel to the conducting plates to generate an H field similar to that of the mode (see fig. 3.16). Due to the implicit dependence of $\varepsilon_r(f_0(\varepsilon_r), a, h)$ the error cannot be determined analytically. In chapter 2.6 it was shown that the

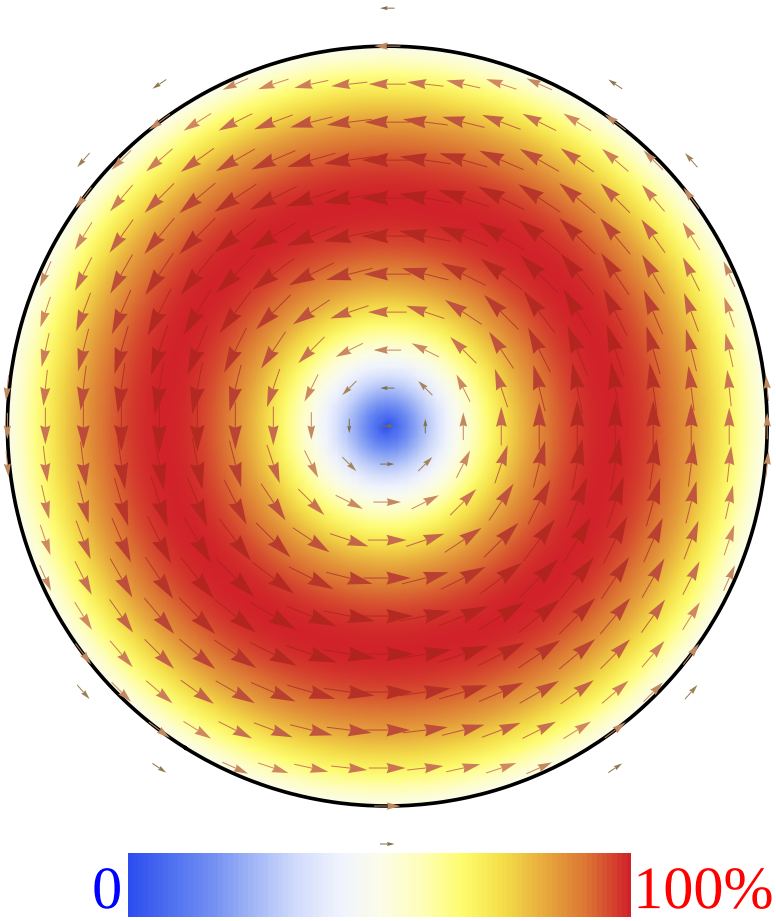

Figure 3.20: Vector plot of the E field distribution of the radial symmetric TE_{011} resonance at the symmetry plane of the cylinder, for d = 10 mm, h = 4 mm, ε_r = 20

eigenvalue x can be assumed constant, leading to eq. (3.38):

$$\varepsilon_r = \left(\frac{c}{2\pi}\right)^2 \left(\frac{\overbrace{x^2}^{\approx\text{const.}}}{a^2} + \frac{(p\pi)^2}{h^2} \right) \cdot \frac{1}{f_0^2} \quad . \tag{3.38}$$

The relative error of ε_r according to Gauß error propagation becomes:

$$\frac{\Delta\varepsilon}{\varepsilon_r} = 2\sqrt{\left(\frac{\Delta f}{f}\right)^2 + \left(\frac{\Delta d}{d}\right)^2 + \left(\frac{\Delta h}{h}\right)^2} \quad . \tag{3.39}$$

The contribution of the measurement error of the resonance frequency is comparatively small (Δf = 10 Hz resp. $\Delta f/f < 10^{-8}$) and can be neglected. The main

contribution is related to the inaccuracy of the sample geometry (Δd, Δh) which can be estimated to one scale division of a caliper ($\Delta d = \Delta h \approx 0.01$ mm). The relative error for the permittivity of a sample with the ratio $d/h = 2.5$ can be approximated to:

$$\frac{\Delta\varepsilon}{\varepsilon} = 2\sqrt{\left(\frac{\Delta f}{f}\right)^2 + \left(\frac{\Delta d}{d}\right)^2 + \left(\frac{\Delta d}{h}\right)^2} \approx 2\frac{\Delta d}{d}\underbrace{\sqrt{1+\left(\frac{d}{h}\right)^2}}_{=\sqrt{1+2.5^2}\approx 2.7} \approx 5.4\frac{\Delta d}{d} \quad . \tag{3.40}$$

The relative error is directly proportional to the relative error of the length measurement. For a usual sample geometry of $d = 10$ mm, $h = 4$ mm the relative error of the permittivity is approximately $\Delta\varepsilon/\varepsilon = 0.5\ \%$, which is sufficiently accurate for the purposes of this work. The measurement accuracy could be further optimized by a more accurate determination of the sample geometry. The relative error of the permittivity is normally estimated to approximately 0.1 % in literature [DZB+97, Cou70, KK85]. Comparative measurements with Hakki-Coleman setups at three different institutes showed a deviation of the permittivity values by maximal 1.0 % and dielectric loss values by maximal 10 %. For the given $\tan(\delta)$ values a relative error of 10 % is therefore estimated. A critical sample requirement is the cylinder geometry. Measurements on high Q teflon samples with different amount of tilting of the cylinder axis in relation to the base area were performed to investigate the influence of deviations from the cylinder symmetry (see fig. 3.21).

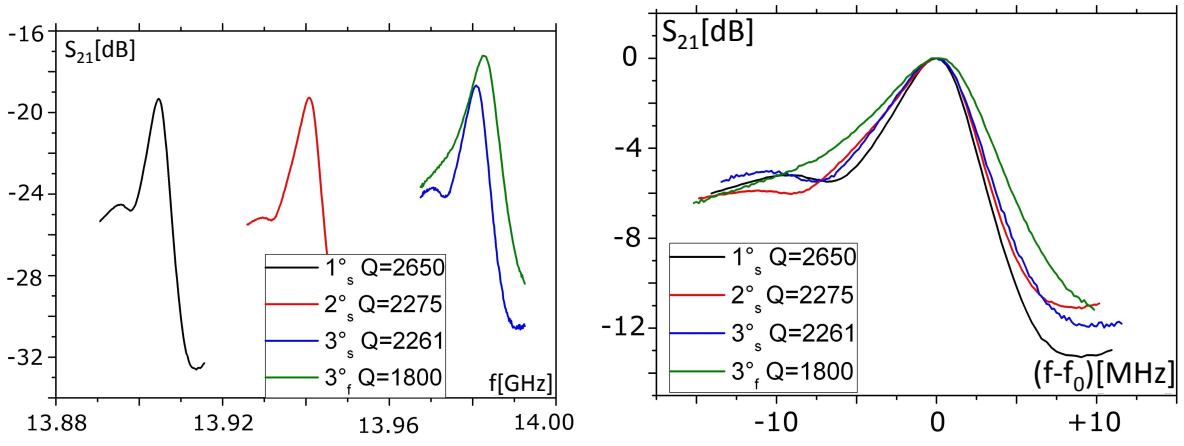

(a) Obvious shift and broadening of the resonance peaks with tilting angle [Bra11]

(b) Superposed resonance curves to visualize the broadening [Bra11]

Figure 3.21: Shift and broadening of the TE_{011} resonance peak by inaccurate sample symmetry (position of the sample relative to the coupling loops: parallel (s) resp. orthogonal (f) to the tilting direction of the cylinder axis)

The measurement error of Q_l itself can be neglected for low dielectric loss values ($\tan(\delta) < 10^{-3}$). The main error contribution for the glass and glass-ceramic samples in this work is caused by sample inhomogeneities which can cause severe variations of the dielectric loss and can hardly be estimated as they vary strongly for every glass melt. The resolution limit for the dielectric loss is mainly determined by the surface resistivity of the metal plates. If $\tan(\delta)$ becomes smaller than B ($B \sim R_S$), the measured resonator loss ($1/Q_l$) becomes dominated by the ohmic loss. For a standard parameter choice $B = 2.1 \cdot 10^{-4}$ (d = 10 mm, h = 4 mm, ε_r = 20, f_0 = 10.735 GHz, σ_{copper} = $5.8 \cdot 10^7$ S/m). The error of B is dominated by the uncertainty of R_S. Theoretically R_S can be calculated from the electric conductivity and the frequency via eq. (2.49) but oxidation, surface scratches or impurities can deteriorate the conductivity. Using eq. (3.32) it follows:

$$\frac{\Delta \tan(\delta)}{\tan(\delta)} = \left|\frac{1}{\tan(\delta)} \Delta R_S \cdot \frac{\partial \tan(\delta)}{\partial R_S}\right| = \frac{\Delta R_S}{R_S} \cdot \frac{B}{\tan(\delta)} \quad . \tag{3.41}$$

Dube et al. [DZB+97] used samples of similar diameter but varying height to determine R_S. He achieved a maximal accuracy of 7.5 %. Assuming a relative error of $\Delta R_S/R_S$ = 10 %, the resolution limit ($\Delta \tan(\delta)/\tan(\delta) > 50$ %) can be estimated to $\tan(\delta) = 4 \cdot 10^{-5}$ (see tab. 3.5). This is one order of magnitude lower than the lowest dielectric loss values measured in this work and therefore the Hakki-Coleman method can be considered as sufficiently accurate for the dielectric loss determination.

$\tan(\delta)$	$5 \cdot 10^{-3}$	$1 \cdot 10^{-3}$	$5 \cdot 10^{-4}$	$1 \cdot 10^{-4}$	$5 \cdot 10^{-5}$	$1 \cdot 10^{-5}$
$\frac{\Delta \tan(\delta)}{\tan(\delta)}$[%]	0.4	2.0	4.0	20	40	200

Table 3.5: Dependence of the relative error of the dielectric loss for $\Delta R_S/R_S$ = 0.1 and d = 10 mm, h = 4 mm, ε_r = 20

3.9.2 Modified Hakki-Coleman method for hollow cylindrical samples

For the evaluation of the helix antenna prototype series it was necessary to directly determine the dielectric properties of hollow cylindrical shaped samples (see chapter 5). This reduced the error due to sample inhomogeneities on the efficiency determination of the antenna, as the dielectric blanks produced from lab melts did show some variation of the $\tan(\delta) = (1.25 \pm 0.25) \cdot 10^{-3}$. Therefore it was necessary to characterize every hollow cylindrical part on its own. It is common to treat the hollow cylindrical samples with the usual Hakki-Coleman equations as the E field amplitude of the

TE_{011} mode is comparatively low in the center and the influence of the hole is usually neglected. The ceramic parts which were used for the antenna prototypes had a hole size of b/a = 31 % and it was necessary to investigate if the standard Hakki-Coleman equations would be still valid.

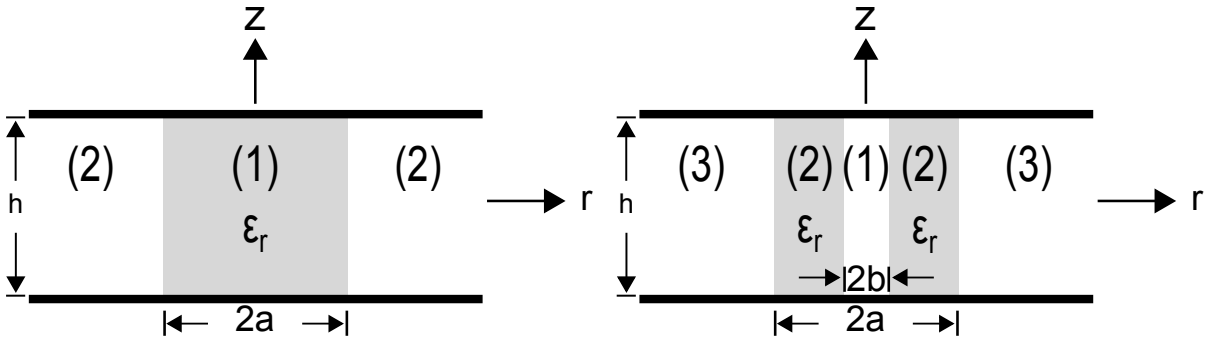

(a) Standard Hakki-Coleman geometry (b) Modified hollow cylindrical geometry

Figure 3.22: Comparison of the boundary value problems

No mathematical description of this measurement setup exists in literature and therefore the calculation is considered here in more detail. The derivation will be analog to the calculations of the Hakki-Coleman method. Starting with the source-free wave equations (derived from eq. (3.16)-(3.19)):

$$(\Delta + k_0^2 \varepsilon_r \mu_r)\mathbf{E} = 0 \qquad (\Delta + k_0^2 \varepsilon_r \mu_r)\mathbf{H} = 0 \quad . \tag{3.42}$$

This can be written in cylindrical coordinates for the longitudinal components:

$$\frac{1}{r}\frac{\partial}{\partial r}\left(r\frac{\partial}{\partial r}\Psi\right) + \frac{1}{r}\frac{\partial^2}{\partial \phi^2}\Psi + \frac{\partial}{\partial z^2}\Psi + k_0^2 \varepsilon_r \mu_r \Psi = 0 \quad , \tag{3.43}$$

whereby Ψ represents E_z or H_z (the fields are also expressed in cylindrical coordinates: longitudinal components E_z, H_z and transverse components E_r, E_ϕ, H_r, H_ϕ). First the longitudinal components are calculated from eq. (3.43) using a separation ansatz:

$$\Psi(r, \phi, z) = R(r)\Theta(\phi)Z(z) \quad . \tag{3.44}$$

For $\Theta(\phi)$ and $Z(z)$ we obtain a simple second order linear differential equation with

exponential resp. sine/cosine solution:

$$\frac{1}{Z}\frac{\partial^2 Z}{\partial z^2} = -\beta^2 \tag{3.45}$$

$$\frac{1}{\Theta}\frac{\partial^2 \Theta}{\partial \phi^2} = -m^2 \quad . \tag{3.46}$$

For $R(r)$ we obtain a m-th order Bessel differential equation:

$$r\frac{\partial}{\partial r}\left(r\frac{\partial}{\partial r}R\right) + \left((k_r r)^2 - m^2\right) R = 0 \quad , \tag{3.47}$$

with the separation constants k_r (radial wave number), β (longitudinal wave number: $\beta = p \cdot \pi/h$, with $p \in \mathbb{N}$, see derivation for the Hakki-Coleman method), $m \in \mathbb{N}$ and k_0 total vacuum wave number. For k_r we obtain:

$$k_r^2 = k_0^2 \varepsilon_r \mu_r - \beta^2 \quad . \tag{3.48}$$

Inside the dielectric (region 2) we obtain:

$$k_r^2 := k^2 = k_0^2 \varepsilon_r \mu_r - \beta^2 \tag{3.49}$$

and a solution in form of a linear combination of the Bessel functions J_m and Y_m. Outside the dielectric (region 1/3) we obtain:

$$k_r^2 := q^2 = \beta^2 - k_0^2 \tag{3.50}$$

leading to a linear combination of the Bessel functions K_m and I_m as solution. Under consideration of the metallic boundary conditions (tangential E fields and orthogonal H fields vanish at the metal surface) and that only non-diverging fields are physically meaningful, the following ansatz is chosen (for the sake of simplicity HEM modes are not considered; upper component for TE modes and lower component for TM modes):
Region 1:

$$E_{z,1} = A I_m(qr)\sin(\beta z)\left\{\begin{array}{c} -\sin(m\phi) \\ \cos(m\phi) \end{array}\right\} \tag{3.51}$$

$$H_{z,1} = E I_m(qr)\cos(\beta z)\left\{\begin{array}{c} \cos(m\phi) \\ \sin(m\phi) \end{array}\right\} \tag{3.52}$$

Region 2:

$$E_{z,2} = [BJ_m(kr) + CY_m(kr)]\sin(\beta z)\left\{\begin{array}{c} -\sin(m\phi) \\ \cos(m\phi) \end{array}\right\} \tag{3.53}$$

$$H_{z,2} = [FJ_m(kr) + GY_m(kr)]\cos(\beta z)\left\{\begin{array}{c} \cos(m\phi) \\ \sin(m\phi) \end{array}\right\} \tag{3.54}$$

Region 3:

$$E_{z,3} = DK_m(qr)\sin(\beta z)\left\{\begin{array}{c} -\sin(m\phi) \\ \cos(m\phi) \end{array}\right\} \tag{3.55}$$

$$H_{z,3} = HK_m(qr)\cos(\beta z)\left\{\begin{array}{c} \cos(m\phi) \\ \sin(m\phi) \end{array}\right\} \quad . \tag{3.56}$$

The direct determination of the transverse components via eq. (3.42) is comparatively complex, therefore the components are calculated from the longitudinal components using relations which can be derived from eq. (3.16) and (3.17) [KG86]:

$$\left(\frac{\partial}{\partial z^2} + k_0^2\varepsilon_r\mu_r\right)E_r = -i\omega\mu_0\mu_r\frac{1}{r}\frac{\partial}{\partial\phi}H_z + \frac{\partial^2}{\partial z\partial r}E_z \tag{3.57}$$

$$\left(\frac{\partial}{\partial z^2} + k_0^2\varepsilon_r\mu_r\right)E_\phi = i\omega\mu_0\mu_r\frac{\partial}{\partial r}H_z + \frac{1}{r}\frac{\partial^2}{\partial z\partial\phi}E_z \tag{3.58}$$

$$\left(\frac{\partial}{\partial z^2} + k_0^2\varepsilon_r\mu_r\right)H_r = i\omega\varepsilon_r\varepsilon_0\frac{1}{r}\frac{\partial}{\partial\phi}E_z + \frac{\partial^2}{\partial z\partial r}H_z \tag{3.59}$$

$$\left(\frac{\partial}{\partial z^2} + k_0^2\varepsilon_r\mu_r\right)H_\phi = -i\omega\varepsilon_r\varepsilon_0\frac{\partial}{\partial r}E_z + \frac{1}{r}\frac{\partial^2}{\partial z\partial\phi}H_z \quad . \tag{3.60}$$

Explicit solutions of the transverse components are not given here. The continuity requirements at the transitions dielectric to air (E_z, E_ϕ, H_z, H_ϕ continuous at $r = a$ and $r = b$) can be written in form of a matrix equation $N_{8\times8}\cdot V_{8\times1} = 0$ whereby the integration constants A-H correspond to the components of V. In case of $m = 0$ the expressions simplify into two independent matrix equations ($M_{4\times4}\cdot\tilde{V}_{4\times1} = 0$) for the TE_{0np} ($\alpha = \mu_r$) and TM_{0np} ($\alpha = \varepsilon_r$) modes:

$$M_{4\times4} = \begin{pmatrix} I_0(qb) & -J_0(kb) & -Y_0(kb) & 0 \\ 0 & -J_0(ka) & -Y_0(ka) & K_0(ka) \\ \frac{1}{q}I_1(qb) & -\frac{\alpha}{k}J_1(kb) & -\frac{\alpha}{k}Y_1(kb) & 0 \\ 0 & \frac{\alpha}{k}J_1(ka) & \frac{\alpha}{k}Y_1(ka) & \frac{1}{q}K_1(qa) \end{pmatrix} \quad . \tag{3.61}$$

The eigenvalue equation is then obtained from $\det(M) = 0$:

$$|M| = 0 \quad \Leftrightarrow \left[\frac{1}{q} I_1(qb)J_0(kb) - \frac{\alpha}{k} I_0(qb)J_1(kb)\right] \cdot \left[\frac{1}{q} K_1(qa)Y_0(ka) + \frac{\alpha}{k} K_0(qa)Y_1(ka)\right]$$
$$= \left[\frac{1}{q} I_1(qb)Y_0(kb) - \frac{\alpha}{k} I_0(qb)Y_1(kb)\right] \cdot \underbrace{\left[\frac{1}{q} K_1(qa)J_0(ka) + \frac{\alpha}{k} K_0(qa)J_1(ka)\right]}_{\rightarrow F_{1,2},\ \text{for}\ \ b\rightarrow 0} \quad . \tag{3.62}$$

It can be shown that for $\lim b \to 0$ the eigenvalue equation takes the form of the Hakki-Coleman eigenvalue equation $F_{1,2}$ (see eq. (3.21)-(3.22)) as expected. The dielectric loss can be expressed similar to eq. (3.32), whereby the constants A' and B' are quite extensive expressions which contain integrals which can not be expressed by analytical functions anymore and have to be calculated numerically:

$$\tan(\delta) = \frac{A'}{Q_u} - B' \quad . \tag{3.63}$$

In tab. 3.6 the influence of the hole size on the measurement error is investigated (for the case that a hollow cylindrical sample is evaluated using the standard Hakki-Coleman equations).

b/a[%]	0	5	10	31	40	50
f_0[GHz]	5.77179	5.77184	5.77257	5.83251	5.92567	6.11481
Δf_{Hakki}[%]		$< 10^{-2}$	$1 \cdot 10^{-2}$	1.1	2.7	5.9
$\Delta\varepsilon_r$[%]		$< 10^{-2}$	$3 \cdot 10^{-2}$	2.2	5.4	11.5
$\Delta\tan(\delta)$[%]		$< 10^{-2}$	$2 \cdot 10^{-2}$	1.2	4.8	74.9

Table 3.6: Errors induced by neglecting the hole for different hole sizes (b) with a = 5 mm, h = 17.75 mm, ε_r = 20, $\tan(\delta) = 2 \cdot 10^{-3}$

The hollow cylinders used in this work had a hole size of b = 1.55 m at an outer radius of a = 5 mm (b/a = 31 %). From tab. 3.6 it can be seen that even a hole of this size only insignificantly influences the TE_{011} mode. For hole sizes greater than approximately 40 % the amount of stored field energy outside the dielectric U_a/U_0 strongly increases leading to large errors in the dielectric loss determination if the standard Hakki-Coleman equations are used.
From fig. 3.23 it can be seen that for the TE_{011} mode the electric field density in the centre is comparatively low which explains why the resonance mode is only slightly influenced by the hole in the centre.

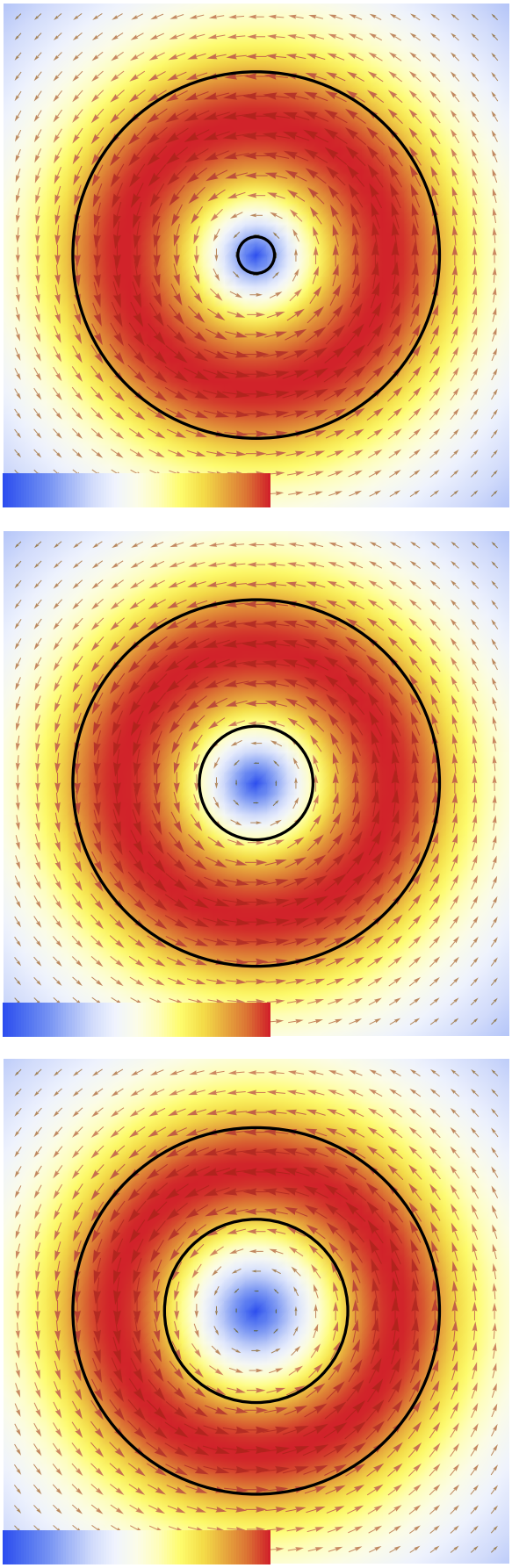

Figure 3.23: Plot of the E field distribution of the radial symmetric TE_{011} resonance at the symmetry plane of the cylinder, for a = 5 mm, h = 17.75 mm, ε_r = 20, with b/a = 10, 31, 50 % (scale bar like in fig. 3.20)

3.9.3 Cylindrical cavity resonance method

A second GHz characterization method was used, motivated by:

- the facilitated implementation of temperature dependent measurements
- the limited measurement accuracy ($\tan(\delta) > 4 \cdot 10^{-5}$) of the Hakki-Coleman method
- the possibility to do comparative measurements

The influence of the ohmic losses in comparison to the Hakki-Coleman method can be significantly reduced by increasing the distance between the sample and the metal surroundings as the amplitude of the electromagnetic fields decreases exponentially outside the dielectric. This leads to a lower field amplitude inside the metal and therefore lower ohmic losses. For the cavity used in this work the B value was approximately $B = 1 \cdot 10^{-6}$ leading to a resolution limit for $\tan(\delta)$ of two orders of magnitude better than the Hakki-Coleman method [She05a]. This method is therefore preferably used for the measurement of ultra low loss materials [DZB+97]. The accuracy for the permittivity determination is comparable to that of the Hakki-Coleman method: $\Delta\varepsilon_r/\varepsilon_r \approx$ 0.5-1 %. The support on which the sample is placed inside the cavity should be a low loss and low permittivity material. In this work mainly fused silica supports (high purity synthetic quartz glass produced by SCHOTT) with ε_r = 3.82 and $\tan(\delta) = 9 \cdot 10^{-5}$ (at 8.7 GHz) [Jan03] were used. For temperature measurements below 70 °C also styrofoam is a suitable material with ε_r = 1.3 and $\tan(\delta) = 8 \cdot 10^{-5}$ (at 3 GHz) [GW07]. In literature different support geometries are used, supports with smaller diameter which do not cover all the base area of the cavity and also additional supports above the sample which can be adjusted in height [Kru06]. The copper cavity is metallized from the inside with silver and the coupling loops are placed inside the cavity through two opposite holes. Analog to the Hakki-Coleman method a resonance inside the sample is excited (lowest transverse electric mode $TE_{01\delta}$, see fig. 3.24(d)). The experimental setup is shown in fig. 3.24.

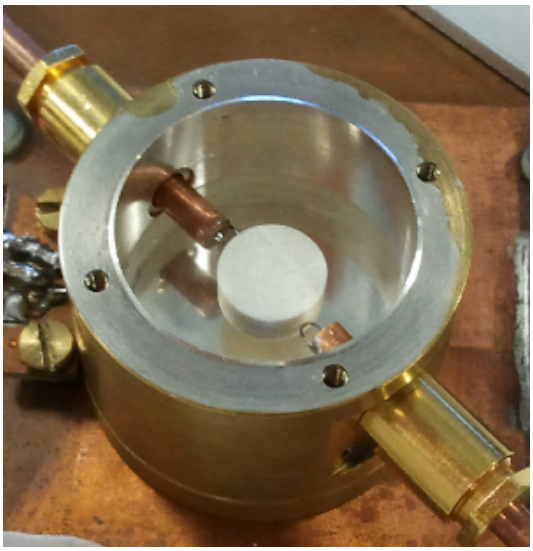

(a) Open cavity with sample on fused silica support

(b) Empty copper cavity without bottom and top walls

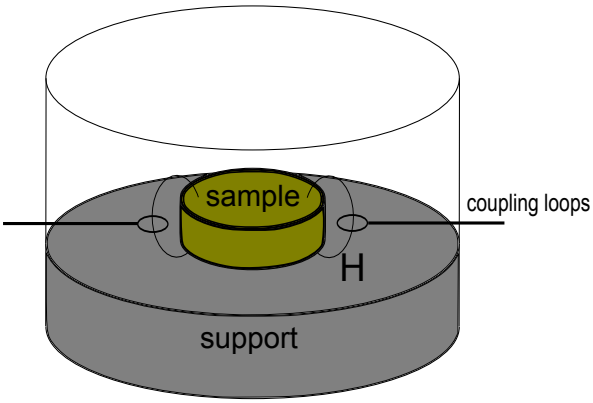

(c) Schematic setup of the cylindrical cavity resonance method

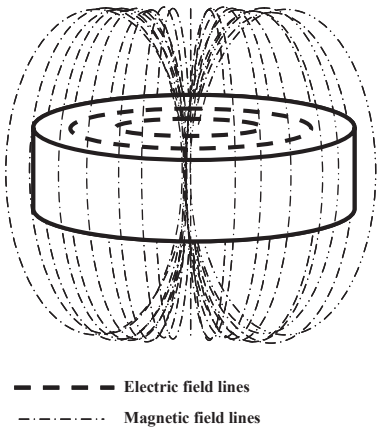

(d) Field geometry of the $TE_{01\delta}$ resonance [RI06]

Figure 3.24: Experimental setup of the cylindrical cavity resonance method

The experimental setup is more complex in comparison to the Hakki-Coleman method which leads to a higher complexity of the mathematical description. Nevertheless due to the still present cylindrical symmetry the eigenvalue equation for the ε_r determination (see eq. (3.64)-(3.68)) and the volume and surface integrals for the $\tan(\delta)$ determination (see eq. (3.71)-(3.73)) can still be written in an analytical form (see chapter A.2). The volume of the cavity is separated in 6 regions (see fig. 3.25) based on a description by Sheen [She07, SCC+09]:

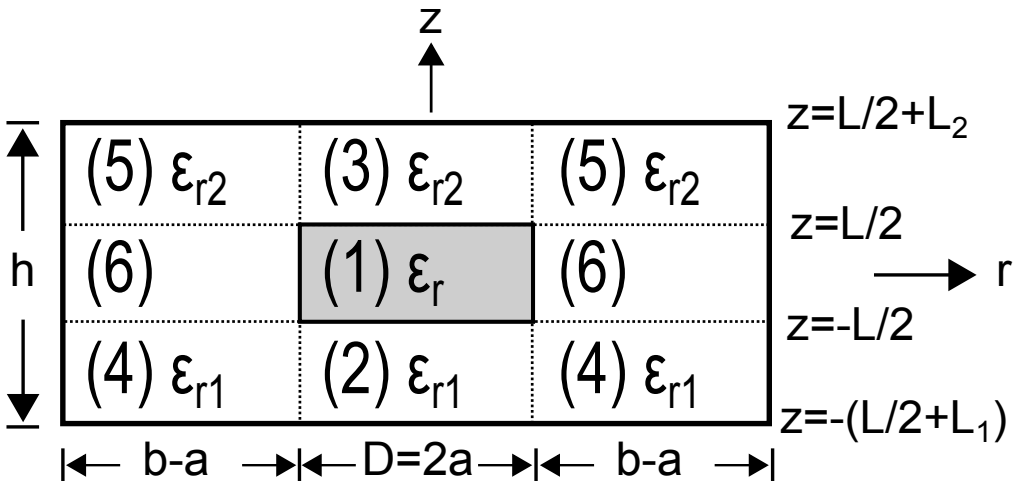

Figure 3.25: Sheen model for the cylindrical cavity resonance method [She07]

The electromagnetic fields can be calculated from Maxwell's equations in cylindrical coordinates and with the use of the boundary conditions between dielectric, air and metal the eigenvalue equation can be derived. Practically only 4 regions need to be considered, as region 2 and 3 resp. 4 and 5 follow from symmetry considerations. The full derivation is not given here, the eigenvalue equation for the relevant $TE_{01\delta}$ mode can be written as:

$$q = \sqrt{\left(\frac{\pi}{h}\right)^2 - k_0^2} \tag{3.64}$$

$$\frac{J_0(ka)}{J_1(ka)} + \frac{qa}{ka}\frac{1}{K_1(qa)}\left[K_0(qa) + \frac{K_1(qb)}{qa}\right] = 0 \tag{3.65}$$

$$\alpha_{1,2} = \sqrt{k^2 - k_0^2\varepsilon_{r1,2}} \tag{3.66}$$

$$\tan(\beta L) = \frac{\alpha_1 \coth(\alpha_1 L_1) + \alpha_2 \coth(\alpha_2 L_2)}{\beta - \frac{\alpha_1\alpha_2}{\beta}\coth(\alpha_1 L_1)\coth(\alpha_2 L_2)} \tag{3.67}$$

$$\varepsilon_r = \frac{1}{k_0^2}(k^2 + \beta^2) \quad , \tag{3.68}$$

with a, L, b, h, L_1, L_2, ε_r, ε_{r1}, ε_{r2} as shown in fig. 3.25. From the measured resonance frequency $f_{TE_{01\delta}} = \frac{c}{2\pi}k_0$ the permittivity ε_r is determined in the following way:

1. Calculation of $q(h,f_0)$ with eq. (3.64)
2. Numerical calculation of $k(q,a,b)$ with eq. (3.65)
3. Calculation of $\alpha_{1,2}(q,f_0,\varepsilon_{r1,2})$ with eq. (3.66)
4. Numerical calculation of $\beta(\alpha_{1,2},L_{1,2},L)$ with eq. (3.67)
5. Calculation of ε_r from eq. (3.68)

The resonance frequency in dependence of the permittivity is shown in fig. 3.26(a). In fig. 3.26(b) a frequency spectrum for two samples with different permittivities is shown. One problem of the cavity resonance technique is that modes from the metal cavity lie in the same frequency regime and can overlap with the $TE_{01\delta}$ peak. Variations of the cavity or sample geometry can be made to separate overlapping modes.

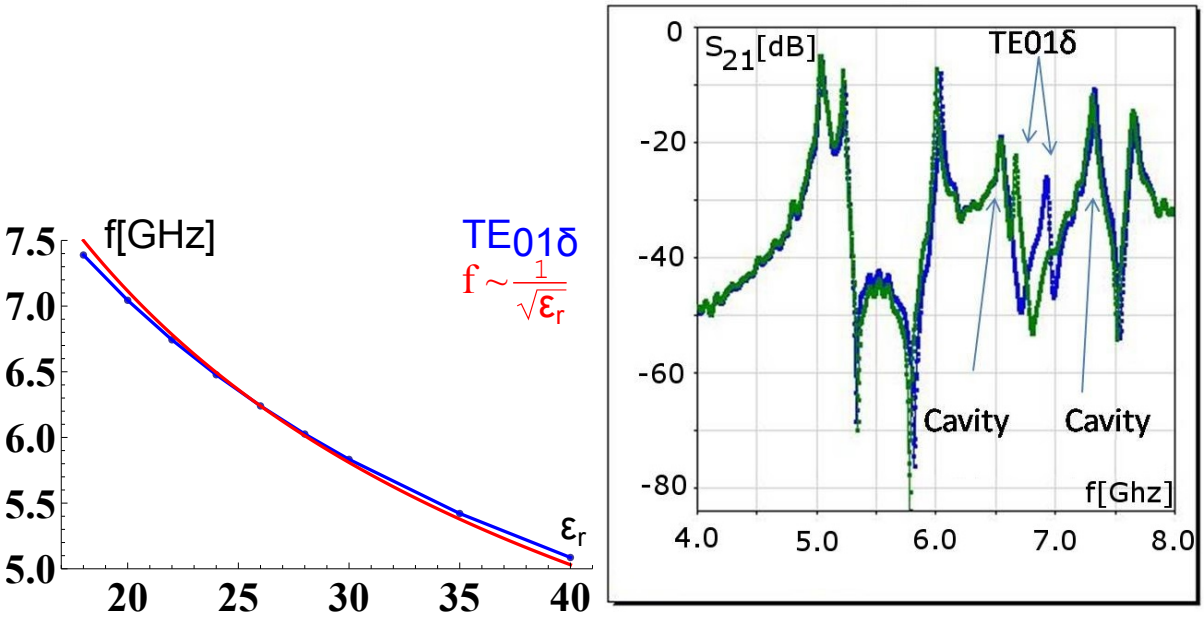

(a) Blue: $TE_{01\delta}$ resonance frequency in dependence of ε_r: (a = 5 mm, L = 4 mm, b = 13.11 mm, h = = 20 mm, $L1$ = 7.93 mm, ε_{r1} = 3.8, ε_{r2} = 1, ε_r = 20)

(b) Frequency spectrum for samples with different permittivity and similar dimensions (blue: ε_r = 20.6, green: ε_r = 22.6) [Bra11]

Figure 3.26: $TE_{01\delta}$ resonance mode

The dielectric loss determination is done in a similar way as for the Hakki-Coleman method (see eq. (3.31) and (3.30)), whereby an additional term $1/Q_S = p_S \cdot \tan(\delta_S)$ for the loss of the support(s) needs to be included. The losses from the support are normally neglectable and the radiation losses $1/Q_R$ are even lower than for the Hakki-Coleman method as the sample is located inside a closed metal cavity.

$$\frac{1}{Q_u} = \frac{1}{Q_d} + \frac{1}{Q_C} + \frac{1}{Q_S} + \frac{1}{Q_R} \quad , \tag{3.69}$$

neglecting the last two terms we get a similar expression as in eq. (3.32):

$$\tan(\delta_d) = \frac{1}{p_d}\left(\frac{1}{Q_u} - \frac{1}{Q_C}\right) = \frac{U_d + U_a}{U_d}\left(\frac{1}{Q_u} - \frac{1}{Q_C}\right) = \frac{\tilde{A}}{Q_u} - \tilde{B} \quad , \tag{3.70}$$

with $\tilde{A} = 1+U_a/U_d$ and $\tilde{B} = P_C/(wU_d)$. Under consideration of the radial symmetry of the $TE_{01\delta}$ mode (E_r, E_z, H_ϕ are zero) we can determine the stored field energy analog to eq. (3.33)-(3.34):

$$U_d = \frac{1}{2}\varepsilon_r\varepsilon_0 \int_V |E_{\phi,1}|^2 \, \mathrm{d}V \tag{3.71}$$

$$U_a = \sum_{i=2}^{6} \frac{1}{2}\varepsilon_{ri}\varepsilon_0 \int_V |E_{\phi,i}|^2 \, \mathrm{d}V \quad . \tag{3.72}$$

ε_{ri} corresponds to the permittivity in the different regions (2-6). P_C can be determined analog to eq. (3.35) whereby in addition to the top and bottom metal plate (O) contributions from the lateral surface (M) of the cylindrical cavity have to be included:

$$P_C = \sum_{i=2}^{6} \frac{1}{2}R_S \int_S |J_{S,i}|^2 \, \mathrm{d}S = \sum_{i=2}^{5} \frac{1}{2}R_S \int_O |H_{r,i}|^2 \, \mathrm{d}S + \sum_{i=4}^{6} \frac{1}{2}R_S \int_M |H_{z,i}|^2 \, \mathrm{d}S \quad . \tag{3.73}$$

Due to the complexity of the setup, the determination of $\tilde{A}$ and $\tilde{B}$ is very extensive and can be found in chapter A.2 directly implemented in a Mathematica8.0 script. The field solutions for the $TE_{01\delta}$ mode (E_ϕ) will be given here as they are necessary to calculate the volume and surface integrals (see eq. (3.71)-(3.73)):

$$E_{\phi 1} = E_0 J_1(kr)\cos(\beta z - \Phi) \tag{3.74}$$

$$E_{\phi 2/3} = E_0 \frac{\cos(\beta\frac{L}{2} \pm \Phi)}{\sinh(\alpha_{1/2}L_{1/2})} J_1(kr)\sinh(\alpha_{1/2}(\pm z + L_{1/2} + \frac{L}{2})) \tag{3.75}$$

$$E_{\phi 4/5} = E_0 \frac{J_1(ka)\cos(\beta\frac{L}{2} \pm \Phi)}{K_1(qa)\sinh(\alpha_{1/2}L_{1/2})} \left[K_1(qr) - K_1(qb)\right]\sinh(\alpha_{1/2}(\pm z + L_{1/2} + \frac{L}{2})) \tag{3.76}$$

$$E_{\phi 6} = E_0 \frac{J_1(ka)}{K_1(qa)} \left[K_1(qr) - K_1(qb)\right]\cos(\beta z - \Phi) \quad . \tag{3.77}$$

Writing eq. (3.17) in cylindrical coordinates we can obtain H_z and H_r from E_ϕ (the calculated fields are given in [Bra11]):

$$H_z = \frac{i}{\omega\mu_0\mu_r}\frac{1}{r}\frac{\partial}{\partial r}(rE_\phi) \tag{3.78}$$

$$H_r = \frac{-i}{\omega\mu_0\mu_r}\frac{\partial E_\phi}{\partial z} \quad . \tag{3.79}$$

Furthermore it can be shown, that the Hakki-Coleman solution is a special case of the cavity geometry for ($b \to \infty$, $L1 = L2 \to 0$).

- Fields: $E_{\text{Cav},\phi_{1/6}} \rightarrow E_{\text{Hak},\phi_{d/a}}$
- Eigenvalue equation: (3.65)$\rightarrow$ (3.22)
- Loss: $(\tilde{A}, \tilde{B})_{\text{Cav}} \rightarrow (A, B)_{\text{Hak}}$

Temperature dependent measurements

The experimental setup of the cavity resonance method is more suitable as the open and comparatively large Hakki-Coleman setup.

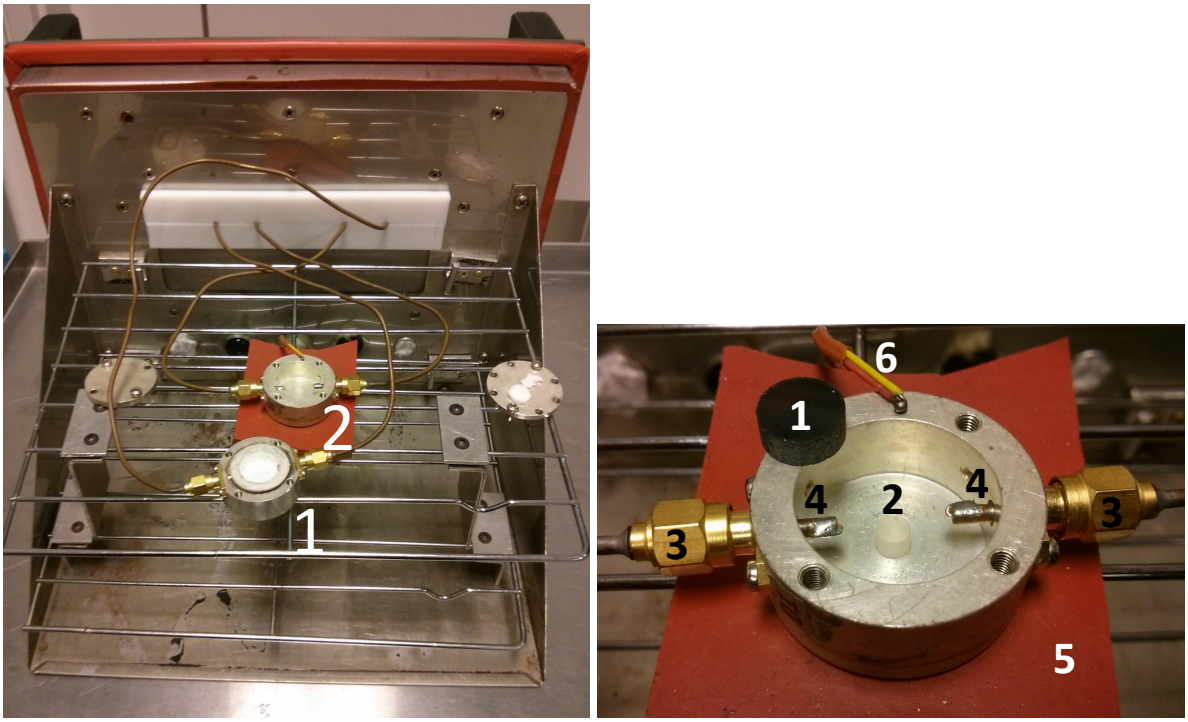

Figure 3.27: Measurement setup for temperature dependent measurements. Left: furnace door with connected cavities ((1): silver coated ceramic cavity (placed inside a metal cavity) with styrofoam support, (2) silver coated steel cavity with fused silica support), right: (1) black glass sample (2) fused silica support (3) coaxial cabels (4) coupling loops (5) rubber for mechanical stabilization (6) K-type thermocouple

The cavity was placed inside a furnace (DELTA 9023, Delta Design) which was capable of temperature measurements between -175 °C and +80 °C (the upper temperature limit is given by the temperature stability of the connector cables). The temperature was monitored using a K-type thermocouple. The resonance frequency is measured at minimum 3 temperatures (usually room temperature $\pm$ 50 K) and the average slope

$\overline{m} = \Delta f_0/\Delta T$ of the $f_0(T)$ curve is fitted by linear regression:

$$\tau_f = \frac{1}{f_0}\frac{\partial f_0}{\partial T} \approx \frac{\overline{m}}{f_0} \quad . \tag{3.80}$$

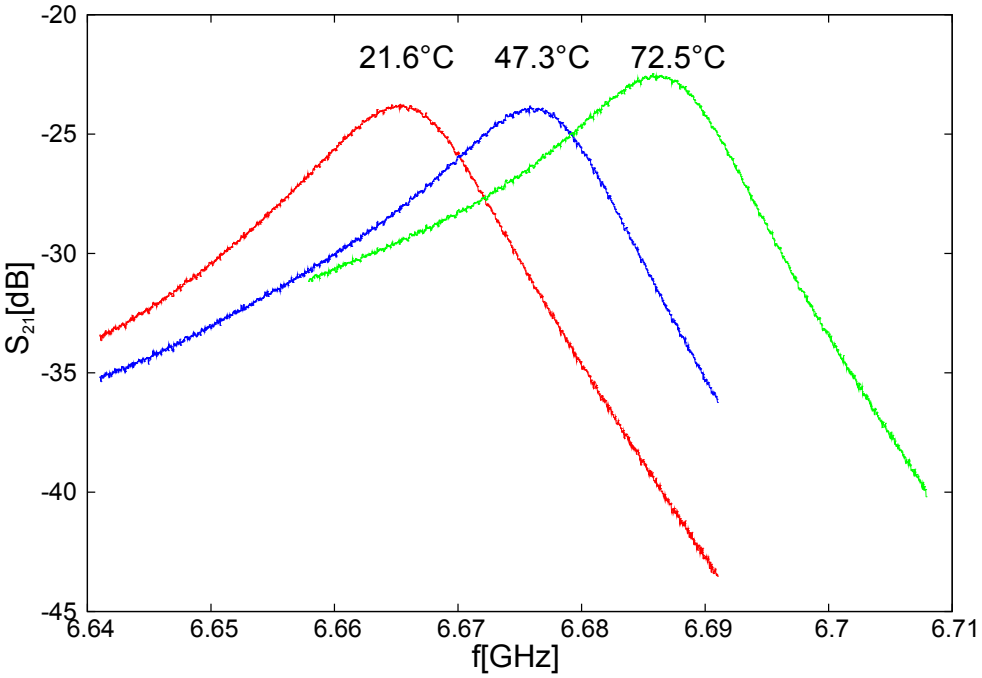

Figure 3.28: Shift of the resonance frequency with temperature

The effect of the thermal expansion of the fused silica support α_{fs} = 0.5 ppm/K [SCH14] can be neglected [83107]. The thermal expansion of the cavity can be considered by modifying eq. (2.50):

$$\tau_f(\tau_\varepsilon, \alpha_L, \tau_{\text{cav}}) = -\frac{1}{2}\tau_\varepsilon - \alpha_L + a_C\tau_{\text{cav}} \quad . \tag{3.81}$$

The parameter a_C is difficult to determine and is estimated in analogy to [83107] to 0.05 < a_C < 1. An estimation for τ_{cav} can be made using (3.64)-(3.68). For α_{copper} = 16.5 ppm/K ($\Delta b/b = \Delta h/h = \alpha_C \Delta T$), ΔT = ±50 K = 100 K and the usual sample parameters (a = 5 mm, L = 4 mm, ε_r = 20) we obtain a frequency shift of Δf = -1.16 · 10^{-3} GHz at f = 7.04411 GHz, equivalent to $|a_C\tau_{\text{cav}}| \leq$ 1.7 ppm/K. Therefore the thermal expansion of the cavity is normally neglected in comparison to other measurement errors. If higher accuracy is necessary metallized low thermal expansion ceramic cavities can be used.
Comparative measurements with setups at different institutes have been made resulting in maximum variations of $|\Delta\tau_f| \leq$ 15 ppm/K which will be estimated as error for the τ_f values.

4 Results

4.1 Glass formation

The motivation for the choice of the investigated system was given in chapter 2.8. The first starting point of this work was motivated by a previous diploma thesis [Bra11] in which a stable glass formation range in the La_2O_3-TiO_2-SiO_2-B_2O_3-Al_2O_3 system was identified. The dielectric properties of the resulting glass-ceramics (ε_r = 18.9, Qf = 4820 GHz; see 36436 in fig. 4.1) were not sufficient for the intended dielectric loaded antenna applications. The key problem for a further enhancement of the dielectric properties is the maximization/increase of the major crystal phase content ($La_4Ti_9O_{24}$), which is directly correlated with the minimization of glass-forming oxides (SiO_2, B_2O_3, Al_2O_3). The best glass melt in [Bra11] (36436) had a glass former content (GFC) of 42.1 at%. The aim of this work was therefore to optimize the composition of the basic glass to achieve a lower content of glass-forming oxides. Different ratios between SiO_2:$BO_{1.5}$:$AlO_{1.5}$ were analyzed and a new narrow glass-forming area in the La_2O_3-TiO_2-SiO_2-B_2O_3 system with GFC < 30 at% (without the use of Al_2O_3) was identified (see fig. 4.1). Two new severe problems arose in this system. A strong tendency of surface devitrification was observed (see fig. 4.2), even though the bulk showed stable glass formation. The melting temperature had to be increased up to at least 1500 °C to ensure a complete melting of the raw materials, which led to an enhanced reduction of Ti^{4+} to Ti^{3+} (see chapter 2.3). The prevention of Ti^{3+} will be discussed in chapter 4.2, whereby solutions for the surface devitrification problem will be summarized in this chapter. In the glass-forming area, the melt with the stoichiometry the closest to the $La_4Ti_9O_{24}$ phase (labeled with 41760) has been chosen for further optimization, as this composition shows the highest potential for a maximization of the major crystalline phase content.
The exact chemical compositions of all melts of this work are summarized in chapter A.4.

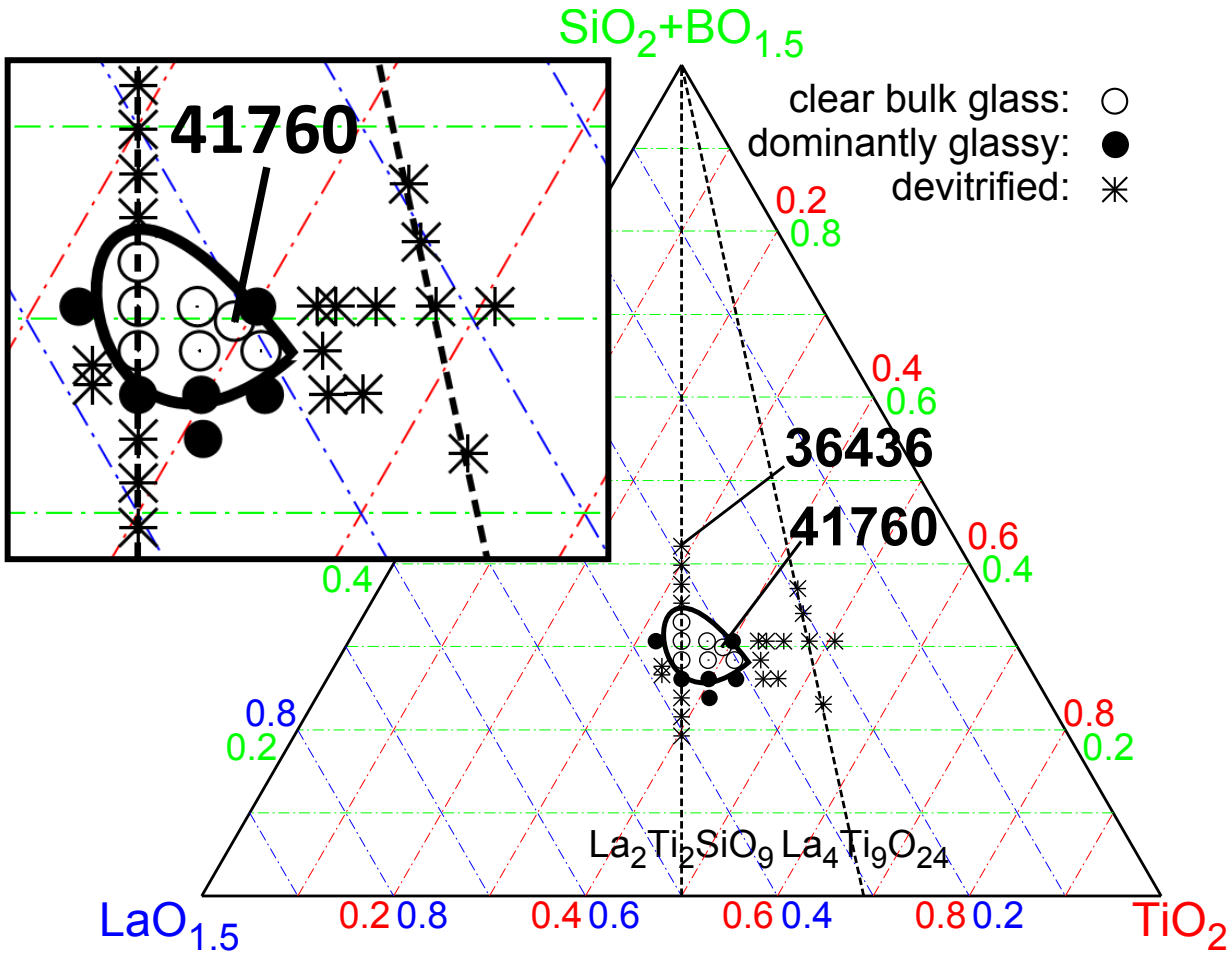

Figure 4.1: Glass-forming area in the La_2O_3-TiO_2-SiO_2-B_2O_3 system, SiO_2:$BO_{1.5}$ = 1.4 (for 36436 the upper corner has to be replaced by SiO_2+$BO_{1.5}$+$AlO_{1.5}$)

4.1.1 Selection of glass-forming oxides

The SiO_2:$BO_{1.5}$ ratio can be varied comparatively flexible in the glass-forming area. Stable bulk glass formation was achieved for ratios between SiO_2:$BO_{1.5}$ = 1.0 - 2.5. An optimum ratio of 1.4 was determined, which showed the most stable glass-forming properties in combination with a comparatively low B_2O_3 content (to minimize the formation of minor crystalline phases during the ceramization process like $LaBO_3$). In fig. 4.2 a comparison between a stable bulk glass and a devitrified glass (due to a too low B_2O_3 content) is shown. Both samples show a strong tendency of surface devitrification on the top surface (the top surface is not in contact with the steel mold during the casting which leads to a lower cooling rate) which was common for all investigated samples in the glass-forming range. The cracks in the bulk of the sample are also directly related to the strong surface devitrification (different thermal expansion coefficient of crystalline phase and glass).

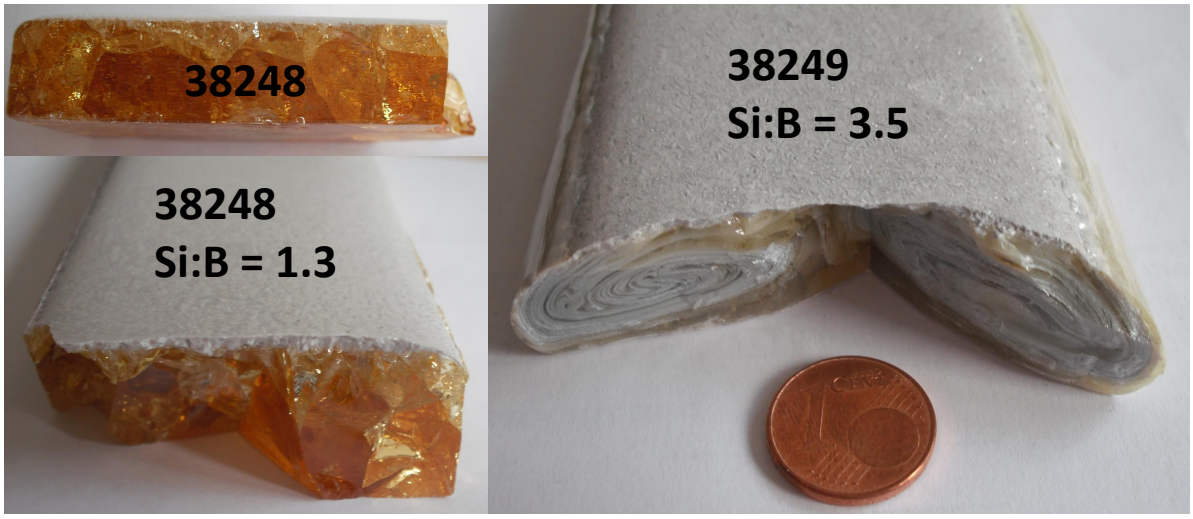

Figure 4.2: Comparison between a stable bulk glass (left) and a devitrified glass (right)

In [Bra11] also Al_2O_3 was used as main glass former component. Therefore a substitution series has been melted (partial replacement of SiO_2-B_2O_3 content by Al_2O_3, for a fixed SiO_2:$BO_{1.5}$ ratio of 1.4). Even low amounts of 2 at% $AlO_{1.5}$ led to a deterioration of the glass quality (see fig. 4.3)

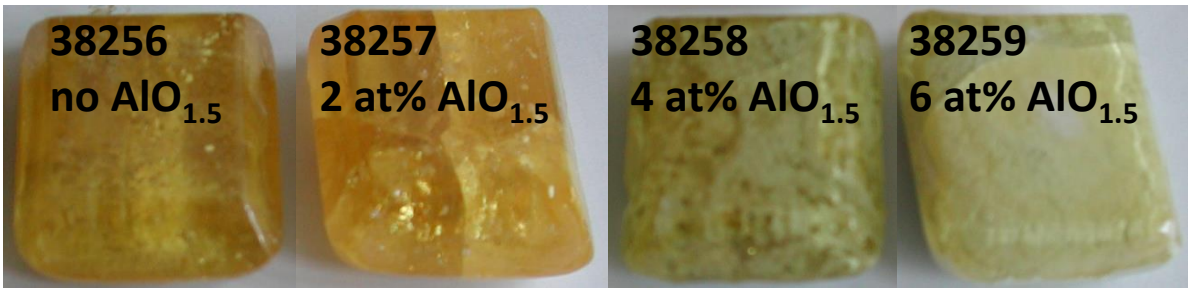

Figure 4.3: Increasing devitrification with increasing Al_2O_3 content

The optimization of the glass-forming oxides led to an improved bulk glass-formation, but still could not solve the problem of surface devitrification. One other common method to stabilize glasses is the method of glass frustration (see chapter 2.1). The amorphous glass structure can be stabilized by introducing more disorder to the system by substituting the major components by other chemically similar oxides. In this way, the chemical behavior of the melt only changes insignificantly but the complexity of the atomic structure can be increased leading to deceleration of the crystallization resp. stabilization of the glass. In commercial technical glasses the use of a combination of various alkali metal oxides instead of only one species is common [McM79a] (e.g. use of Li_2O, Na_2O and K_2O) or more relevant for the here investigated system is the substitution of La_2O_3 by other rare earth oxides (e.g. partial substitution

by Gd_2O_3 in La_2O_3-rich optical glasses). In the following different dopants for the A (La) and B-site (Ti) and their influence on the glass properties are summarized.

4.1.2 A-site doping

As mentioned above, a doping series of various rare earth metal oxides has been made to investigate its influence on the glass-forming behavior and a possible reduction of the surface devitrification. Nearly all of the rare earth oxides are not polyvalent (only 3+) and have a similar ionic radius ($r_{La^{3+}}$ = 116 pm). A substitution of 5 % of the used La by Ce, Nd, Sm, Gd has been made without any significant change of the glass properties and the dielectric properties of the glass-ceramic. For Gd, the substitution series was extended until 90 % and up to 50 % substitution no significant changes in the glass stability was observed. Only for a nearly complete exchange of the La by Ce or Gd the melts showed strong devitrification (see 41417 and 42415 in fig. 4.4). Ce is the only rare earth metal which allows two stable valencies (3+/4+) due to its special electronic configuration and therefore it can be used in addition as oxidizing agent to prevent Ti^{3+}. Even though in the glass it is mainly present as Ce^{3+} and behaves similar as the other rare earth oxides. In conclusion it can be stated that, the exchangeability of the different rare earth metal oxides is given, but no improvement for the glass-formation (especially the reduction of surface devitrification) has been observed. For the given composition in the ternary diagram (41760) only La_2O_3 seems to form stable glasses. In tab. 4.1 the doping series and their effects are summarized.

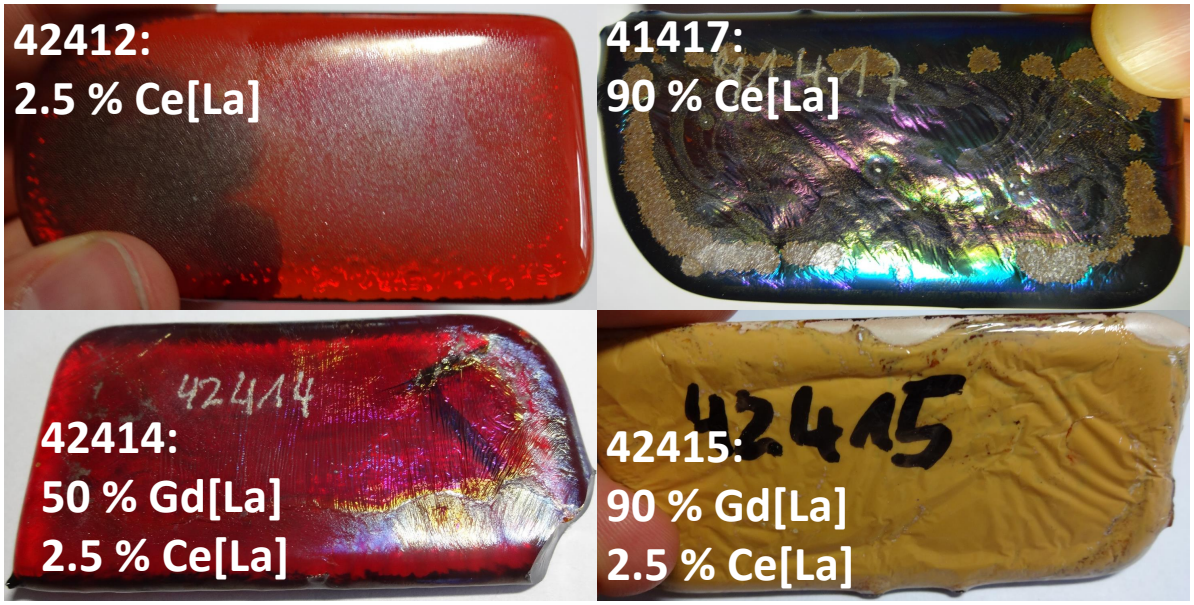

Figure 4.4: Rare earth doping series (in all shown glasses 10 % of the TiO_2 is replaced by ZrO_2 to reduce surface devitrification)

Melt	Dopant	r_{ion}[pm]	BGQ	SQ	other effects
42414	2.5 % CeO_2	114	-	-	Ti^{3+} prevention
39563	5 % CeO_2	114	-	-	Ti^{3+} prevention
42418	10 % CeO_2	114	-	-	Ti^{3+} prevention
41417	90 % CeO_2	114	↓	↓	
39564	5 % $NdO_{1.5}$	111	-	-	
39565	5 % $SmO_{1.5}$	108	-	-	
41675	5 % $GdO_{1.5}$	105	-	-	
41676	10 % $GdO_{1.5}$	105	-	-	
41677	20 % $GdO_{1.5}$	105	-	-	
42414	50 % $GdO_{1.5}$	105	-	↘	
42415	90 % $GdO_{1.5}$	105	↓	↓	
41674	2.5 % $YO_{1.5}$	102	↘	↘	
40937	5 % $BiO_{1.5}$	117	↘	-	
41496	2.5 % BaO	142	↘	-	

Table 4.1: A-site doping series ($LaO_{1.5}$ is substituted by the dopant by the given percentage, r_{ion}: ionic radius after Shannon [Sha76] for coordination number of 8, BGQ: bulk glass quality, SQ: surface quality)

For the melts which did not decrease their glass stability in comparison to the undoped glass, further ceramization and subsequent investigations of the dielectric properties in the GHz range and the formed crystalline phases via XRD has been performed. But no relevant change in properties was observed.

4.1.3 B-site doping

For the doping of the B-Site, elements of the same subgroup as Ti ($r_{Ti^{4+}}$ = 61 pm) have been chosen (Zr, Hf) and some adjacent elements with similar ionic radii (V, Nb, Ta). The latter caused already in small amounts of 5 % substitution a deterioration of the bulk glass stability, whereby Zr and Hf led to a reduction of the surface devitrification. For 10 % Ti substitution by Zr only a thin neglectable crystal layer is observed and for 15-20 % substitution the surface devitrification completely disappeared (see fig. 4.5). For even higher amounts of Zr the glass stability in the bulk and on the surface started to decrease again. Hf showed similar effects as Zr, as both elements are very similar in their chemical behavior and also their ionic radii are nearly identical as a consequence of the lanthanide contraction. Due to the better availability and lower cost only Zr was used as main dopant in the following. In tab. 4.2 the doping series and their effects are summarized.

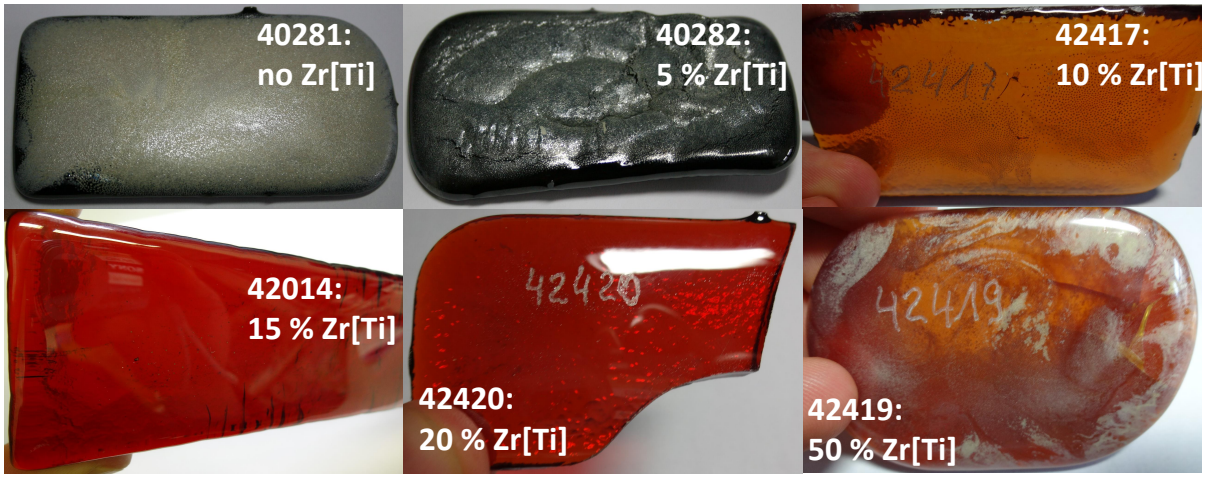

Figure 4.5: ZrO_2 doping series (the difference in the glass color is due to a slight variation in the CeO_2 content (x_{CeO_2} < 1.0 mol% for all melts) which had no effect on the surface devitrification)

Melt	Dopant	r_{ion}[pm]	BGQ	SQ	other effects
40282	5 % ZrO_2	72	-	↗	
42417	10 % ZrO_2	72	-	↑	
42014	15 % ZrO_2	72	-	⇑	no surf. cryst.
42420	20 % ZrO_2	72	-	⇑	no surf. cryst.
44086	30 % ZrO_2	72	-	↑	
42419	50 % ZrO_2	72	↘	↗	
40935	5 % HfO_2	71	-	↗	
41416	5 % $VO_{2.5}$	54	↓	-	
39568	5 % $NbO_{2.5}$	64	↓	-	
40938	5 % $TaO_{2.5}$	64	↘	-	

Table 4.2: B-site doping series (TiO_2 is substituted by the dopant by the given percentage, r_{ion}: ionic radius after Shannon [Sha76] for coordination number of 6, BGQ: bulk glass quality, SQ: surface quality)

4.1.4 Influence of common raw material impurities

In this work high purity raw materials for the optical glass production were used. Even in these materials ppm amounts of impurities can be present. Common impurities like Fe_2O_3, alkali metals (Na_2O, K_2O) and earth alkaline metals (MgO, CaO) were added to the batch composition by 500 ppm (wt%), but no change in the glass-forming and dielectric properties of the ceramized samples has been observed. Only the expected color change in case of the iron addition (see chapter 4.2) was observed, which is not relevant for the purpose of this work.

4.1.5 Conclusive decision for the melt composition

The two key problems of the system could be solved by the use of adequate dopants. The prevention of Ti^{3+} was achieved by the use of an oxidizing agent (CeO_2 and also Sb_2O_5, will be discussed in detail in chapter 4.2). The surface devitrification could be totally removed by a partial substitution of the TiO_2 content with ZrO_2. On the basis of these results, liter melts with ZrO_2 contents of 5-10 mol% and a sufficient amount of CeO_2 were prepared and ceramized (41760: 5.0 mol% ZrO_2, 42014: 7.5 mol% ZrO_2, 42732: 10.0 mol% ZrO_2; all: 1.0 mol% CeO_2). The glass-ceramics were investigated in detail concerning their dielectric properties and the existing crystalline phases. The results are shown in the chapter 4.4.

4.2 Redox behavior

In the previous chapter a suitable glass-forming system could be identified. To achieve a homogeneous glass it is essential to melt the raw materials completely during the melting process and for the investigated system melting temperatures of T_m > 1500 °C were found to be necessary (see chapter 4.3). Due to these high melting temperatures, a partial reduction of redox ions in the melt occurs, like described in chapter 2.3. In the here investigated system, mainly the reduction of Ti^{4+} to Ti^{3+} is of significant importance, as the Ti^{3+} formation has a strong influence on the nucleation/crystallization behavior of the glass-ceramic and also on the dielectric properties. In this chapter the amount of Ti^{3+} is determined by the use of EPR and optical methods and ways of preventing or reducing its formation are shown.

4.2.1 $Ti^{3+/4+}$ determination

The detection of Ti^{3+} in glasses via EPR methods has been performed in various kind of glasses (see tab. 3.3). A typical signal shows a simple, but asymmetrical shaped peak with g values around 1.943 $\pm$ 0.035 (see fig. 4.6). All measurements are normalized concerning amplifier gain and number of Ti atoms (intensity: I[arb. units]). The amount of Ti^{3+} is proportional to the area under the absorption curve (see chapter 3.7) which is derived by numerical integration from the measured EPR signal (see fig. 4.6). The error of the EPR analysis is estimated to around 10 $\%$, as the measurement results could be reproduced from different samples of similar melting conditions by maximum 10 $\%$ deviation. Fig. 4.6 shows that the amount of Ti^{3+} is strongly dependent on the melting temperature and the keeping time. Even at very low temperatures (T_m = 1450 °C) a significant amount of Ti^{3+} is formed. Additionally it can be seen, that the keeping times t_k are still below the redox equilibration times, as the signal intensity varies with t_k.

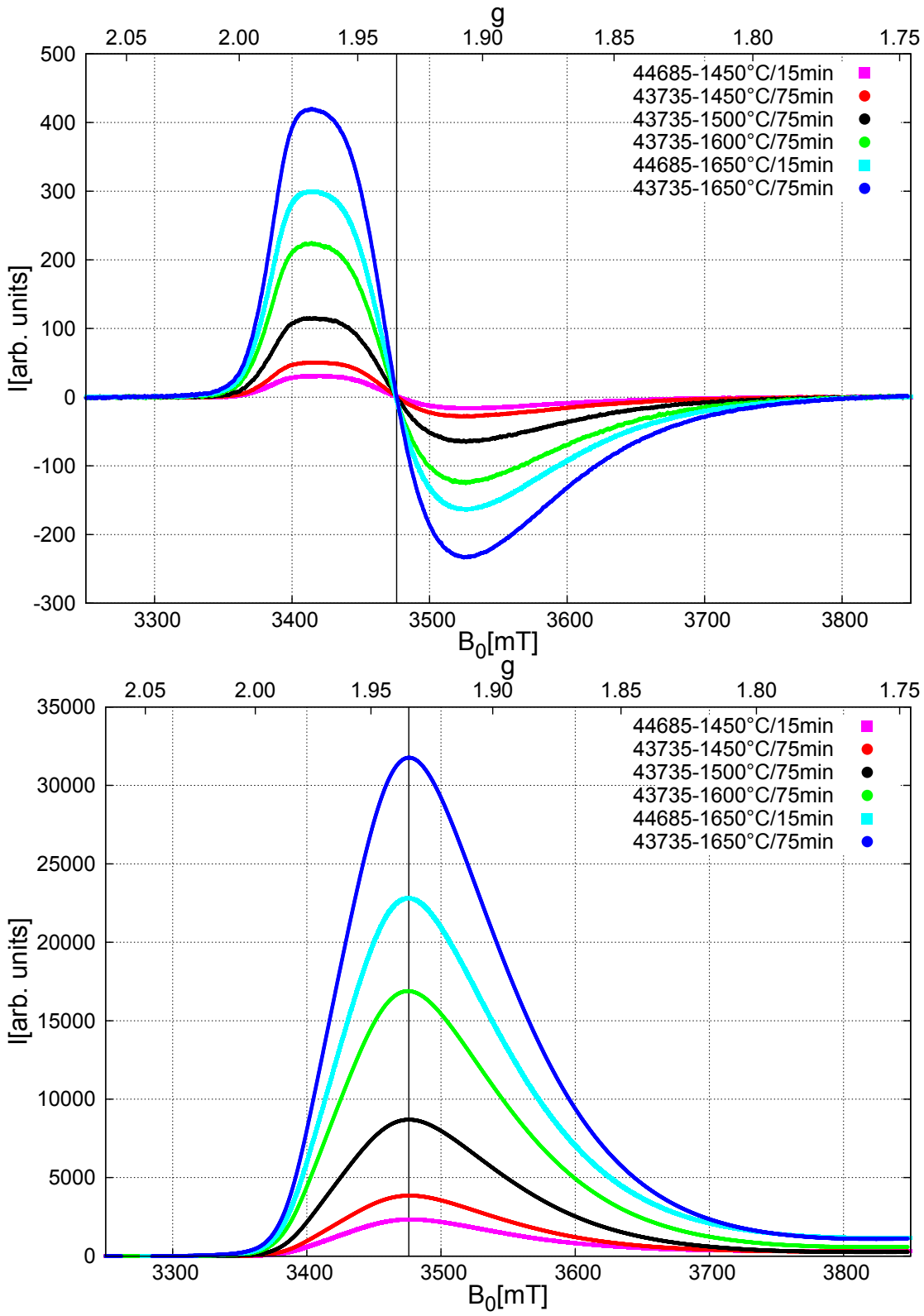

Figure 4.6: EPR measurement showing the formation of Ti^{3+} for varying melting temperature T_m and keeping time t_k (top: measured EPR signal, bottom: numerically integrated signal)

An attempt has been made to use Ti_2O_3 (100 % Ti^{3+}) as a reference standard to determine the Ti^{3+} content by EPR analysis (see fig. 4.7). Ti_2O_3 showed an around 2 order of magnitude lower intensity than expected and therefore has to be considered as unsuitable for the intended purpose, possible reasons for its unsuitability are summarized in chapter 3.7. χ_{red} is determined by the ratio of I/N_{Ti} (integrated EPR intensity per Ti atom) of the sample and Ti_2O_3 reference standard ($\chi_{red} = [I/N_{Ti}]_{sample}/[I/N_{Ti}]_{Ti_2O_3}$).

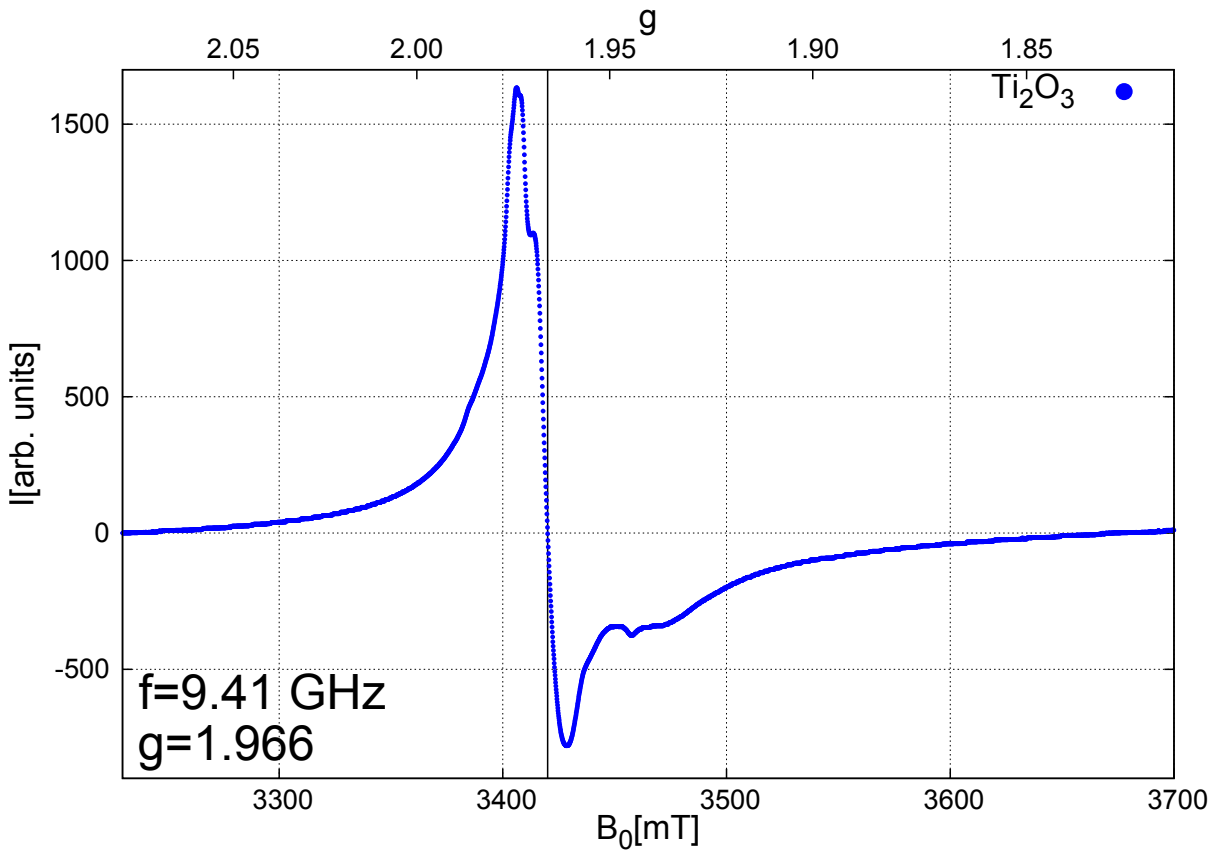

Figure 4.7: EPR measurement of Ti_2O_3, showing a less broad EPR peak in comparison to the investigated amorphous systems and also a shifted g value of 1.966

In tab. 4.3 it can be seen that the low signal intensity of Ti_2O_3 leads to χ_{red} values of more than 100 %, which can only be explained by the fact that the signal intensity is lowered by additional loss mechanisms which are not present in the investigated samples. Therefore it has to be stated that the EPR method is a suitable method to determine the relative change of the Ti^{3+} amount for different samples, but an absolute quantitative determination is only possible with a suitable reference standard with externally determined amount of Ti^{3+} which was not available during this work.

Sample	m[mg]	w_{TiO_2}[%]	N_{Ti}	I/N_{Ti}[arb.u.]	χ_{red}[%]
Ti_2O_3	150	100*	$1.26 \cdot 10^{21}$	$7.32 \cdot 10^{8}$	100
43735(1450°C,75min)	237.4	28.885	$5.17 \cdot 10^{20}$	$6.01 \cdot 10^{8}$	82
43735(1500°C,75min)	241.0	28.885	$5.25 \cdot 10^{20}$	$1.36 \cdot 10^{9}$	186
43735(1600°C,75min)	254.2	28.885	$5.54 \cdot 10^{20}$	$2.70 \cdot 10^{9}$	368
43735(1650°C,75min)	254.9	28.885	$5.55 \cdot 10^{20}$	$5.02 \cdot 10^{9}$	686

Table 4.3: Attempt to determine the Ti^{3+} content by a reference measurement with Ti_2O_3 (N_{Ti}: number of Ti atoms, I/N_{Ti}: intensity per Ti atom (normalized for gain and other experimental parameters))

As second method for the investigation of the Ti^{3+} content optical transmission measurements were used. Despite the numerous publications concerning the peak position and width of the optical transitions of Ti^{3+} (see tab. 3.3), no published literature data concerning the oscillator strength of the transition was found. The only way to estimate the absolute amount of Ti^{3+} was using data from an internal SCHOTT source [Pfe14], derived by chemical analysis of Ti^{3+} containing aluminosilicate glasses (see tab. 4.4). The investigated system is of different chemical composition, therefore the use of the oscillator strength from [Pfe14] would be theoretically not allowed, but as both systems are silica-based glasses an estimation of the right order of magnitude of the present amounts of Ti^{3+} is still possible. Even though the determined quantitative results have to be treated with care as the accuracy of the given data is also unknown. As in the case of EPR the valuable information of the relative change of the Ti^{3+} content with the melting conditions can still be determined with suitable accuracy.

Transition	λ_0[nm]	ν_0[cm^{-1}]	Γ[cm^{-1}]	α_0/x_i	A/x_i[cm^{-2}]	P	σ_{abs}[m^2]
$^2B_{2g} \rightarrow {}^2B_{1g}$	541	18501	5104	45	$2.44 \cdot 10^{5}$	$1.3 \cdot 10^{-3}$	$2.1 \cdot 10^{-23}$

Table 4.4: Gaussian parameters for the $^2B_{2g} \rightarrow {}^2B_{1g}$ (3d-3d) transition of Ti^{3+} in aluminosilicate glass [Pfe14] (α_0/x_i in $cm^{-1}/mol\%$)

From every glass 2×2 samples of two thicknesses d were prepared from which 4 transmission measurements were made (see fig. 4.8), resulting in 4 absorption curves $\alpha(\nu)$ via eq. (3.12). The absorption spectra were fitted using gaussian absorption bands:

$$\alpha(\nu) = \alpha_0 \cdot \exp\left(-\ln(2)\left(\frac{\nu - \nu_0}{(\Gamma/2)}\right)^2\right) \quad , \tag{4.1}$$

with resonance wave number ν_0, peak absorption $\alpha_0 = \alpha(\nu{=}\nu_0)$ and FWHM Γ. In fig. 4.9 the absorption curves, inc. the fitted transitions are shown.

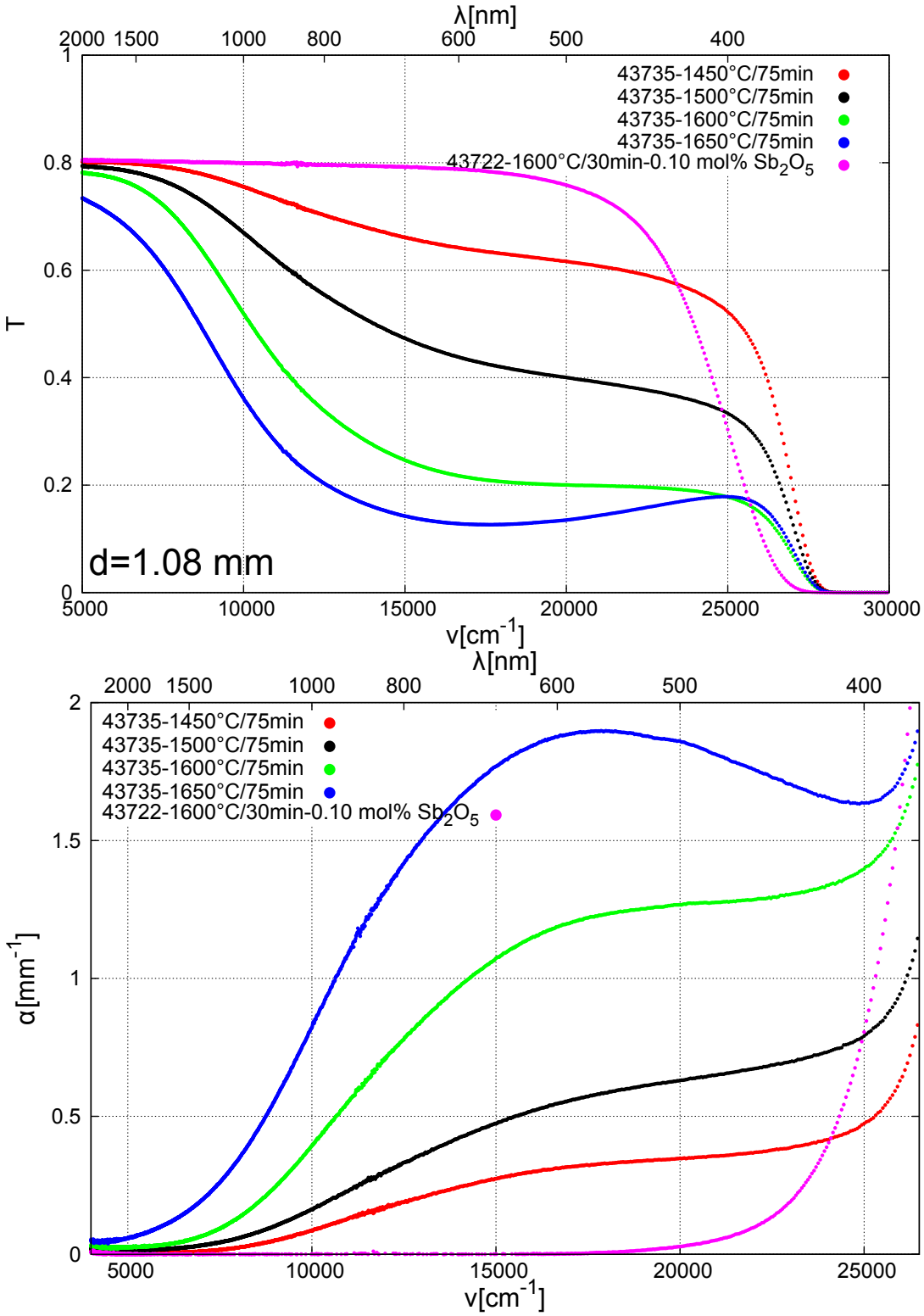

Figure 4.8: Top: transmission measurement of glasses with different melting temperature T_m resp. Ti^{3+} content, bottom: absorption curves derived via eq. (3.12) (the one of the 4 absorption curves the closest to the average value was chosen exemplarily for representation)

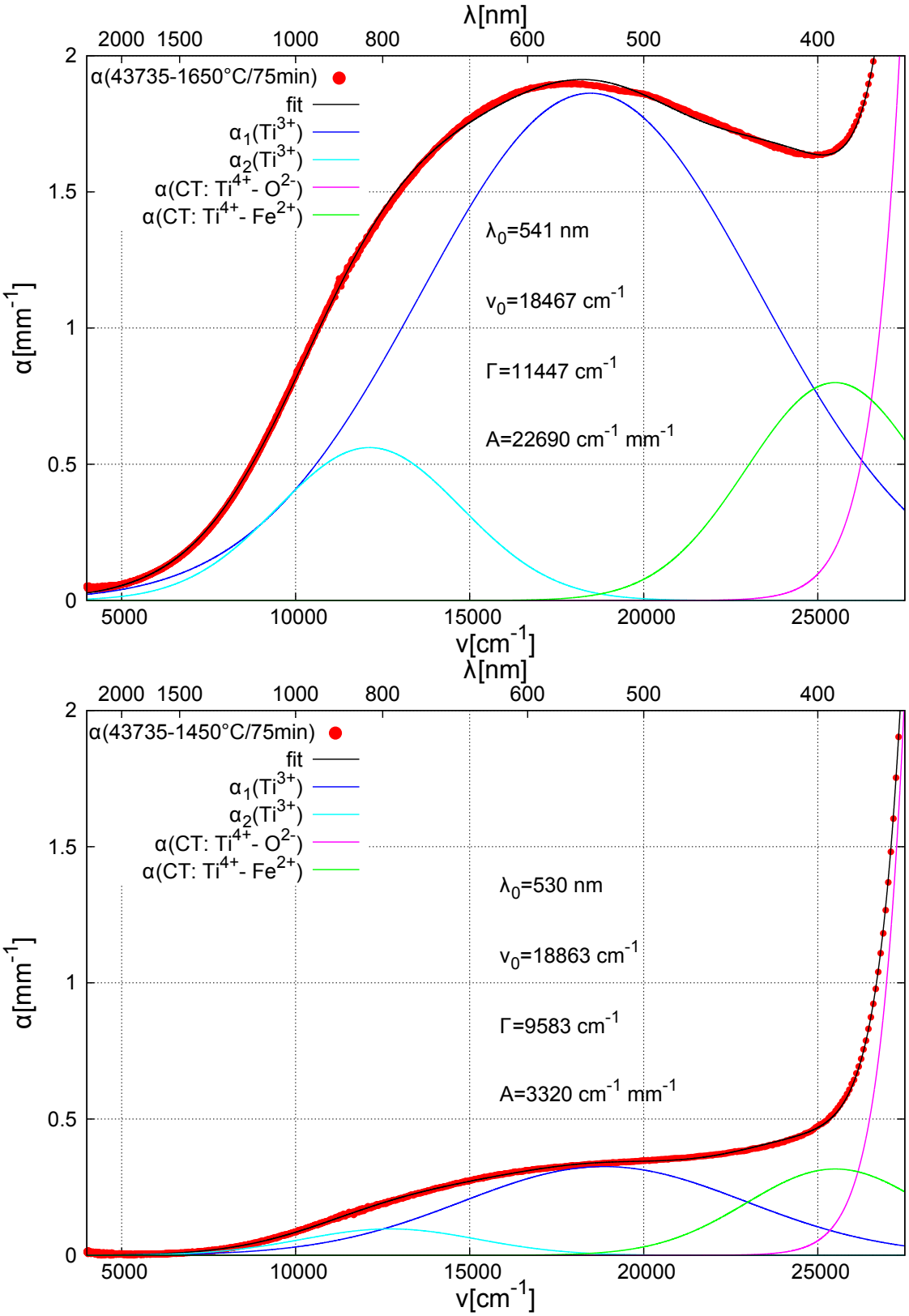

Figure 4.9: Fitted absorption curves of glasses melted at different temperatures for t_k = 75 min (top: T_m = 1650 °C, bottom: T_m = 1450 °C)

Other absorption peaks were identified (see chapter 3.8.2). The second Ti^{3+} absorption ($^2B_{2g} \rightarrow {}^2A_{1g}$) and the $Ti^{4+} \leftarrow O^{2-}$ CT absorption. The peak around 24000 cm^{-1} is attributed to the $Ti^{4+} \leftarrow Fe^{2+}$ CT transition [Nol80], which is caused by iron impurities. The iron content was determined by LA-ICP-MS to < 5 ppm, similar results were obtained from the optical absorption spectra. The obtained gaussian parameters from all measured samples for these 4 absorptions are summarized in tab. 4.5:

Transition	λ_0[nm]	ν_0[cm^{-1}]	Γ[cm^{-1}]
$^2B_{2g} \rightarrow {}^2B_{1g}$	535	18700	11410
$^2B_{2g} \rightarrow {}^2A_{1g}$	800	12500	5600
$Ti^{4+} \leftarrow O^{2-}$	222	45100	8830
$Ti^{4+} \leftarrow Fe^{2+}$	392	25500	6080

Table 4.5: Average gaussian parameters for the contributing transitions

Even for small variations in the iron content (caused by the use of different raw materials), the $Ti^{4+} \leftarrow Fe^{2+}$ intensity changed for different samples (see fig. 4.10).

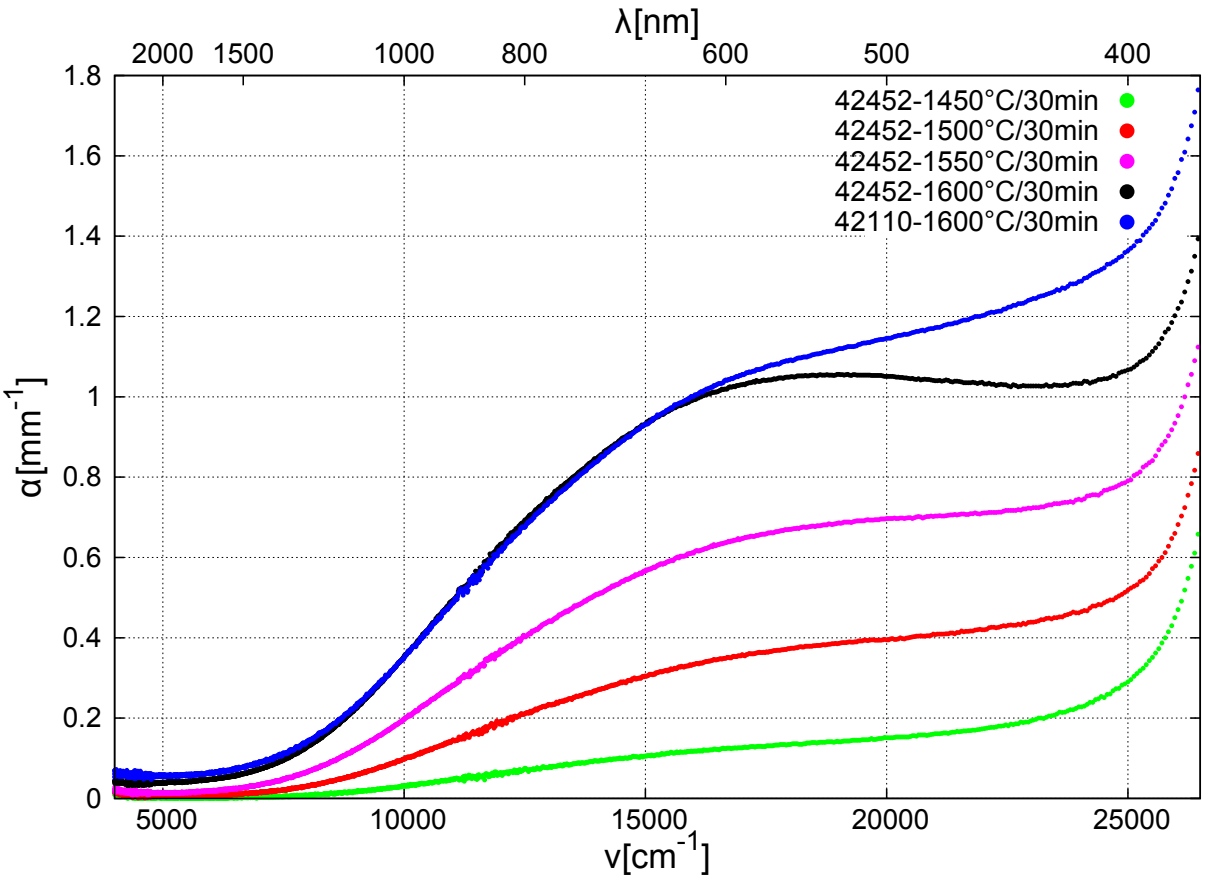

Figure 4.10: Absorption curve of glasses melted under similar melting conditions but with different content of iron impurities ($x_{Fe^{2+}}$(42110) > $x_{Fe^{2+}}$(42452))

In tab. 4.6 the results for different melts with varying amount of Ti^{3+} are summarized. The Ti^{3+} content was determined using the data from tab. 4.4 (A/x_i = 2.44 · 10^5 cm^{-2}/mol%).

Melt(T_m[°C],t_k[min])	λ_0[nm]	ν_0[cm^{-1}]	Γ[cm^{-1}]	α_0	A[cm^{-2}]	$x_{Ti^{3+}}$	χ_{red}
42452(1450,30)	555	18030	10730	1.36	$1.55 \cdot 10^4$	0.06	0.14
42452(1500,30)	529	18900	10670	3.74	$4.25 \cdot 10^4$	0.17	0.38
42452(1550,30)	531	18820	11040	6.70	$7.87 \cdot 10^4$	0.32	0.71
42452(1600,30)	543	18410	11690	10.50	$1.31 \cdot 10^5$	0.53	1.18
42110(1600,30)	525	19060	12520	10.22	$1.36 \cdot 10^5$	0.56	1.23
43735(1450,75)	533	18760	9950	2.89	$3.05 \cdot 10^4$	0.12	0.28
43735(1500,75)	524	19090	11610	5.95	$7.35 \cdot 10^4$	0.30	0.67
43735(1600,75)	531	18820	10880	12.24	$1.42 \cdot 10^5$	0.58	1.28
43735(1650,75)	570	17540	12670	17.17	$2.32 \cdot 10^5$	0.95	2.09
average	535	18700	11410				

Table 4.6: Average fit results of the main Ti^{3+} absorption peak ($^2B_{2g} \rightarrow {}^2B_{1g}$) for the investigated glasses with varying Ti^{3+} content ($x_{Ti^{3+}}$: mol% Ti^{3+}), all melts were of similar composition (w_{TiO_2} = 28.885 %, x_{TiO_2} = 45.23 %, ϱ_{Ti} = 9.8 · 10^{27} m^{-3}), α_0 in cm^{-1}, χ_{red} in % and $x_{Ti^{3+}}$ in mol%

The average peak position ν_0 is close to the value of [Pfe14], but the peak width Γ is approximately twice as big. The obtained values also follow the expected temperature behavior (see eq. (2.15) and fig. 2.8). The logarithm of the redox ratio is plotted in dependence of the inverse temperature in fig. 4.11(a). The obtained value for ΔH = -23.5 kJ/mol is approximately one order of magnitude smaller than the values obtained by Schreiber et al. [SJT80a] (ΔH = (-293 ± 105) kJ/mol) and Johnston [Joh65] (ΔH = -481 kJ/mol), but it has to be considered that they investigated different glass systems and also in the here investigated system the redox equilibrium is not reached due to the comparatively short keeping times (t_k = 30 min). In fig. 4.11(b) the consistency between both methods was examined. The measured intensities (I_{EPR} for EPR and A_{OPT} for optical measurements) were normalized on the melt with the highest amount of Ti^{3+} and it could be shown that both methods lead to similar results (considering the error tolerance) for the relative change of the Ti^{3+} content with the melting temperature T_m.

Additionally it was investigated how the ceramization process effects the amount of Ti^{3+} in the glass-ceramic. A first hint is given by its optical appearance, as the color of a dark Ti^{3+}-rich glass changes to white after the ceramization process. Unfortunately the glass-ceramic loses its optical transparency due to scattering on the grain boundaries of the crystals and optical transmission methods can not be used

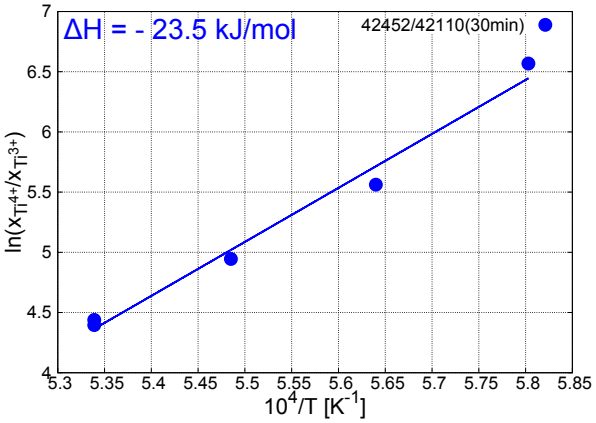

(a) Change of the redox ratio with melting temperature T_m (t_k = 30 min)

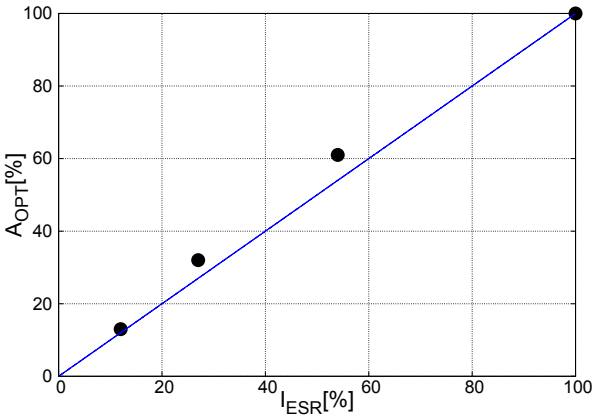

(b) Consistency examination of ESR and optical methods (intensities normalized on the melt with the highest amount of Ti^{3+})

Figure 4.11

anymore. In fig. 4.12 it can be seen that the amount of Ti^{3+} decreases strongly during the ceramization process. For ceramization holding times of t_h = 50 h, no signal could be detected anymore. Similar effects were found by [BB70].

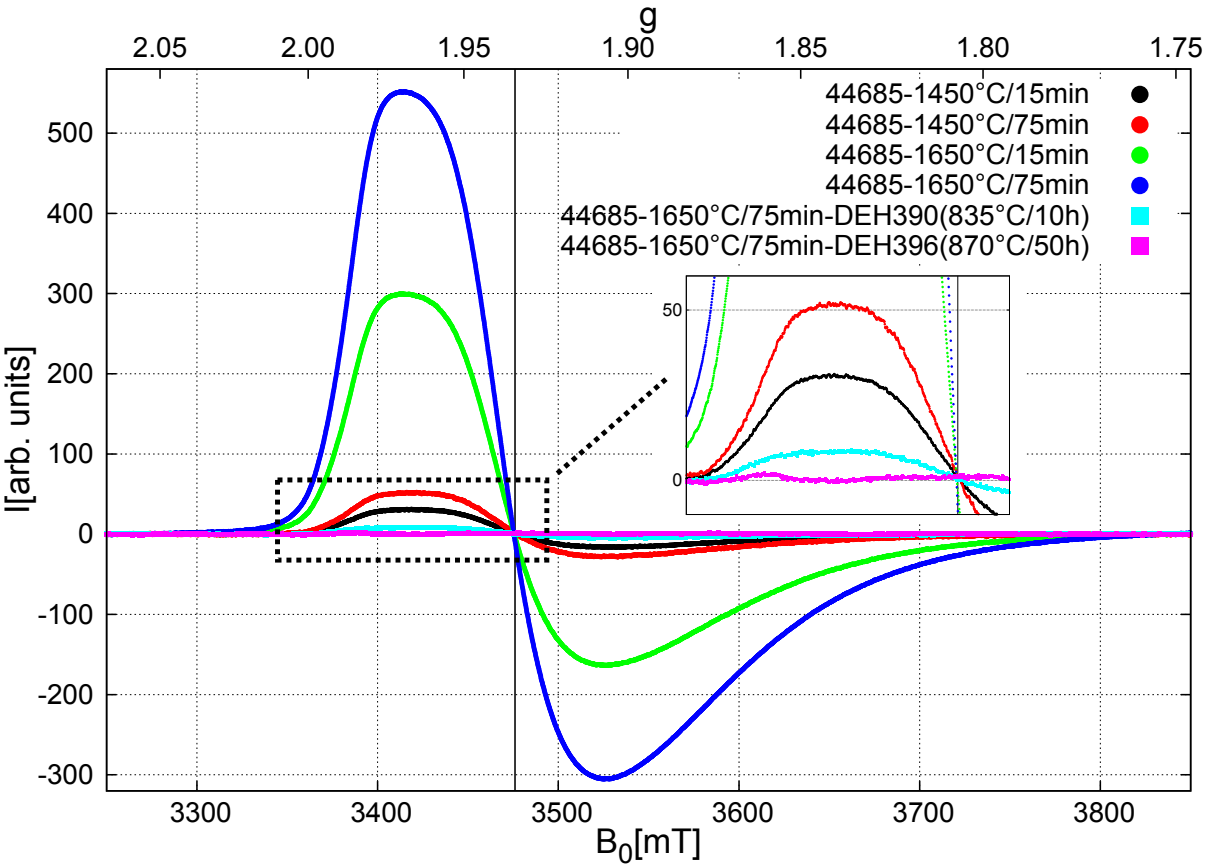

Figure 4.12: EPR measurement for glasses before and after ceramization

Even though, the amount of Ti^{3+} significantly reduces during the ceramization. Even small amounts seem to have severe effects on the dielectric properties and nucleation behavior of the glass-ceramic. Therefore other ways to prevent Ti^{3+} formation had to be investigated.

4.2.2 Prevention of Ti^{3+} by the use of oxidizing agents

In chapter 2.3.4 the effect of refining/oxidizing agents on the melting conditions was explained. To prevent the Ti^{3+} formation various dopants have been investigated. The first choice were the most commonly used refining agents for commercial glasses Sb_2O_5 and As_2O_5. As_2O_5 was excluded from further investigations due to its high level of toxicity, therefore Sb_2O_5 was investigated at first. The addition of already small amounts (0.1 mol% Sb_2O_5) led to a reduction of the Ti^{3+} below the detection limit of EPR and optical transmission methods (see fig. 4.13). The mutual redox interaction between the Sb and Ti ions could not be investigated as antimony oxide itself has no EPR active ions and the frequencies of the atomic transition lie in the UV range [EE03] ($Sb^{5+} \leftarrow O^{2-}$: ν > 50000 cm^{-1}, Sb^{3+}: ν_1 = 46300 cm^{-1} (216 nm) and ν_2 = 42900 cm^{-1} (233 nm)), which are hidden by the strong $Ti^{4+} \leftarrow O^{2-}$ transitions. Therefore it was not possible to evaluate the redox state of the Sb ions via transmission measurements. One possible method to determine the ratio of $Sb^{3+/5+}$ would be Mössbauer spectroscopy [SMMW88]. Unfortunately the partial substitution of Sb^{5+} on the Ti^{4+}-site in the crystalline phases of the ceramized samples was connected with the formation of Ti^{3+} and thereby an increase of the conductivity resp. $\tan(\delta)$ in the GHz range (see chapter 2.7.1 and 4.4.2). Therefore Sb_2O_5 has to be considered as not suitable for the use in titanate-based glass-ceramic systems. Further polyvalent resp. redox active oxides have been tested (SnO_2, MnO_2, CeO_2) but except for CeO_2 led to a deterioration of the glass quality. In the case of SnO_2 the devitrification was very intense even for small amounts of doping (< 0.1 mol%) as can be seen in fig. 4.13.

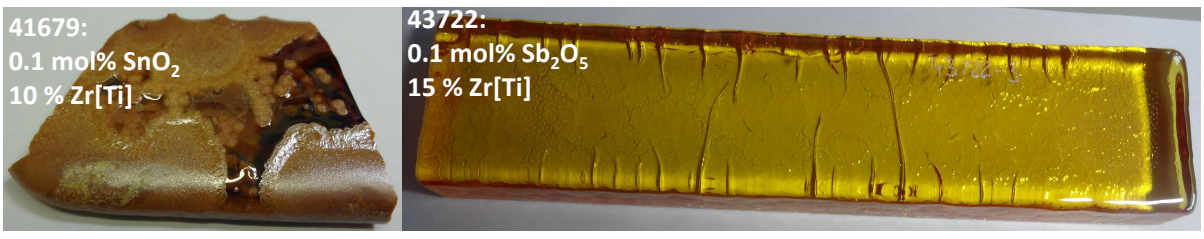

Figure 4.13: Left: strong devitrification induced by doping with 0.1 mol% SnO_2, right: clear Ti^{3+}-free glass doped with 0.1 mol% Sb_2O_5 (the cracks on the backside are caused by a non-optimized cooling procedure

4.2.3 $Ce^{3+/4+}$ as oxidizing agent

CeO_2 is a weaker refining agent as Sb_2O_5 or As_2O_5 (see chapter 2.3), but does not lead to a deterioration of the dielectric loss of the glass-ceramic like in the case of Sb_2O_5 (see chapter 2.7.1 and 4.4.2). Due to very short spin-lattice relaxation times of rare earth ions, the weak and comparatively broad Ce^{3+} EPR signals can only be detected at very low temperatures ($T < 10$ K) [BQP74, Gan92]. The detection of Ce^{3+} in the investigated glasses (which even would be more broadened due to the amorphous glass matrix) at liquid nitrogen temperatures did not succeed as expected from literature data [SRGN+03]. Therefore the only way to investigate the formation of Ce^{3+} was possible by optical methods as described in chapter 3.8.2. The transmission curves $T(\nu)$ of a Ce-free (39561) and a 2.0 mol% CeO_2 (39563) containing glass are shown in fig. 4.14. The weak, but comparatively sharp 4f-4f transition of Ce^{3+} can be seen at around 2140 cm^{-1}. A CeO_2 doping series is shown in fig. 4.15. It can be seen, that the absorption can be detected for $x_{CeO_2} \geq 0.5$ mol% (≈ 0.7 wt% or $\varrho_{Ce} \approx 10^{26}/m^3$).

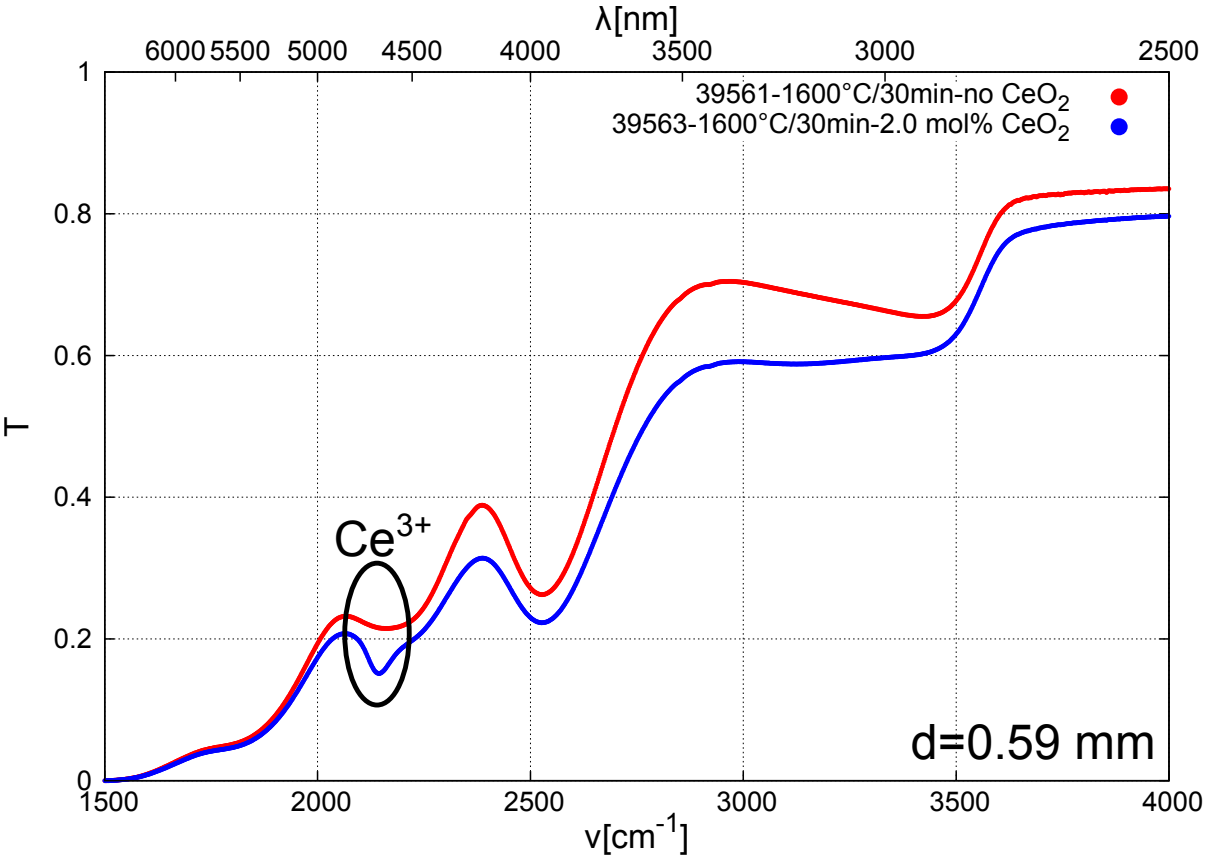

Figure 4.14: Comparison of the transmission curves for a Ce-free (39561) and a Ce-doped (39563) glass

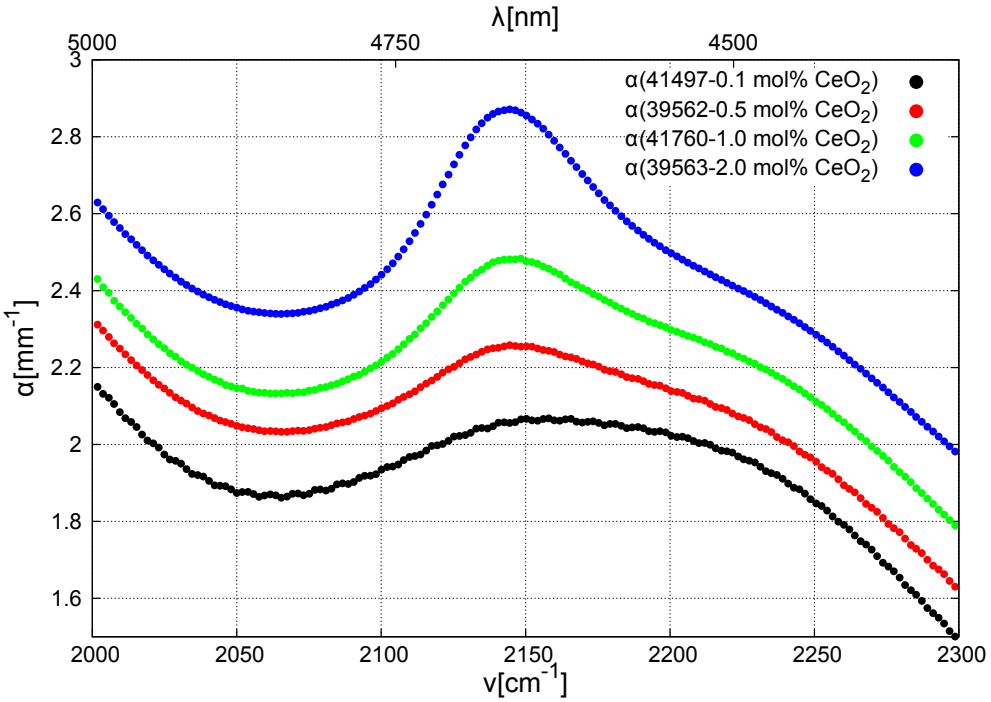

Figure 4.15: Absorption curves of a CeO_2 doping series (the horizontal shift of the absorption curves is accidentally due to different background contributions, but helps to see the difference between the curves)

One example for the evaluation of an absorption curve of a 2.0 mol% CeO_2 containing glass is shown in fig. 4.16:

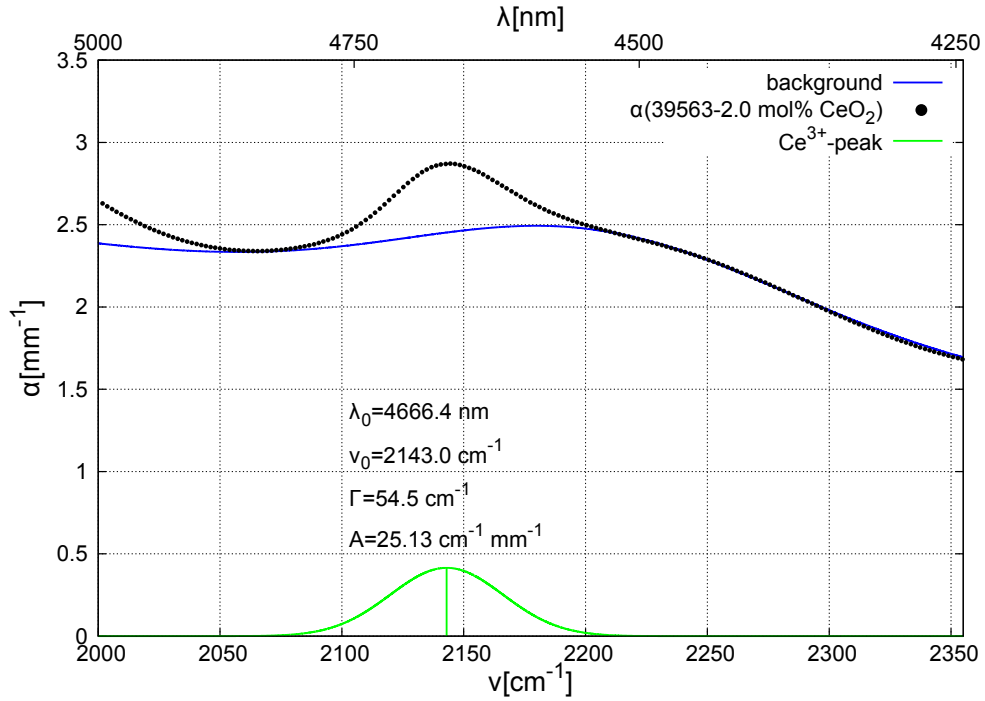

Figure 4.16: Absorption curve of 2.0 mol% CeO_2-doped glass (39563)

The oscillator strength P is calculated from the integrated absorption intensity A and the Ce^{3+} particle density $\varrho_{Ce^{3+}}$ via eq. (3.13):

$$P = \left(\frac{1}{\pi r_0}\right) \frac{1}{\varrho_{Ce^{3+}}} \underbrace{\int_{\text{peak}} \alpha(\nu)\, \mathrm{d}\nu}_{:=A} \quad , \tag{4.2}$$

whereby $\varrho_{Ce^{3+}} = \varrho_{Ce} \cdot \chi_{red}$. The particle density ϱ_{Ce} was determined via $\varrho_{Ce} = w_{CeO_2}/M_{CeO_2} \cdot \rho$ (w_{CeO_2}: CeO_2 weight fraction, M_{CeO_2}: atomic mass of CeO_2 = 172.19 u and ρ: glass density $\approx$ 4.5 g/cm^3 for all melts). The absorption cross section σ_{abs} follows from:

$$\sigma_{abs} = \frac{\alpha_0}{\varrho_{Ce^{3+}}} \quad . \tag{4.3}$$

The major error contribution for the determination of P and σ_{abs} is the unknown value of χ_{red}. In fig. 4.17 the integrated absorption intensity A is plotted in dependence of the melting temperature (T_m: 1450-1600 °C, t_k: 30 min).

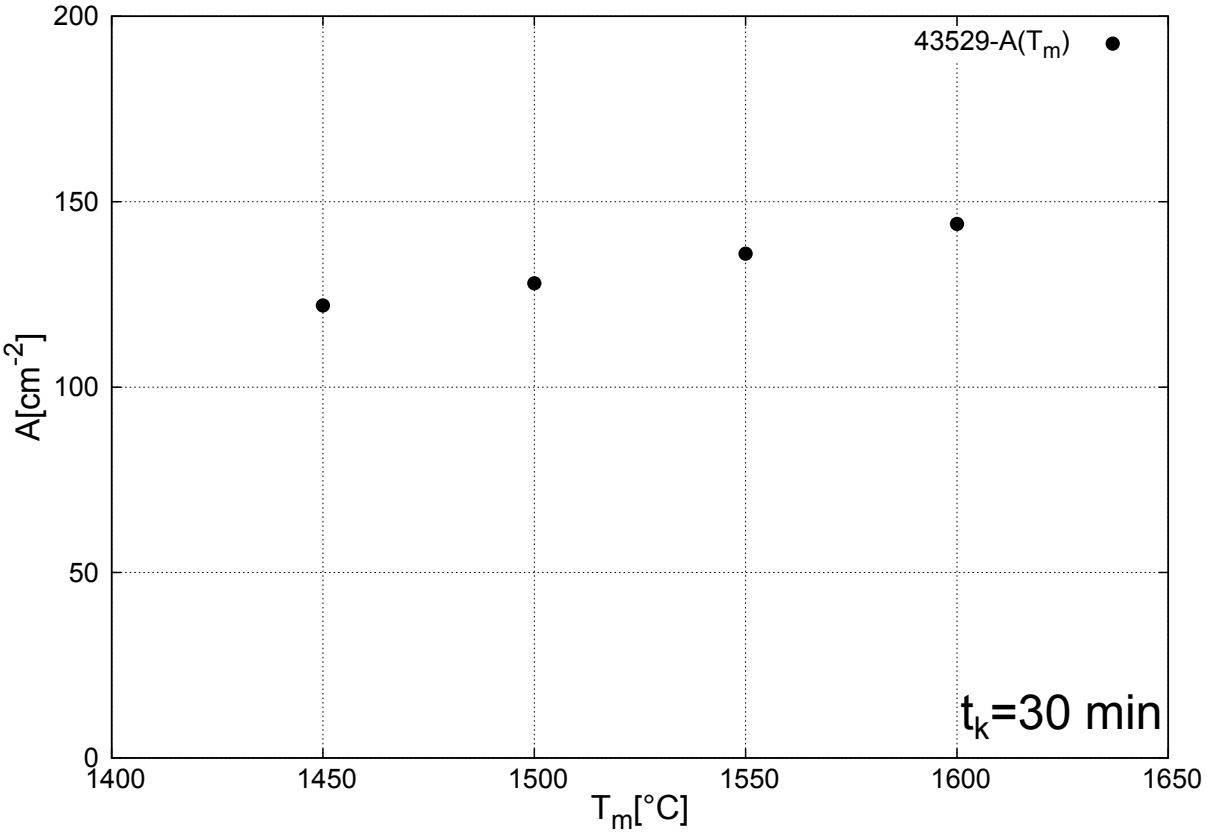

Figure 4.17: Absorption intensity in dependence of the melting temperature T_m for a 1.0 mol% CeO_2-doped glass (43529)

It can be seen, that the intensity only slightly increases ($\approx$ 18 %) over 150 °C of temperature variation. Considering fig. 2.12, we can therefore assume that χ_{red} is

already in the high-temperature saturation zone and the majority of the Ce-ions is present in the reduced state as Ce^{3+}. All the glasses in tab. 4.7 are melted at T_m = 1600 °C, therefore we can make a realistic estimation of χ_{red} = 0.80 ± 0.20, assuming a relative error of 25 % which also directly follows for P and σ_{abs} (neglecting all other minor error contributions). In tab. 4.7 the results for different melts with varying amount of doping are summarized.

Melt(x_{CeO_2})	ϱ_{Ce}[m^{-3}]	ν_0[cm^{-1}]	Γ[cm^{-1}]	α_0[cm^{-1}]	A	P	σ_{abs}[m^2]
39562(0.5)	$1.08 \cdot 10^{26}$	2141	56.1	1.24	74	$9.7 \cdot 10^{-7}$	$1.4 \cdot 10^{-24}$
41498(0.5)	$1.08 \cdot 10^{26}$	2141	57.1	1.44	87	$11 \cdot 10^{-7}$	$1.7 \cdot 10^{-24}$
40932(1.0)	$2.18 \cdot 10^{26}$	2143	55.9	2.28	136	$8.8 \cdot 10^{-7}$	$1.3 \cdot 10^{-24}$
41418(1.0)	$2.16 \cdot 10^{26}$	2142	56.1	2.46	147	$9.6 \cdot 10^{-7}$	$1.4 \cdot 10^{-24}$
41760(1.0)	$2.18 \cdot 10^{26}$	2142	55.8	2.29	136	$8.8 \cdot 10^{-7}$	$1.3 \cdot 10^{-24}$
43529(1.0)	$2.16 \cdot 10^{26}$	2142	55.8	2.39	144	$9.4 \cdot 10^{-7}$	$1.4 \cdot 10^{-24}$
39563(2.0)	$4.40 \cdot 10^{26}$	2143	54.5	4.24	246	$7.9 \cdot 10^{-7}$	$1.2 \cdot 10^{-24}$

Table 4.7: Fit results of the investigated glasses with varying CeO_2 content (x_{CeO_2}: mol% CeO_2), all melts were melted under similar melting conditions (T_m: 1600 °C, t_k: 30 min), A in cm^{-2}

The average values of tab. 4.7 are given in tab. 4.8 (α_0 normalized per mol% CeO_2):

λ_0[nm]	ν_0[cm^{-1}]	Γ[cm^{-1}]	α_0 / x_{CeO_2}	P	σ_{abs}[m^2]
4468	2142	55.9	2.38	$(9.2 \pm 2.3) \cdot 10^{-7}$	$(1.4 \pm 0.3) \cdot 10^{-24}$

Table 4.8: Average values for the $^2F_{5/2}$-$^2F_{7/2}$ (4f-4f) transition of Ce^{3+} in La_2O_3-TiO_2-SiO_2-B_2O_3 glass, α_0 / x_{CeO_2} in cm^{-1}/mol%

Due to the unknown oscillator strength of the Ce^{3+} 4f-4f transition, a quantitative determination of the Ce^{3+} content was not possible. From the estimation of χ_{red}, we can calculate P to $(9.2 \pm 2.3) \cdot 10^{-7}$. This value seems to be reasonable and also is consistent with the values given by Paul [Pau82] for a spin-forbidden and Laporte-forbidden transition (see tab. 3.2). An attempt to measure the transmission curve of CeF_3-doped KBr pellets to determine the oscillator strength of the transition, did not succeed due to the insufficient transparency of the samples. Also the additional splitting into 4 absorptions peaks would make the evaluation more difficult (see fig. 3.11(a)). It could be shown that the dominant part of the Ce-ions releases oxygen during the melting process (leading to a more oxidizing atmosphere in comparison to a melt without CeO_2) and therefore will be in the reduced state at the melting temperature. A minor amount of Ce^{4+} is still available at higher temperatures which is then able to reoxidize Ti^{3+} ions during the cooling process via eq. (2.25):

$$\mathrm{Ti^{3+}} + \mathrm{Ce^{4+}} \longrightarrow \mathrm{Ti^{4+}} + \mathrm{Ce^{3+}} \quad . \tag{4.4}$$

In fig. 4.18 the influence of Ce-doping on the formation of $\mathrm{Ti^{3+}}$ is shown. It can be seen, that for amounts of $x_{\mathrm{CeO_2}} \geq 0.1$ mol% no $\mathrm{Ti^{3+}}$ is detected anymore.
It could be shown in this chapter that doping with a sufficient amount of $\mathrm{CeO_2}$ totally prevents, the formation of $\mathrm{Ti^{3+}}$. Similar results were obtained by [Pau76] with similar methods (EPR and optical transmission) even under strongly reducing conditions (e.g. addition of carbon as reducing agent). From eq. (4.4) it would be expected that the $\mathrm{CeO_2}$ content has to be at least of the same amount as the $\mathrm{Ti^{3+}}$ content to achieve a complete prevention of $\mathrm{Ti^{3+}}$. For a melt of similar conditions as the glasses investigated in the $\mathrm{CeO_2}$-doping series, an amount of $x_{\mathrm{Ti^{3+}}} \approx 0.5$ mol% was determined, which is 5 times more than the used amount of $\mathrm{CeO_2}$. This means that the real $\mathrm{Ti^{3+}}$ content is probably lower than the one determined via [Pfe14].

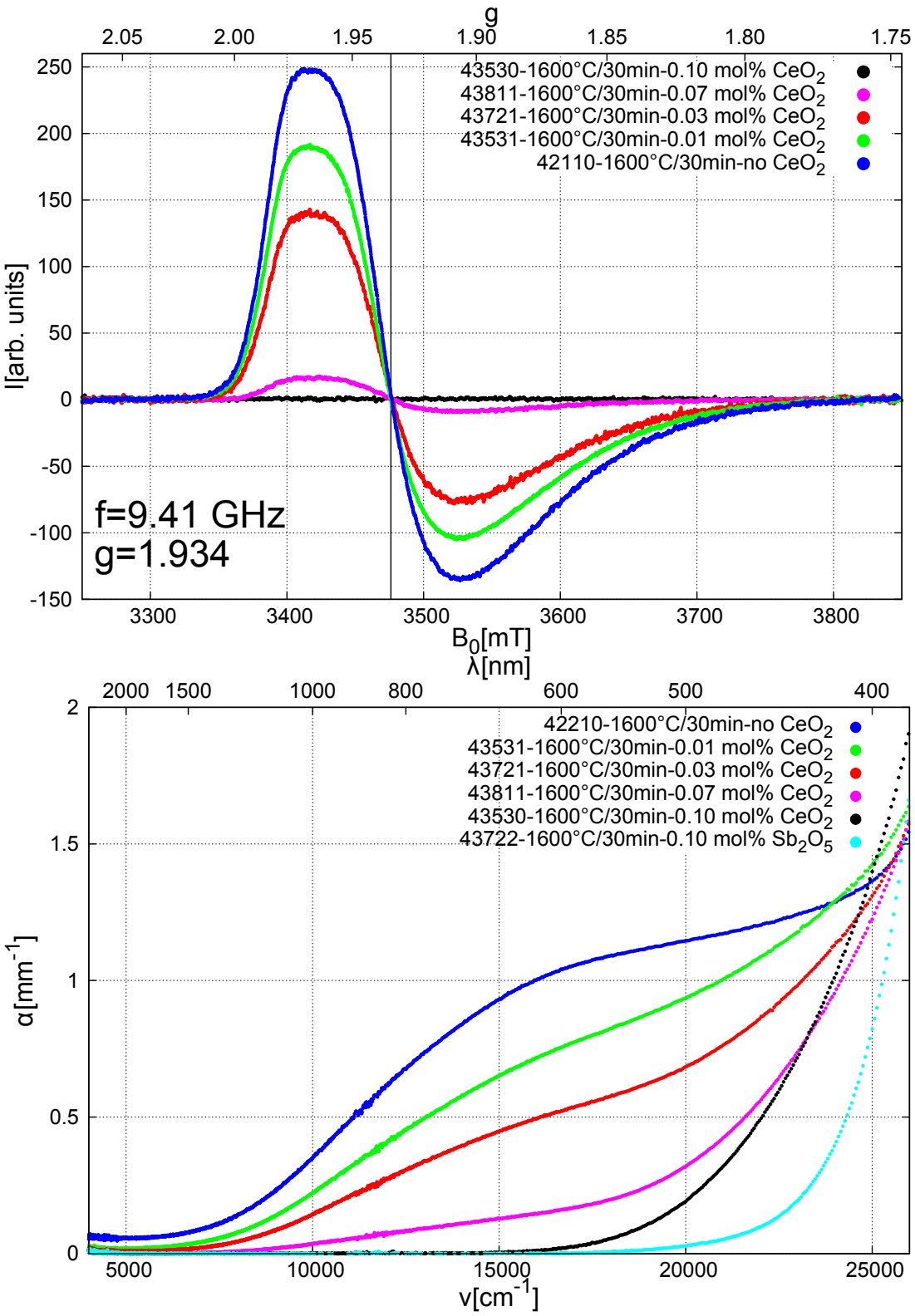

Figure 4.18: Influence of Ce-doping on the formation of Ti^{3+} investigated via EPR (top) and optical transmission (bottom) measurements (glasses melted under similar melting conditions)

Color change due to the presence of Ce^{3+}

It is known, that the simultaneous presence of Ti and Ce ions produces greater coloring intensities than those caused by each ion individually [SDN91]. This is generally explained by the formation of a Ce^{3+}-Ti^{4+}-complex [KUCS03, Pau76] causing a wide color range from deep yellow to amber (see fig. 4.20). The broad $Ti^{4+}\leftarrow Ce^{3+}$ CT band at around 30000 cm^{-1} (345 nm) extends even more in the visible region [Pau76] as the oxygen-cation CT bands ($Ti^{4+}\leftarrow O^{2-}$ CT (200 nm) [EE03, WT98], $Ce^{4+}\leftarrow O^{2-}$ (240 nm) and $Ce^{3+}\leftarrow O^{2-}$ (300-320 nm) [Str61, BALGG10, Gan92]) which normally determine the UV edge and individually only would cause a yellowish hue for high concentrations [SDN91].

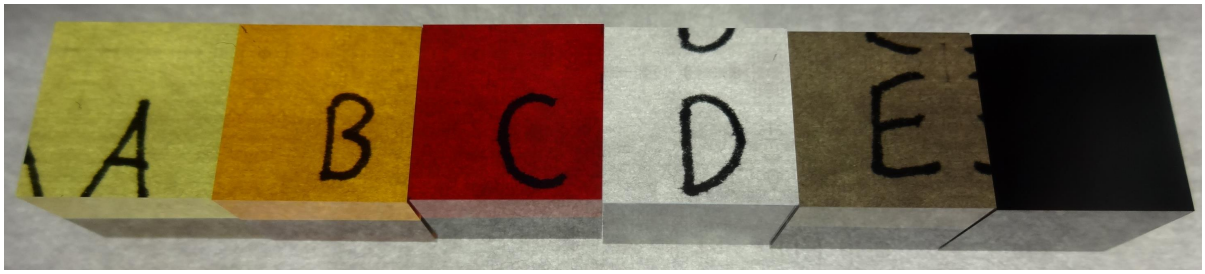

Figure 4.19: Doping series shown by 1 cm^3 glass cubes: A: 0.1 mol% Sb_2O_5 (43722), B: 0.1 mol% CeO_2 (43530), C: 1.0 mol% CeO_2 (42014), D: colorless pure SiO_2 glass, E: low amount of Ti^{3+} (42452, melted at 1450 °C), F: high amount of Ti^{3+} (42452, melted at 1600 °C)

The glass investigated in this work which contains a quite large amount of TiO_2 shows a color shifts from yellow to red with increasing Ce content (see B/C in fig. 4.19), as due to the high amount of TiO_2 the intensity of the $Ce^{3+}\leftarrow Ti^{4+}$ CT complex only depends on the CeO_2 resp. Ce^{3+} concentration. Similar complexes like the $Ce^{3+}\leftarrow Fe^{3+}$ CT complex [SJT80a, SJT80b] are also well known.

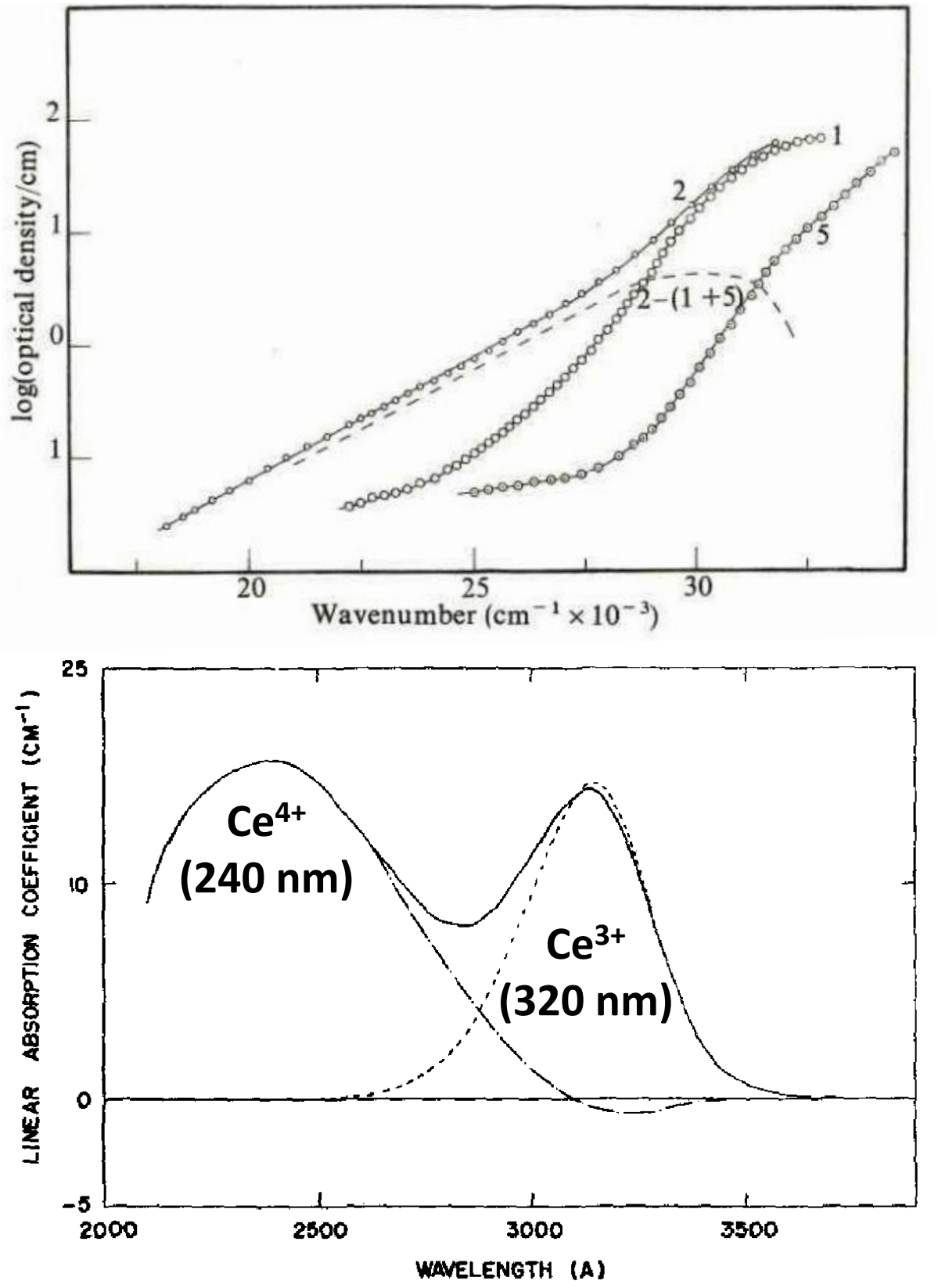

Figure 4.20: Top: optical absorption of 1: pure CeO_2-doped glass, 5: pure TiO_2-doped glass, 2: glass containg CeO_2 and TiO_2 [Pau76], bottom: CT Absorptions of Ce^{3+} and Ce^{4+} in 0.06 mol% CeO_2-doped $75SiO_2$-$25Na_2O$ glass (modified from [Str61])

4.3 Nucleation and ceramization

In this chapter the influence of the different glass defect structures (surface and bulk devitrification, dissolved Pt particles, formation of Ti^{3+}, glass-glass phase separation) on the nucleation/crystallization behavior of the investigated glass-ceramics is discussed. In case of optimal melting conditions (standard melting conditions: temperature T_m = 1600 °C and keeping time t_k = 30 min) the bulk of the glass is completely amorphous and no crystallization/devitrification inside the glass was detected by SEM/TEM investigations. In fig. 4.21 a TEM image of the bulk glass is shown, including the associated diffraction pattern indicating a completely amorphous material structure (typical diffraction rings).

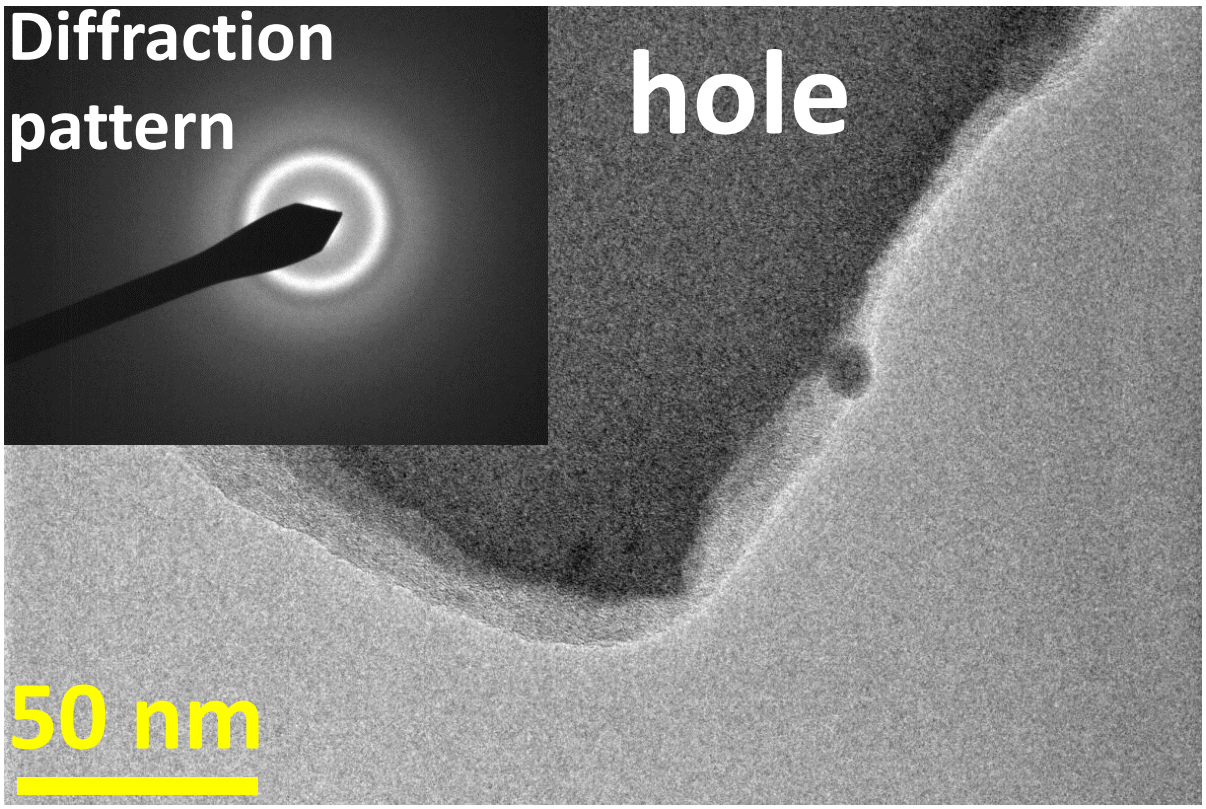

Figure 4.21: TEM image of the bulk of glass 42014, including typical amorphous diffraction pattern

4.3.1 Surface devitrification

In chapter 4.1 the problem of surface devitrification was discussed (see fig. 4.2) and it could be shown that doping with ZrO_2 reduced the devitrification tendency. In fig. 4.22 an optical microscope image of the surface crystals is shown, the crystals were

identified as $La_2Ti_2SiO_9$ by SEM/EDX. This result also indicates that doping by ZrO_2 destabilizes the formation of $La_2Ti_2SiO_9$.

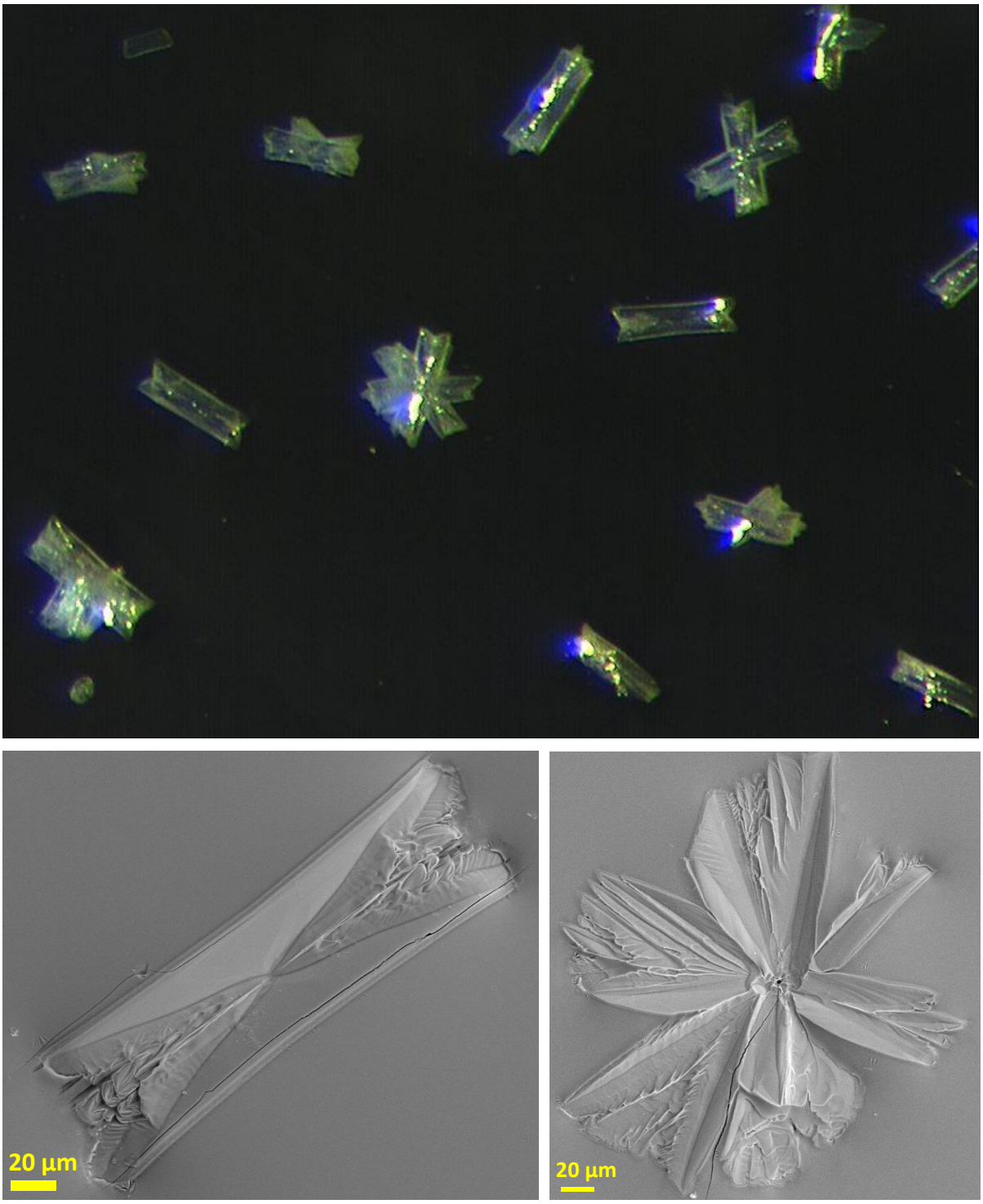

Figure 4.22: Top: optical microscope image of the surface crystals on sample 39561, bottom: SEM magnification of the crystals

4.3.2 Bulk devitrification due to unmelted raw material

Glasses which were melted at comparatively low temperatures (T_m < 1500 °C) showed striae of small crystals inside the bulk (see fig. 4.23). The formation of these crystals is probably caused by unmelted raw materials which provide nuclei for crystal growth already during the casting/cooling process.

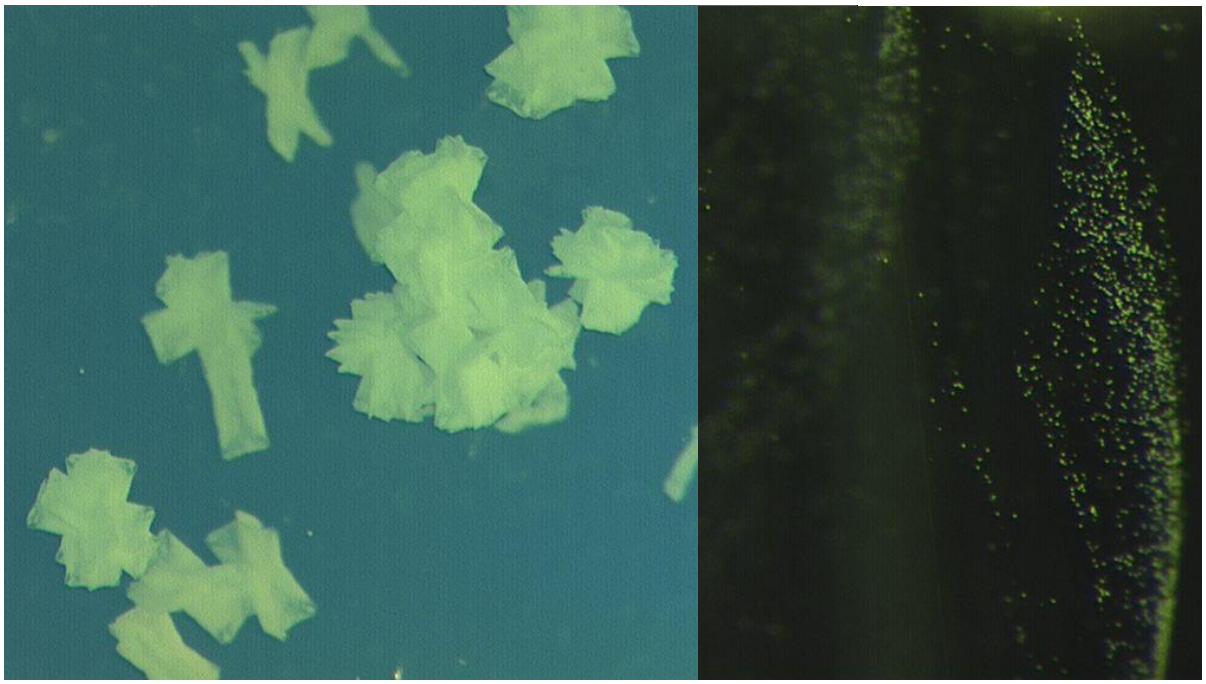

Figure 4.23: Optical microscope images of bulk glass devitrification (left: magnification of crystals, right: crystal striae inside the bulk)

4.3.3 Nucleation by dissolved Pt particles

In [Bra11] the investigations concerning the dominant nucleation mechanisms could not be completed entirely but a nucleation by dissolved Pt particles caused by corrosion of the crucible material was assumed. It is known that the increase of melting time t_k, temperature T_m and also the degree of reduction of the melting conditions favors Pt corrosion. Reducing atmosphere leads to a higher amount of raw material ions in the metallic state and thereby to a higher degree of alloying with the Pt crucible. This alloying process is associated with a reduction of the melting temperature of the Pt-crucible material and thereby leads to a faster corrosion process. Another contribution is simply given by mechanical abrasion of the crucible material by the liquid glass melt. Under the standard melting conditions the number density of Pt particles inside the glass is so small that no isolated particles were detected by

SEM investigations. Even though due to their role as nucleation agents, Pt could be detected in the center of dendritic crystals inside glass-ceramic samples (see lower picture in fig. 4.24 and fig. 4.29). For glasses with increased Pt corrosion tendency due to increased T_m, t_k and no use of oxidizing agents, isolated Pt particles also could be found in the basic glass, proving that no crystallization occurred during the casting/cooling process. The size of the found particles varied between approximately 50-500 nm. First SEM investigations with the use of a basic glass (36436) of [Bra11] showed that Pt particles in principle nucleate both main crystalline phases $\mathrm{La_4Ti_9O_{24}}$ and $\mathrm{La_2Ti_2SiO_9}$ (upper picture in fig. 4.25), but dominantly the $\mathrm{La_4Ti_9O_{24}}$ phase is nucleated by Pt (lower picture in fig. 4.25). This is especially of interest as the knowledge about the nucleation mechanisms can be used to favor respectively suppress the crystallization of selected phases during the ceramization process and thereby achieve a lower number of present phases inside the glass-ceramic.
To investigate the relevance of different nucleation contributions a melting series of a 1.0 mol% $\mathrm{CeO_2}$-doped glass with varying melting temperature has been made. The glass 43529 was melted at 1450 °C for a keeping time of 30 min, then one glass bar was casted and the crucible was put back in the oven and heated up to 1500 °C where it was kept another 30 min and then the next bar was casted. According to this procedure 4 samples melted at different temperatures (1450, 1500, 1550, 1600 °C) were made and their nucleation behavior was investigated. The samples were ceramized at different temperatures T_{cer} between 850-950 °C and ceramization times t_{cer}. All samples contained no detectable amount of $\mathrm{Ti^{3+}}$, therefore the nucleation was dominantly caused by dissolved Pt particles and by surface nucleation. Crystal growth caused by surface nucleation can be seen as thin bright layer growing towards the inside of the bulk (see fig. 4.26), whereby the Pt-nucleated crystals appear as spherical respectively circular bright spots inside the glass. It is obvious that the number of Pt particles strongly increases with the melting temperature. 43529-1500 shows almost no crystallization inside the bulk due to the lack of dissolved Pt, whereby 43529-1600 is nearly completely crystallized already at low ceramization temperatures. Normally it would be expected that 43529-1450 even shows the smallest amount of bulk crystallization due to the lowest Pt content. In the case of 43529-1450 the crystallization is probably caused by unmelted raw materials due to the low melting temperature as shown in fig. 4.23 above. The amount of surface crystallization is independent of the melting temperature as expected and starts to contribute dominantly for ceramization temperatures above 920 °C and for ceramization times above 20 h (at 950 °C) the crystallization front reached to the center of the sample. The analysis of the different crystalline phases will be discussed in chapter 4.4.

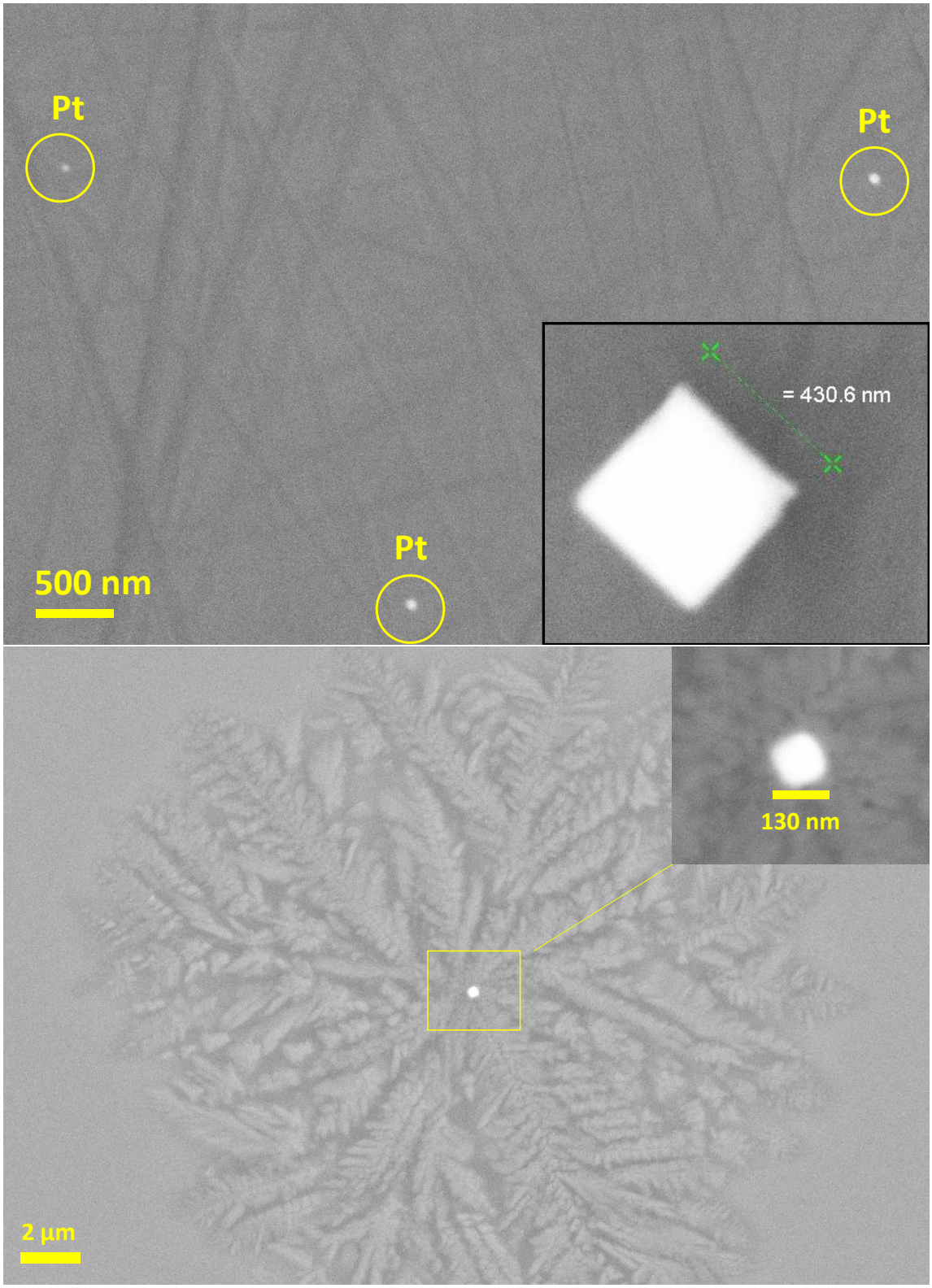

Figure 4.24: Top: glass 44685-1650 melted at T_m = 1650 °C and keeping time t_k = 75 min without oxidizing agents, bottom: glass-ceramic of basic glass from [Bra11] ceramized at 870 °C showing a Pt-nucleated $La_4Ti_9O_{24}$ crystal

Figure 4.25: Top: $La_4Ti_9O_{24}$ (L4) and $La_2Ti_2SiO_9$ (L2) crystal (both nucleated by Pt particle), bottom: Pt-striae containing a comparatively large number density of Pt particles with mainly nucleated $La_4Ti_9O_{24}$ crystals

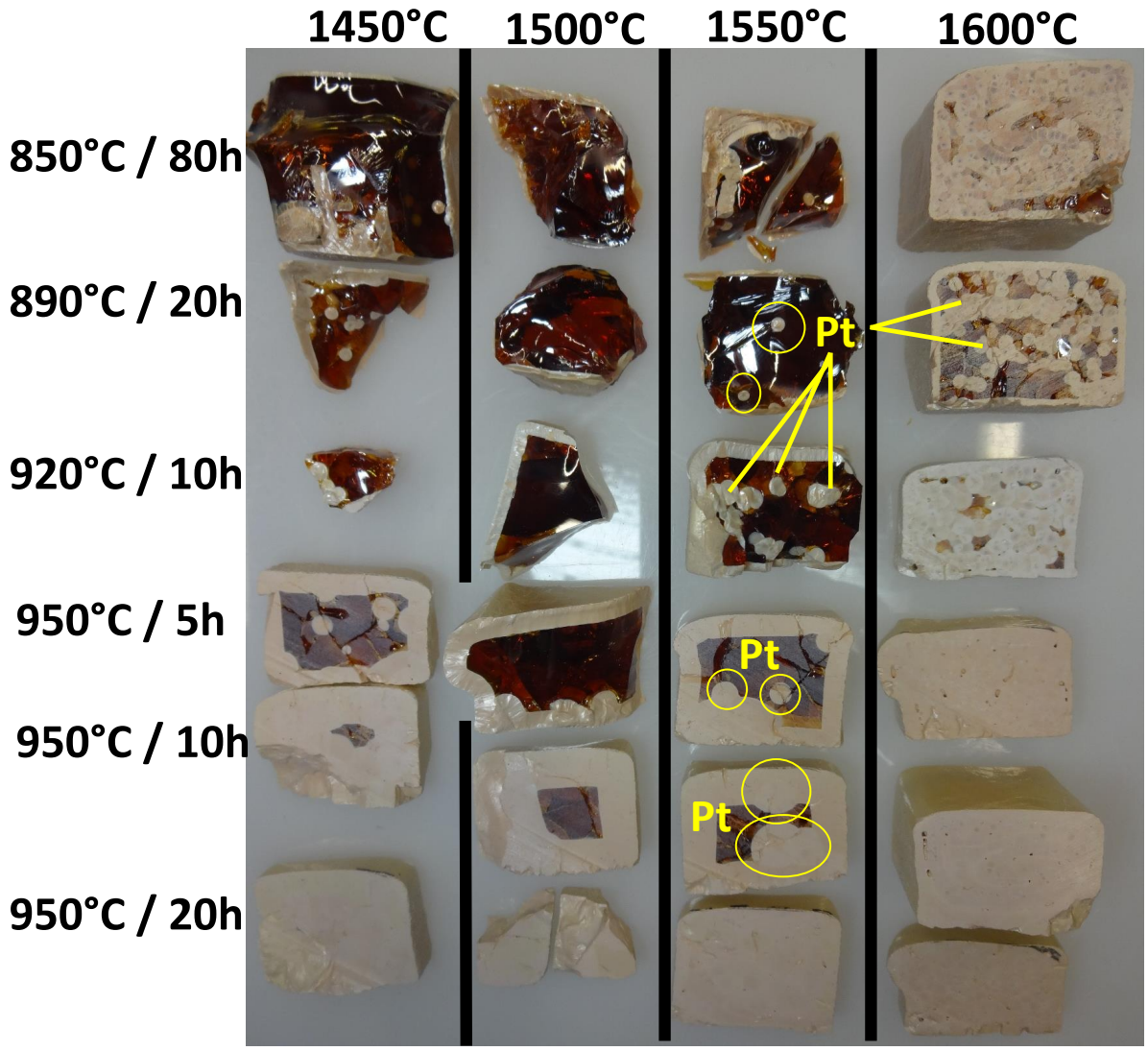

Figure 4.26: Ceramization series 43529DEH showing the influence of the different nucleation mechanism contributions and their dominant temperature ranges (left: T_{cer}/t_{cer}, top: T_m; Pt nucleation shown in yellow)

Similar Pt-nucleated samples as shown in fig. 4.26 were further investigated by SEM. In fig. 4.27 a sample ceramized at low T_{cer} and short t_{cer} (42014DEH388: T_{cer} = 840 °C, t_{cer} = 10 h) shows the onset of crystallization during which isolated crystal clusters are growing distributed randomly in the bulk. Fig. 4.28 and 4.29 show a fully crystallized sample (42014DEH373: T_{cer} = 870 °C, t_{cer} = 50 h) in which the crystal growth fronts of different clusters already met each other. Further ceramization series also showed that crystallization processes either by surface or Pt nucleation are observed for T_{cer} > 820 °C, but only temperatures above 850 °C were sufficient to fully crystallize the glasses in relevant time scales (t_{cer} < 100 h). At T_{cer} < 900 °C surface crystallization is spatially restricted to a small layer close to the surface.

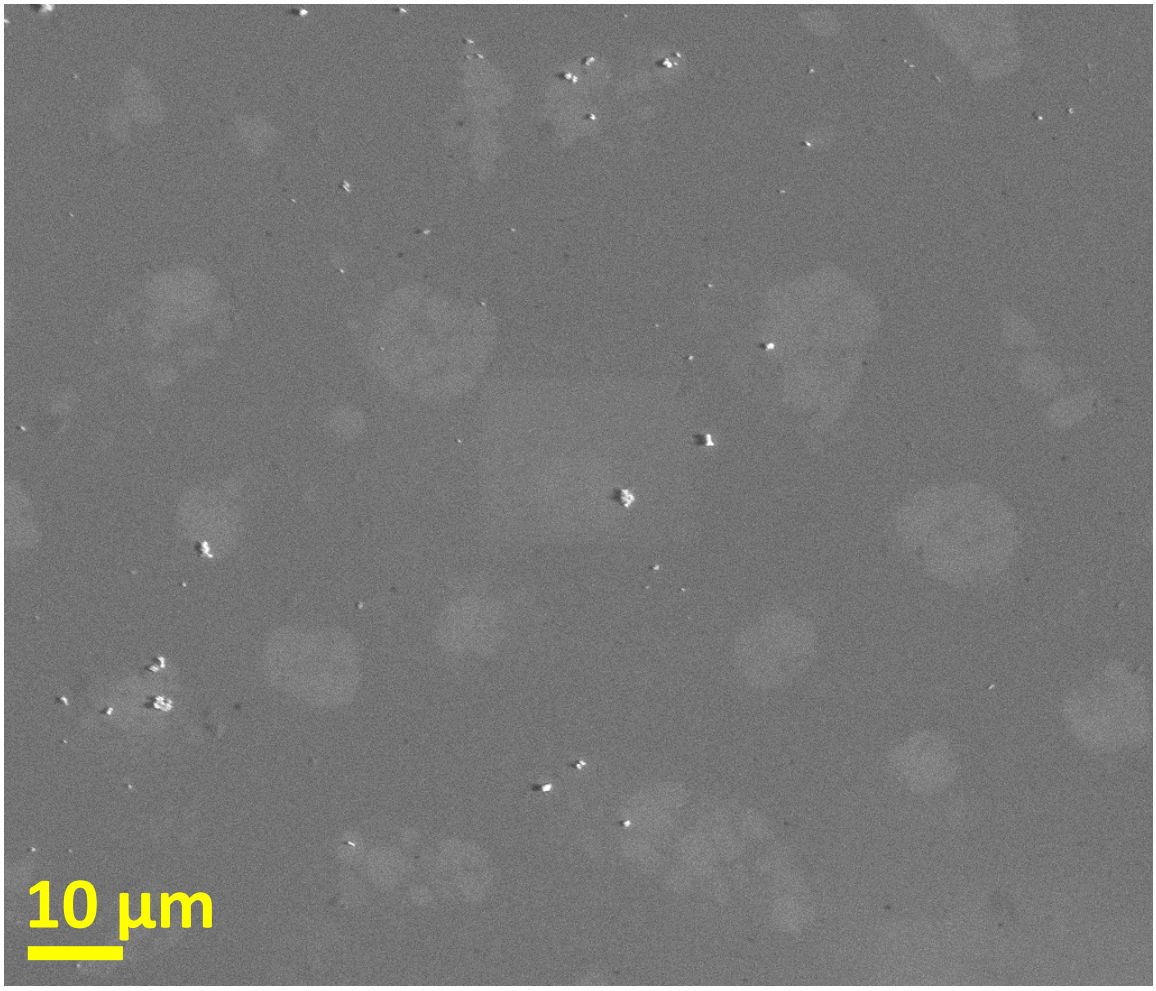

Figure 4.27: SEM image showing the onset of crystallization for a dominantly Pt-nucleated glass (42014DEH388: T_{cer} = 840 °C, t_{cer} = 10 h), remark: the rectangular area in the center was damaged by the electron beam

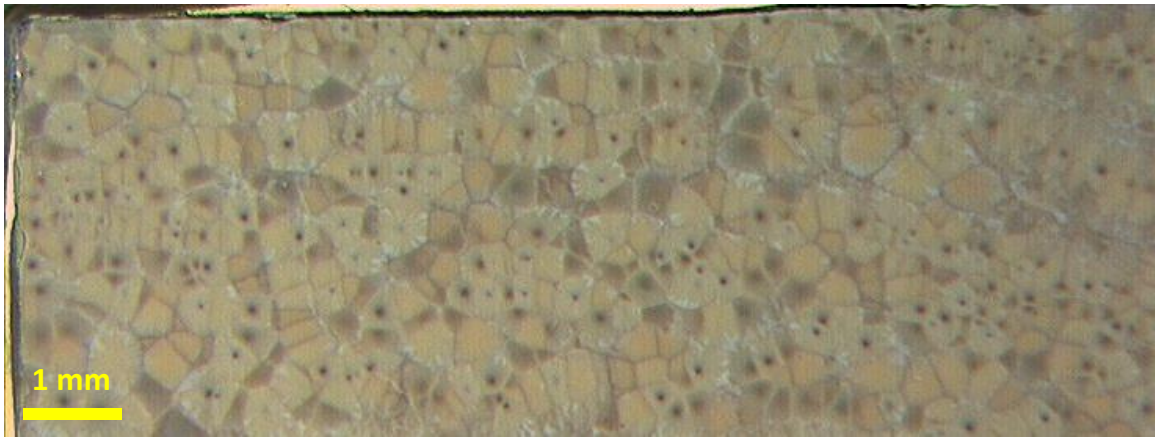

Figure 4.28: Optical image of a fully crystallized Pt-nucleated glass (42014DEH373: T_{cer} = 870 °C, t_{cer} = 50 h)

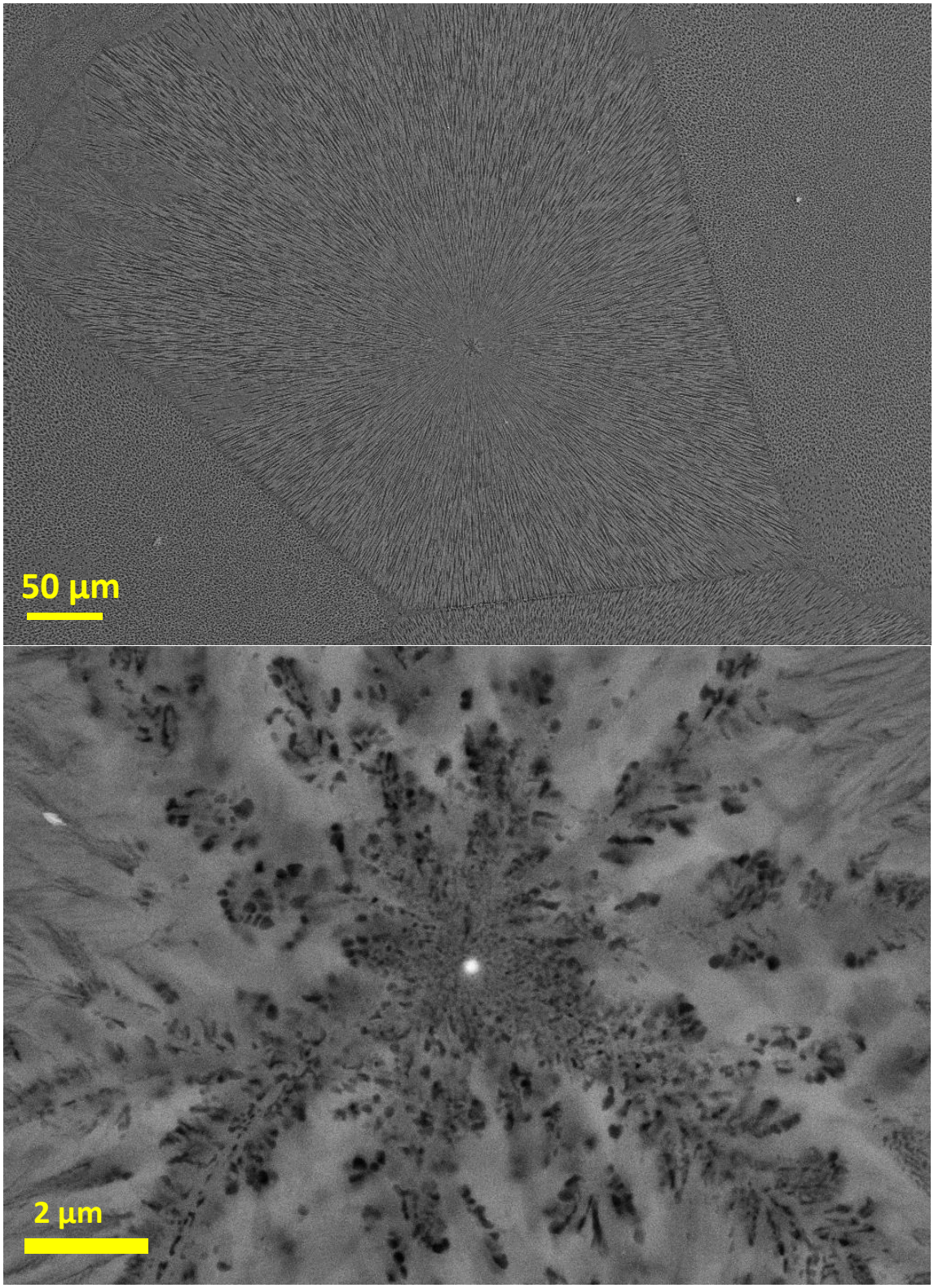

Figure 4.29: Top: SEM magnification of 42014DEH373 (fig. 4.28) showing a dendritic crystal growth induced by Pt, bottom: Pt particle as nucleus in the center of the crystal

4.3.4 Ti^{3+}-induced nucleation

Glasses which were melted without the use of oxidizing agents showed a partial reduction of the containing Ti^{4+} to Ti^{3+} as discussed in chapter 4.2. The presence of Ti^{3+} in the glass led to an additional nucleation mechanism as the ones already described above. The catalytic effect of Ti^{3+} on the nucleation was already described in chapter 2.2. Similar results were also found by Boehm et al. [BB70]. In fig. 4.30 the ceramized glass 43531 melted under standard melting conditions (43531DEH379: T_{cer} = 850 °C, t_{cer} = 10 h) is shown. The glass is homogeneously crystallized everywhere except in the region which was facing the air inside in the steel mold when the glass was casted. This surface cooled slower and therefore enabled a partial reoxidation in a thin layer close to the surface. This region stayed amorphous during the ceramization process due to the lack of Ti^{3+}. In fig. 4.31 it can be seen that the main crystal phase is $La_2Ti_2SiO_9$ and the darker regions at the boundary region of the crystallites is amorphous SiO_2. It is generally the case that any impurities are swept to the grain boundaries by diffusion [ABW+01]. In this case the residual glass phase is depleted in TiO_2 after the ceramization of the main phase and therefore $LaBO_3$ and amorphous SiO_2 is found in the regions between the crystallites.

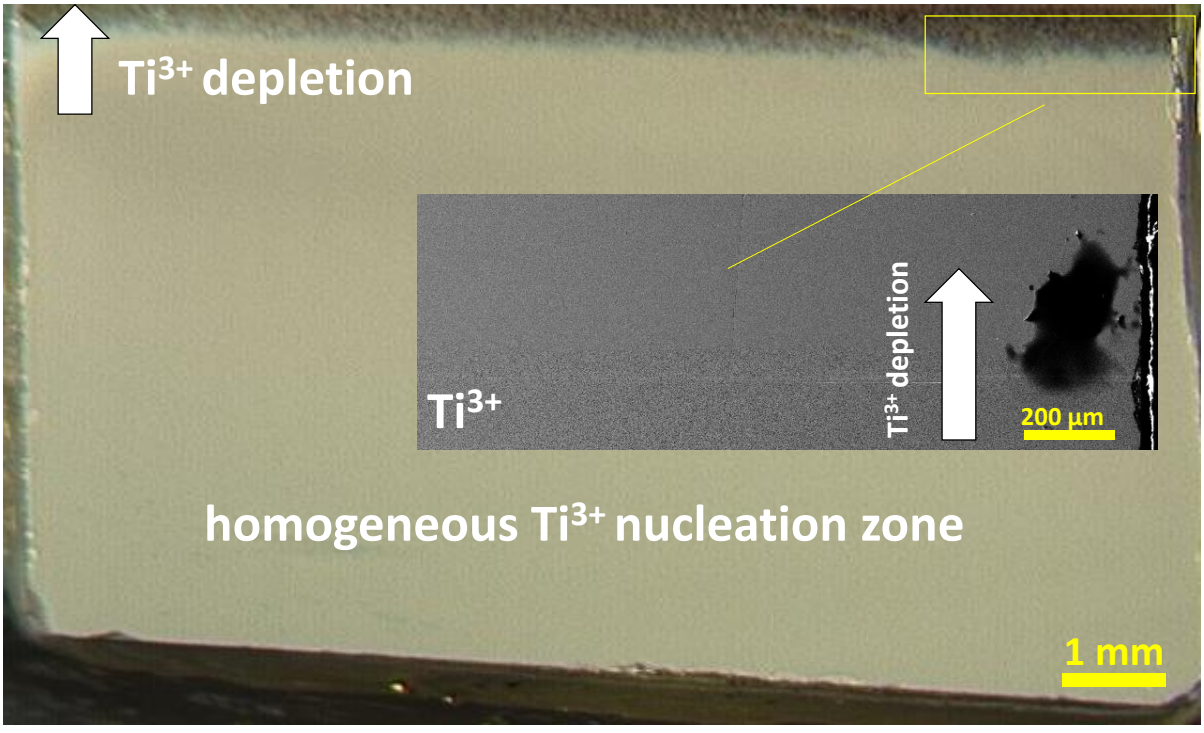

Figure 4.30: Optical image of 43531DEH379 showing a homogeneously crystallized glass due to the presence of Ti^{3+}; remark: the black spot in the SEM image is a sample marker

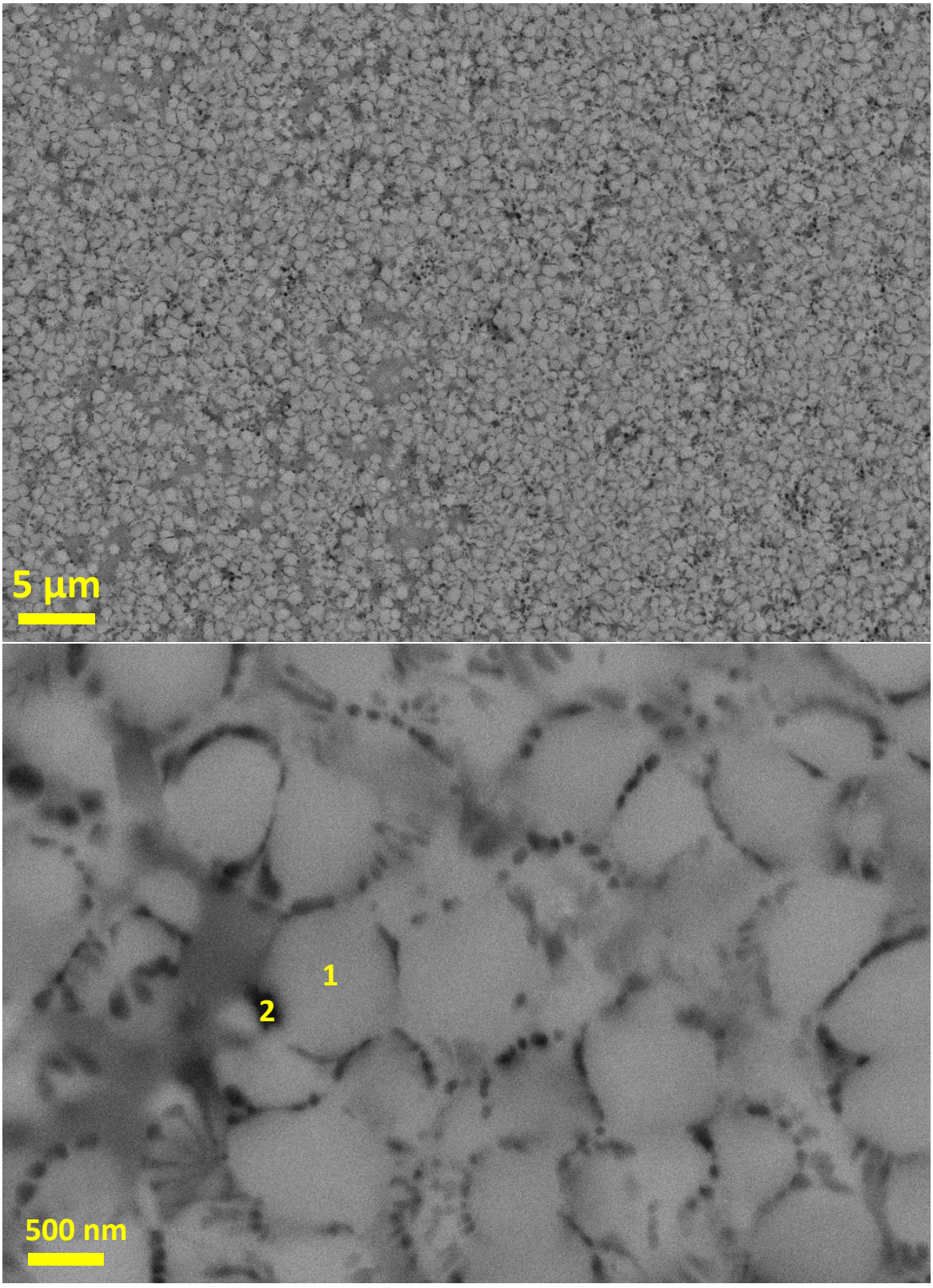

Figure 4.31: Magnification of the microstructure in the Ti^{3+}-nucleated zone of fig. 4.30 (1: $La_2Ti_2SiO_9$, 2: amorphous SiO_2)

4.3.5 Glass-glass phase separation

The formation of amorphous SiO_2 was also found outside the crystallized regions and could be induced in glasses by heating to temperatures slightly above T_g (see upper picture in fig. 4.32). The formation of the amorphous SiO_2 regions can be understood as a glass-glass phase separation which can already occur during the cooling of the glass in case of high cooling temperatures and slow cooling rates. Similar glass-glass phase separation into a SiO_2-rich and TiO_2-rich phase was also found in TiO_2-containing Na_2O-TiO_2-SiO_2 glass systems by Bayer et al. [BFHS66] and are considered as preliminary stage before the onset of crystallization. These SiO_2 regions caused by phase separation (labeled as PS1 in fig. 4.32 and 4.33) can be distinguished from the ones formed at the boundary of the main crystalline phases (see fig. 4.33, labeled 1A and 1B) by their difference in size and in case of 1A also by their shape. XRD measurements and diffraction analysis by TEM showed that all the SiO_2 regions are not crystalline. In fig. 4.33 it can be seen that the PS1-regions do not interfere with the crystallization process and therefore can be considered as irrelevant for the nucleation process. Even though their formation reveals that before the start of the actual crystallization, the SiO_2 separates from the crystal forming oxides ($Ti(Zr)O_2$, La_2O_3) and thereby initiates the first step of the crystallization process. The 1A/1B-SiO_2 regions are formed during the crystallization of the main phases on their boundaries due to the depletion of the crystal forming oxides mentioned above. In fig. 4.34 this depletion process was shown by a TEM/EDX line scan over one of the dendritic structures (labeled with 3 in fig. 4.33).

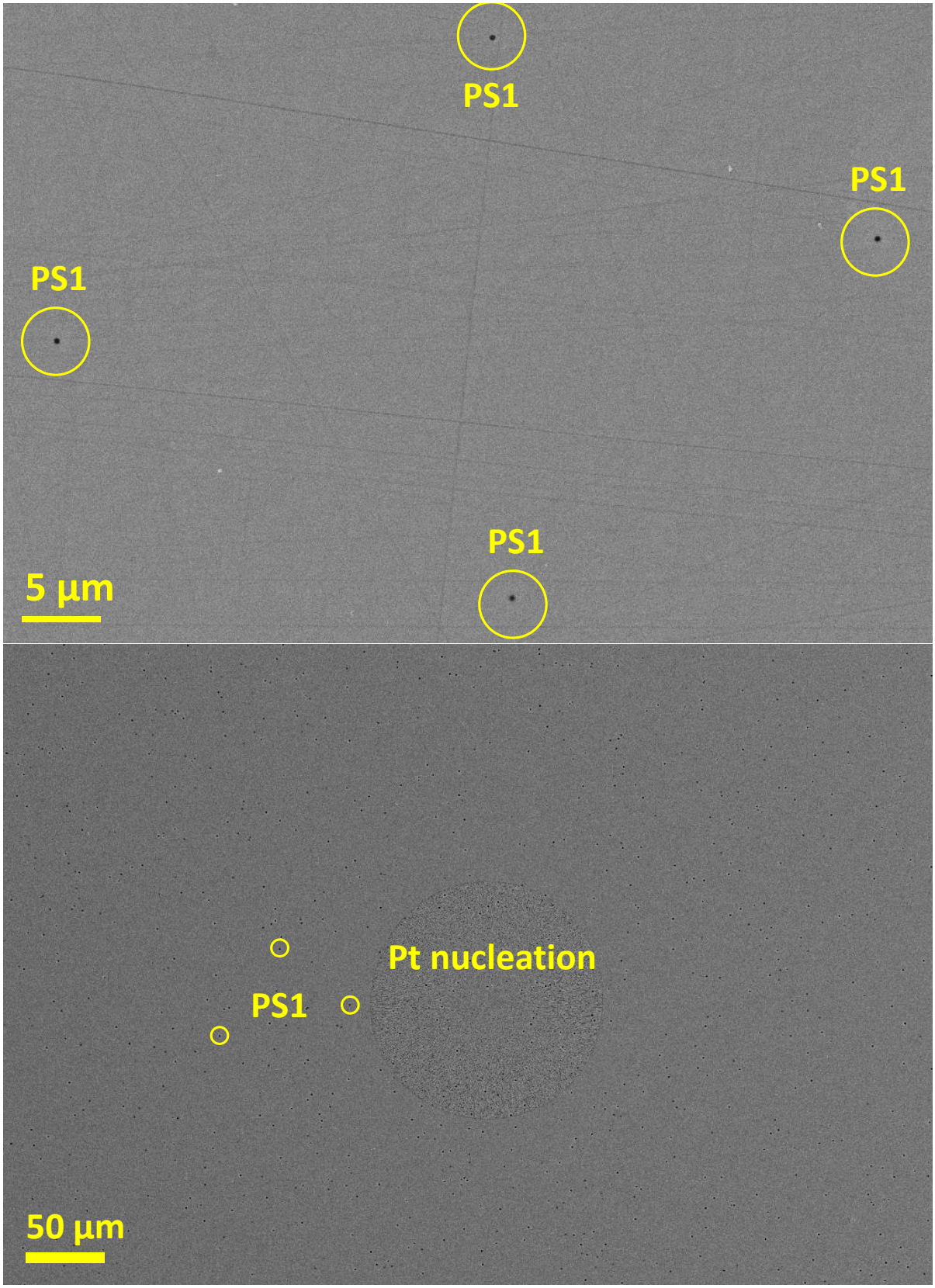

Figure 4.32: Top: glass-glass phase separation inside the glass 44685-1650 after heating below onset of crystallization (44685-1650DEH393: T_{cer} = 815 °C, t_{cer} = 10 h, T_g = 770 °C), bottom: Pt-nucleated crystal after ceramization at T_{cer} = 850 °C inside a phase separated glass

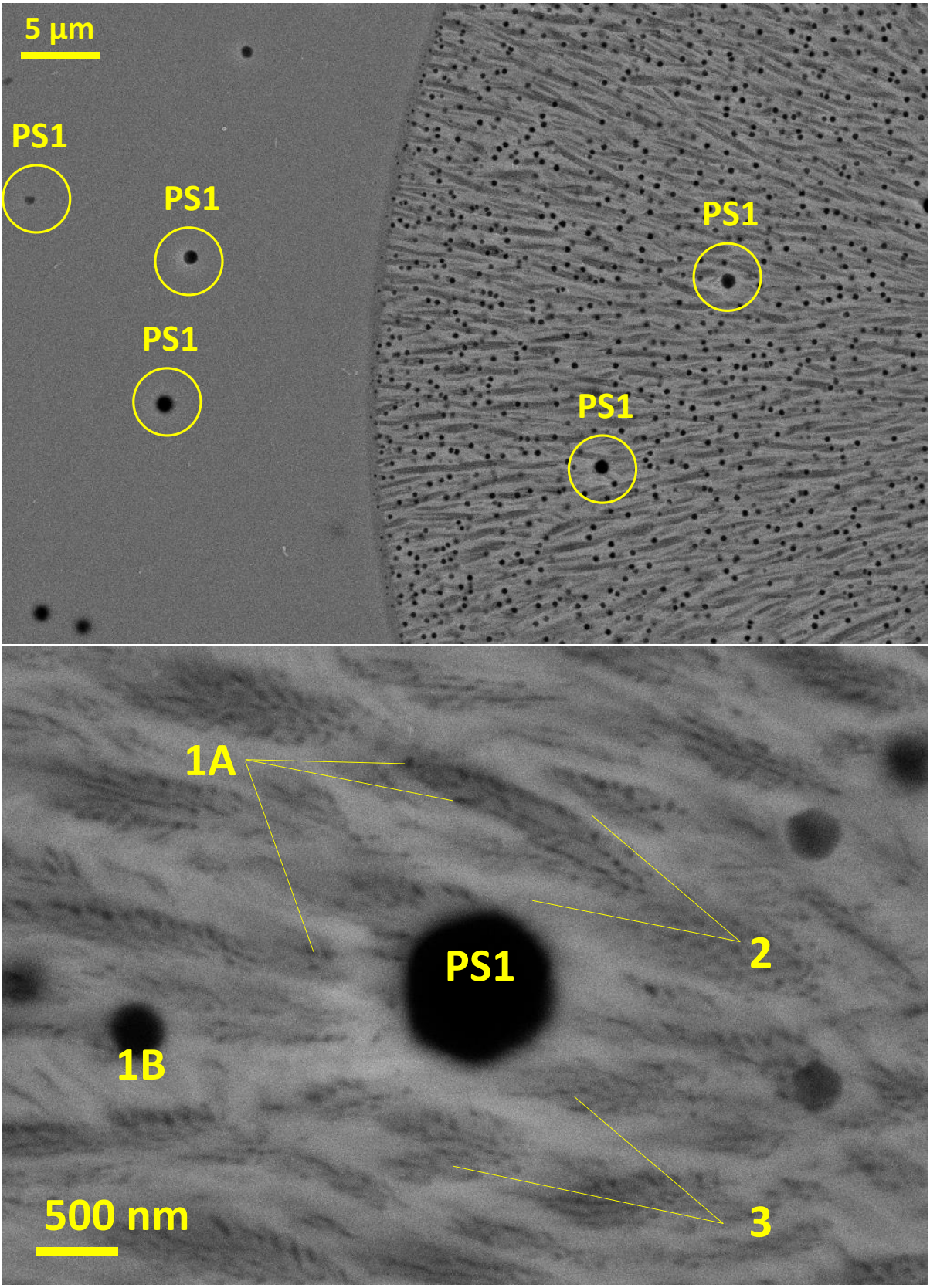

Figure 4.33: Magnification of fig. 4.32 (PS1,1A,1B: amorphous SiO_2, 2: $La_2Ti_2SiO_9$, 3: $La_4Ti_9O_{24}$)

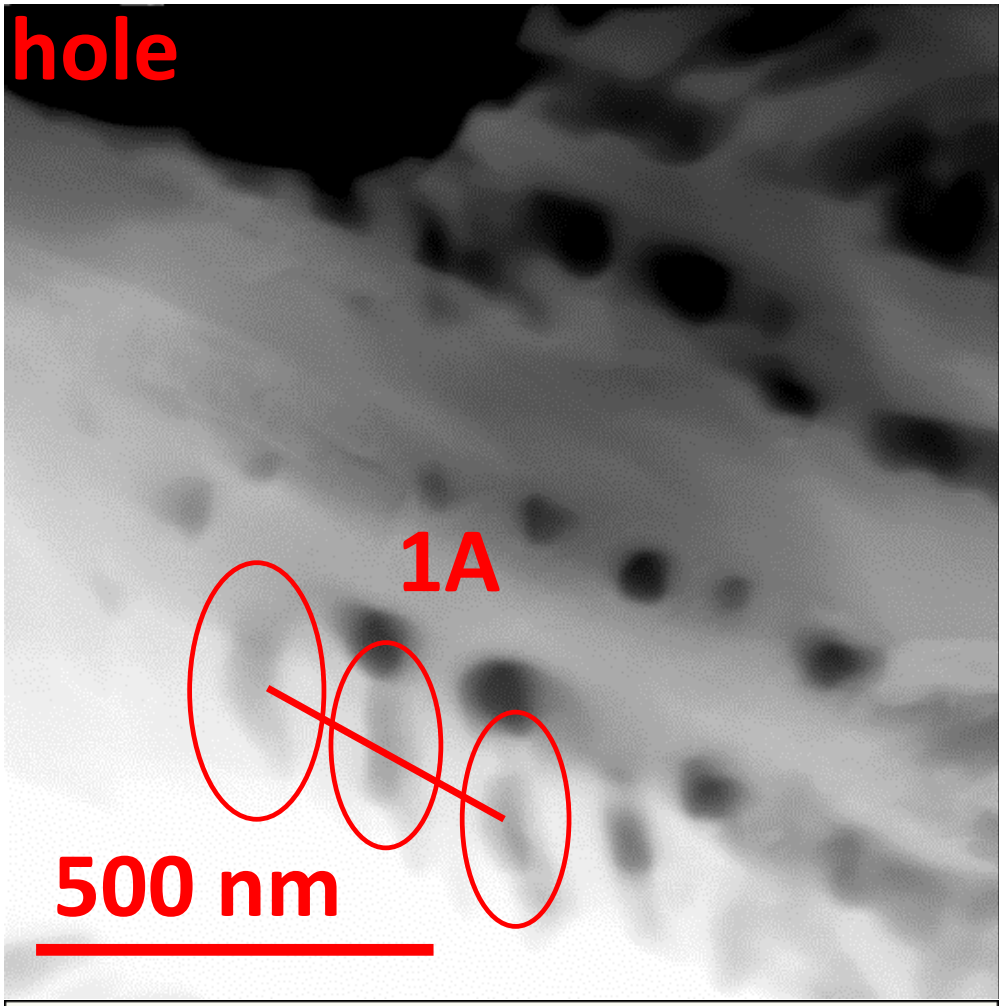

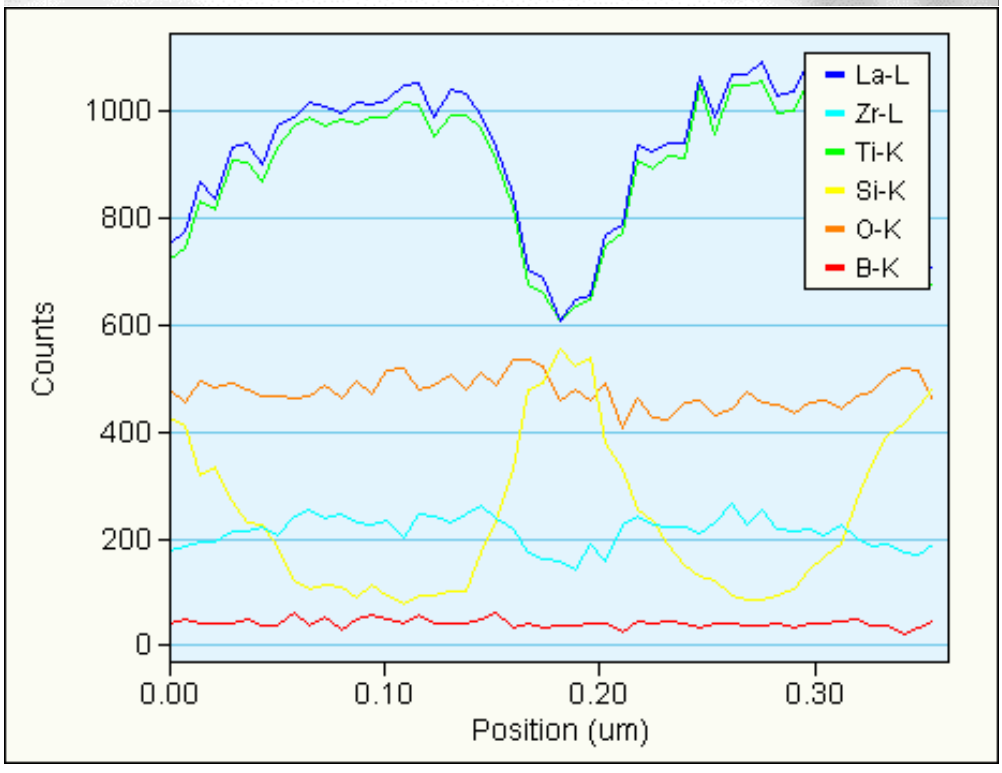

Figure 4.34: Dark field TEM/EDX line scan over one of the dendritic structures (see label 3 in fig. 4.33)

4.4 Selected melts

In this chapter the most relevant compositions are shown (see fig. 4.55). First the Ti^{3+} containing glasses are mentioned (42110, 42452, 43735; all 5.0 mol% ZrO_2 to prevent surface devitrification) and the influence of the Ti^{3+} formation on the dielectric properties will be discussed (error estimation given in chapter 3.9). Then the results of the oxidizing agent containing Ti^{3+}-free glasses will be summarized (43722: 0.1 mol% Sb_2O_5 and 7.5 mol% ZrO_2, 41760/42014/42732: all 1.0 mol% CeO_2 and 5.0/7.5/10.0 mol% ZrO_2). The standard ceramization program is given by tab. 4.9:

R1	Z1	H1	R2	Z2	H2	R3	Z3	H3	R4	Z4
200	T_{cer}	t_{cer}	40	750	0	20	550	0	40	20

Table 4.9: Standard ceramization program (abbr.: R: Rate [K/h], Z: holding temperature [°C], H: holding time [h])

Variations of the heating rate (R1) did not lead to any significant change in the crystallization behavior, as well as additional nucleation steps before the actual ceramization at T_{cer} (see fig. 2.3(b)). This is consistent with the results from the previous chapter as surface, Pt and Ti^{3+} nuclei are already present in the glass.

4.4.1 Ti^{3+} containing glasses (42110, 42452, 43735)

The glass-ceramic samples ceramized from Ti^{3+} containing glasses showed very similar dielectric properties over a broad ceramization temperature range (see fig. 4.35). For fully crystallized samples and T_{cer} between 850 to 950 °C the permittivity was around 27.5 in combination with a low Qf value of < 2000 GHz, even lower than the basic glass before the ceramization. XRD measurements showed that the samples all contain similar crystalline phases $La_2Ti_2SiO_9$ as main phase (relative content ≈ 65 wt%) and $LaBO_3$ (≈ 25 wt%) and TiO_2 (≈ 10 wt%) as minor phases. The comparatively large ε_r value is due to the presence of TiO_2. The results of the ceramization series 42110DEH are shown in tab. 4.10. The $La_4Ti_9O_{24}$ phase was only found in traces and the XRD intensities were too low for a Rietveld analysis. It seems that only $La_2Ti_2SiO_9$ is nucleated by Ti^{3+} and therefore the formation of $La_4Ti_9O_{24}$ is suppressed in Ti^{3+} containing glasses, even at low ceramization temperatures (850 to 900 °C) where $La_4Ti_9O_{24}$ is normally present as major phase in the investigated systems. For ceramization temperatures T_{cer} > 1000 °C the Qf value even decreased further, probably due to the formation of $LaBSiO_5$. This high temperature behavior was also observed in the other investigated systems. Regarding the measured

dielectric properties of the ceramized samples, the low Qf value is not obvious on first sight, as all 3 present crystalline phases have high Qf values (see tab. 2.5). One hypothesis, that the Ti^{3+} leads to an increased conductivity (see chapter 2.7.1) and thereby associated higher dielectric losses in the GHz region, could be disproved (see conductivity measurement in chapter 4.5.1). The most probable reason for the increased loss seems to be that the incorporation of the coupled $V_O^{\bullet\bullet}$-Ti^{3+} pair in the crystal lattice leads to an increased phonon damping/anharmonicity resulting in a higher dielectric loss after the model of Sparks (see fig. 2.23). Iddles et al. [IBM92] investigated the incorporation of different charged dopant ions on the Ti-site in low-loss sintered ceramics and came to the conclusion that the oxygen vacancy itself leads to the dominant decrease of Qf (see eq. (2.80)-(2.81) and also [FA08]). It also has to be mentioned that the Ti^{3+} content decreases during the ceramization process due to reoxidation far below the amount present in the glass (see fig. 4.12) and still a severe Qf deterioration is found. Even though these observations are consistent with results from other authors working on reduced titanate-based sintered ceramics indicating that already smallest amounts of Ti^{3+} can have a large influence on the dielectric loss (Templeton et al. [TWP+00] and Negas et al. [NYB+93], see end of chapter 2.7.2).

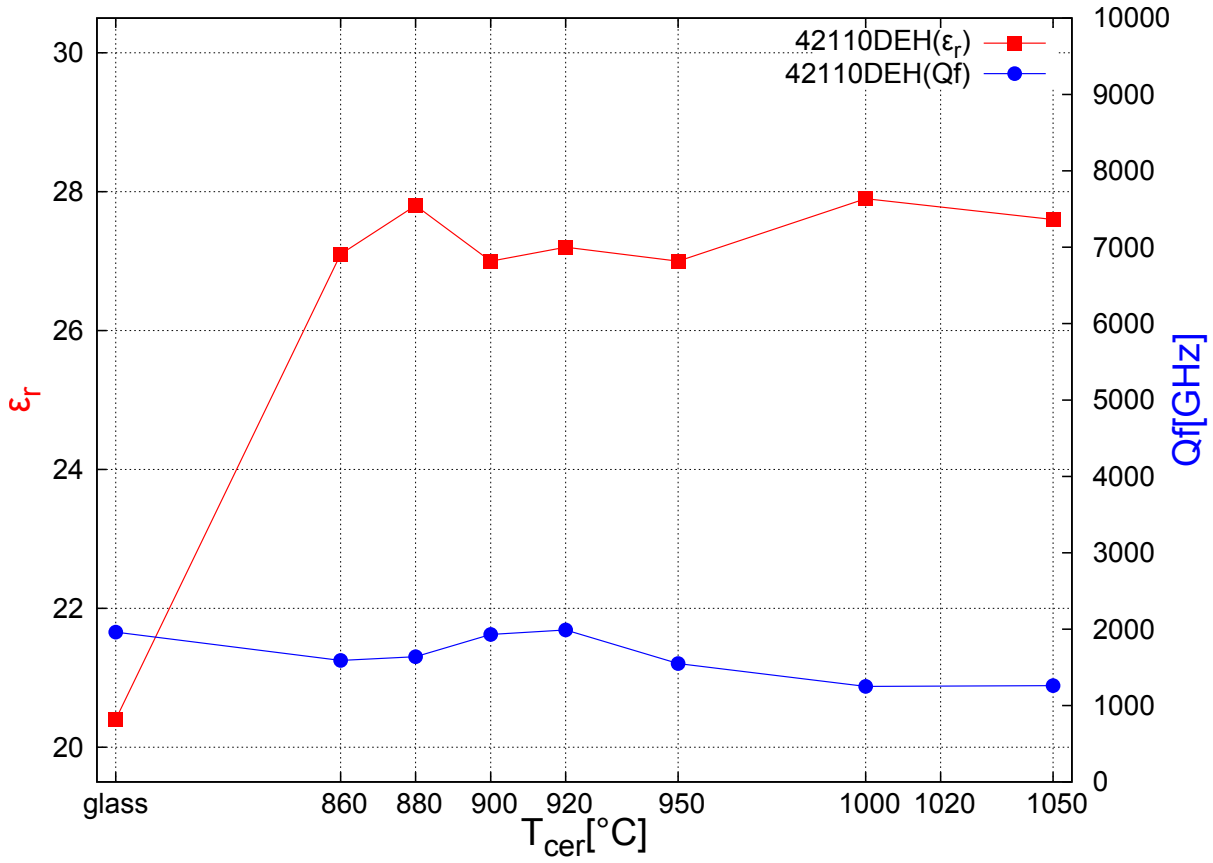

Figure 4.35: Dielectric properties of the ceramized samples 42110DEH (see tab. 4.10)

DEH(T_{cer}/t_{cer})	ε_r	Qf[GHz]	f[GHz]	L4	L2	TiO_2	LB	LBS
glass	20.4	1960	10.57					
357(860°C/50h)	27.1	1590	9.30					
260(880°C/20h)	27.8	1640	9.07	min	66.8	8.1	25.1	
261(900°C/20h)	27.0	1930	9.24	min	64.9	11.2	23.9	
310(920°C/20h)	27.2	1990	9.12	min	66.4	9.2	24.4	
257(950°C/5h)	27.0	1550	9.25		67.2	10.5	22.3	
258(1000°C/5h)	27.9	1250	9.05		60.3	11.4	15.9	12.4
259(1050°C/5h)	27.6	1260	9.13					

Table 4.10: Dielectric properties of the ceramized samples of 42110DEH (L4/L2/TiO_2/LB/LBS: relative percentage of the crystalline phases $La_4Ti_9O_{24}/La_2Ti_2SiO_9/TiO_2/LaBO_3/LaBSiO_5$ in wt% determined by Rietveld XRD analysis, min: minor amounts too low for evaluation)

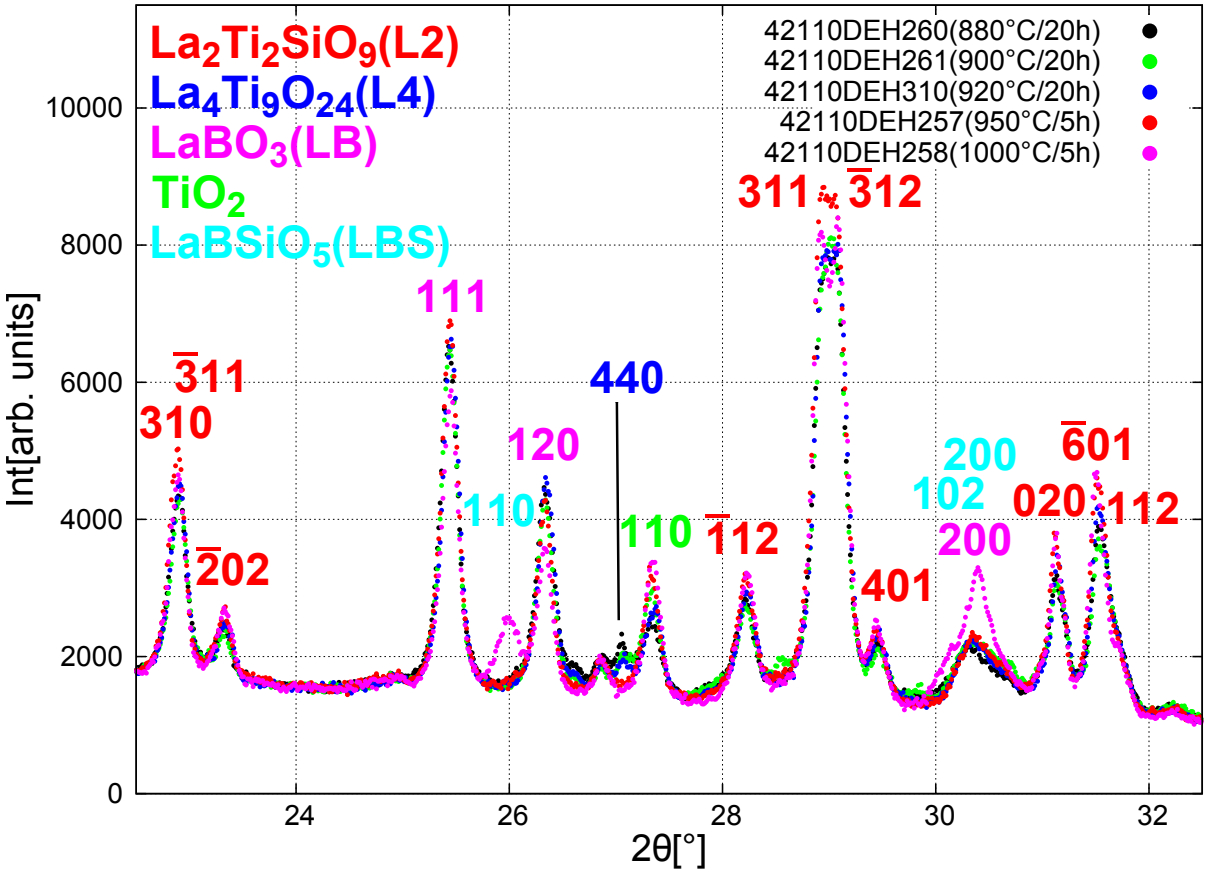

Figure 4.36: XRD diffractograms of the ceramized samples of 42110DEH (see tab. 4.10)

A melting series (42452) of 4 samples melted at different temperatures 1450, 1500, 1550, 1600 °C for a keeping time of 30 min (similar to 43529 described in chapter 4.3.3) has been made to investigate the influence of different amounts of Ti^{3+} on the dielectric properties and formed crystalline phases. In contrast to 43529 the glass

42452 does not contain any oxidizing agents and therefore a melting temperature dependent partial reduction of Ti^{4+} to Ti^{3+} takes place (see fig. 4.10). The 3 samples melted at 1450, 1500, 1550 °C show similar Ti^{3+}-based crystallization behavior and dielectric properties as the above presented 42110DEH ceramization series as can be seen in tab. 4.11 and fig. 4.37. It can be seen that the Qf value is not decreased below 1500 GHz which could be explained by assuming that the dominant $La_2Ti_2SiO_9$ phase only can incorporate a limited amount of $V_O^{\bullet\bullet}$-Ti^{3+} defect pairs.

T_m[°C]	ε_r	Qf[GHz]	τ_f[ppm/K]	L4	L2	TiO_2	LB
1450	26.9	1630	80	min	63.5	14.4	22.1
1500	26.8	1690					
1550	27.0	1600		0	65.3	12.7	22.0
1600	21.5	9710	16	55.2	24.0	0	20.8

Table 4.11: Dielectric properties of the ceramized samples of 42452 for different melting temperatures T_m (DEH325-328: T_{cer} = 900 °C, t_{cer} = 20 h). L4/L2/TiO_2/LB: relative percentage of the crystalline phases $La_4Ti_9O_{24}$/$La_2Ti_2SiO_9$/TiO_2/$LaBO_3$ in wt%

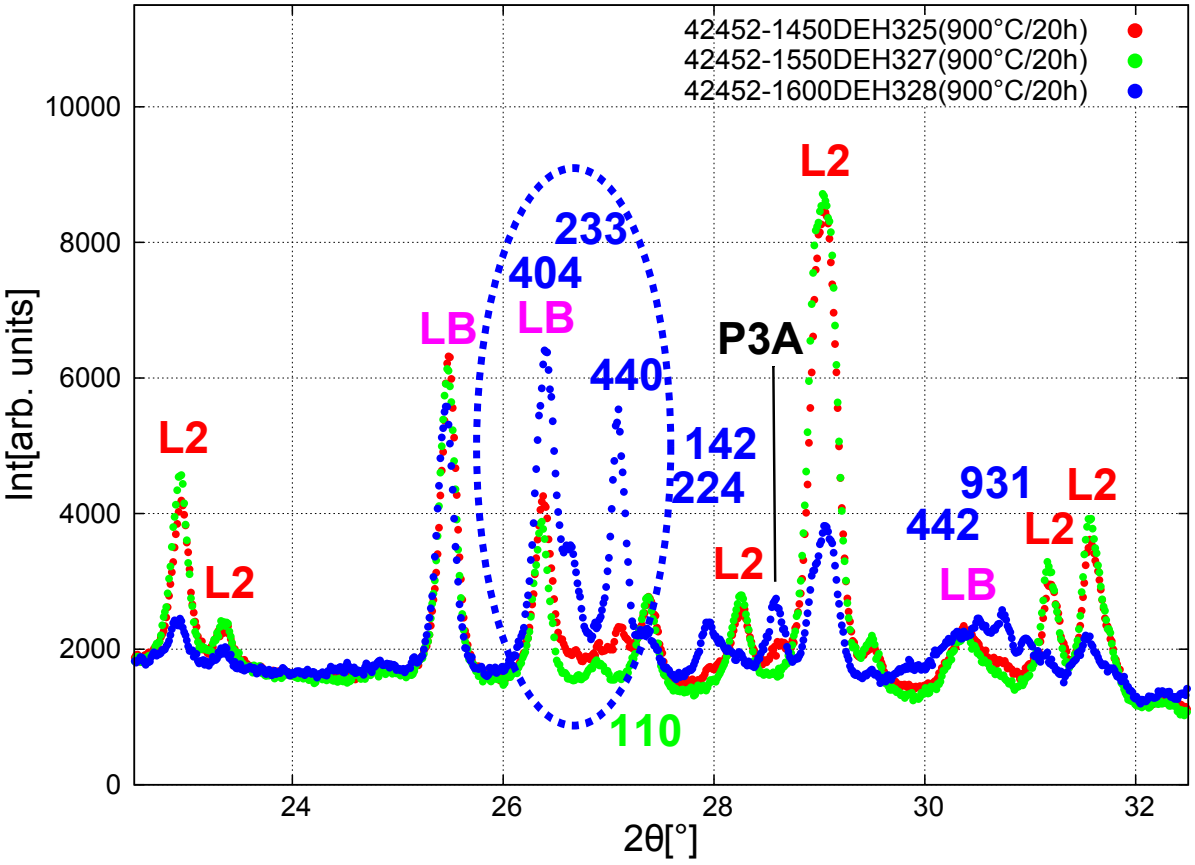

Figure 4.37: XRD diffractograms of the ceramized samples 42452DEH325-328 (see tab. 4.11)

The melt with the highest melting temperature shows a totally different crystallization behavior and is able to form $La_4Ti_9O_{24}$ as main phase in combination with an approximately 6 times larger Qf value than the 3 other samples, even despite its high amount of Ti^{3+} (highest of all 4 samples). On first sight this result is surprising, but can be understood by evaluation of the microscopic structure (see fig. 4.38-4.40). Due to the high melting temperature the Pt content reaches such a high level that the Pt nucleation becomes dominant over the Ti^{3+} nucleation and therefore the crystallization of $La_2Ti_2SiO_9$ is significantly reduced. Additionally it is concluded that the high Qf value of $La_4Ti_9O_{24}$ is not affected by the presence of Ti^{3+}. The glass 43735 was melted similar to 42452 with 4 different temperatures 1450, 1500, 1600, 1650 °C whereby the latter two showed a dominant Pt nucleation. With increasing T_{cer} the $La_4Ti_9O_{24}$ becomes less stable and the $La_2Ti_2SiO_9$ becomes dominant leading to an increase in the dielectric loss, as can be seen in fig. 4.41.

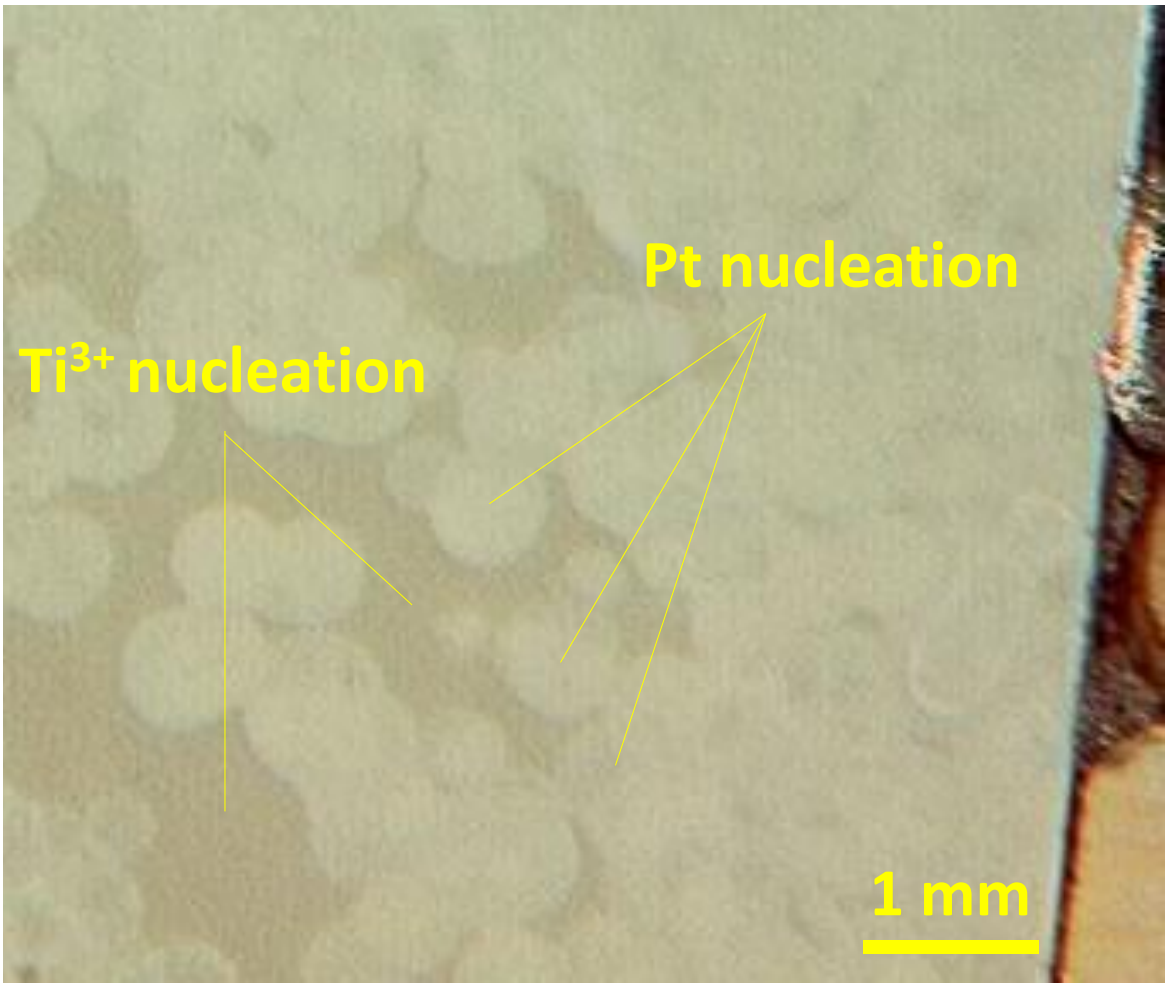

Figure 4.38: Optical microscope image of 42452-1600DEH328 showing two different crystallization areas: isotropic Ti^{3+}-nucleated and dendritic crystal growth caused by Pt nucleation

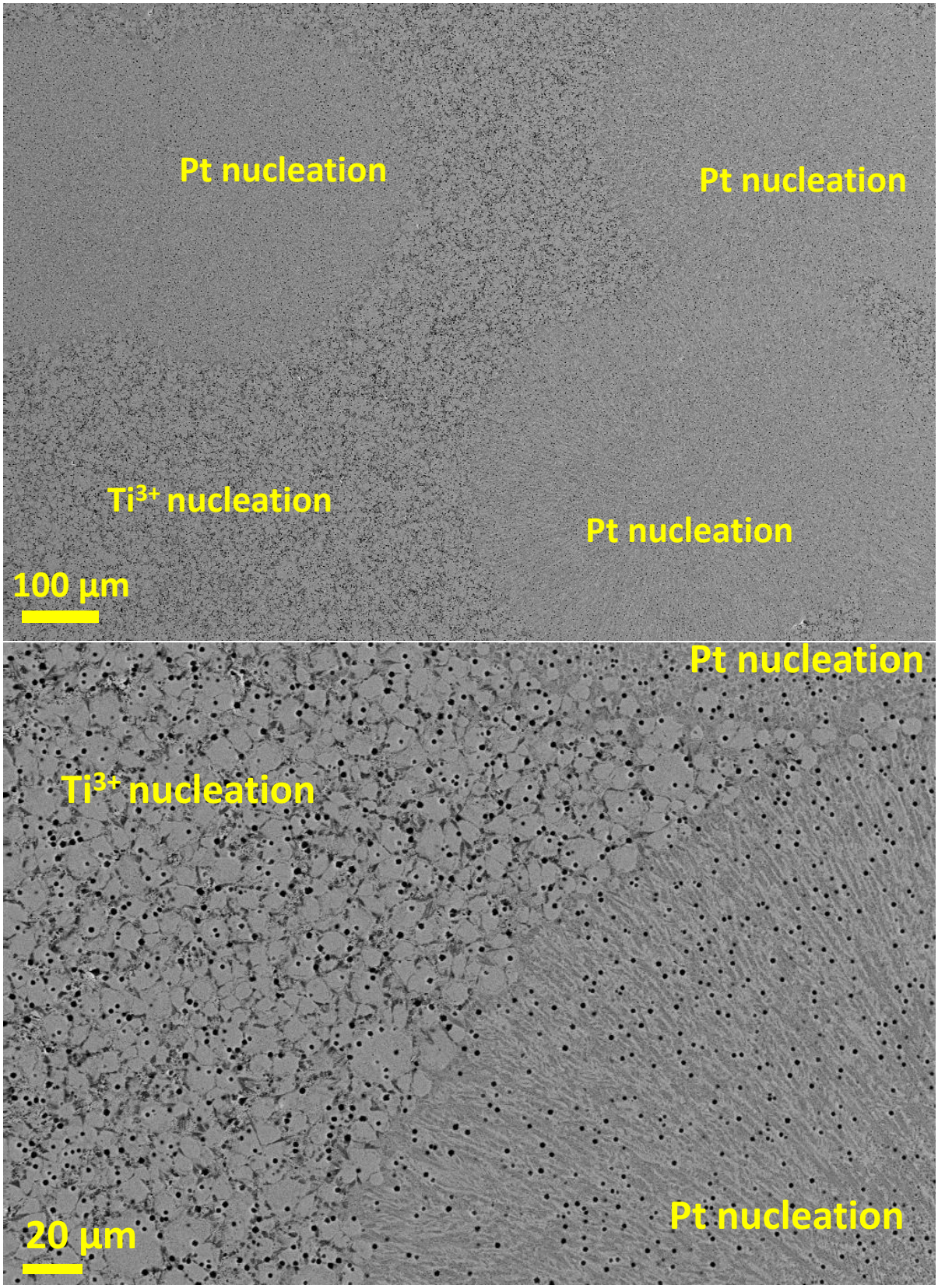

Figure 4.39: SEM magnification of fig. 4.38

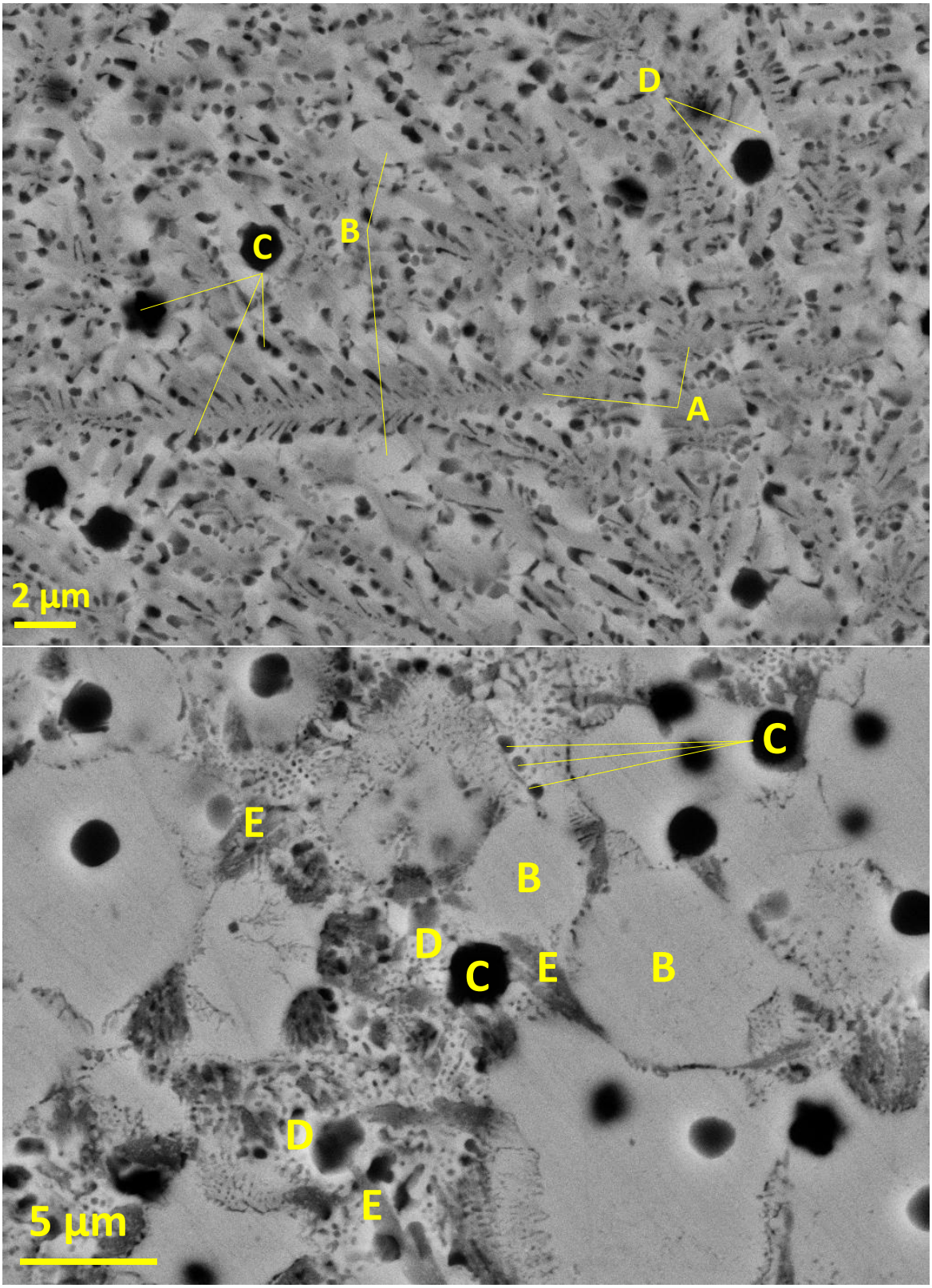

Figure 4.40: Magnification of the Pt nucleation zone (top) and the Ti^{3+} nucleation zone (bottom), A: $La_4Ti_9O_{24}$, B: $La_2Ti_2SiO_9$, C: SiO_2, D: $LaBO_3$, E: TiO_2

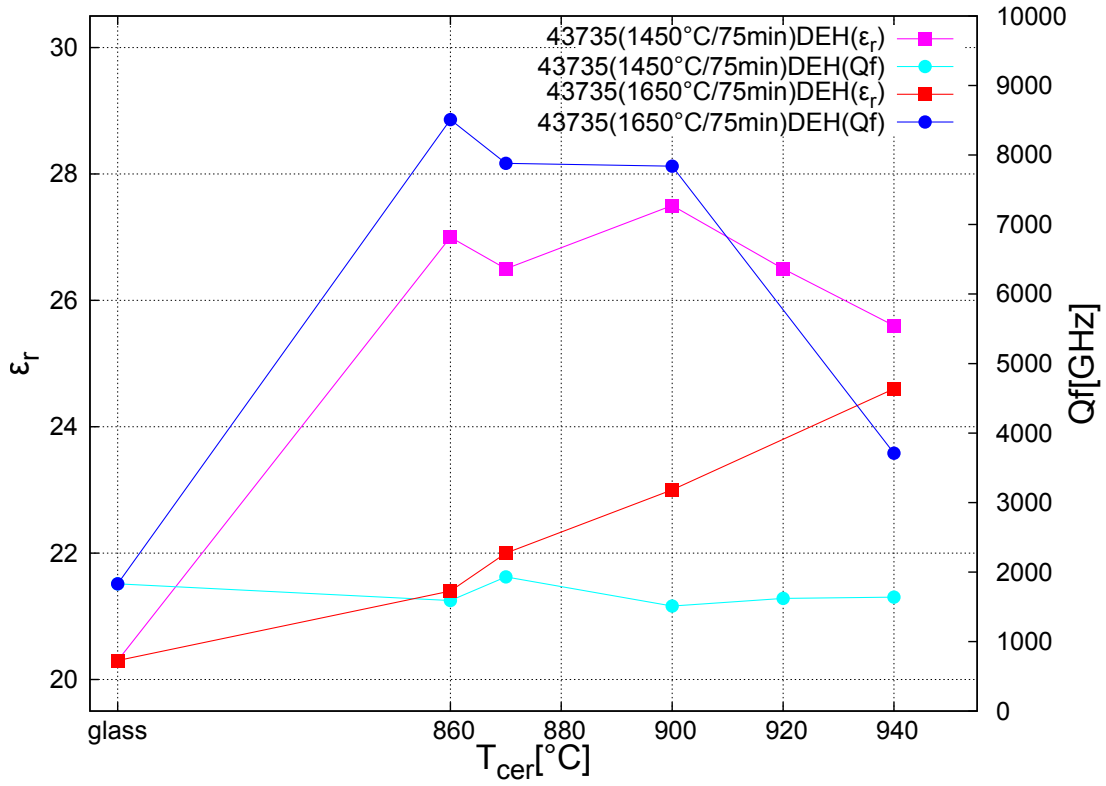

Figure 4.41: Difference in the dielectric properties of the ceramized samples of 43735DEH due to the different nucleation/crystallization behavior

The oxides which are not incorporated in the main crystalline phases (B_2O_3 and remaining SiO_2 and La_2O_3 are swept to the grain boundaries by diffusion and form minor phases like amorphous SiO_2 or crystalline $LaBO_3$ as can be seen in fig. 4.40. Sample 42110DEH257 has been used to estimate the absolute amount of residual glass phase (APC) inside the ceramized glass-ceramic. Therefore the sample is mixed at a 1:1 ratio (wt%) with a reference standard and then the relative difference between reference (REF) and sum of all crystalline phases (CPC) is determined via Rietveld analysis. APC can then be determined by APC + CPC + REF = 100 % (for known CPC/REF and REF = 50 %). The results for different reference materials are shown in tab. 4.12. The amount of crystalline phase is probably underestimated and for different reference materials the values also differ quite much. A reason could be the large difference in the average mass number and therefore X-ray absorption coefficient of the sample and the reference standard.

Ref. st.	CaF_2	ZnO	SnO_2
CPC[wt%]	32.6	33.6	52.8

Table 4.12: CPC: crystal phase content, ref. st.: reference standard for Rietveld determination of the amorphous phase content of the glass-ceramic

4.4.2 Doping with 0.1 mol% Sb_2O_5 and 7.5 mol% ZrO_2 (43722)

In chapter 4.2 it has been shown that Sb doping is suitable to prevent the Ti^{3+} formation in the glass. Unfortunately Sb^{5+}-ions are able to substitute for Ti^{4+} in the crystalline phases due to their similar ionic radius which is associated with the formation of Ti^{3+} due to the necessity of charge compensation (see chapter 2.7.1). Additionally the Ti^{3+} formed due to Sb^{5+} is not coupled to an oxygen vacancy, so that a reoxidation during the ceramization does not occur. In fig. 4.42 the increase of Ti^{3+} can be seen by EPR analysis. The Ti^{3+}-free glass (43722) shows no EPR signal, whereby the signal intensity strongly increases during the ceramization process. A prove that the Ti^{3+} is dominantly present in the crystalline phase is given by the fact that the shape of the signal is less broadened (similar to the Ti_2O_3 signal, see fig. 4.7) and its g value of 1.967 is representative for a crystalline environment ($g_{Ti_2O_3}$ = 1.966).

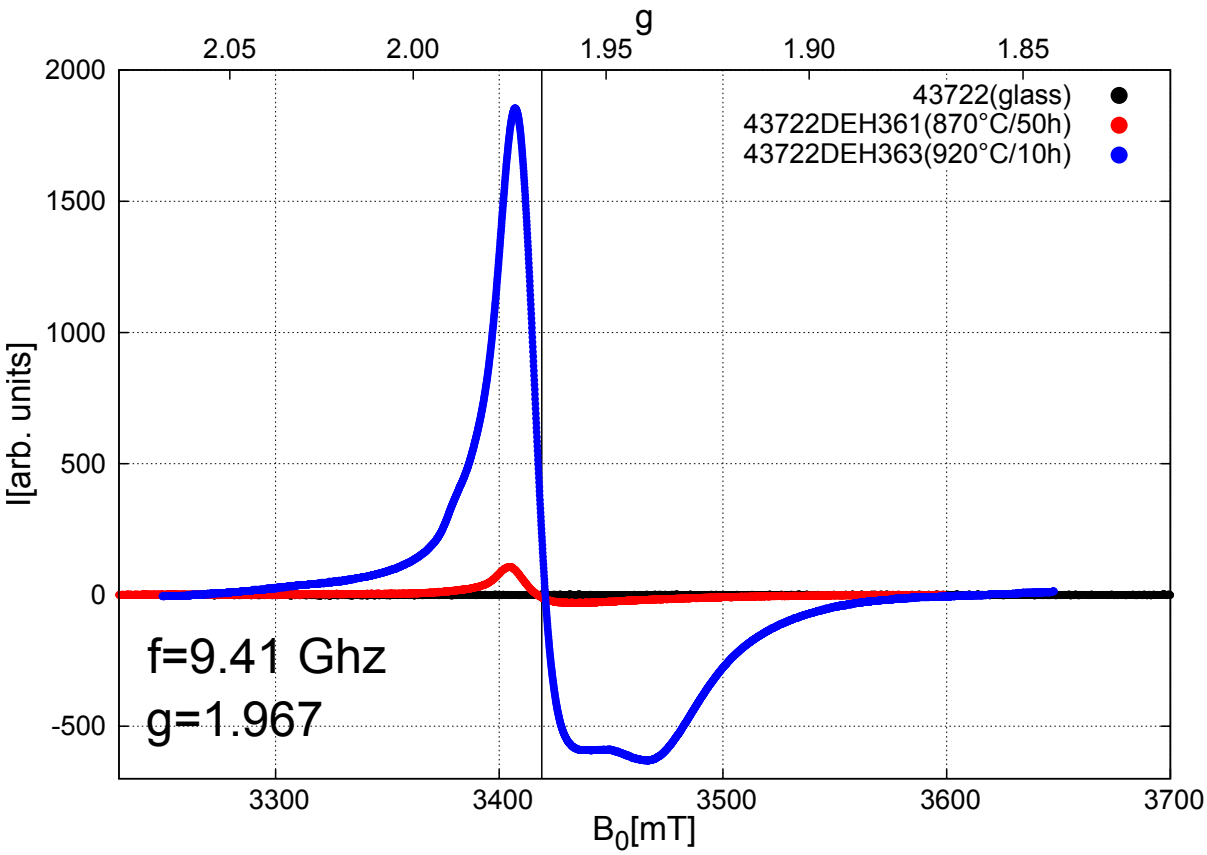

Figure 4.42: EPR measurement of glass 43722 (doped with 0.1 mol% Sb_2O_5) before and after ceramization, showing a less broad EPR peak in comparison to the investigated amorphous systems and also a shifted g value (1.967)

The glass 43722 was ceramized at different temperatures (see tab. 4.13) and all glass-ceramic samples showed comparatively high dielectric loss values. In some case the Q values were below the detection limit of the Hakki-Coleman setup ($\tan(\delta) \gtrsim 2 \cdot 10^{-2}$).

DEH(T_{cer}/t_{cer})	ε_r	Qf[GHz]	f[GHz]
glass	20.4	1790	10.58
357(860°C/50h)	21.5	1300	10.44
361(870°C/50h)	21.4	1570	10.36
366(900°C/15h)		< 500	
363(920°C/10h)		< 500	
376(940°C/5h)		< 500	

Table 4.13: Dielectric properties of the ceramized samples of 43722DEH

In contrast to the investigated glasses in the chapter above, the high Ti^{3+} content in the crystal leads to a significant increase of the conductivity (see fig. 4.43) and thereby also becomes the dominant dielectric loss contribution in the GHz range. Additionally no oxygen vacancies are coupled with the Ti^{3+} ions, so that the loss contribution due to increased phonon damping should be less severe. In fig. 4.43 a comparison of the conductivity of 43722 before and after ceramization is shown.

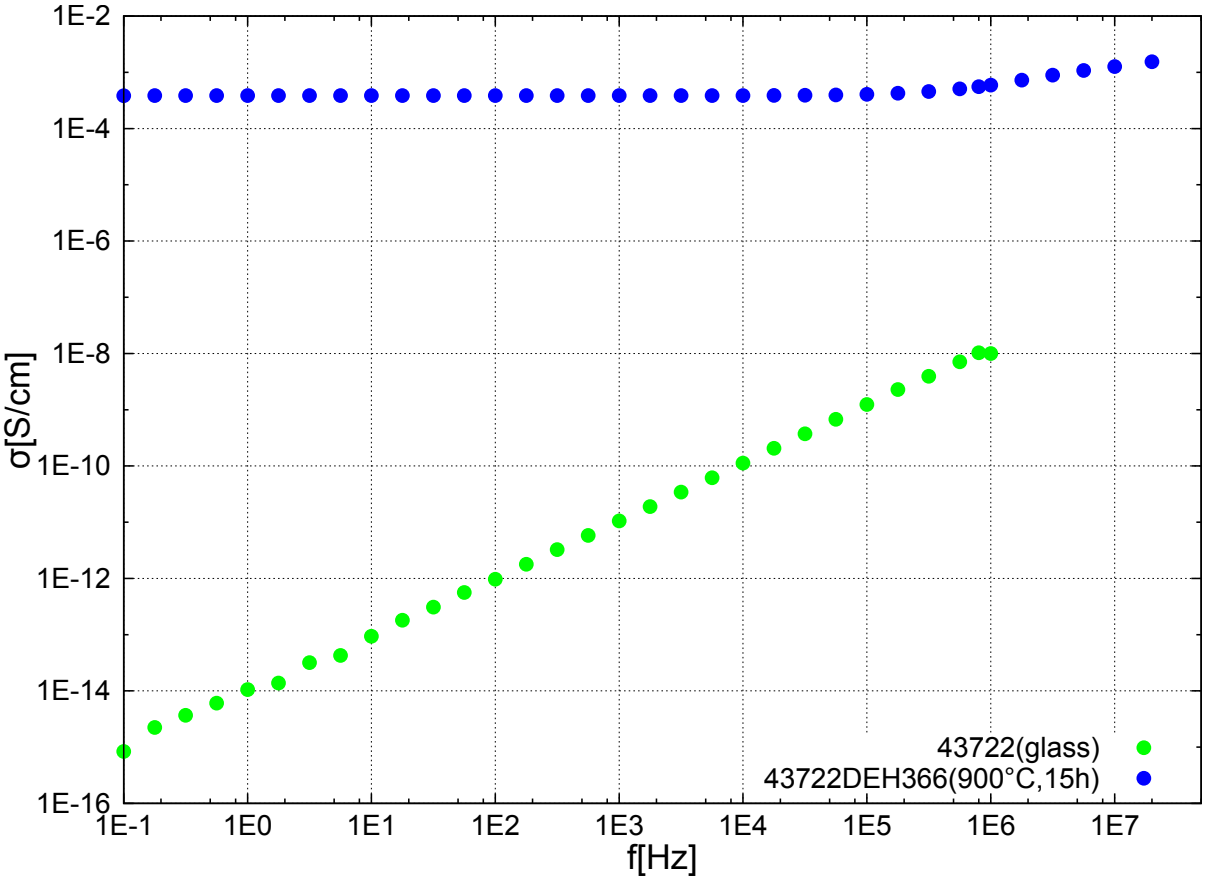

Figure 4.43: Room temperature conductivity measurement of a Sb-doped glass (43722: 0.1 mol% Sb_2O_5) before and after ceramization (see fig. 2.21), showing a huge increase in conductivity due to the incorporation of Sb^{5+} on the crystal lattice and the associated formation of Ti^{3+}

The conductivities of glass and glass-ceramic follow the Jonscher model (see eq. (2.63)). The glass-ceramic (43722DEH366) shows a much larger DC contribution which is characteristic for small polaron hopping processes as in the case of polyvalent ion containing glasses (see fig. 2.20(b)). The room temperature conductivity was fitted according to eq. (2.63) ($\sigma_{DC} = 3.85 \cdot 10^{-4}$ S/cm, $\sigma_0 = 6.5 \cdot 10^{-6}$ S/cm Hz^{-s}, $s = 0.33$) and the conductivity extrapolated to the GHz region leading to $\sigma_{ex} = 1.2 \cdot 10^{-2}$ S/cm resp. $\tan(\delta)_{ex} = 9.7 \cdot 10^{-2}$ at $f = 10$ GHz (calculated via eq. (2.32), estimated $\varepsilon_r = 22$). The extrapolated values are consistent with the loss measurements in the GHz range and also indicate that the conductivity caused by Ti^{3+} gives the dominant contribution to the $\tan(\delta)$ in the microwave frequency range.

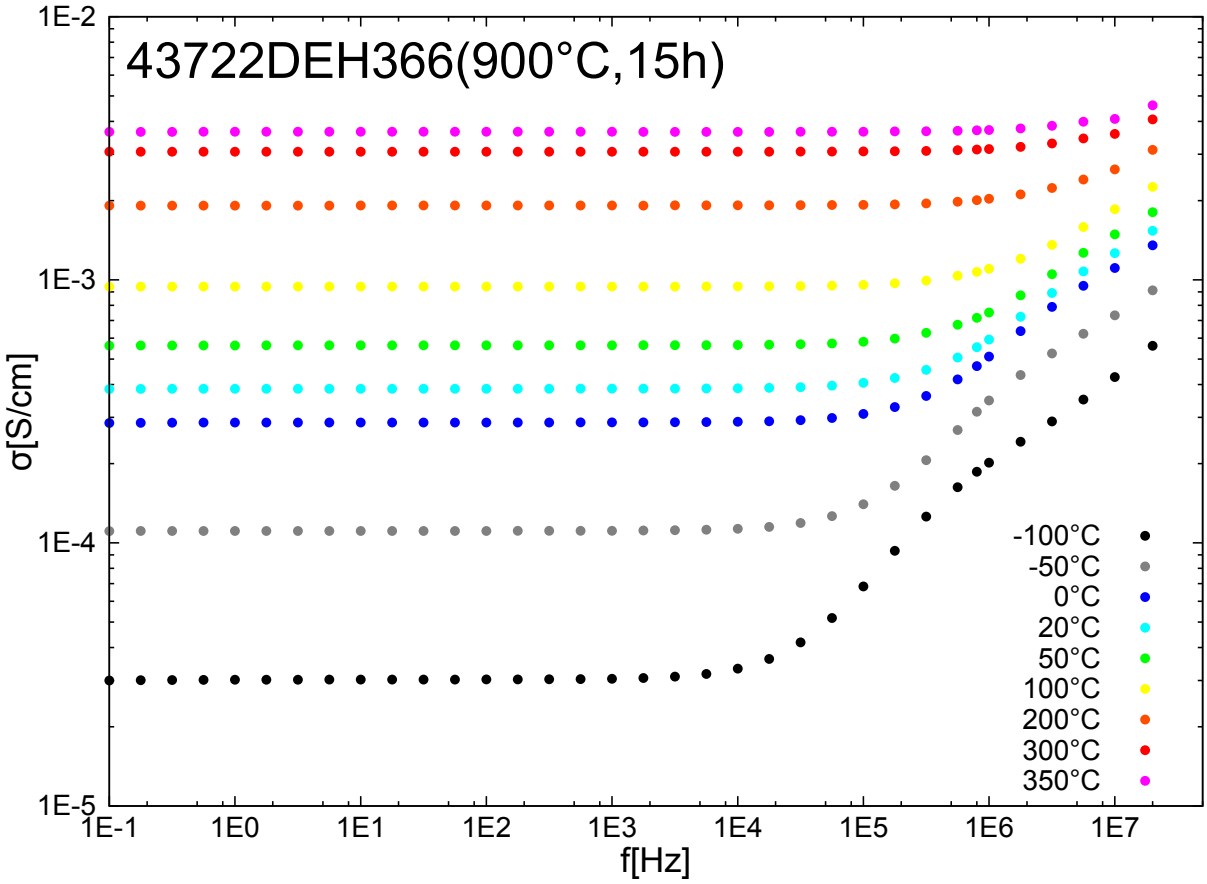

Figure 4.44: Frequency dependent conductivity for different temperatures of the Ti^{3+} containing glass-ceramic (43722DEH366)

In tab. 4.14 a comparison is shown between the dielectric properties of two glass-ceramics from the same basic glass which were ceramized by the same ceramization program (T_{cer} = 870 °C, t_{cer} = 50 h) but contain different oxidizing agents (43722: 0.1 mol% Sb_2O_5 and 42014: 1.0 mol% CeO_2). The Qf value of the equivalent CeO_2 containing glass-ceramic 42014DEH373 is approximately 6 times higher.

Sample(T_{cer}/t_{cer})	Dopant	ε_r	Qf[GHz]
43722DEH361(870°C/50h)	0.1 mol% Sb_2O_5	21.4	1570
42014DEH373(870°C/50h)	1.0 mol% CeO_2	21.4	9170

Table 4.14: Comparison between two glass-ceramics from the same basic glass and same ceramization program containing different dopants

The crystalline phases in 43722DEH366 were analyzed by XRD/SEM (see fig. 4.45) and were shown to be similar to 42014DEH373 (the identification of the phases of the XRD diffractogram will be done in chapter 4.4.4).

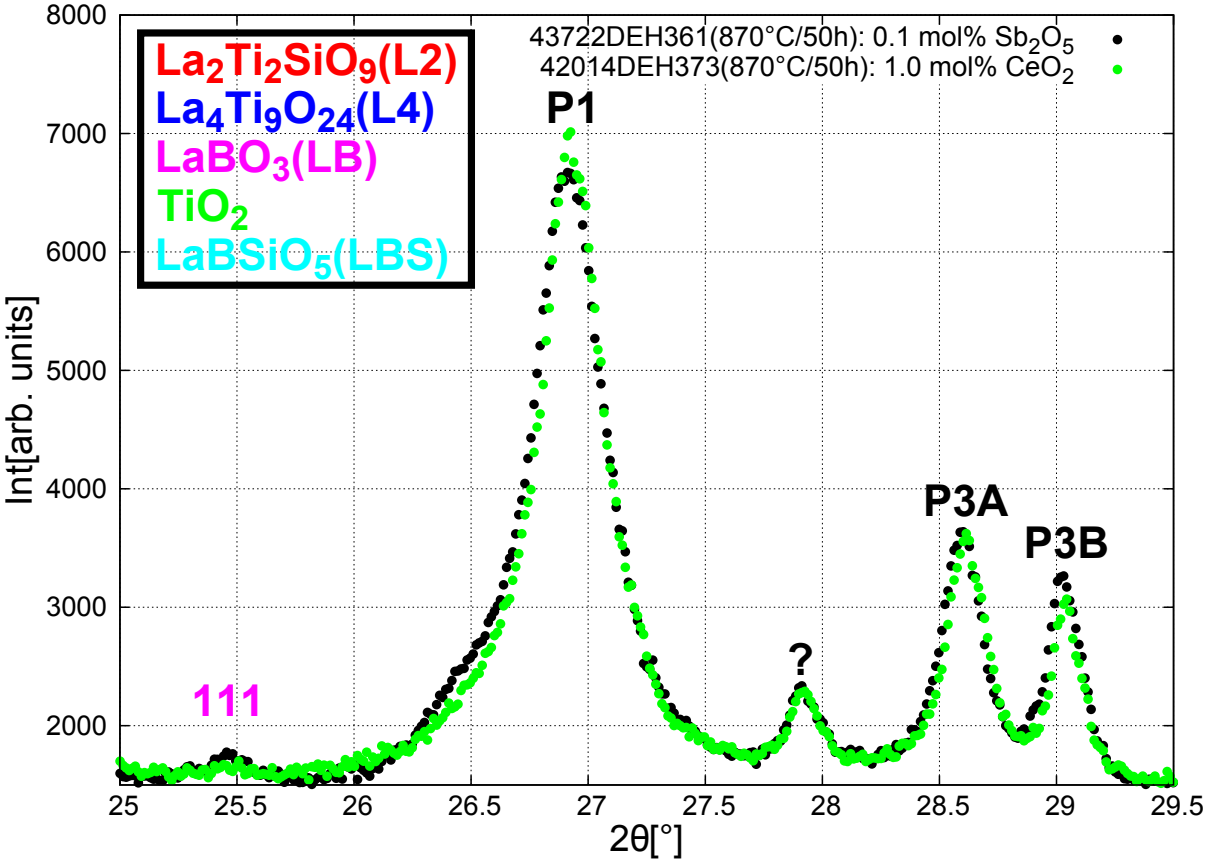

Figure 4.45: Comparison of the XRD diffractograms of the samples of 43722DEH373 and 42014DEH373 (both: T_{cer} = 870 °C and t_{cer} = 50 h)

In conclusion, it can be stated that Sb_2O_5 is not suitable as oxidizing agent for low-loss titanate-based glass-ceramic systems. Despite its ability to prevent the formation of Ti^{3+} in the glass, it leads to a severe increase of the dielectric loss respectively conductivity when its substituted on the Ti-site of the crystalline phases inside the glass-ceramic during the ceramization process.

4.4.3 Doping with 1.0 mol% CeO_2 and 5.0 mol% ZrO_2 (41760)

To prevent the formation of Ti^{3+} and its negative influence on the Qf value of the glass-ceramic, an alternative oxidizing agent (CeO_2) was used (see chapter 4.2). The composition of 42110 was modified and 1.0 mol% of the present $LaO_{1.5}$ was replaced by CeO_2, as in the glass dominantly Ce^{3+} is present which has a similar ionic radius and chemical behavior as La^{3+}. No increase in conductivity due to CeO_2 doping has been observed in contrast to the use of Sb_2O_5 (see explanation in chapter 2.7.1).

DEH(T_{cer}/t_{cer})	ε_r	Qf[GHz]	τ_f[ppm/K]	f[GHz]
glass	20.4	1840	-79	10.57
227(860°C/100h)	23.5	3670	33	9.63
228(870°C/100h)	23.3	3860		9.64
244(880°C/20h)	23.3	3800		9.94
231(890°C/10h)	23.1	3900	38	9.67
292(900°C/10h)	23.3	3880		9.91
236(910°C/5h)	23.4	3840		9.91
331(920°C/10h)	23.8	4430	58	9.77
237(930°C/5h)	25.0	3790		9.58
238(950°C/5h)	26.3	3700		9.37
239(980°C/5h)	27.9	2180		9.09
251(1000°C/5h)	27.2	1770		9.19
241(1020°C/5h)	27.9	1230		9.12
253(1050°C/5h)	27.8	1270		9.06
254(1100°C/5h)	28.2	1300		9.02

Table 4.15: Dielectric properties of the ceramized samples of 41760DEH

In tab. 4.15 and fig. 4.47 the results of the dielectric characterization of the ceramization series 41760DEH are summarized. Fig. 4.48 shows the XRD diffractograms of the samples. Due to the appearance of at least two unknown phases (labeled as P1 and P3A/P3B) a Rietveld analysis with sufficient accuracy was not possible anymore which makes it impossible to predict relative changes of the phases. Therefore the intensity values of the characteristic XRD main peaks of the present phases were used to describe the temperature behavior during the ceramization process (see tab. 4.16). In fig. 4.46 the normalized values of tab. 4.16 are summarized. At low ceramization temperatures T_{cer} = 860-910 °C the dielectric properties are dominated by the presence of $La_4Ti_9O_{24}$ and $La_2Ti_2SiO_9$ as major phases and a minor amount of $LaBO_3$ which is present over the complete temperature range up to T_{cer} = 1000 °C. The presence of both main phases results in a permittivity value of around 23.5 with a Qf value around 4000 GHz and τ_f around 35 ppm/K, which already is an improvement to the Ti^{3+} containing system but is still slightly below the requirements for Qf (Qf > 5000

GHz) and τ_f (τ_f < 20 ppm/K). For T_{cer} > 920 °C ε_r and τ_f start to increase due to the formation of TiO_2 and the $La_4Ti_9O_{24}$ phase starts to destabilize accompanied by a decrease in Qf while $La_2Ti_2SiO_9$ increases, similar to fig. 4.41. At temperatures above T_{cer} > 980 °C the formation of $LaBSiO_5$ begins probably as $LaBO_3$ + SiO_2 → $LaBSiO_5$, leading to a further reduction of Qf. The unknown phases P1/P3 will be discussed in the following chapters as they are present only in minor amounts in 41760DEH.

DEH(T_{cer}/t_{cer})	L4	L2	TiO_2	LB	LBS	P1
227(860°C/100h)	3250	3400	0	2500	0	2000
231(890°C/10h)	3300	3600	0	2700	0	1500
292(900°C/10h)	3300	3700	0	4000	0	800
331(920°C/10h)	3150	3700	500	4300	0	0
238(950°C/5h)	1700	4900	1600	4100	0	0
239(980°C/5h)	800	4900	2300	4000	0	0
251(1000°C/5h)	0	6500	2500	4300	800	0
253(1050°C/5h)	0	7100	2800	1700	2700	0
254(1100°C/5h)	0	7100	3600	1400	4100	0
2Θ(peak)	27.17	29.14	27.45	25.49	26.13	26.92
hkl(peak)	440	$\bar{3}12$	110	111	110	

Table 4.16: 41760DEH XRD main peak intensities in dependence of T_{cer} (abbreviations analog to tab. 4.10)

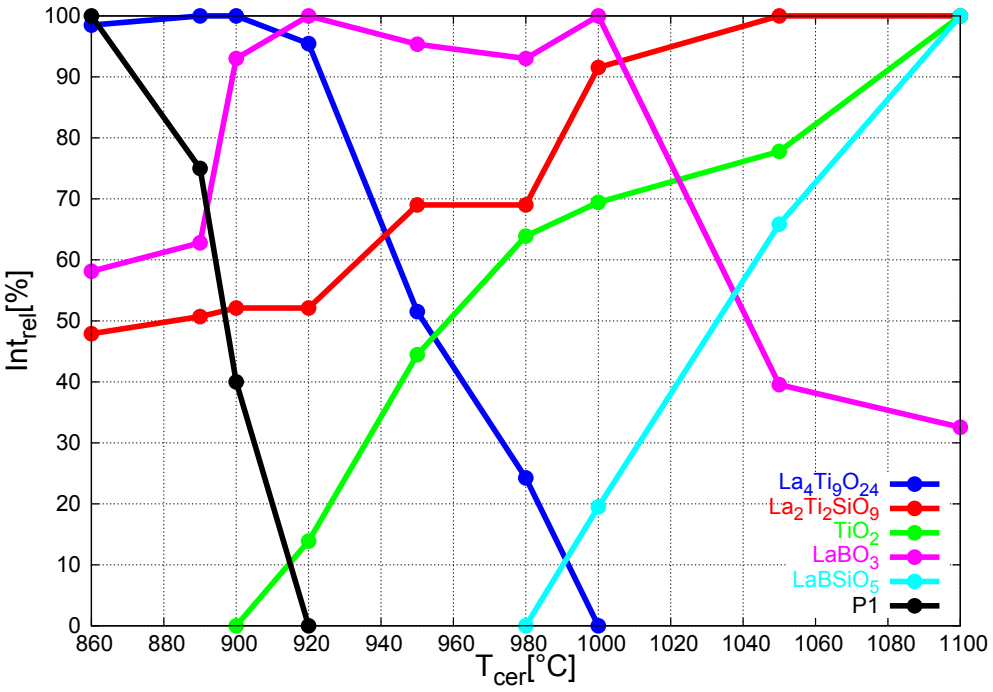

Figure 4.46: Illustration of tab. 4.16 (the intensity values are normalized on the highest intensity for every phase)

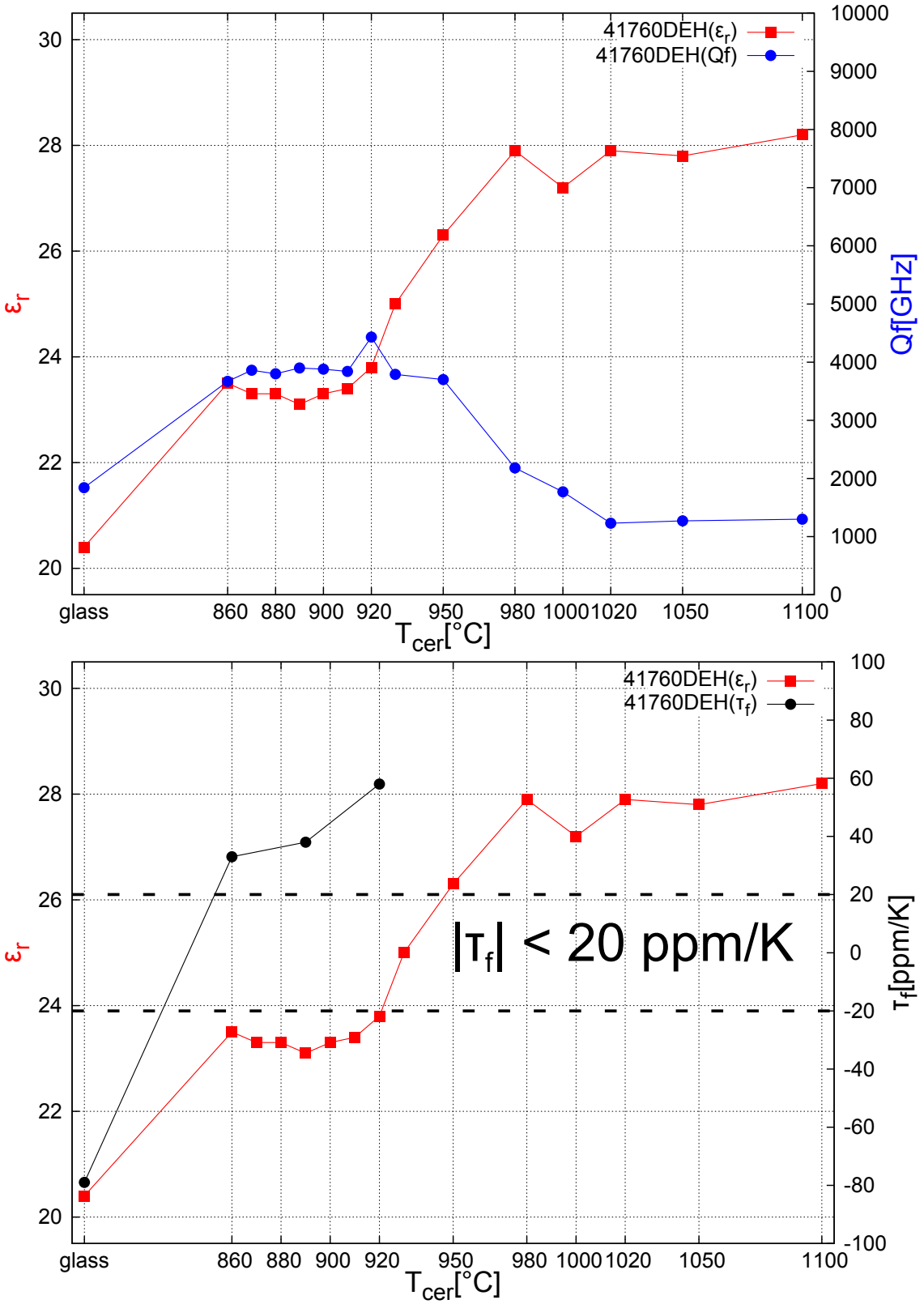

Figure 4.47: Dielectric properties of the ceramized samples 41760DEH according to tab. 4.15 (top: ε_r and Qf, bottom: ε_r and τ_f)

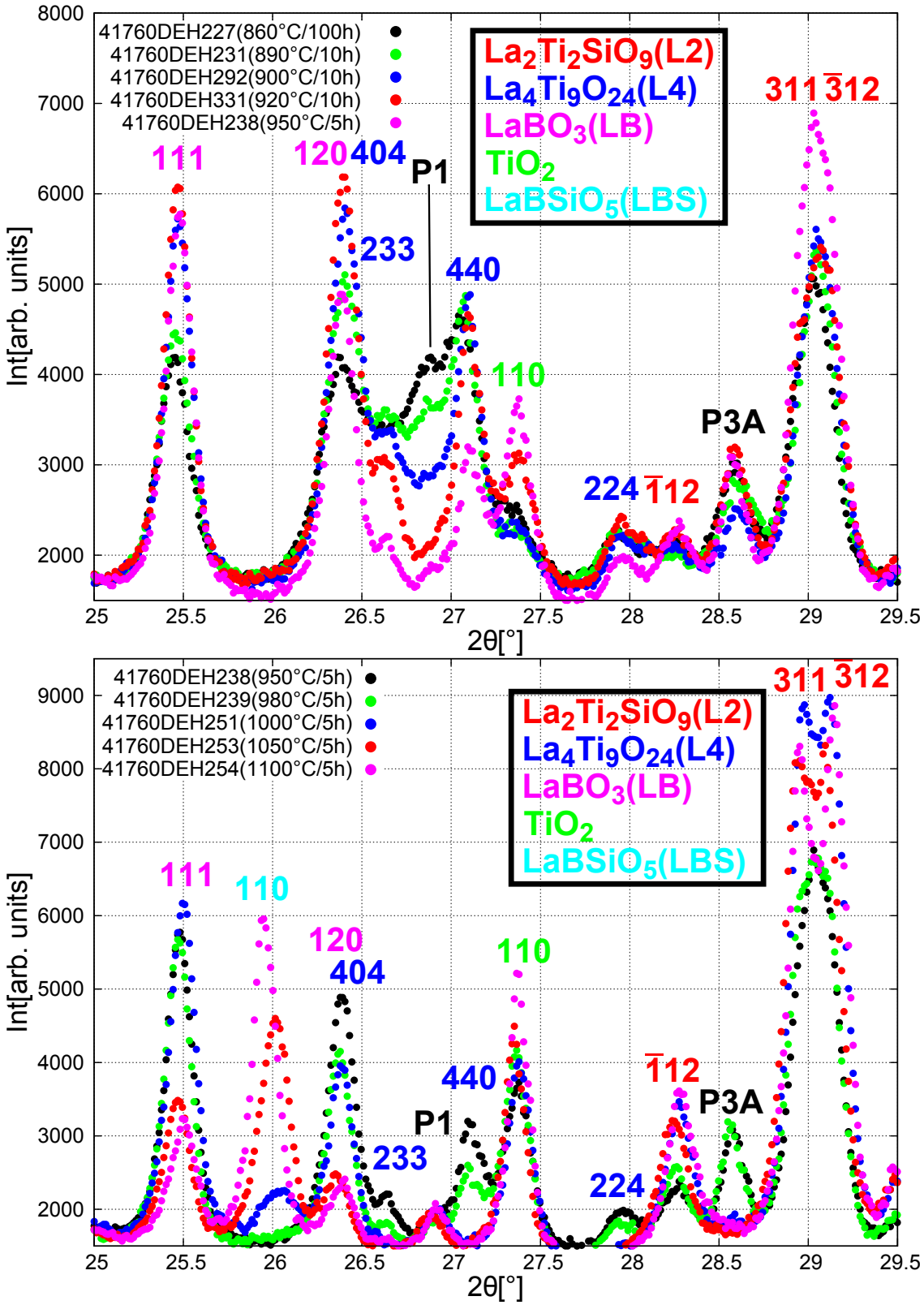

Figure 4.48: XRD diffractograms of the ceramized samples 41760DEH (top: T_{cer}: 860-950 °C, bottom: T_{cer}: 950-1100 °C)

In conclusion it has to be stated that 41760DEH showed improved dielectric properties due to the prevention of Ti^{3+} but due to the multiplicity of existing crystalline phases in all temperature ranges the Qf value still stays comparatively low (see fig. 2.26(a)). A reduction of the τ_f value below 20 ppm/K seems only possible by a reduced amount of crystalline phases (possible by using lower ceramization times) but this would also cause a further decrease in ε_r and Qf.

4.4.4 Doping with 1.0 mol% CeO_2 and 7.5 mol% ZrO_2 (42014)

In glass 42014 the ZrO_2 content was increased to 7.5 mol% (substitution of 15 % of the TiO_2 content), originally to further reduce the amount of surface devitrification (see fig. 4.55). Additionally the doping led to the stabilization of the three unknown phases P1-P3, from which P1 and P3 already appeared in minor amounts for a doping of 5.0 mol% ZrO_2 in 41760 and 42110. In tab. 4.17 and fig. 4.50 the dielectric properties of the ceramization series 42014DEH are shown. Fig. 4.51 shows the XRD diffractograms of the samples, in analogy to 41760DEH the intensity values of the characteristic XRD main peaks were used to describe the temperature behavior of the formed phases (see tab. 4.18 and fig. 4.49).

DEH(T_{cer}/t_{cer})	ε_r	Qf[GHz]	τ_f[ppm/K]	f[GHz]
glass	20.1	1900	-83	10.63
389(850°C/50h)	20.8	6460	-25	10.41
357(860°C/50h)	21.1	9170	-2	10.53
373(870°C/50h)	21.4	9500	-1	10.42
354(880°C/50h)	22.5	9590	18	10.23
335(890°C/40h)	23.0	8650	46	10.15
374(900°C/15h)	26.5	7310	61	9.37
343(910°C/10h)	28.7	6370	153	9.06
347(920°C/20h)	30.1	6860	169	8.93
380(930°C/10h)	29.5	6960		8.84
376(940°C/5h)	25.7	6020		9.44
272(950°C/10h)	25.3	7870	72	9.53
268(1000°C/5h)	25.9	1530		9.35
269(1050°C/5h)	26.0	1460		9.37

Table 4.17: Dielectric properties of the ceramized samples of 42014

At low ceramization temperatures T_{cer} = 850-890 °C the dielectric properties are dominated by the presence of P1 which becomes the main phase. The formation of $La_2Ti_2SiO_9$ is suppressed in comparison to 41760 and is not present anymore until T_{cer} > 950 °C. It seems that with increasing ZrO_2 content, the $La_2Ti_2SiO_9$ phase becomes

less stable, which is also consistent with the reduction of the surface devitrification which consists of $La_2Ti_2SiO_9$ crystals. Additionally also $LaBO_3$ is significantly reduced in comparison to 41760/42110. The unknown phase P3 stabilizes as minor phase at low temperatures and is stable until T_{cer} < 950 °C. It seems to take the place of $La_2Ti_2SiO_9$ in the low temperature regime. The reduction of $La_2Ti_2SiO_9$ and $LaBO_3$ in the low ceramization temperature range leads to a significant increase of the Qf value up to 9000-9500 GHz in combination with a sufficiently high ε_r = 21.5-22.5 and τ_f close to 0 ppm/K, fulfilling all dielectric requirements. From T_{cer} = 890-940 °C the P1 phase reduces and P2 starts to become the dominant phase accompanied by a large increase in permittivity (up to ε_r = 30) and temperature coefficient (τ_f = 170 ppm/K), whereby the Qf value stays around 7000 GHz. The temperature range of P2 is comparatively narrow with maximum P2 contents at T_{cer} = 910-930 °C. The high τ_f value of this phase makes it unsuitable for the given DLA requirements. P2 shows similar properties as TiO_2 and its 3 main XRD peaks are located slightly lower than the TiO_2 main peaks at 2θ = 27.45°, 36.10°, 54.34°. Therefore it is possible that P2 is a Zr-doped TiO_2 crystal. The small peak at 2θ = 27.9° stays stable over the complete temperature range and could not be matched to one of the phases. Above 940 °C the system behaves similar to 41760DEH. The $La_2Ti_2SiO_9$ becomes the dominant main phase with increasing temperature and also $LaBSiO_5$ is present for T_{cer} > 980 °C.
As P1 seems to be a crystalline phase providing optimal dielectric properties a TEM/EELS analysis on the sample with the maximum P1 content (42014DEH357: T_{cer} = 860 °C, t_{cer} = 50 h) has been performed to identify its stoichiometry (see fig. 4.52 and 4.53). The EELS analysis identified the main phase to $La_4(Ti_{1-\delta}Zr_\delta)_9O_{24}$ with $\delta \approx$ 0.2 and the stoichiometry of the minor phase as $La_2Si_2O_7$, even though a match of the XRD pattern of $La_2Si_2O_7$ (ICCD-PDF: 01-082-0729) was not successful.
P1 appears in a similar dendritic Pt-nucleated structure as $La_4Ti_9O_{24}$ and the dielectric properties are also similar to other glass-ceramic samples with $La_4Ti_9O_{24}$ as main phase (42452DEH328, see tab. 4.11). Therefore it is assumed that P1 is a Zr-doped modification of the $La_4Ti_9O_{24}$ phase as it shows similar dielectric, structural and temperature behavior but different XRD peaks. A melting series (44685) with varying melting temperature and keeping time (analog to 42452/43735) but with 7.5 mol% ZrO_2 has been made to show the influence of the Pt content on the phase formation (see fig. 4.54) and it was found that the P1 content increases with the amount of Pt in analogy to the increase of $La_4Ti_9O_{24}$ in 42452/43735 also indicating that P1 is a modification of $La_4Ti_9O_{24}$.

DEH(T_{cer}/t_{cer})	L4	L2	TiO_2	LB	LBS	P1	P2	P3A
389(850°C/50h)	0	0	0	0	0	5000	0*	1400
357(860°C/50h)	0	0	0	300	0	5900	0*	1500
354(880°C/50h)	0	0	0	800	0	5700	500*	2200
335(890°C/40h)	0	0	0	900	0	4700	900*	2600
343(910°C/10h)	0	0	0	1800	0	1800	2100	3600
347(920°C/20h)	0	0	0	2200	0	400	2400	4100
376(940°C/5h)	2800	0**	800	3400	0	0	400*	2600**
272(950°C/10h)	3500	0**	1400	3700	0	0	100*	2200**
268(1000°C/5h)	0	6500	1600	4800	500	0	0	0
269(1050°C/5h)	0	5300	1800	1400	2700	0	0	0
2Θ(peak)	27.17	29.14	27.45	25.49	26.13	26.92	27.24	28.59
hkl(peak)	440	$\bar{3}12$	110	111	110			

Table 4.18: 42014DEH XRD main peak intensities in dependence of T_{cer}, *: peak overlaps with adjacent peaks P1, L4 and TiO_2, **: minimal amounts of L2, but overlapping with P3B (abbreviations analog to tab. 4.10)

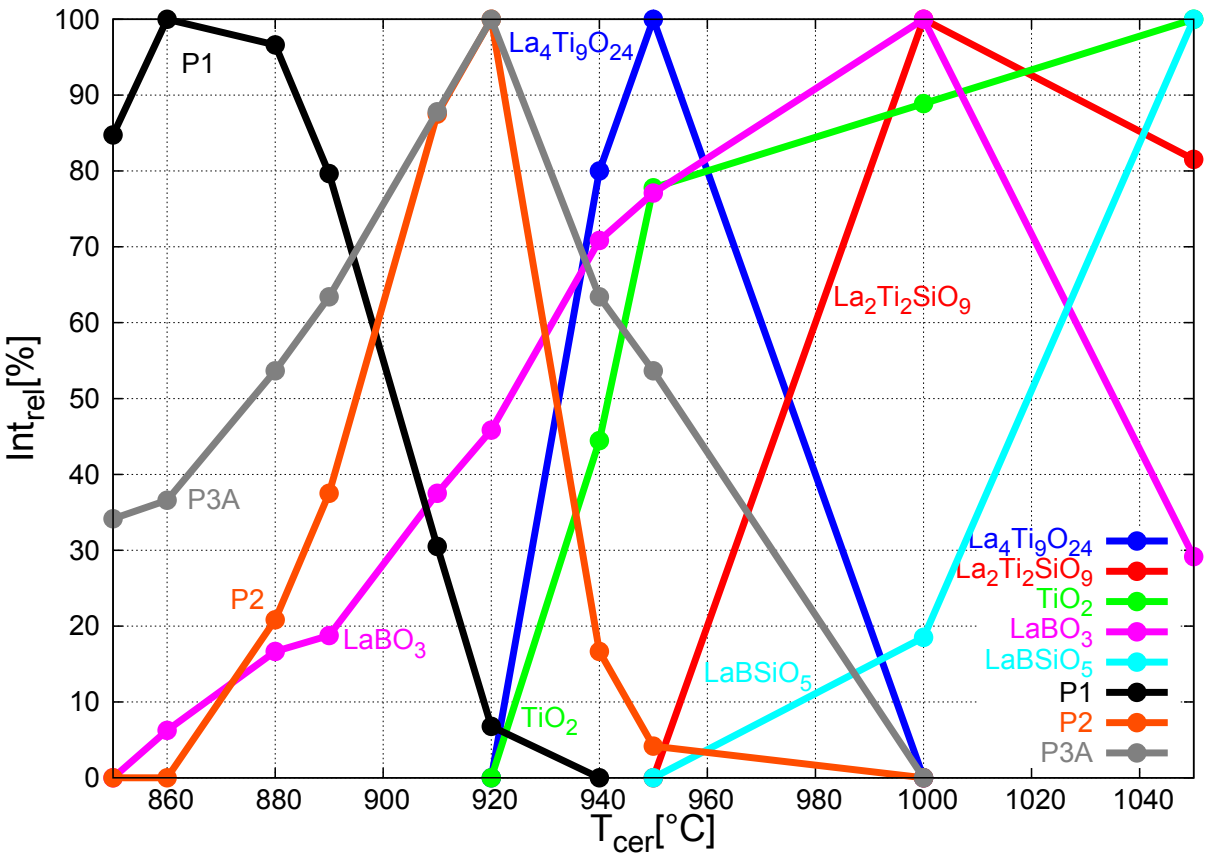

Figure 4.49: Illustration of tab. 4.18 (the intensity values are normalized on the highest intensity for every phase)

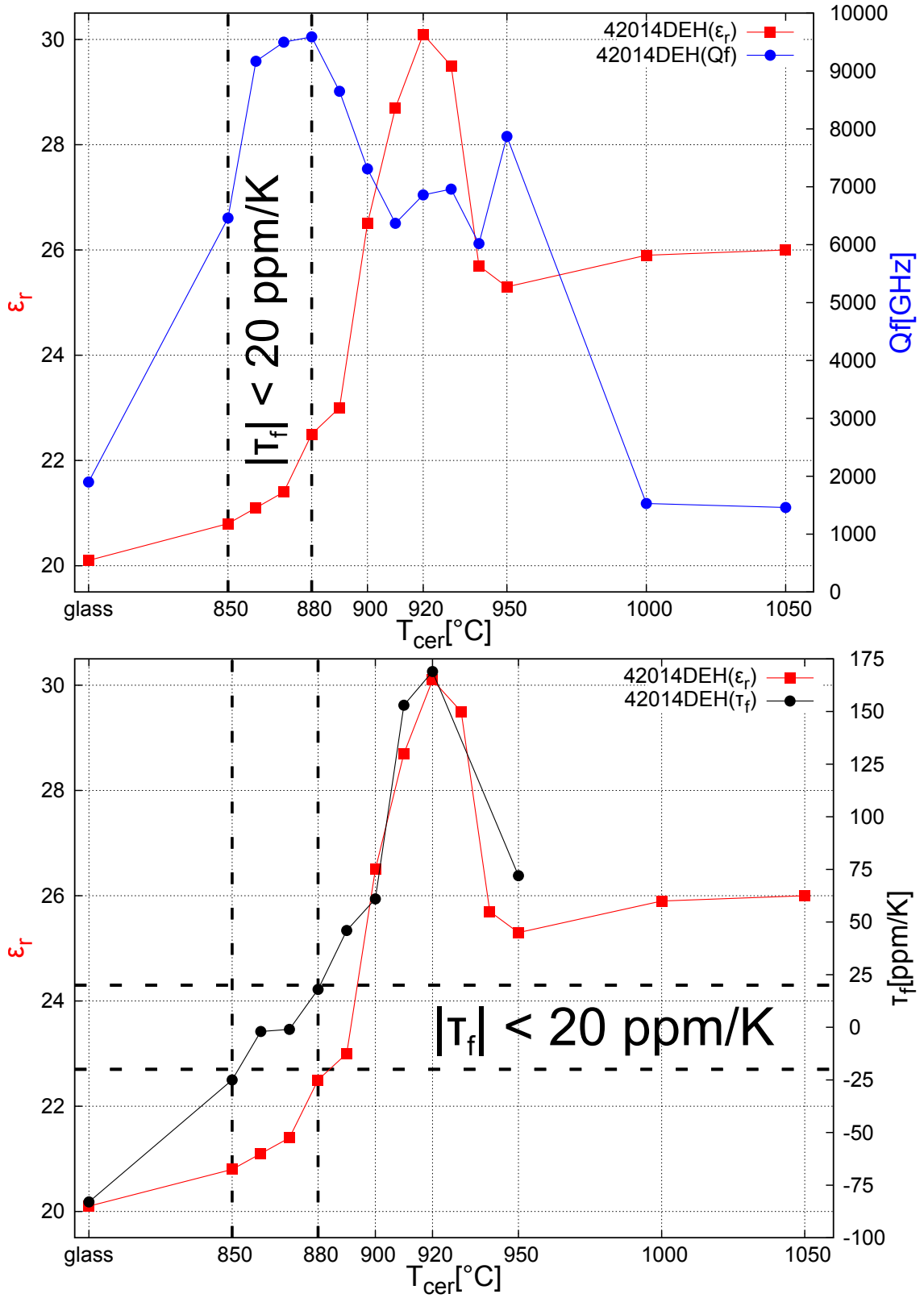

Figure 4.50: Dielectric properties of the ceramized samples 42014DEH according to tab. 4.17 (top: ε_r and Qf, bottom: ε_r and τ_f)

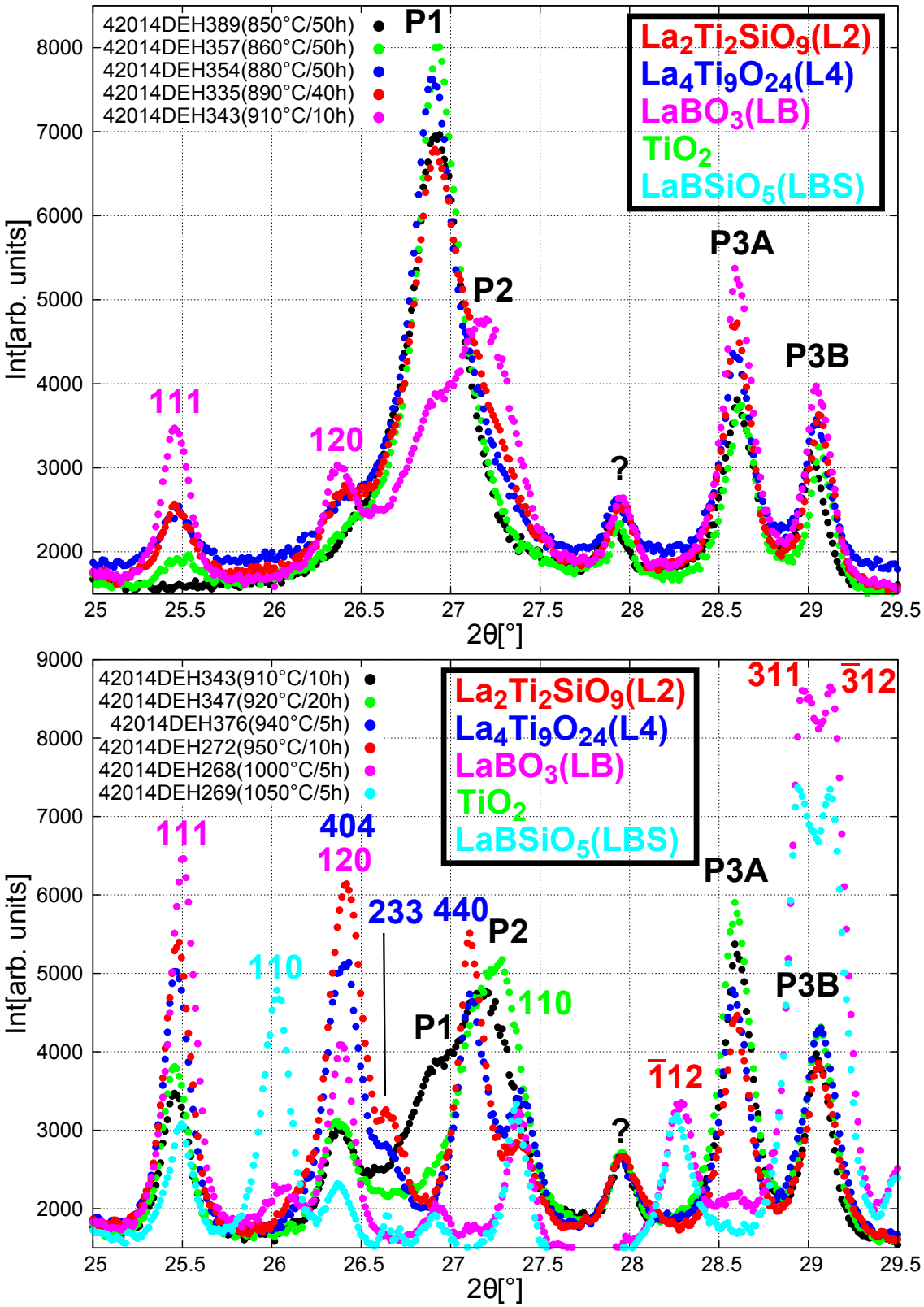

Figure 4.51: XRD diffractograms of the ceramized samples 42014DEH (top: T_{cer}: 850-910 °C, bottom: T_{cer}: 910-1050 °C)

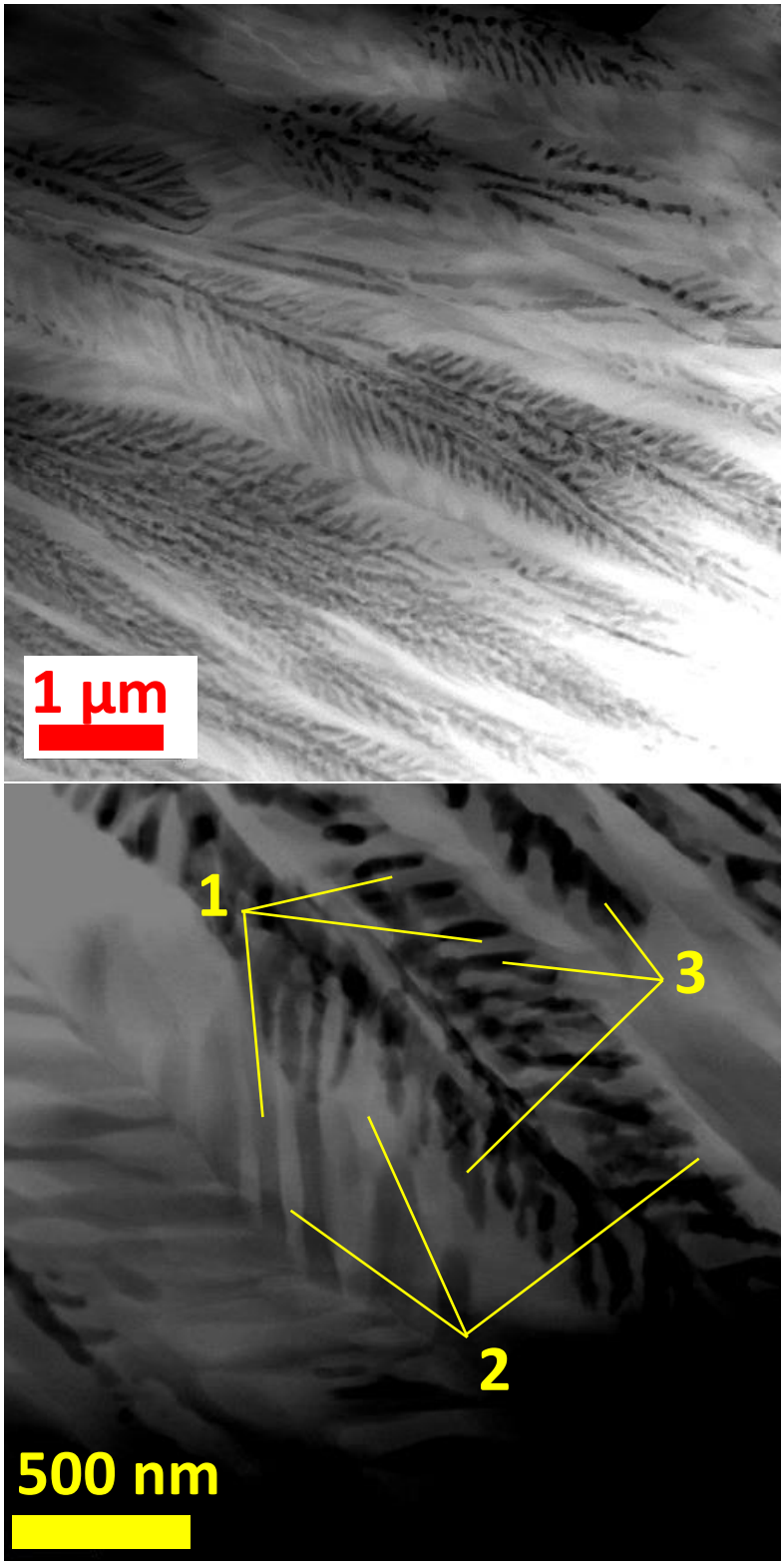

Figure 4.52: Dark field TEM image of 42014DEH357 (T_{cer} = 860 °C, t_{cer} = 50 h), dendrite growth direction parallel to the image plane, phases: 1: P1/$La_4(Ti_{1-\delta}Zr_\delta)_9O_{24}$, 2: P3/$La_2Si_2O_7$, 3: amorphous SiO_2

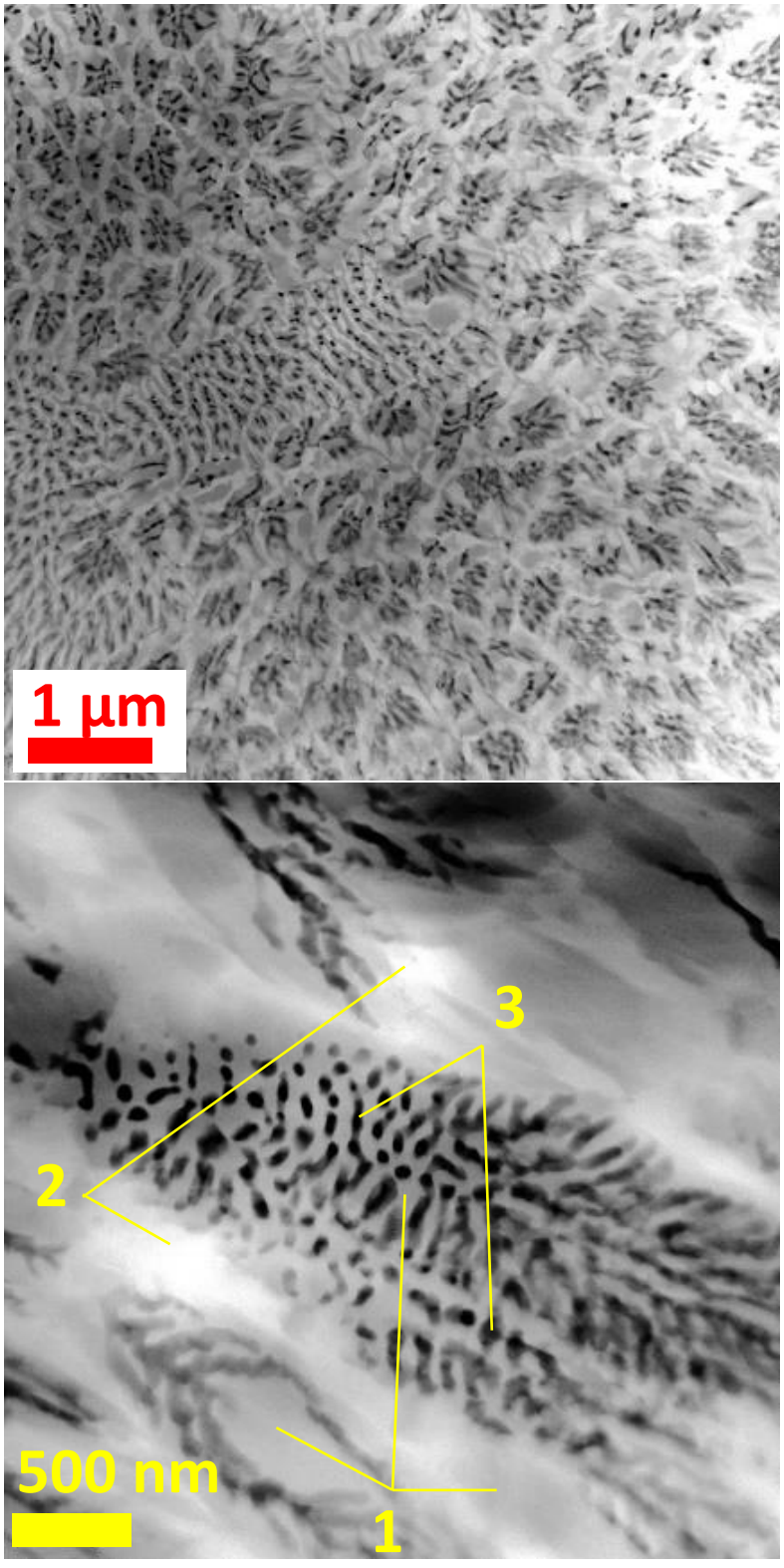

Figure 4.53: Dark field TEM image of 42014DEH357 (T_{cer} = 860 °C, t_{cer} = 50 h), dendrite growth direction orthogonal to the image plane, phases: 1: P1/$La_4(Ti_{1-\delta}Zr_\delta)_9O_{24}$, 2: P3/$La_2Si_2O_7$, 3: amorphous SiO_2

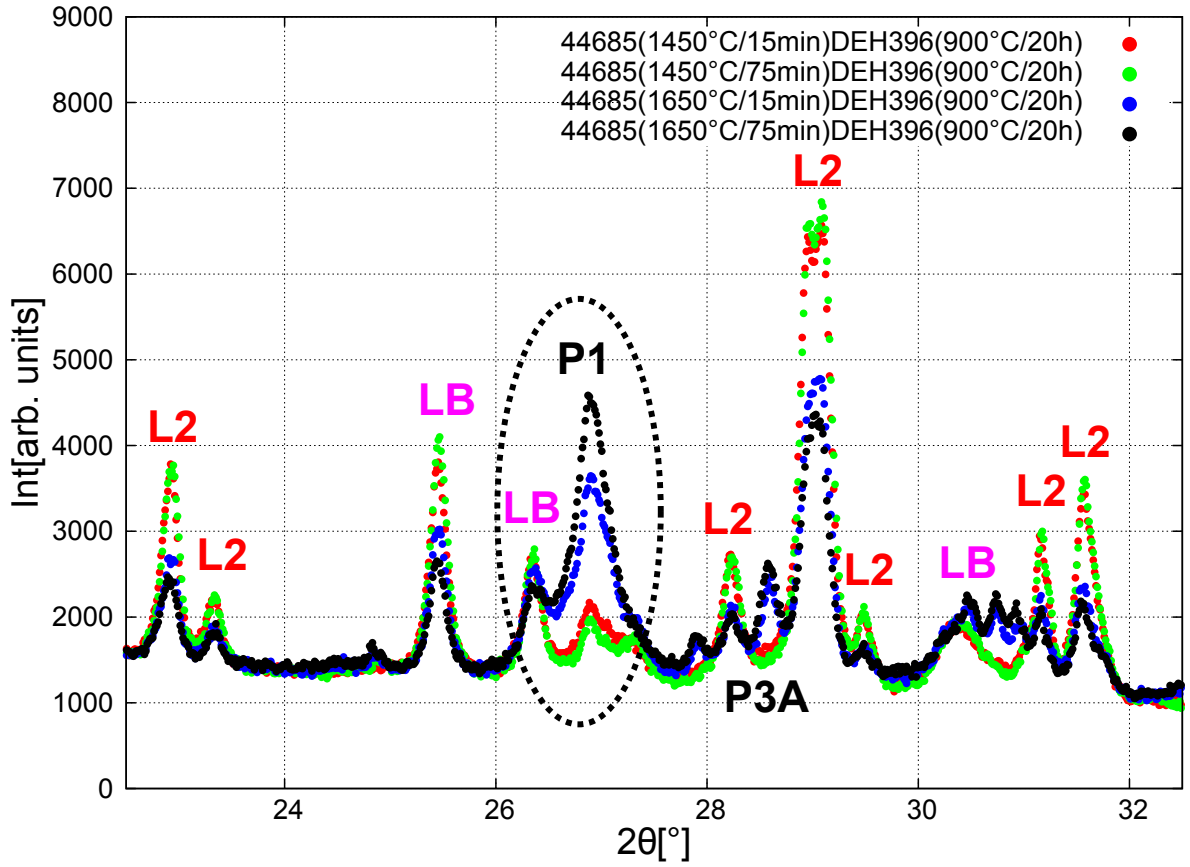

Figure 4.54: XRD diffractograms of the ceramized samples of the melting series 44685 (DEH396: T_{cer} = 900 °C, t_{cer} = 20 h)

In tab. 4.19 the results for a variation of the amount of CeO_2 is shown. Even though doping with 0.1 mol% CeO_2 reduced the amount of Ti^{3+} below the detection limit (see fig. 4.18), it still seems to have a significant effect on the Qf value.

DEH(T_{cer}/t_{cer})	ε_r(0.1)	ε_r(1.0)	Qf[GHz](0.1)	Qf[GHz](1.0)
357(860°C/50h)	21.6	21.1	5610	9170
335(890°C/40h)	22.2	23.0	6660	8650
347(920°C/20h)	29.0	30.1	4140	6860
376(940°C/5h)	27.1	25.7	4490	6020

Table 4.19: Influence of the CeO_2 content on the dielectric loss (comparison of 42014 (1.0 mol%) and 43530 (0.1 mol%), both 7.5 mol% ZrO_2)

In conclusion it has to be stated that 42014DEH showed optimal dielectric properties due to the crystallization of one dominant main phase (P1) at low ceramization temperatures (T_{cer} = 850-890 °C). The τ_f parameters can be adjusted close to 0 ppm/K and tuned by T_{cer} (with increasing T_{cer} the contribution of P2 shifts τ_f to higher values). It was shown that for the suitable range of τ_f = -2 to +18 ppm/K the permittivity and Qf value stayed comparatively stable at 21.1-22.5 resp. 9170-9590 GHz.

4.4.5 Doping with 1.0 mol% CeO_2 and 10.0 mol% ZrO_2 (42732)

In glass 42732 the ZrO_2 content was increased further to 10.0 mol% (substitution of 20 % of the TiO_2) to investigate its effect on the surface devitrification and phase formation. Fig. 4.55 shows that the surface devitrification is not present anymore.

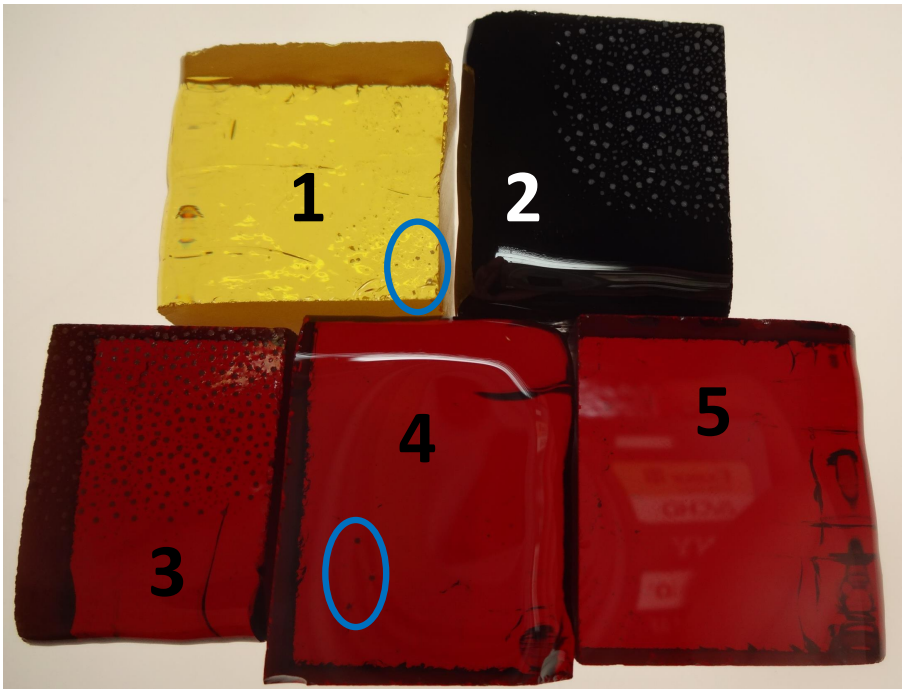

Figure 4.55: Comparison of the selected glasses 1-5: 43722, 42110, 41760, 42014, 42732 (1/4: low amount of surf. devitrification shown in blue, 2/3: thin crystal layer on surface, 5: no surf. dev.)

The substitution of ZrO_2 only slightly reduces ε_r of the glass (see tab. 4.20).

Melt	40281	41760	42014	42732
TiO_2/ZrO_2 [mol%]	50/0	45/5	42.5/7.5	40/10
ε_r(10 GHz)	20.8	20.4	20.1	19.9

Table 4.20: Variation of ε_r of the basic glass with amount of doped ZrO_2

In tab. 4.21 and fig. 4.57 the dielectric properties of the ceramization series 42732DEH are shown. Fig. 4.56 shows a comparison of the XRD diffractograms of low temperature ceramized samples with different amount of ZrO_2 doping. It can be seen that the P2 phase, which only was stable in a narrow temperature regime around T_{cer} = 910-930 °C in 42014, now dominates already at lower temperatures from 860-950 °C accompanied by a comparatively large τ_f value, a Qf around 7000 GHz and permittivity values reaching up to 33.7 (at T_{cer} = 950 °C) which are the highest measured ε_r values of all samples. As minor phases P1 and P3 are also present in

lower amounts but the dielectric properties seem to be dominated by the presence of P2. At low temperatures T_{cer} < 860 °C the P1/P2 ratio could be shifted more towards P1 and a τ_f < 20 ppm/K material is possible. Even though in comparison to a similar glass-ceramic of the 42014DEH system, this glass-ceramic would probably show a lower Qf around 6000 GHz (to 9000 GHz in 42014DEH) and a slightly larger ε_r around 23. Therefore 42014 seems more suitable for the given DLA requirements.

DEH(T_{cer}/t_{cer})	ε_r	Qf[GHz]	τ_f[ppm/K]	f[GHz]
glass	19.9	1840	-93	10.65
357(860°C/50h)	23.0	6380	23	10.09
373(870°C/50h)	24.9	7900	62	9.61
336(880°C/40h)	27.1	6520		9.33
358(900°C/15h)	31.1	6650		8.68
359(920°C/20h)	30.9	6650		8.67
360(940°C/5h)	31.6	6390		8.54
352(950°C/5h)	33.7	6140		8.34

Table 4.21: Dielectric properties of the ceramized samples of 42732

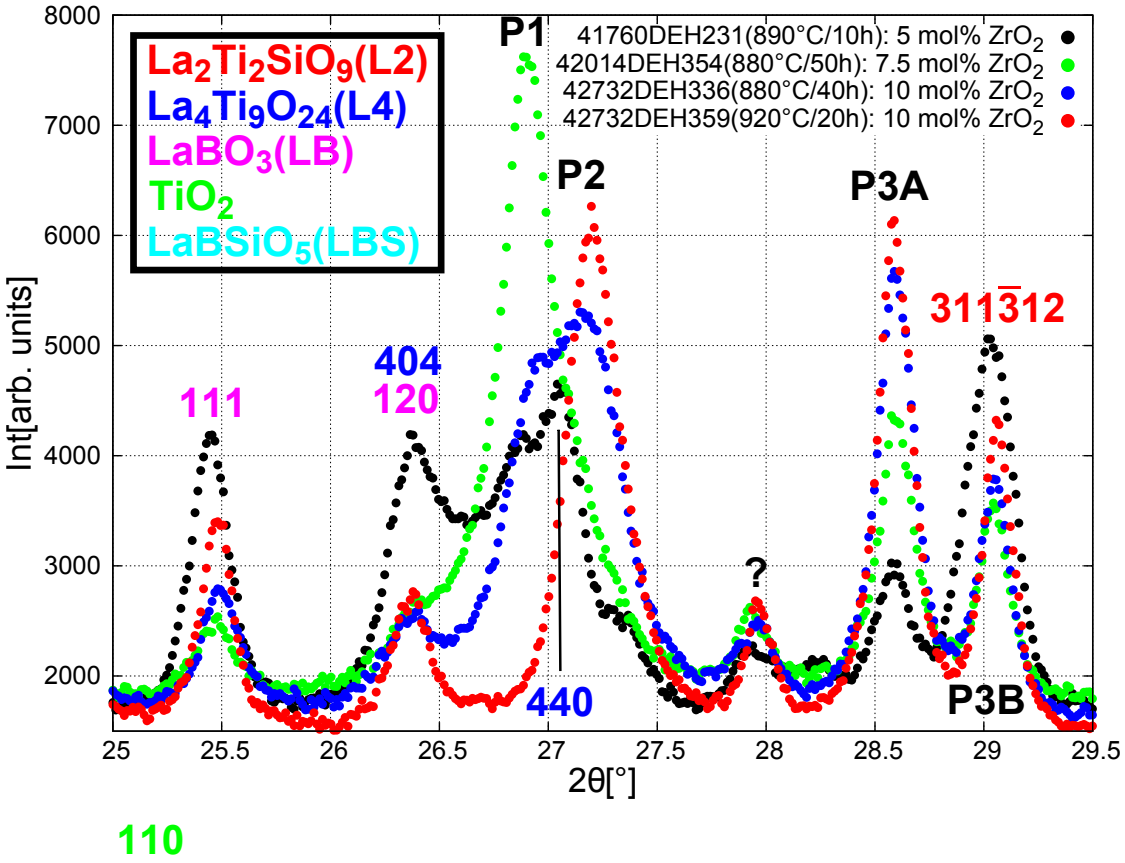

Figure 4.56: Comparison of the XRD diffractograms of the ceramized samples of 42732DEH, 42014DEH and 41760DEH exemplary for low T_{cer}

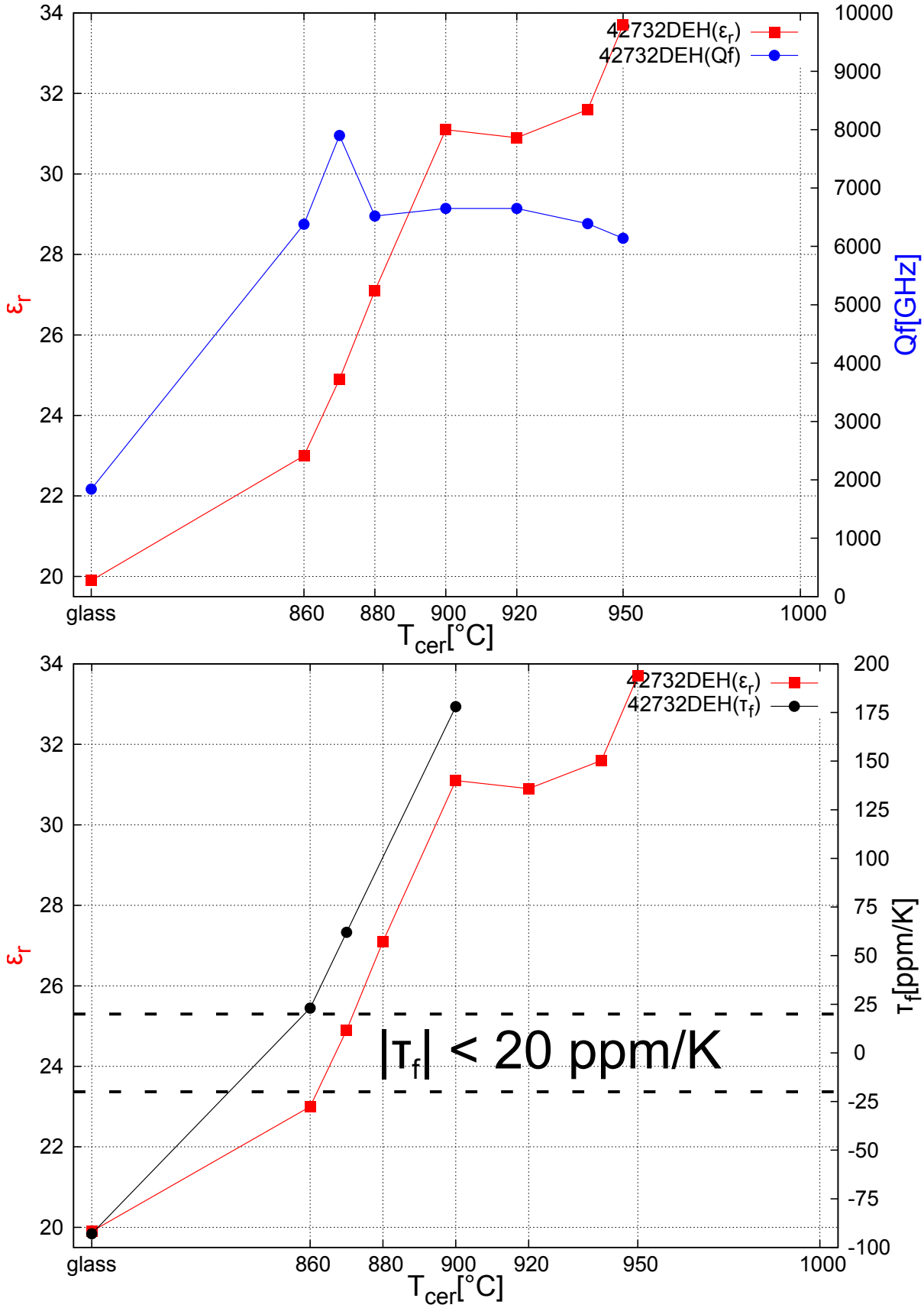

Figure 4.57: Dielectric properties of the ceramized samples 42732DEH according to tab. 4.21 (top: ε_r and Qf, bottom: ε_r and τ_f)

4.5 GHz loss contributions

As mentioned in chapter 2.7 the loss mechanisms in the GHz frequency range can be analyzed by their frequency and temperature dependence. In this chapter, the dielectric loss is measured in different frequency ranges, as for example in the Hz to MHz range (conductivity measurement, see chapter 3.6) and the THz range (THz ellipsometry, see chapter 3.8.3). The dielectric loss is then extrapolated in the GHz region to estimate the contributions from the adjacent frequency ranges. Additionally a temperature dependent measurement of the dielectric loss is performed.

4.5.1 Conductivity contribution

The conductivity of different samples (different doped glasses and glass-ceramics) has been measurement frequency (0.1 Hz to 1 MHz) and temperature (20 °C to 350 °C) dependent. A comparison of the room temperature values is shown in fig. 4.58.

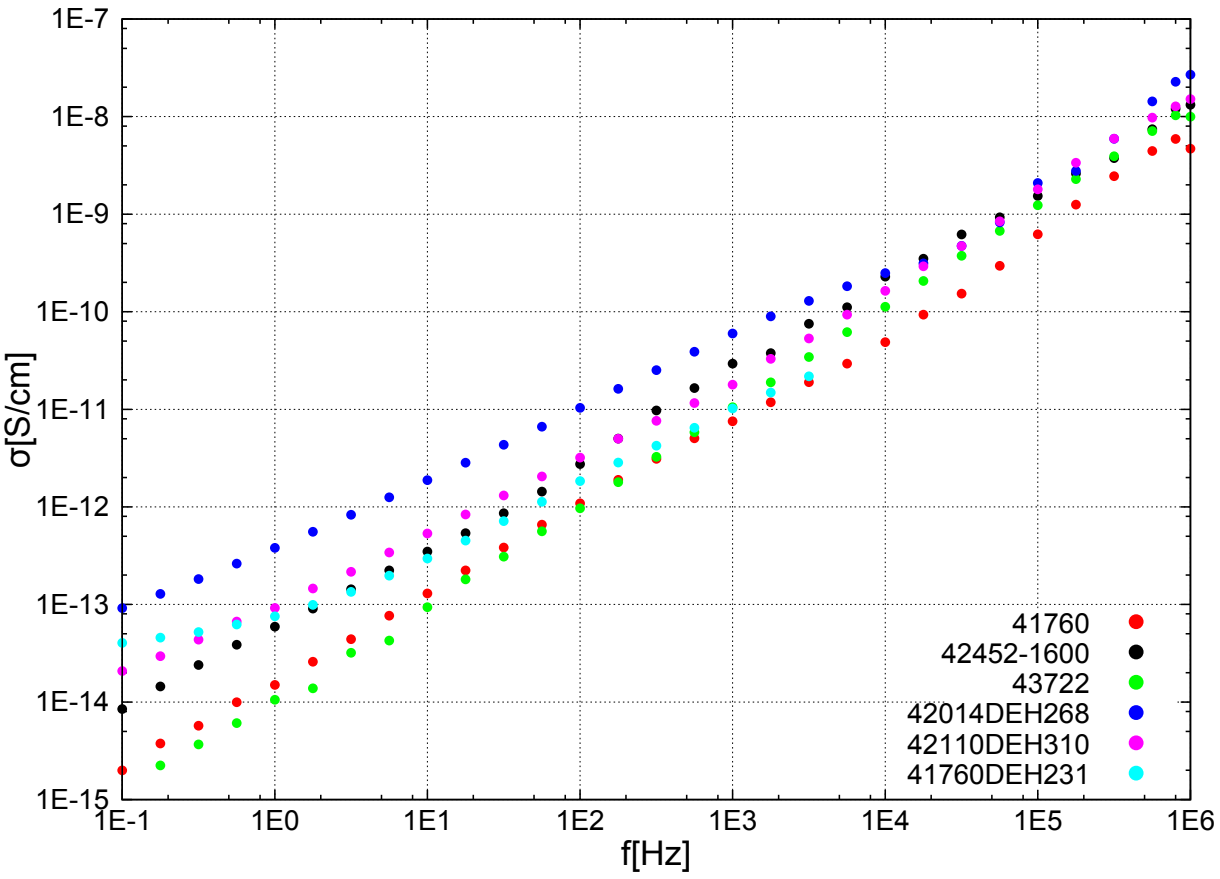

Figure 4.58: Room temperature (20 °C) conductivity measurement of the investigated samples (the values of 41760DEH231 for $f > 10$ kHz could not be measured due to experimental problems)

- 41760: glass doped with 1.0 mol% CeO_2
- 42452-1600: glass containing ≈ 0.5 mol% Ti^{3+}
- 43722: glass doped with 0.1 mol% Sb_2O_5
- 42014DEH268: high loss glass-ceramic (1.0 mol% CeO_2)
- 42110DEH310: high loss Ti^{3+}-containing glass-ceramic
- 41760DEH231: low loss glass-ceramic (1.0 mol% CeO_2)

The temperature dependent measurements show the expected behavior with a comparatively strong temperature dependence of the σ_{DC}-contribution. A measurement of sample 41760 is shown exemplarily in fig. 4.59. The other investigated samples show similar behavior. It can be seen that the conductivity at room temperature is dominated by the frequency dependent contribution and only for higher temperatures (> 300 °C) the DC contribution becomes more relevant.

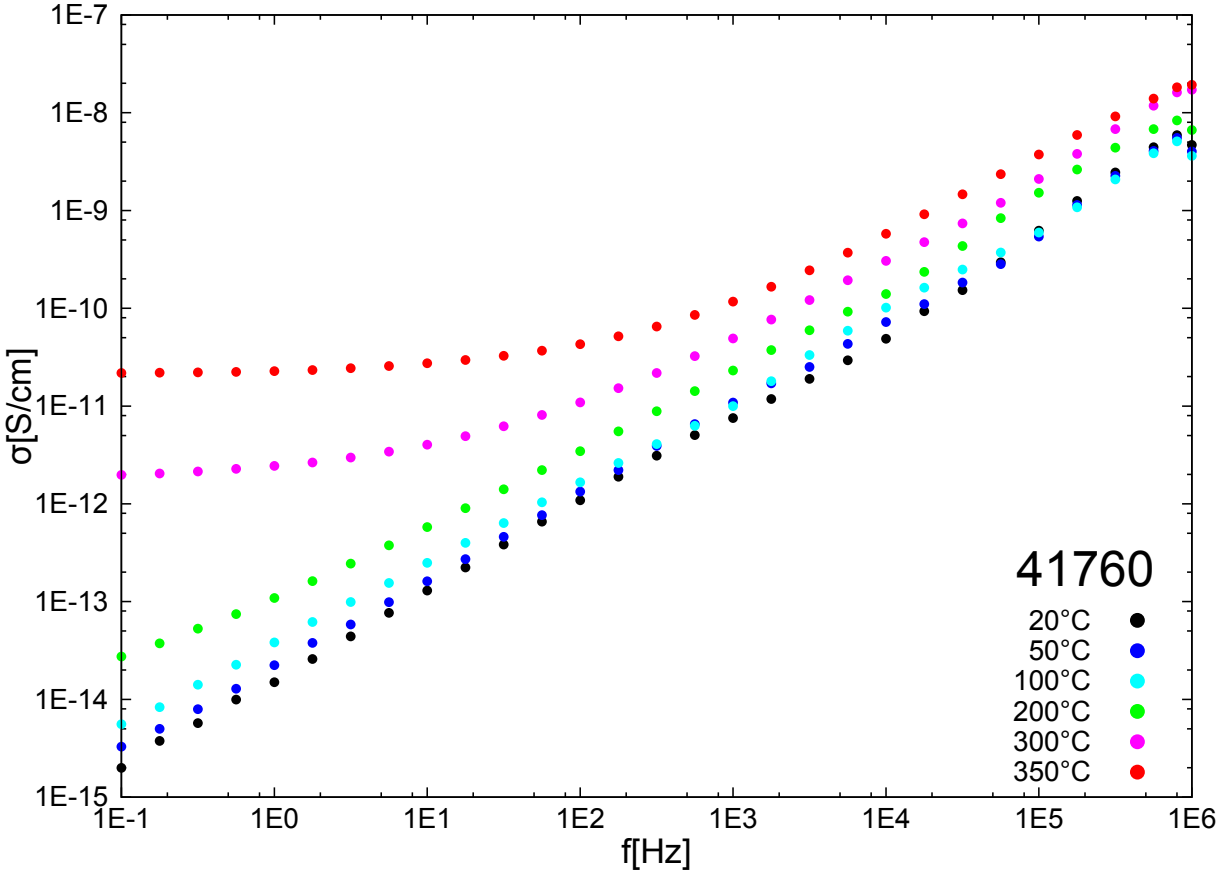

Figure 4.59: Temperature dependent conductivity measurement of sample 41760 (20 °C to 350 °C)

The room temperature conductivity is fitted by the Jonscher model (see chapter 2.7.1 eq. (2.63)), exemplarily shown for sample 42452-1600:

$$\sigma(f) = \sigma_{DC} + \sigma_0 f^s \quad . \tag{4.5}$$

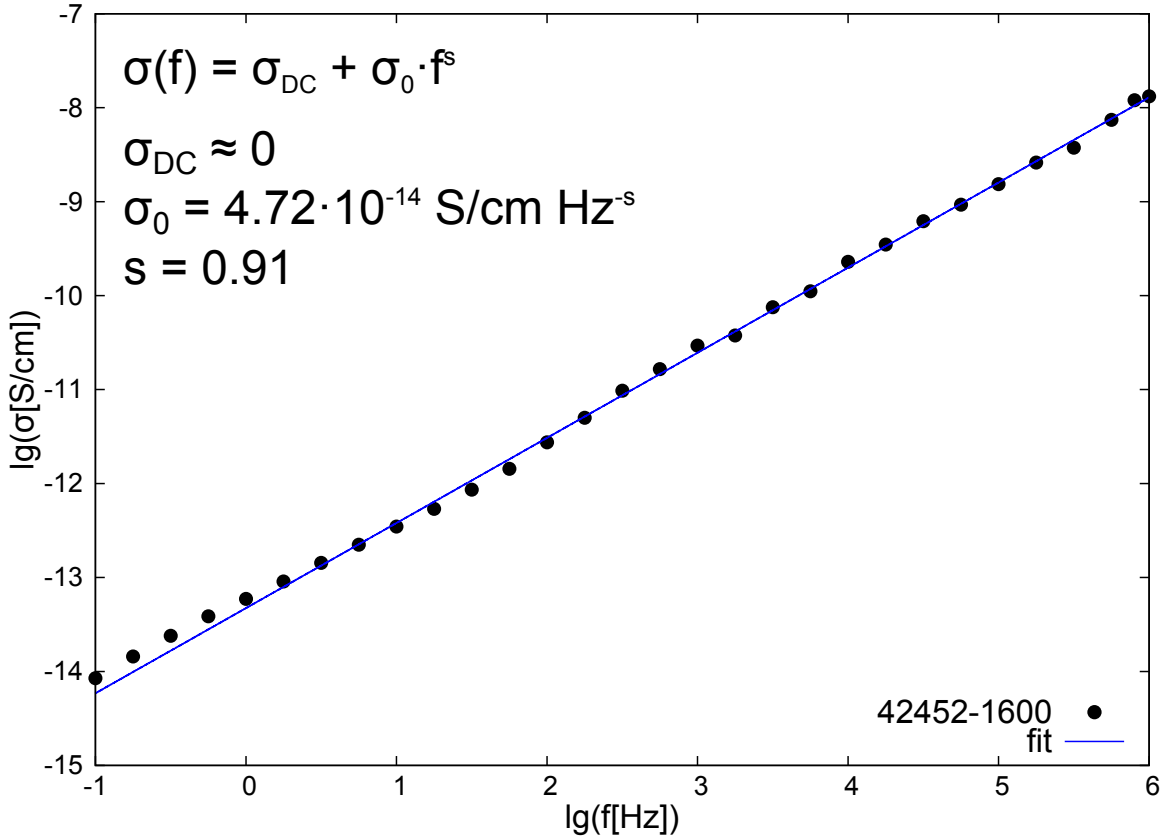

Figure 4.60: Fit of the room temperature (20 °C) conductivity by the Jonscher model

In tab. 4.22 a comparison between the extrapolated $\tan(\delta)_{\text{ex}}$ values and the ones measured in the GHz range via Hakki-Coleman is made.

Melt	f[GHz]	ε_r	$\tan(\delta)$	σ_0	s	σ_{ex}[S/cm]	$\tan(\delta)_{\text{ex}}$	q[%]
41760	10.57	20.4	5.76	$1.55 \cdot 10^{-14}$	0.92	$2.4 \cdot 10^{-5}$	0.20	3.5
42452-1600	10.57	20.4	5.91	$4.72 \cdot 10^{-14}$	0.91	$5.7 \cdot 10^{-5}$	0.48	8.1
43722	10.58	20.4	5.93	$2.24 \cdot 10^{-14}$	0.95	$7.3 \cdot 10^{-5}$	0.61	10.3
42014DEH268	9.35	25.9	6.13	$3.72 \cdot 10^{-13}$	0.73	$6.3 \cdot 10^{-6}$	0.05	0.8
42110DEH310	9.24	27.2	4.65	$9.33 \cdot 10^{-14}$	0.76	$3.6 \cdot 10^{-6}$	0.03	0.5
41760DEH231	9.67	23.1	2.48	$5.18 \cdot 10^{-14}$	0.76	$2.2 \cdot 10^{-6}$	0.02	0.7

Table 4.22: Extrapolation of the conductivity loss contribution to the GHz frequency range by using the Jonscher model (whereby $\sigma_{\text{DC}} \approx 0$ for all shown samples), $q = \tan(\delta)_{\text{ex}}/\tan(\delta)$ (ex: extrapolated), $\tan(\delta)_{(\text{ex})}$ values given in 10^{-3} and σ_0 in S/cm Hz^{-s} (not shown above due to the lack of space)

The conductivity of all investigated samples is at least one order of magnitude too low to significantly contribute to the overall dielectric loss in the GHz range. The conductivity for all samples whether glass or glass-ceramic lie also in the same order of magnitude for the measured frequency range and do not correlate with the different loss values in the GHz range (e.g. 42014DEH231 is comparatively lossy in the GHz range, but has a comparatively low conductivity). The glasses have a stronger frequency dependence $s \approx$ 0.91-0.95 vs. 0.73-0.76 which leads to a comparatively higher GHz contribution. The s value is characteristic for different types of materials resp. the conductivity mechanism (see chapter 2.7.1). From the comparison of the different samples it is concluded that the Ti^{3+} content in glass 42452-1600 ($\approx$ 0.5 mol% Ti^{3+}) and glass-ceramic 42110DEH310 do not lead to an increase in conductivity. This can be only explained by the fact that the present amounts are just too low to give a significant conductivity contribution. Furthermore, a Ti^{3+} dominated conductivity would show a significant σ_{DC} at low frequencies even at room temperature (see fig. 4.44). The other polyvalent ion containing glasses 41760 (1.0 mol% CeO_2) and 43722 (0.1 mol% Sb_2O_5) also do not differ significantly from 42452-1600.

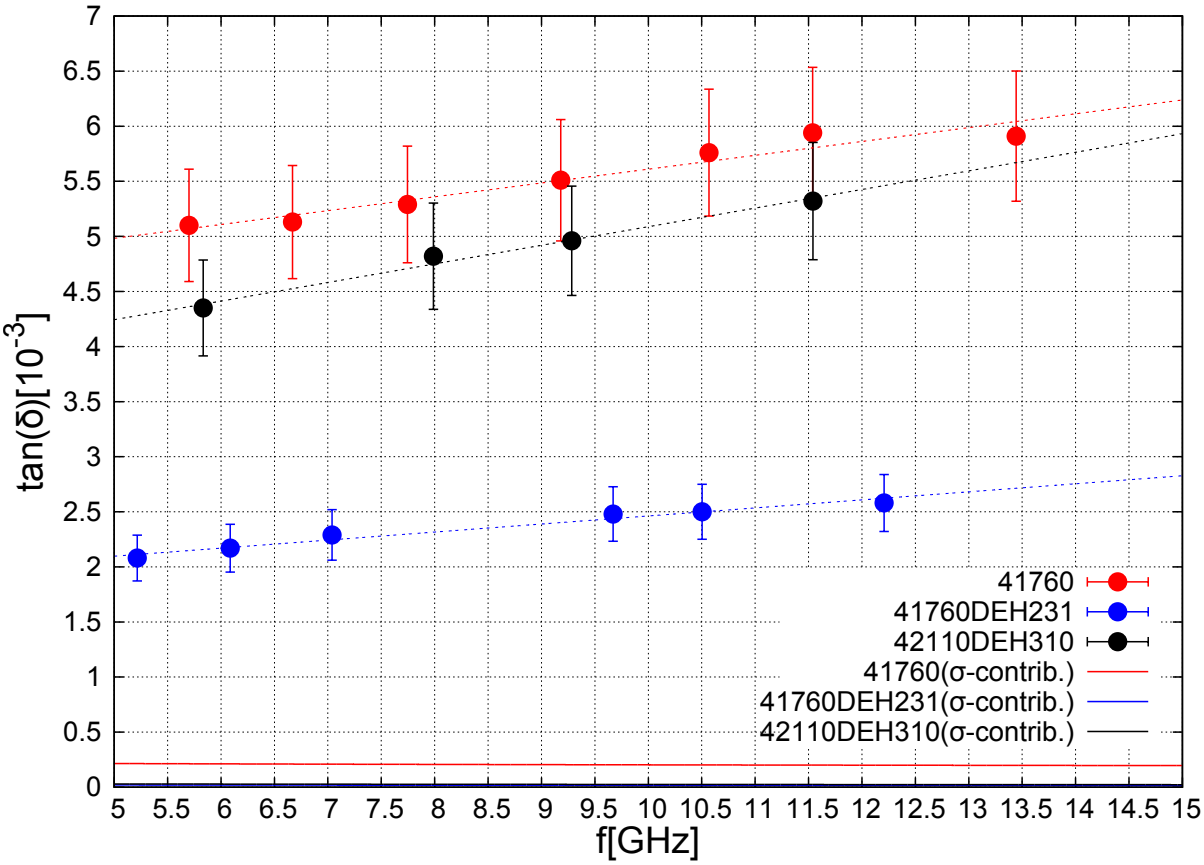

Figure 4.61: Frequency dependence of $\tan(\delta)$ in the GHz region and comparison with the extrapolated conductivity contribution from the MHz region

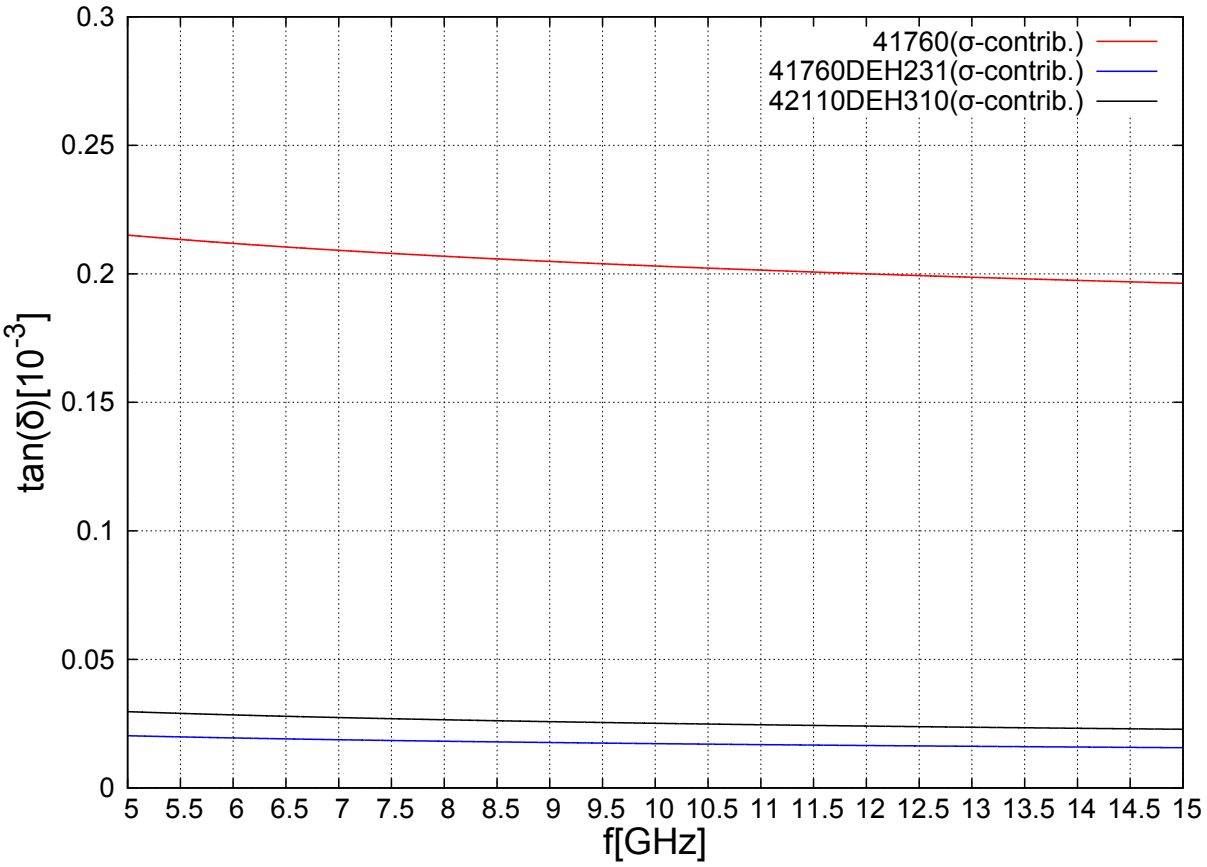

Figure 4.62: Frequency dependence of $\tan(\delta)_{\text{ex}}$ in the GHz region

$\tan(\delta)$ was measured frequency dependent for 3 chosen samples (41760, 41760DEH231, 42110DEH310), see fig. 4.61 (assumption of a relative error of 10 %, see chapter 3.9.1) and the conductivity contribution $\tan(\delta)_{\text{ex}}$ from the extrapolated conductivity (see fig. 4.62) was added for comparison. The frequency dependence of $\tan(\delta)$ is much weaker as the by the damped harmonic oscillator model predicted frequency proportionality (see eq. (2.40)). The GHz values were fitted by $\tan(\delta) = a_0 + b \cdot f$ (dashed curves in fig. 4.61). It can be seen, that the constant background a_0 gives the dominant contribution. Additionally the conductivity contribution $\tan(\delta)_{\text{ex}}$ is also nearly frequency independent (see fig. 4.62) which would make the separation of the different contributions even more difficult (in case of a dominant conductivity contribution which is not present for the investigated samples). Similar results were obtained by Tamura [Tam06] for defect containing ceramics (see fig. 4.63). The a_0 contribution is related to imperfections resp. deviations from the perfect periodically arranged crystal lattice structure. A random distribution of the ions like in the case of an amorphous glassy phase therefore causes an increase of the loss tangent by a constant background contribution.

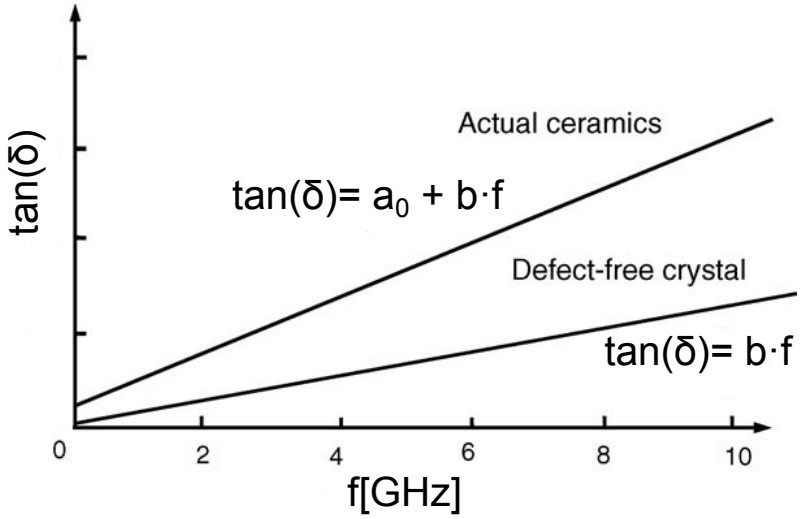

Figure 4.63: Frequency dependence of $\tan(\delta)$ of a defect-free crystal and actual ceramics (modified from [Tam06])

In fig. 4.64, Qf and ε_r are plotted in dependence of the frequency. The Qf value can not be considered constant in the investigated GHz region. The permittivity stays constant as expected (see chapter 2.4.1).

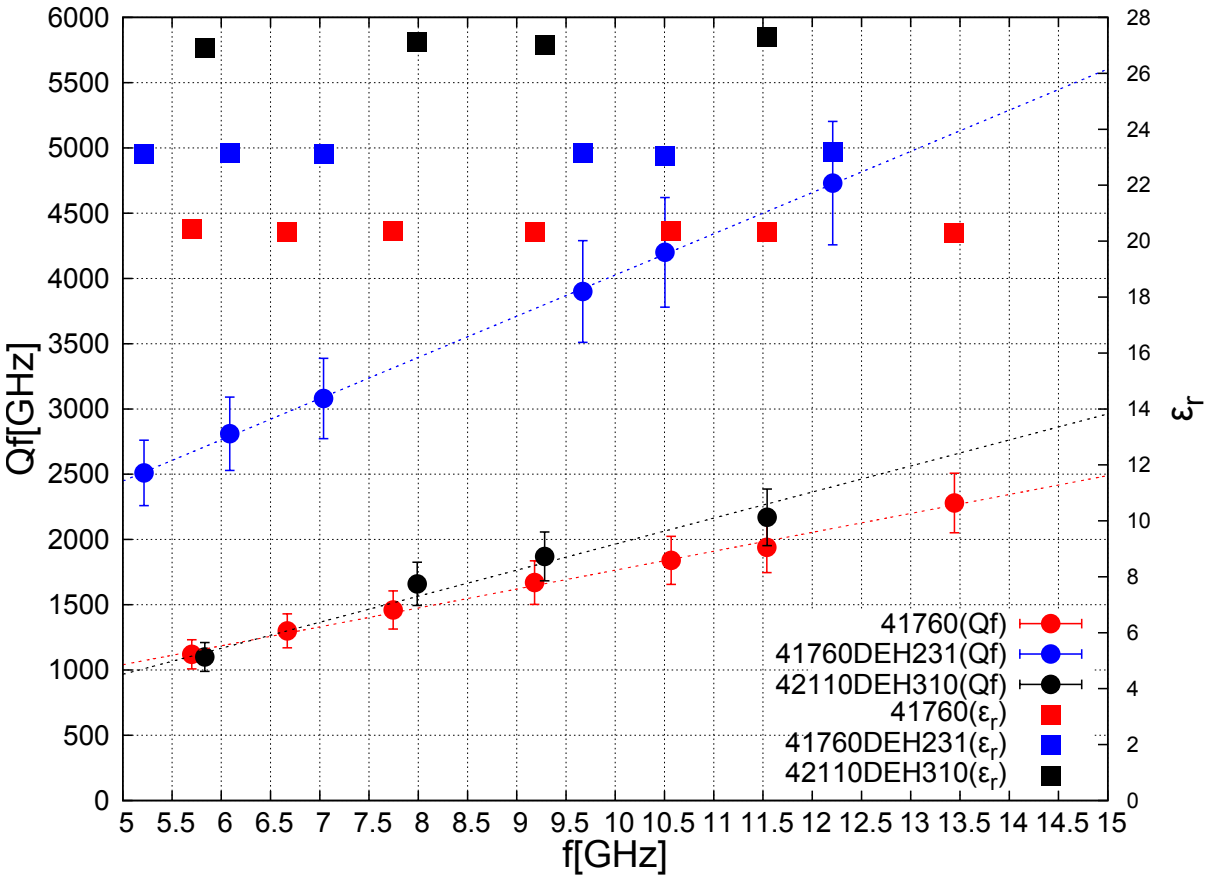

Figure 4.64: Frequency dependence of Qf and ε_r in the GHz region

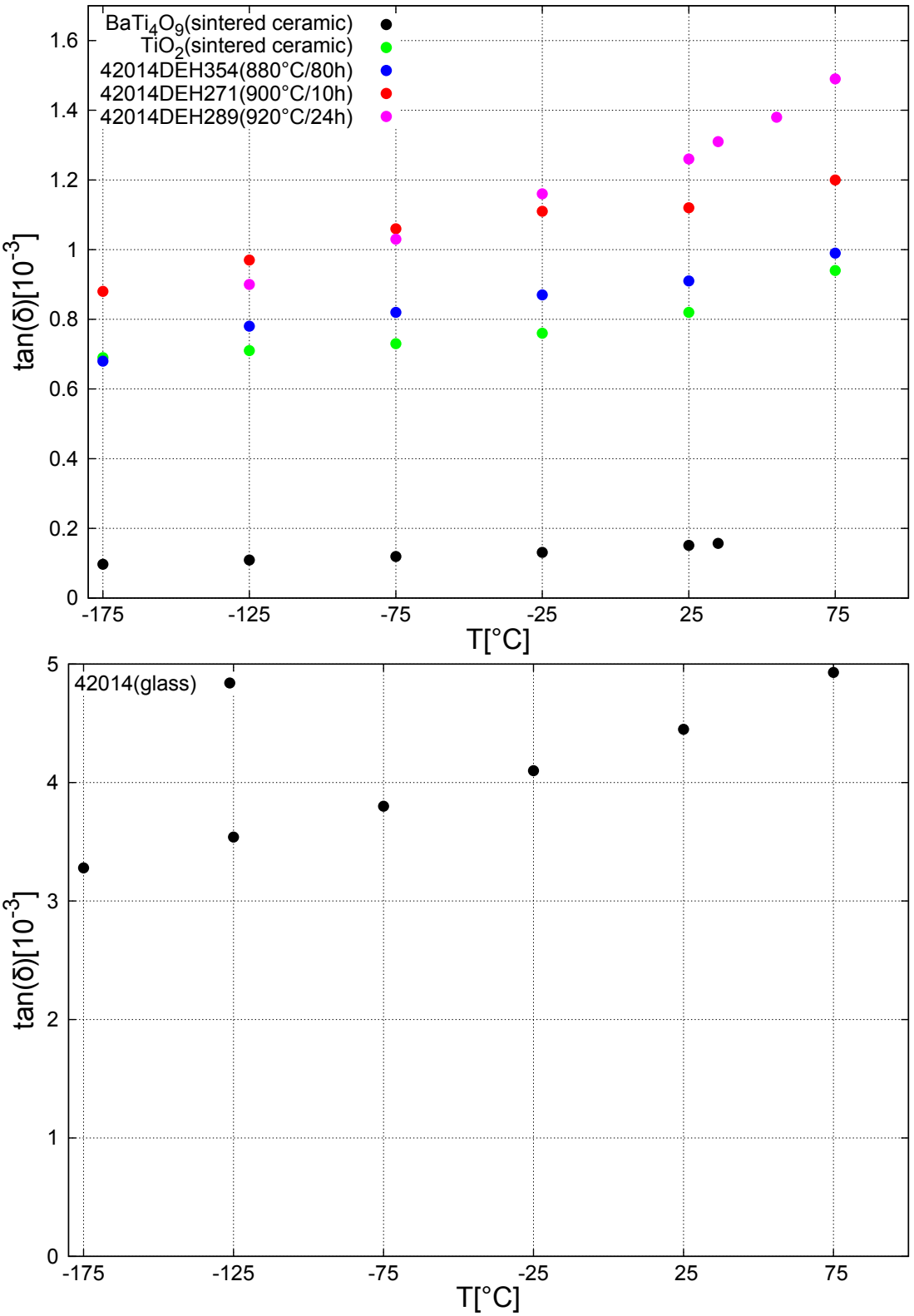

Figure 4.65: Temperature dependent measurement of the dielectric loss, top: glass-ceramic (42014DEH354, 42014DEH271, 42014DEH289) and two sintered ceramic samples ($BaTi_4O_9$, TiO_2), bottom: glass (42014)

In fig. 4.65 the dielectric loss is plotted in dependence of the temperature from -175 °C to +75 °C (the loss of the TiO_2-ceramic is comparatively high due to a bad sample quality). For all measured samples (glasses, glass-ceramics and sintered ceramics) the loss decreased with decreasing temperature but the temperature dependence is comparatively weak. Over a temperature difference of 200 K, the dielectric loss reduced by less than 50 %. The weak temperature dependence could also be a hint for a large defect contribution to the overall loss.

4.5.2 Phonon contribution

Ellipsometry measurements of selected samples haven been made to determine their dielectric properties in the THz range (1.5 to 20 THz). Three glasses (42014, 42452-1450, 42452-1600), associated glass-ceramics (42014DEH335, 42452-1450DEH325, 42452-1600DEH328), one sintered ceramic (CMT) and a fused silica sample (FS: high purity SiO_2-glass) haven been measured. Their GHz properties are summarized in tab. 4.23. The samples 42452-1450 and 42452-1600 were chosen because they contain different amounts of Ti^{3+}, 42014 is Ti^{3+}-free. The CMT and FS sample were chosen, to compare a low-loss pure crystalline resp. amorphous sample with the mixed glass-ceramics.

Melt	f[GHz]	ε_r	Qf[GHz]	$\tan(\delta)[10^{-3}]$	material
42014	10.63	20.1	1900	5.58	glass
42014DEH335	10.09	23.2	8600	1.18	glass-ceramic
42452-1450	10.54	20.4	1840	5.72	glass
42452-1450DEH325	9.22	26.9	1630	5.66	glass-ceramic
42452-1600	10.57	20.4	1790	5.91	glass
42452-1600DEH328	10.25	21.5	9710	1.06	glass-ceramic
CMT	5.70	21.1	51580	0.11	sint. ceramic
FS	10.90	3.8	59540	0.18	quartz glass

Table 4.23: Selected samples for the ellipsometry measurement

The investigated glasses (fig. 4.67-4.69) showed similar dielectric properties as expected (only different levels of dopants). Comparatively broad resonances can be seen which extend far in the lower frequency range below the detection limit of the measurement setup (below around 4 THz, the noise starts to dominate). For all samples, the real part of the permittivity should approach the GHz value below the lowest resonance, which was consistent with all measured samples. It is possible that other resonances located at lower frequencies than the measured range are still present. The

glass-ceramic samples show sharper resonances but a difference between the high-loss glass-ceramic (42452-1450DEH325) and the low-loss ones (42452-1600DEH328 and 42014DEH335) is not obvious (see fig. 4.66).
The real and imaginary part of the permittivity were fitted separately by the harmonic oscillator model (see eq. (2.37)/(2.38)) but due to the large overlap between the resonances of the glass and glass-ceramic samples, the data could not be fitted for those samples. For the CMT and especially the FS sample, it can be seen that the data is not consistent with the ideal oscillator model. The disorder broadened resonance of an amorphous glass probably would be better represented by an oscillator function convoluted with a gaussian distribution. As we are mainly interested in the extrapolated loss values in the GHz range far below the resonance frequency, the exponentially decreasing gaussian loss contribution is neglectable in comparison to the dampled harmonic oscillator loss contribution (see eq. (2.38)) and therefore the used fit functions are suitable enough.
In tab. 4.24 the fit results of the two low loss samples (CMT and FS) are shown and their contribution to the GHz region is calculated. It can be seen that the extrapolated loss values ($\tan(\delta)_{\text{ex}}$) are around one order of magnitude lower than the GHz values. This is consistent with measurements from other authors (see chapter 2.7.2) and confirms that the low frequency influence of the direct one-phonon absorption is not the relevant loss mechanism in the GHz frequency range.

Melt	f[GHz]	ε_r	Qf[GHz]	$\tan(\delta)[10^{-3}]$	$\varepsilon_{r,\text{ex}}$	$\tan(\delta)_{\text{ex}}[10^{-3}]$	$q[\%]$
CMT	5.70	21.1	51580	0.11	13.7	0.024	21.8
FS	10.90	3.8	59540	0.18	3.3	0.022	11.9

Table 4.24: Comparison of the dielectric properties measured in the GHz range and the extrapolated results from the THz region, with $q = \tan(\delta)_{\text{ex}}/\tan(\delta)$

Unfortunately no quantitative results for the investigated glass-ceramics were obtained due to the large overlap of the resonance peaks. But the fit results of the CMT and FS indicate that the one-phonon absorption is not the dominate loss mechanism. The measured glass samples show that due to the deviation from the regular crystal lattice structure a large disorder broadening of the resonances occurs. In combination with the results obtained from the conductivity measurements and the temperature dependent loss measurements in the GHz range. It is assumed, that the loss in the GHz region is most probably dominated by the defect-broadened two-phonon difference process after fig. 2.23.

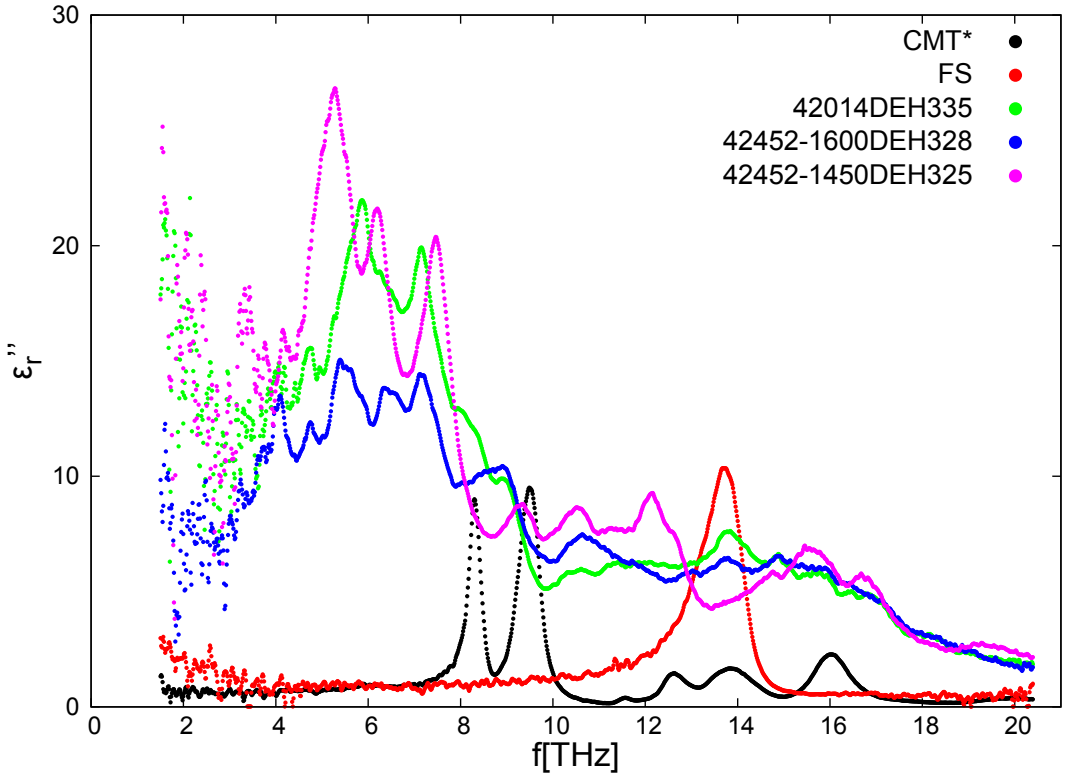

Figure 4.66: Comparison of the resonance modes for the investigated glass-ceramics, CMT and FS (*: CMT values are scaled down by a factor of 10 to enable a better comparison)

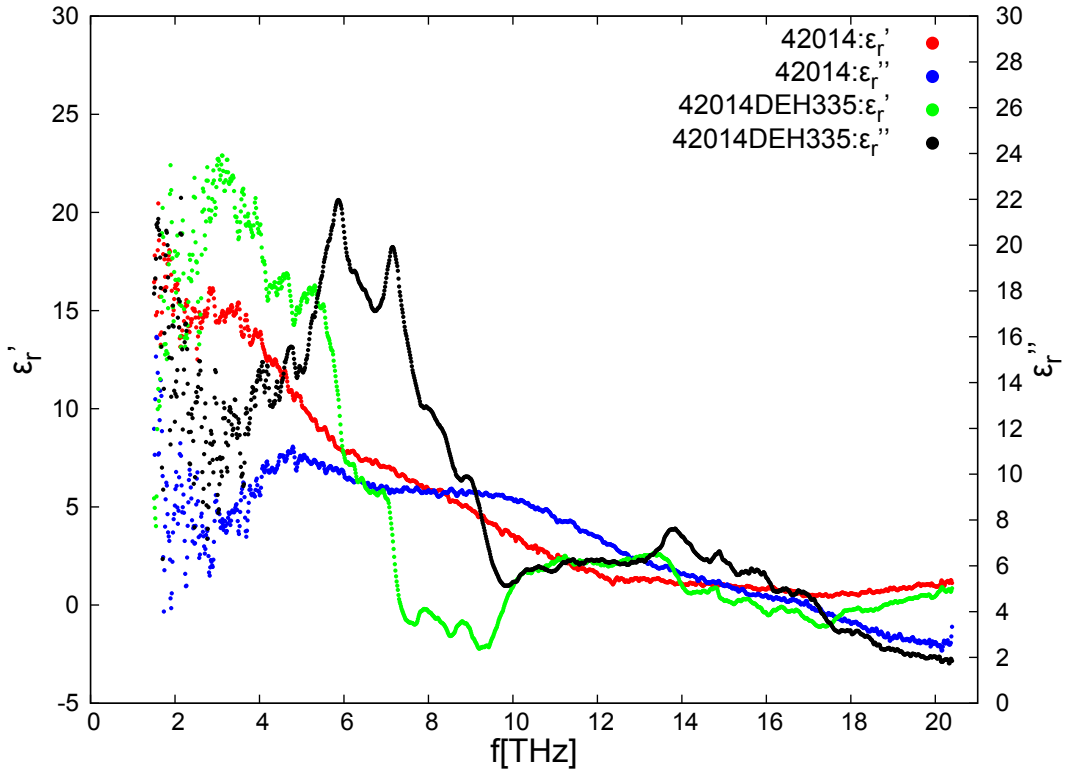

Figure 4.67: Dielectric properties of 42014 and 42014DEH335

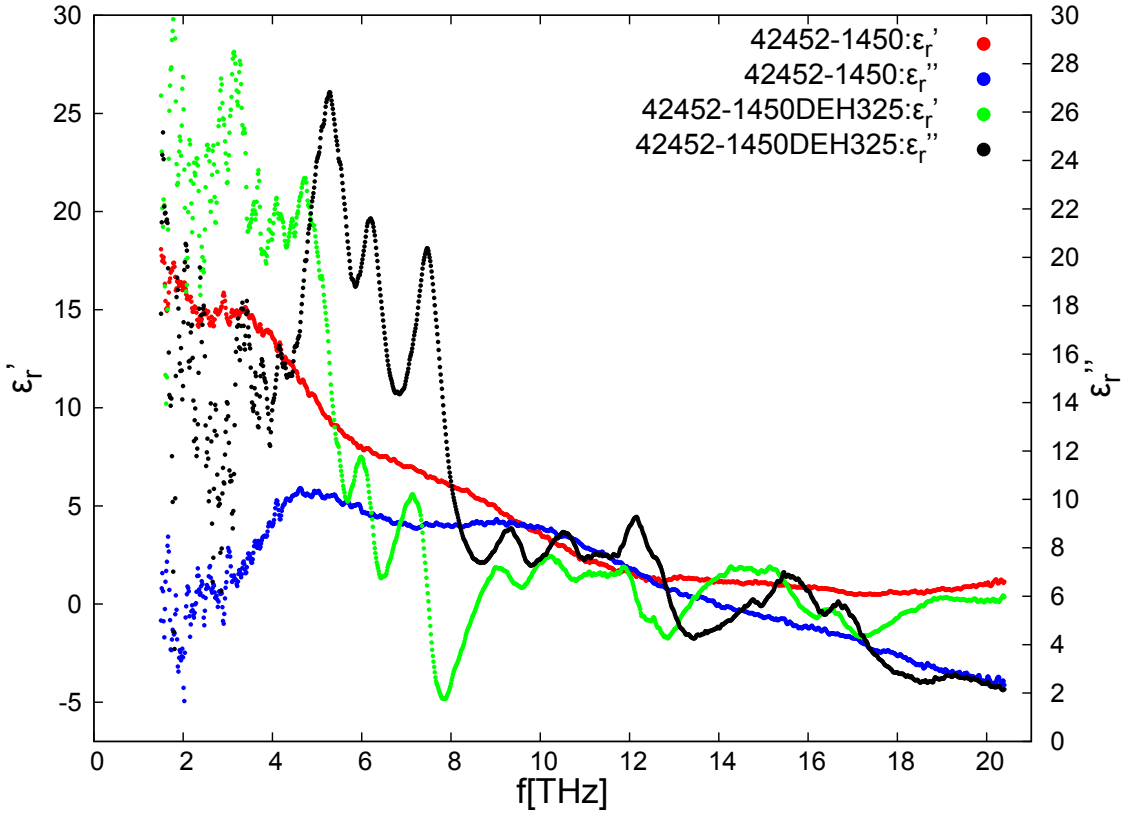

Figure 4.68: Dielectric properties of 42452-1450 and 42452-1450DEH325

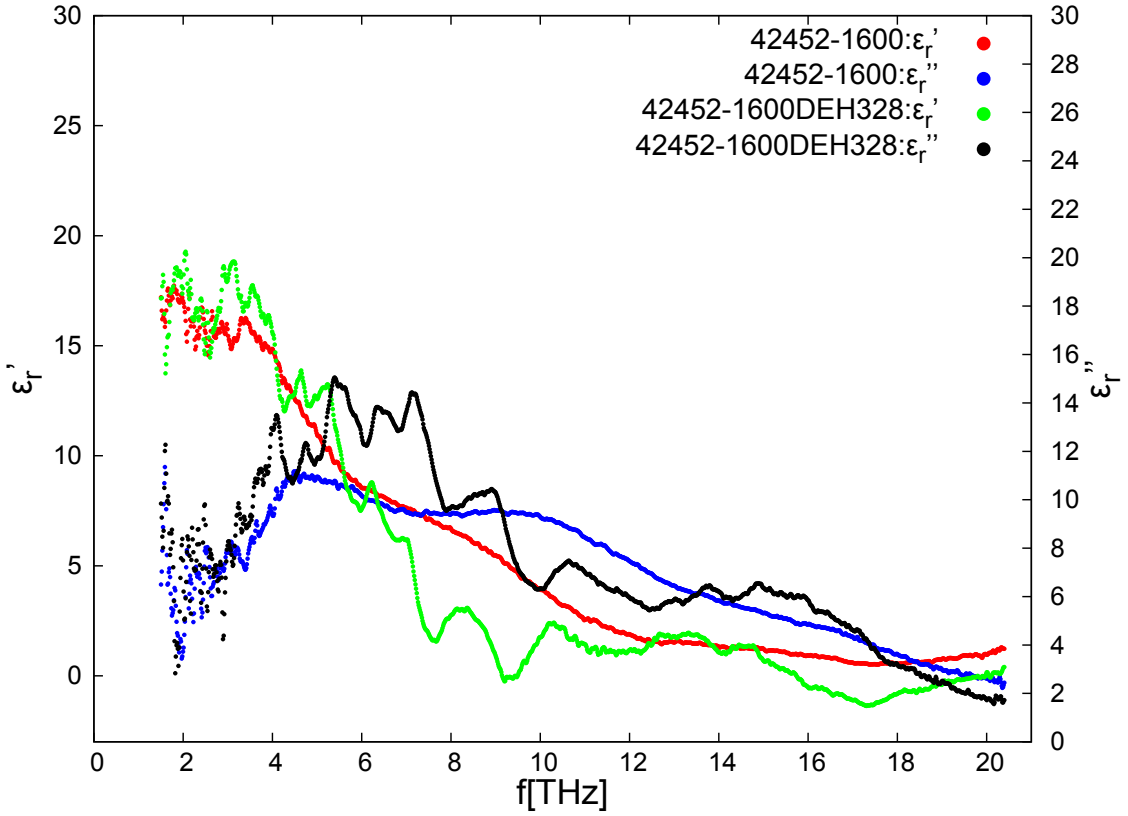

Figure 4.69: Dielectric properties of 42452-1600 and 42452-1600DEH328

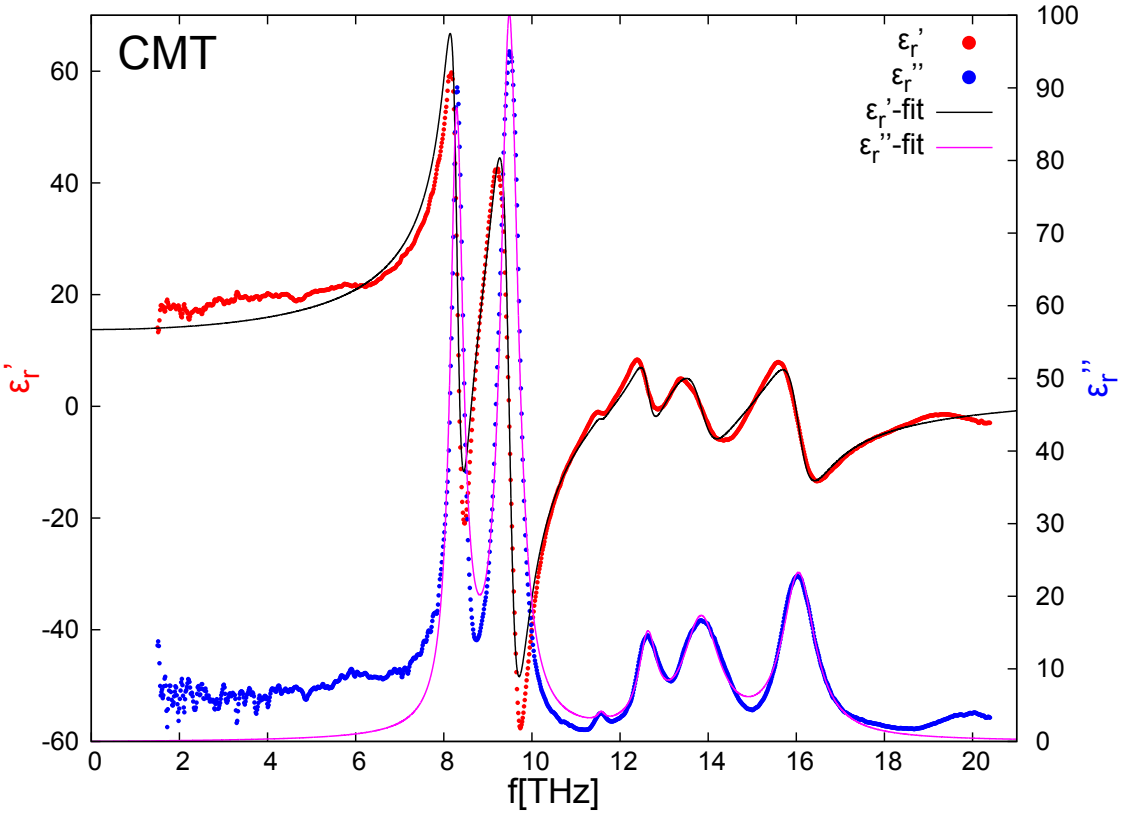

Figure 4.70: Dielectric properties of CMT ($Ca_{0.05}Mg_{0.95}TiO_3$)

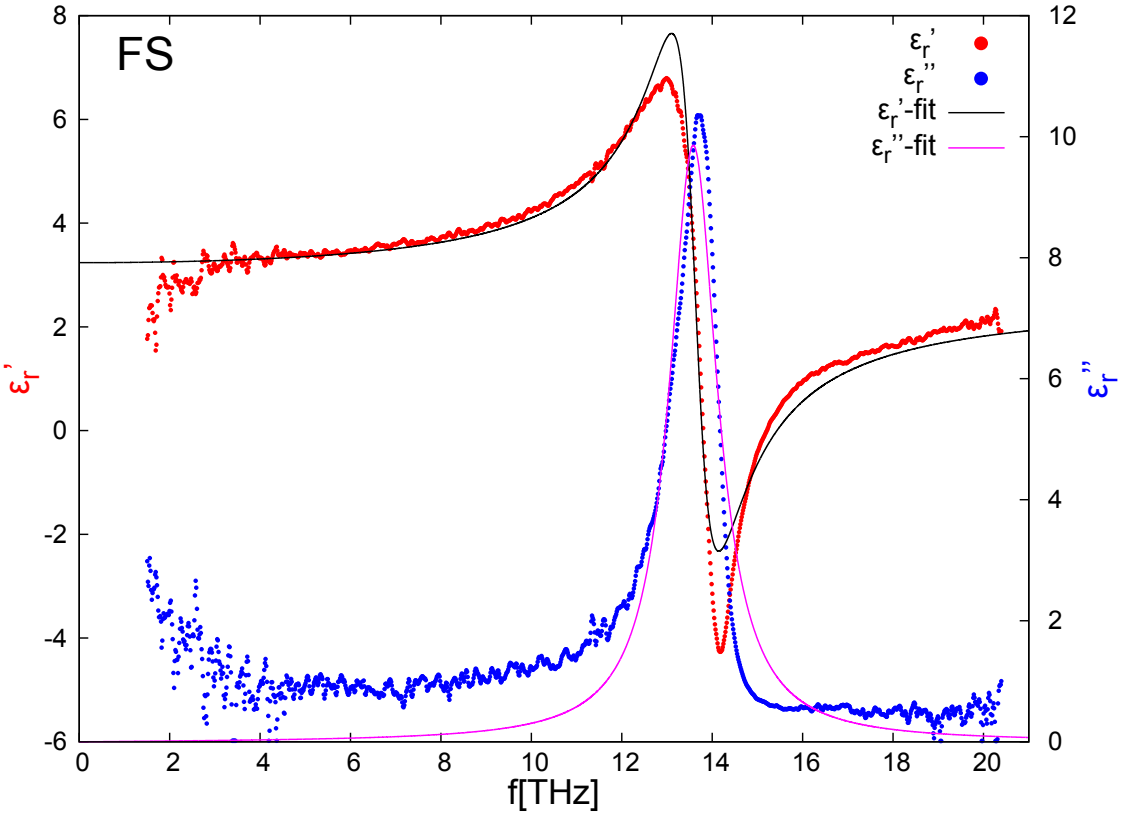

Figure 4.71: Dielectric properties of FS (fused silica/amorphous SiO_2)

5 Dielectric loaded antennas (DLA)

5.1 DLA basics

In this chapter the basic working principle of the DLA will be shortly summarized. The antenna type used for the implementation of the investigated dielectric glass-ceramic was a dielectric loaded helical antenna (helix antenna, see fig. 5.4(b)). These antennas are used in GPS applications, where circularly polarized radiation is of advantage due to the varying orientation of emitter (GPS satellite) and receiver. The antenna polarization is fixed to either RHCP or LHCP (right/left hand circularly polarized). The optimal radiation characteristic (directional dependence of the radiation intensity) should be semispherically oriented in upwards direction to cover the complete hemisphere (see fig. 5.1(a)).

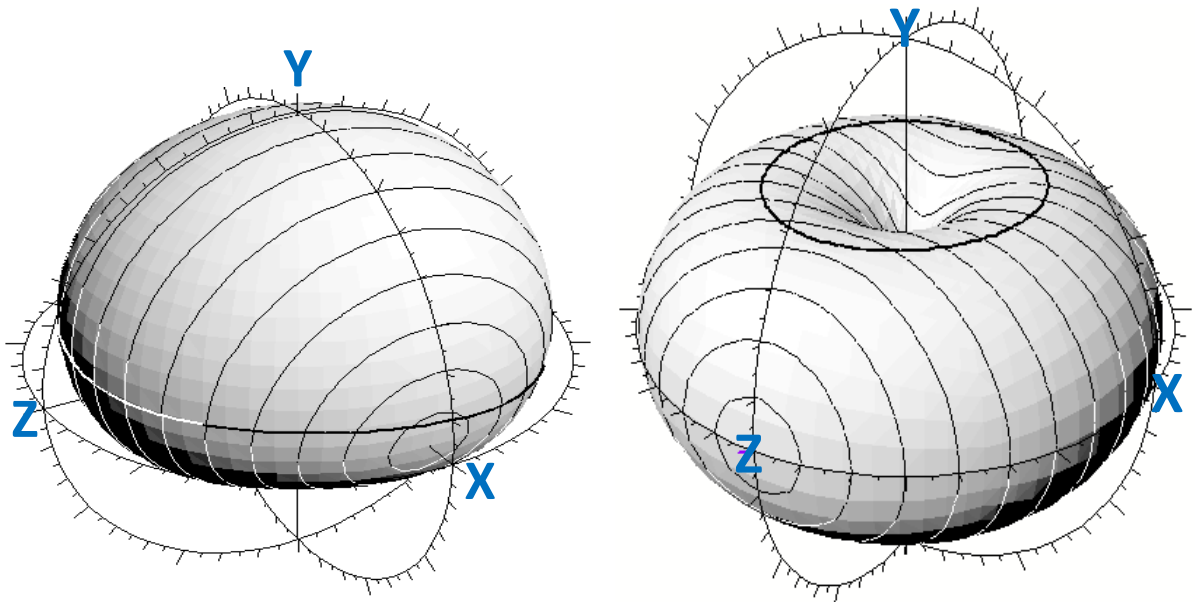

(a) Ideal radiation characteristic for GPS antennas (cardiod pattern)

(b) Typical dipole radiation characteristic (toroid pattern, dipole oriented along the Y-axis)

Figure 5.1: 3D radiation characteristics [Lei11]

To fulfill these requirements an antenna with multifilar helix design can be used. The working principle can be explained on the basis of the radiation characteristic of a Hertzian dipole. A resting dipole (resp. dipole antenna) emits linearly polarized (LP) radiation with maximum intensity in direction orthogonal to the dipole axis resp. minimum intensity in axial direction (see fig. 5.1(b)). A rotating dipole emits circularly polarized (CP) radiation, but splitted into 50 % RHCP and 50 % LHCP radiation depending on the orientation to the plane of rotation (see fig. 5.2(a)). One possibility to transform the unwanted circular polarization direction is the use of a reflective metal plate (see fig. 5.2(b)). This method leads to additional losses and is sometimes not compatible as implementation with other microelectronic components in the device. A helically rotating dipole can focus the radiation pattern in the direction of the helix and thereby surpress emission in the opposite direction, creating a mainly RHCP or LHCP radiation pattern which suits the requirements mentioned above (see fig. 5.2(c)). This helically rotating dipole can be implemented in an antenna by metallizing a helix structure on a dielectric of hollow cylindrical shape (see tab. 5.1).

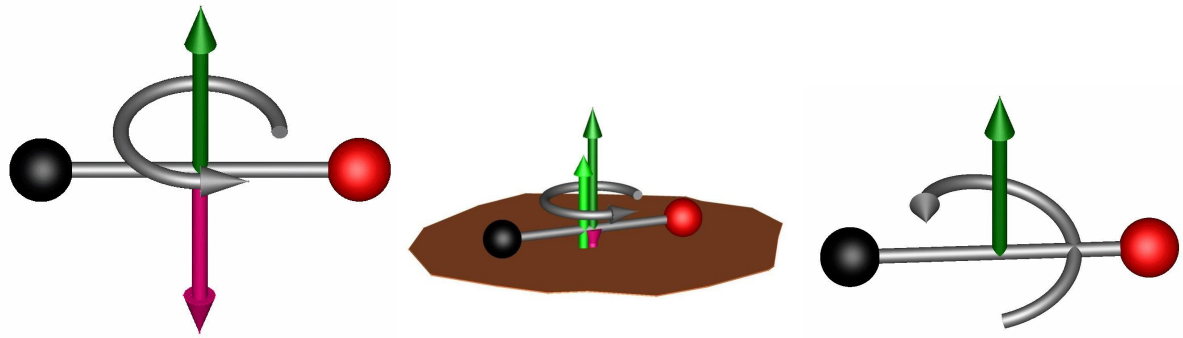

(a) Circularly rotating dipole

(b) Use of a reflective metal plate to transform LHCP amount to RHCP

(c) Helically rotating dipole

Figure 5.2: Explanation of the helix structure (green: RHCP, red: LHCP) [Lei11]

5.2 Antenna manufacturing

The antenna manufacturing and the characterization of the radiation patterns was performed at the research facilities of Sarantel Ltd. (UK). The glass-ceramics were prepared mechanically to the required hollow cylindrical geometry (see fig. 5.3). The metallization is brought on the dielectric blank using a 3D photolithography process. The 5 steps are shown in tab. 5.1:

1. The hole surface is coated galvanically with a copper layer of ($\approx$ 20 µm)
2. Complete coating with a polymer photoresist (blue) and subsequent radiation with a 355 nm laser along the helix path (laser radiation stabilizes the polymer against weak acids)
3. Detachment of the non-radiated photoresist using a weak acid
4. Dissolving of the exposed copper with a highly concentrated $FeCl_3$ - solution
5. Complete detachment of the photoresist using a strong acid
6. Assemblage of the antenna feed (cable and matching network)

Table 5.1: Helix antenna manufacturing process

5.3 Comparative measurement with antennas made from sintered ceramics

For the characterization of the antennas (which are used as receiving antennas in application) one can benefit from the reciprocity theorem (follows directly from the symmetry properties of the Maxwell equations). It states that passive components as antennas have identical receive and transmit properties [Poz04]. The characterization of the antennas is therefore performed by measuring their radiation emission in a full 4π solid angle (see fig. 5.4(a))

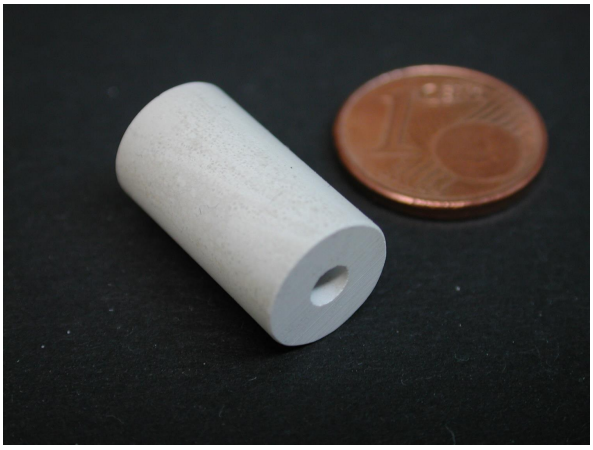

(a) Glass-ceramic blank

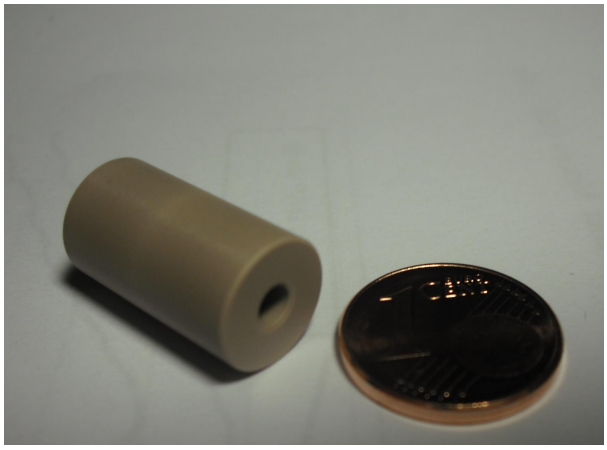

(b) Sintered ceramic blank from CMT

Figure 5.3: Hollow cylindrical dielectric blank (H = 17.75 mm, D_{out} = 10.0 mm, D_{in} = 3.1 mm)

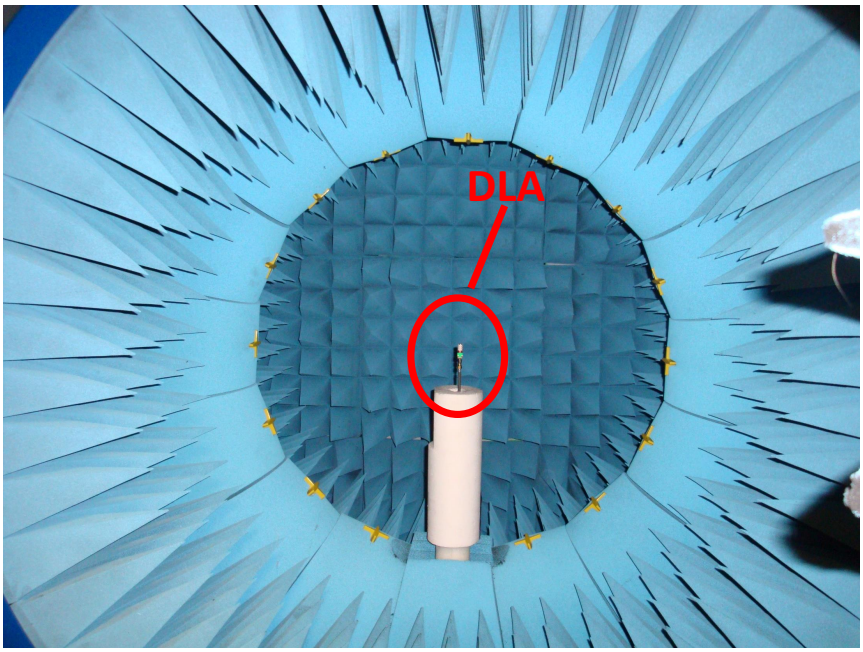

(a) Anechoic antenna measurement chamber for a full 4π solid angle characterization of the radiation pattern

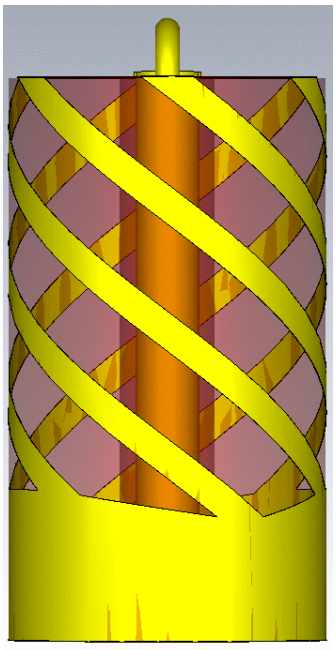

(b) Model of the hexafilar artwork

Figure 5.4

Two test series were analyzed using glass-ceramics with similar permittivity but comparatively higher dielectric loss than the used sintered ceramic blanks. An identical artwork (metallization geometry and hexafilar type, see fig. 5.4(b)) was chosen so that the ohmic/copper losses could be assumed identical for glass-ceramic and sintered ceramic antennas.

5.3.1 First prototype series

The first glass-ceramic antenna series was made to check if any technical problems (metal adhesion, resistance against the used chemicals, etc.) would appear and if glass-ceramic dielectric blanks in general are suitable to be used in this type of dielectric loaded antenna applications. 4 glass-ceramic blanks of an early (non-optimized) La_2O_3-TiO_2-SiO_2-B_2O_3 system with the dielectric properties ε_r = 21.2, Qf = (2100 $\pm$ 200) GHz (measured at 10.6 GHz) were compared with 5 commercial sintered ceramics ($Ca_{0.05}Mg_{0.95}TiO_3$, abbr.: CMT) with ε_r = 21.1, Qf = (50000 $\pm$ 2000) GHz (measured at 5.6 GHz). In the further discussion the two systems will be referred as GC1 and CMT. The data from the best antenna of each ceramic type was selected and shown in comparison. The antennas were characterized concerning radiation efficiency $\eta = P_R/P_0$ (P_R: total radiated power (RHCP and LHCP) in the full solid angle, P_0 power provided by the source), maximum gain G_M and radiation pattern $G(\theta, \phi)$ in dependence of polarization (RHCP/LHCP). The radiation efficiency and the gain (due to its direct dependence on η) needed to be corrected for impedance mismatch, as the antenna impedance is difficult to adjust to the source impedance of Z_0 = 50 Ω. Due to the impedance mismatch a part (P_{refl}) of the provided power P_0 is reflected back to the source (analog to eq. (3.8)):

$$P_{\text{refl}} = |\Gamma|^2 P_0 \quad \text{, with} \quad \Gamma = \frac{Z_A - Z_0}{Z_A + Z_0} \quad . \tag{5.1}$$

The real (for the case of perfect match corrected) efficiency η therefore follows from the measured efficiency by (analog for the gain):

$$\eta = \eta_{\text{meas}} \cdot \frac{1}{1 - |\Gamma|^2} \quad \text{, with} \quad P_0 = P_{\text{refl}} + P_{0,\text{meas}} \quad . \tag{5.2}$$

The antenna gain $G(\theta, \phi) = \eta \cdot D(\theta, \phi)$ is the product of efficiency and directivity D. $D(\theta, \phi)$ is the ratio of radiated power $P(\theta, \phi)$ in direction of (θ, ϕ) (spherical coordinates) to the over the full solid angle averaged radiated power $\bar{P} = \frac{1}{4\pi} \int P(\theta, \phi)\, \mathrm{d}\Omega = P_R/4\pi$.

$$D(\theta, \phi) = \frac{P(\theta, \phi)}{P_R/4\pi} \quad \text{, with} \quad \int P(\theta, \phi)\, \mathrm{d}\Omega = P_R \quad . \tag{5.3}$$

D can also be interpreted as ratio of radiated power relative to an (ideal) isotropic antenna with $P_{\text{iso}}(\theta, \phi) = P_R/4\pi$. The radiation pattern $G(\theta, \phi)$ can be represented by an elevation plot which is a 2D G-θ polar plot for fixed angles of ϕ. In fig. 5.5 the radiation patterns of the best glass-ceramic and CMT antenna are shown.

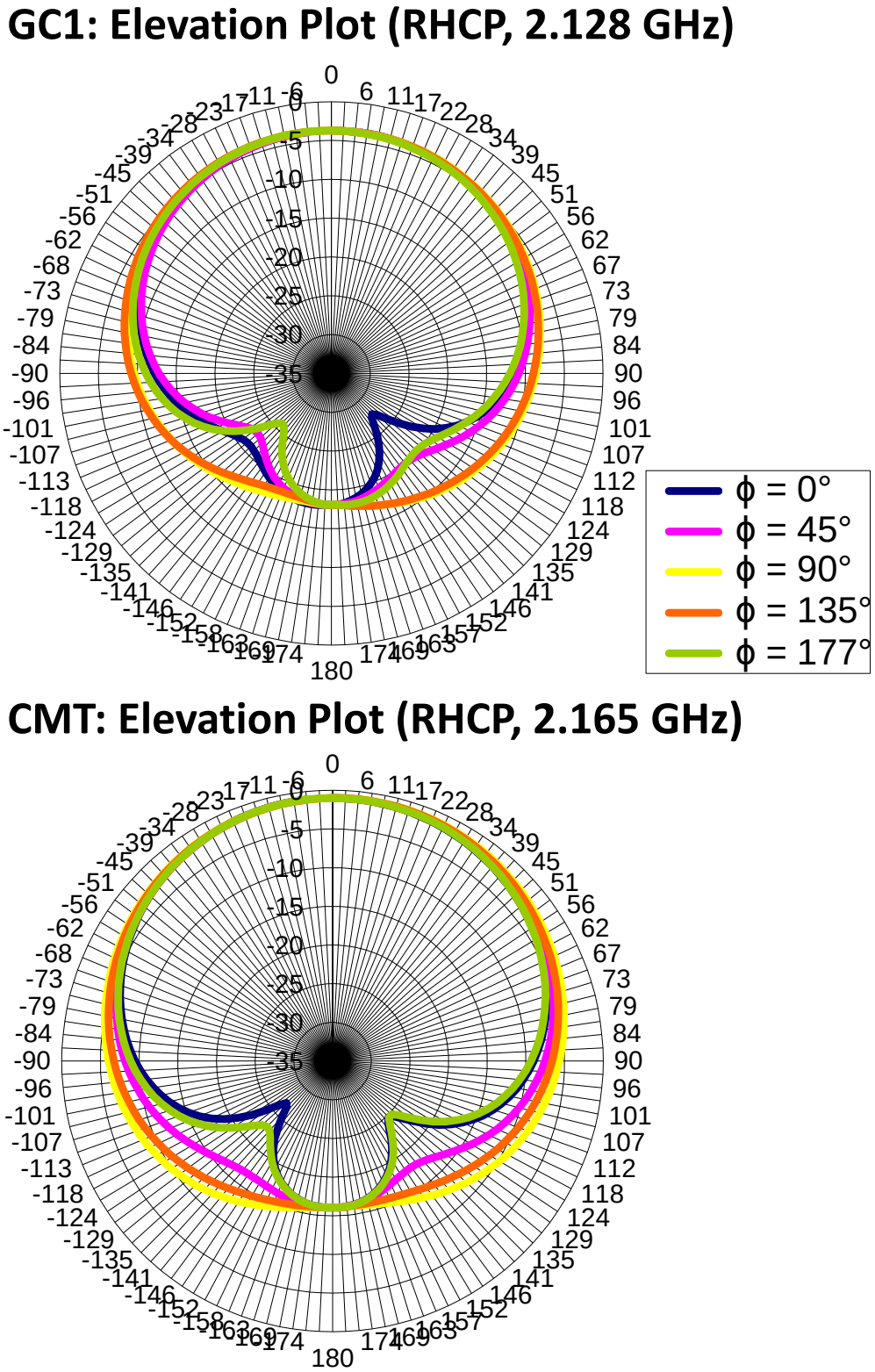

Figure 5.5: Comparison of the elevation plots $G_\phi(\theta)$ for GC1 glass-ceramic (top) and CMT ceramic (bottom)

It can be seen, that except of the difference in radiation efficiency, both antennas provide a similar and optimal spatial radiation distribution (cardiod pattern). In tab. 5.2 the maximum (zenith) gain and the efficiency are given (measured and impedance mismatch corrected). The glass-ceramic antenna already has around 70 % of the efficiency of the CMT antenna, which is remarkably considering the large difference in dielectric loss of both materials ($Qf_{\mathrm{CMT}}/Qf_{\mathrm{GC1}} \approx 25$). Furthermore, tests concerning the mechanical stability of the metallization were performed. SEM investigations on the sintered ceramic blanks showed that their poor metal adhesion is related to the porosity of the material (see fig. 5.6). The surface grinding process, which is used to prepare the hollow cylindrical shape leads to a smooth surface but loose and mechanically unstable surface structure beneath. Parts of the surface can therefore easily be lifted off with the attached metal. A further problem is outgassing of liquids (mostly chemicals from the metallization process) which are enclosed in the pores below the surface. Outgassing can cause a lift off of the metallization and destroy the device during further manufacturing processes during which temperatures up to 400 °C can be reached. The adhesion tests on the intrinsically pore-free glass-ceramics and also tests on pure glass cylinders showed a one order of magnitude better metal to dielectric adhesion.

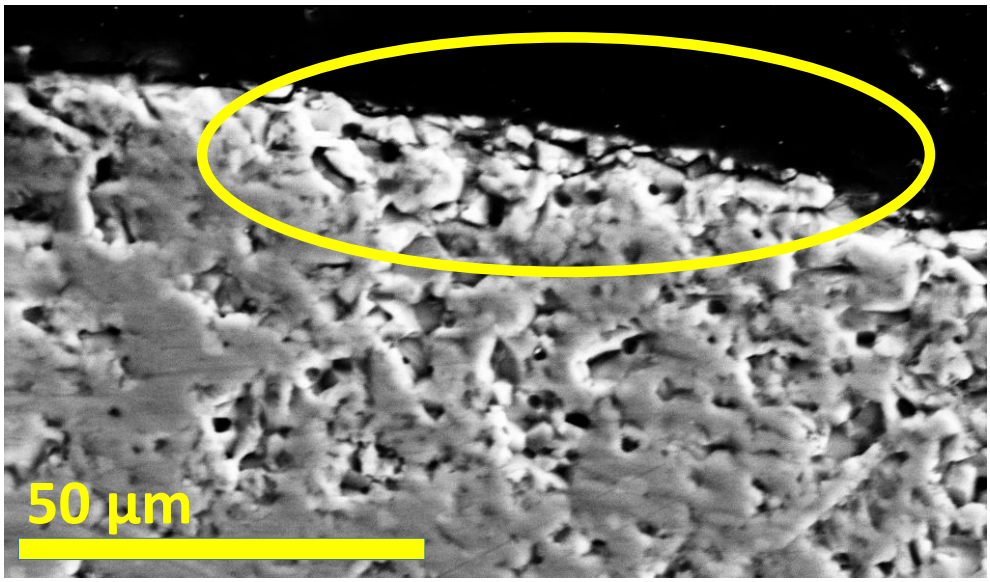

Figure 5.6: SEM image of the CMT surface showing a loose surface structure due to the high level of porosity

In conclusion it can be stated that in the first series it was proven that the glass-ceramic antennas could solve the manufacturing related problems mentioned above, but their efficiency still needed to be increased. Therefore a second antenna series with a higher Qf material was made.

Material	f_{res}[GHz]	Z_A/Z_0	η_{meas}	η	$G_{M,\text{meas}}$[dB]	G_M[dB]
GC1	2.128	0.297-i 0.213	0.193	0.283	-3.72	-2.09
CMT	2.165	0.714+i 0.397	0.368	0.398	-0.98	-0.63

Table 5.2: Direct comparison of maximum gain and efficiency of sintered ceramic (CMT) and glass-ceramic (GC1) antenna

5.3.2 Second prototype series

In the second series a glass-ceramic with a higher Qf from a BaO-$\mathrm{TiO_2}$-$\mathrm{SiO_2}$-$\mathrm{Al_2O_3}$ system was investigated as it showed a higher potential for a commercialization than the investigated $\mathrm{La_2O_3}$-based system of this work. But to answer the question, if the efficiency of a glass-ceramic antenna can reach similar values as a ceramic-based antenna, the choice of the glass-ceramic system is not relevant. 10 glass-ceramics blanks with average dielectric properties of ε_r = 32.2, Qf = (8200 $\pm$ 1000) GHz (measured at 4.7 GHz) were compared with 15 commercial sintered ceramics (BaO-$\mathrm{TiO_2}$-based) with ε_r = 37.4, Qf = (30000 $\pm$ 1000) GHz (measured at 4.3 GHz). In the further discussion the two systems will be referred as GC2 and BT. In tab. 5.3 a direct comparison of the average results for the antenna efficiency and maximum gain are shown. For a difference of $Qf_{\text{BT}}/Qf_{\text{GC2}} \approx 3.6$ the efficiency difference only becomes 28.6 to 32.9 $\%$. This shows that for such low dielectric loss values (as in the case of GC2), the dielectric losses only give a minor contribution to the total losses of the antenna (mainly dominated by ohmic losses in the copper and the electronic components). Considering the antenna gain, which is the even more important performance parameter for antenna engineers, the glass-ceramic antennas are even slightly better (-2.37 to -2.47 dB). An explanation for the better directivity/gain could be the better uniformity of the glass-ceramic blanks. The radiation pattern (fig. 5.7) and the RHCP to LHCP polarization (fig. 5.8) show optimum values (nearly ideal cardoid pattern and full RHCP polarization). In conclusion it can be stated that the prototype series proved that glass-ceramics can provide the necessary dielectric requirements and show in addition superior manufacturing related advantages due to their intrinsic pore-freeness and homogeneity.

Material	f_{res}[GHz]	Δf[MHz]	$\bar{\eta}$	$\bar{G}_M$[dB]
GC2	1.5821	2.14	0.286	-2.37
BT	1.6584	0.66	0.329	-2.47

Table 5.3: Direct comparison of the average results for glass-ceramic (GC2) and ceramic (BT) antenna series ($\bar{f}_{\text{res}}$: average resonance frequency, Δf: standard deviation, $\bar{\eta}$: average efficiency, $\bar{G}_M$: average maximum gain)

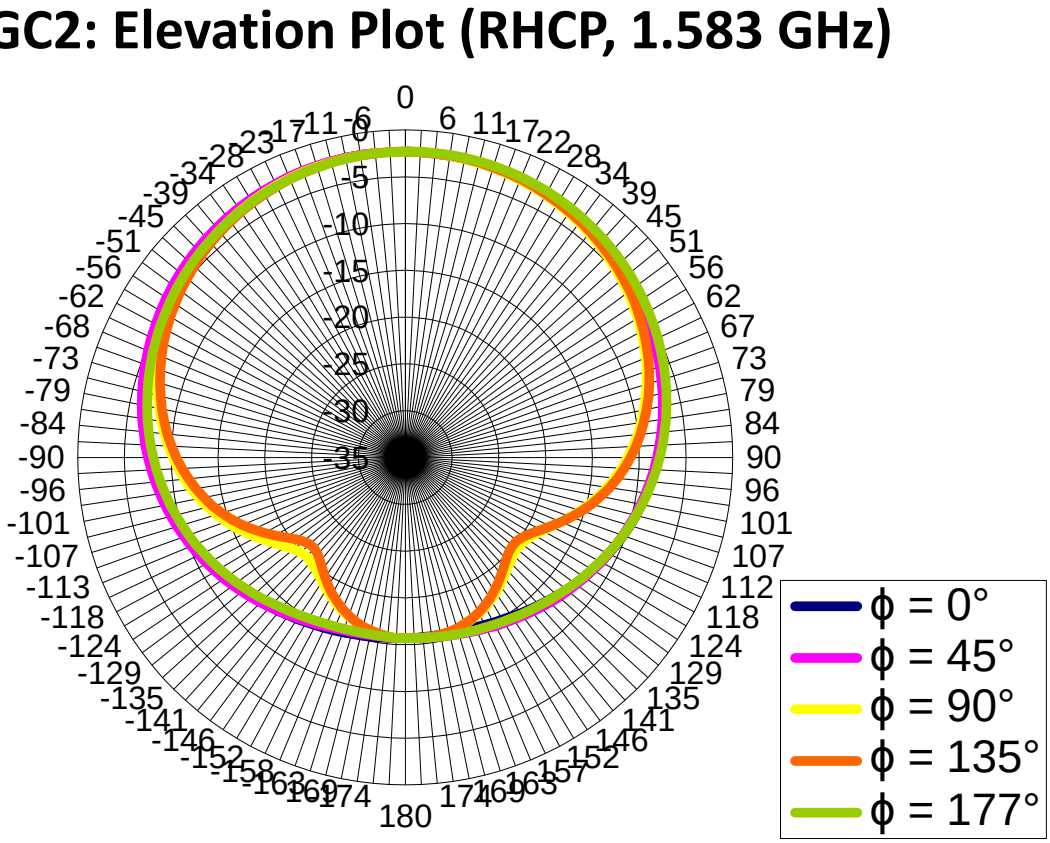

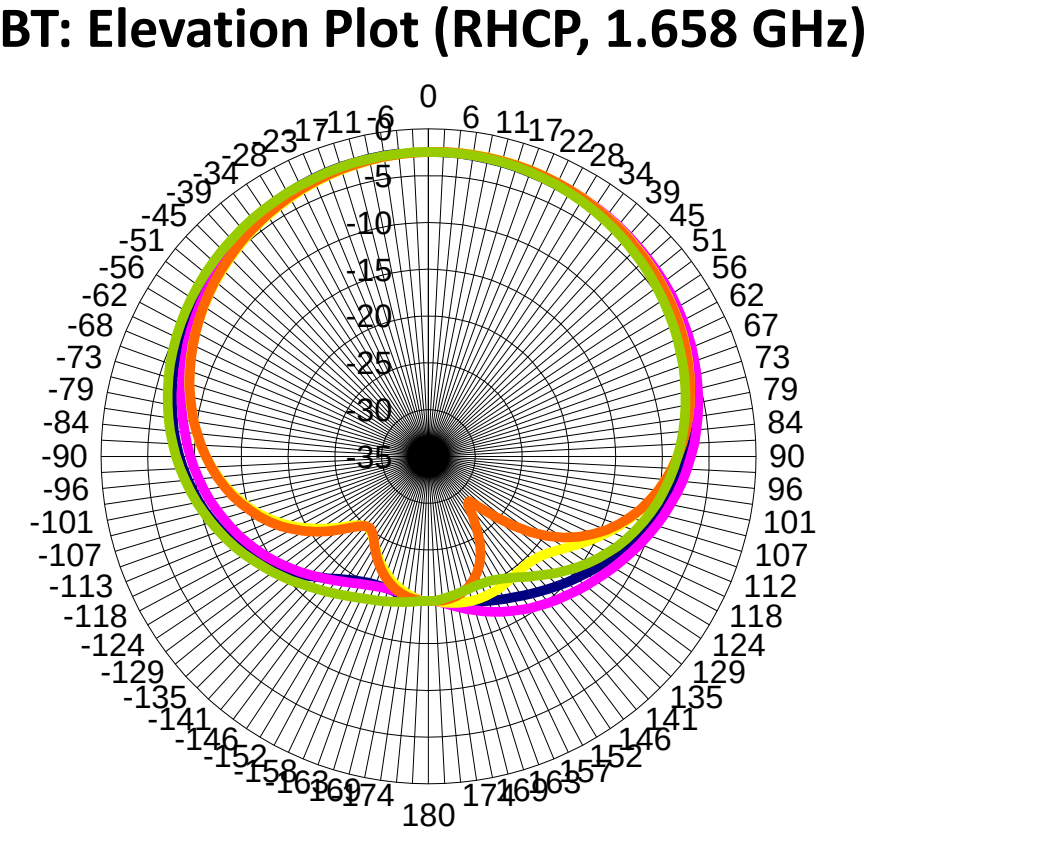

Figure 5.7: Comparison of the elevation plots $G_\phi(\theta)$ of the best prototypes for GC2 glass-ceramic (top) and BT ceramic (bottom)

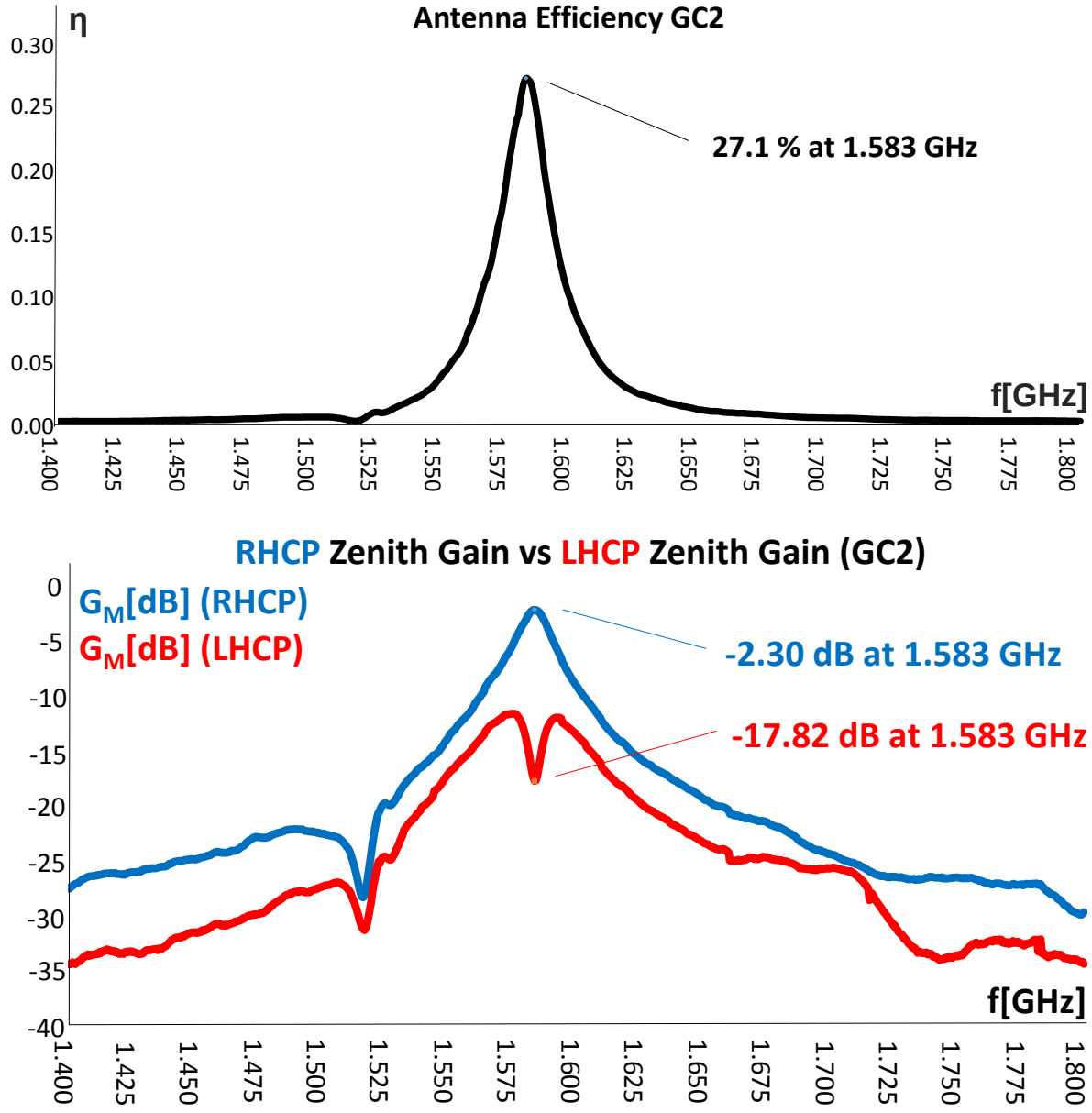

Figure 5.8: Top: measured antenna efficiency, bottom: measured RHCP and LHCP gain (both plots not corrected for impedance mismatch, Z_A/Z_0 = 1.352+i 0.145; plot of the best GC2 prototype)

6 Conclusion

The aim of this work was the development and characterization of a dielectric glass-ceramic material in the La_2O_3-TiO_2-SiO_2-B_2O_3 system. Based on a previous work [Bra11], the material needed further optimization to achieve suitable dielectric properties in consideration of the given requirements for DLA applications ($\varepsilon_r > 20$, $Qf > 5000$ GHz, $|\tau_f| < 20$ ppm/K).

The first step was the modification of the glass composition to achieve a stable glass with a lower amount of glass-forming oxides. A stable glass-forming region could be identified and the amount of glass-forming oxides could be reduced from 42.1 at% (36436: best melt of [Bra11]) to 29.9 at% (42014) leading to dielectric properties of the associated glass-ceramics which could fulfill the given requirements. In fig. 6.1 a direct comparison between the best melts of this work and [Bra11] is shown. In the range of $|\tau_f| < 20$ ppm/K, ε_r values of 22.5 and $Qf = 9590$ GHz could be achieved.

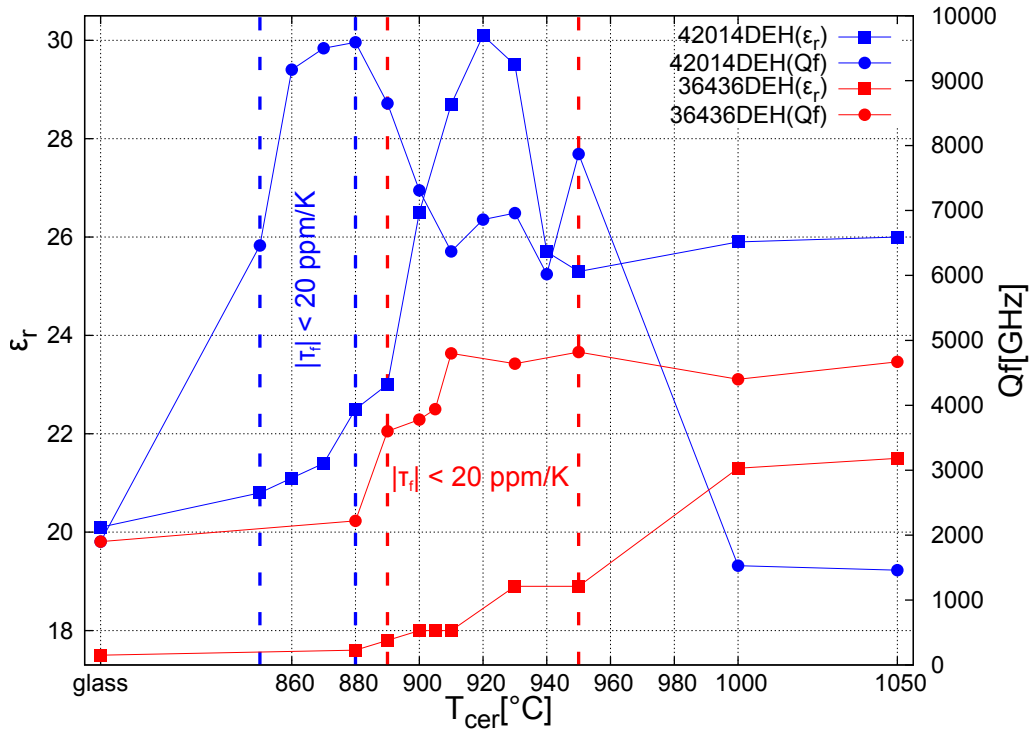

Figure 6.1: Comparison of the dielectric properties (ε_r: ■, Qf: •) of the best melt of this work (42014) and of [Bra11] (36436)

The undoped basic glass composition needed to be stabilized against surface devitrification, which could be solved by a partial substitution of the TiO_2 content by ZrO_2. The formation of Ti^{3+}, which led to a significant increase of the dielectric loss could be successfully prevented by using CeO_2 as oxidizing agent. The redox interaction of the polyvalent ions inside the glass could be understood and verified by the use of combined EPR and optical transmission methods. Sb_2O_5 was shown to be unsuitable as oxidizing agent for the use in titanate-based glass-ceramics. The Sb^{5+} ion is able to substitute on the Ti-site inside the crystal leading to a reduction of the Ti^{4+} to Ti^{3+} due to charge compensation. The relevant nucleation mechanisms (surface, Pt, Ti^{3+}) could be identified and correlated to the formation of certain crystalline phases. The influence of the used dopants and the ceramization process on the formation of the crystalline phases inside the glass-ceramic was investigated via XRD and SEM/TEM in combination with EDX/EELS for a compositional analysis. The GHz characterization was performed using the Hakki-Coleman and the cylindrical cavity resonance method. The general high frequency loss mechanisms (conductivity, phonon interaction) and their contribution to the loss in the GHz range were investigated. Conductivity measurements in the MHz range and THz synchrotron ellipsometry were made. The evaluated dielectric properties were extrapolated from the adjacent frequency ranges to the GHz region, showing that conductivity and one-phonon absorption losses are no major contributions to the dielectric loss in the GHz range. It was shown that the investigated glass-ceramics are suitable for the use in DLA applications. Two prototype series were made and evaluated which proved that glass-ceramic based dielectrics are a suitable alternative to existing sintered ceramics. Additionally the theoretical description of the Hakki-Coleman method was modified to enable the measurement of hollow-cylindrically shaped samples. In tab. 6.1 the most relevant samples of this work are summarized.

Sample	ε_r	Qf	$\tan(\delta)$	τ_f	f	description
42014	20.1	1900	5.6	-83	10.6	glass
42014DEH373	21.4	9500	1.1	-1	10.4	1 mol% CeO_2, 7.5 mol% ZrO_2
42014DEH354	22.5	9590	1.1	+18	10.2	1 mol% CeO_2, 7.5 mol% ZrO_2
42014DEH347	30.1	6860	1.3	+169	8.9	1 mol% CeO_2, 7.5 mol% ZrO_2
42732DEH357	23.0	6380	1.6	+23	10.1	1 mol% CeO_2, 10 mol% ZrO_2
42732DEH352	33.7	6140	1.4	>170	8.3	1 mol% CeO_2, 10 mol% ZrO_2
42452-1450DEH325	26.9	1630	5.7	80	9.2	Ti^{3+} nucleated
42452-1600DEH328	21.5	9710	1.1	16	10.3	Pt(+Ti^{3+}) nucleated

Table 6.1: Summary of the most relevant samples (Qf in GHz, τ_f in ppm/K, $\tan(\delta)$ in 10^{-3}, f in GHz)

Further optimization of the material properties could be still achieved by minimizing the doping content of CeO_2 in the range between 0.1-1.0 mol% CeO_2. The optimum amount of ZrO_2 for a maximum P1 phase content in combination with a low surface devitrification should be between 5-10 mol%. An important improvement, especially regarding a possible commercialization of the investigated system, would be the minimization of the Pt corrosion. It was shown that with appropriate melting conditions (T_m = 1500 °C, low keeping time, use of oxidizing agents) the Pt content could be reduced drastically, even though another alternative nucleation mechanism for the $La_4Ti_9O_{24}$/P1 phase would be necessary (e.g. additives as SnO_2 showed already in small amounts a strong effect on the crystallization behavior).
In conclusion, it can be summarized that within the framework of this work, the suitability of the investigated La_2O_3-TiO_2-SiO_2-B_2O_3-based glass-ceramics for the use in DLA applications was proved and the macroscopic dielectric properties could be correlated resp. modified by the control of the microstructure of the material.

A Appendix

A.1 XRD data

	$La_2Ti_2SiO_9$	$La_4Ti_9O_{24}$	TiO_2	$LaBO_3$	$LaBSiO_5$
JCPDS(ICCD)	01-082-1490	00-036-0137	01-086-0148	00-012-0762	01-077-0989
CIF(COD)	1008953	80052	9001681	2208746	1511205
Data Source	[BMT94]	[MOC95]	[SSL95]	[NOA$^+$06]	[MGSL93]
ρ[g/cm^3]	5.21	4.97	4.23	5.30	4.72
Crystal system	monoclinic	orthorhombic	tetragonal	orthorhombic	hexagonal
Space group	C2/m	Fddd	P42/mnm	Pnam	P31
a[$\mathring{A}$]	17.0290	35.4100	4.5922	5.8720	6.8150
b[$\mathring{A}$]	5.7415	14.1400	4.5922	8.2570	6.8150
c[$\mathring{A}$]	7.6310	14.5800	2.9574	5.1070	6.7580
α[°]	90.00	90.00	90.00	90.00	90.00
β[°]	111.22	90.00	90.00	90.00	90.00
γ[°]	90.00	90.00	90.00	90.00	120.00

Table A.1: XRD reference data

A.2 Sample composition

The chemical composition of the samples can be given in 3 different ways. Considering an example of a melt of the stoichiometry a AO - b B_2O_3 - c CO_2 - d D_2O_5:

- mole fraction x_i (mol%): $x_a[\%] = a/(a+b+c+d) \cdot 100$
- atomic fraction p_i (at%): $p_a[\%] = a/(a+2b+c+2d) \cdot 100$
- weight fraction w_i (wt%): $w_a[\%] = x_a \cdot M_a/M \cdot 100$,

with M_i molar mass of compound i and $M = \sum_i x_i M_i$ average molar mass.

A.3 Mathematica8.0 scripts for the GHz characterization

```
(* HAKKI-COLEMAN SCRIPT *)

(* Definition of J'm(x) // K'm(x) // y(f,a,h,p) // x(f,e,a,h,p) *)
dj = Function[{x, m}, 1/2 (BesselJ[-1 + m, x] - BesselJ[1 + m, x])] ;
dk = Function[{x, m}, 1/2 (-BesselK[-1 + m, x] - BesselK[1 + m, x])];
y = Function[{f, a, h, p}, Sqrt[(a / h * p * Pi)^2 - (20 / 3 * Pi * f * a)^2]];
x = Function[{f, e, a, h, p}, Sqrt[-(a / h * p * Pi)^2 + (20 / 3 * Pi * f * a)^2 * e]];
(* Definition of F1(TM), F2(TE), F3(HEM) and the eigenvalue equation ew *)
f1 = Function[{f, e, a, h, p, m},
   dj[x[f, e, a, h, p], m] / x[f, e, a, h, p] + dk[y[f, a, h, p], m] *
     BesselJ[m, x[f, e, a, h, p]] / (e * y[f, a, h, p] * BesselK[m, y[f, a, h, p]] )];
f2 = Function[{f, e, a, h, p, m}, dj[x[f, e, a, h, p], m] / x[f, e, a, h, p] +
    dk[y[f, a, h, p], m] *
     BesselJ[m, x[f, e, a, h, p]] / ( y[f, a, h, p] * BesselK[m, y[f, a, h, p]] )];
f3 = Function[{f, e, a, h, p, m}, p * Pi / h * m / ((20 / 3 * Pi * f) * Sqrt[e])
    BesselJ[m, x[f, e, a, h, p]] * (1 / x[f, e, a, h, p]^2 + 1 / y[f, a, h, p]^2)];
ew = Function[{f, e, a, h, p, m}, f1[f, e, a, h, p, m] * f2[f, e, a, h, p, m] -
    f3[f, e, a, h, p, m]^2];
(* Definition tanδ = A/Qu - B *)
aq = Function[{f0, ϵ, a, h, p},
   1 + (BesselJ[1, x[f0, ϵ, a, h, p]] / BesselK[1, y[f0, a, h, p]])^2 / ϵ *
     ((BesselK[0, y[f0, a, h, p]] * BesselK[2, y[f0, a, h, p]] -
          BesselK[1, y[f0, a, h, p]]^2) / (BesselJ[1, x[f0, ϵ, a, h, p]]^2 -
          BesselJ[0, x[f0, ϵ, a, h, p]] * BesselJ[2, x[f0, ϵ, a, h, p]])) ] ;
rs = Function[{f0, σ}, (20 * Pi * Sqrt[f0 / σ])];
bq =
  Function[{f0, ϵ, a, h, p, σ}, p^2 * 9 * rs[f0, σ] / (8 * 10^4 * Pi^2 * f0^3 * h^3 * ϵ) *
    (1 + (BesselJ[1, x[f0, ϵ, a, h, p]] / BesselK[1, y[f0, a, h, p]])^2 *
       ((BesselK[0, y[f0, a, h, p]] * BesselK[2, y[f0, a, h, p]] -
            BesselK[1, y[f0, a, h, p]]^2) / (BesselJ[1, x[f0, ϵ, a, h, p]]^2 -
            BesselJ[0, x[f0, ϵ, a, h, p]] * BesselJ[2, x[f0, ϵ, a, h, p]]))) ] ;

(* Measurement parameters *)
a = 0.01000 / 2 ;  (* Sample radius a[m] *)
h = 0.00400 ;  (* Sample height h[m] *)
p = 1 ;  (* Node number p (0np-Modes) *)
σ = 5.8 * 10^7;
(* Conductivity of metal plates σ[S/m]: copper: 5.8*10^7silver: 6.3*10^7 *)

(* Determination of permittivity from
 measured TE011 resonance frequency f0[GHz] *)
f0 = 10 ;
FindRoot[f2[f0, ϵ, a, h, p, 0] == 0,
  {ϵ, (3 / 20 / Pi / f0)^2 (3.13979^2 / a^2 + (p * Pi / h)^2)}];
ϵ =
 ϵ /.
  %
```

```
(* Determination of tanδ from measured Q-
 loaded Qm and insertion loss S21[dB] *)
Qm = 500 ;
S21 = -30.0 ;
tanδ = aq[f0, ϵ, a, h, p] / (Qm / (1 - 10^(S21 / 20))) - bq[f0, ϵ, a, h, p, σ]
Qf = f0 / tanδ
Qd = 1 / tanδ

(* OPTIONAL: Identification of the resonance modes for unknown samples *)
ContourPlot[{f2[f, e, a, h, p, 0] == 0, f1[f, e, a, h, p, 0] == 0,
  ew[f, e, a, h, p, 1] == 0, ew[f, e, a, h, p, 2] == 0}, {e, 10, 30}, {f, 5, 15}]
(* mode chart to estimate permittivity / identify modes *)
```

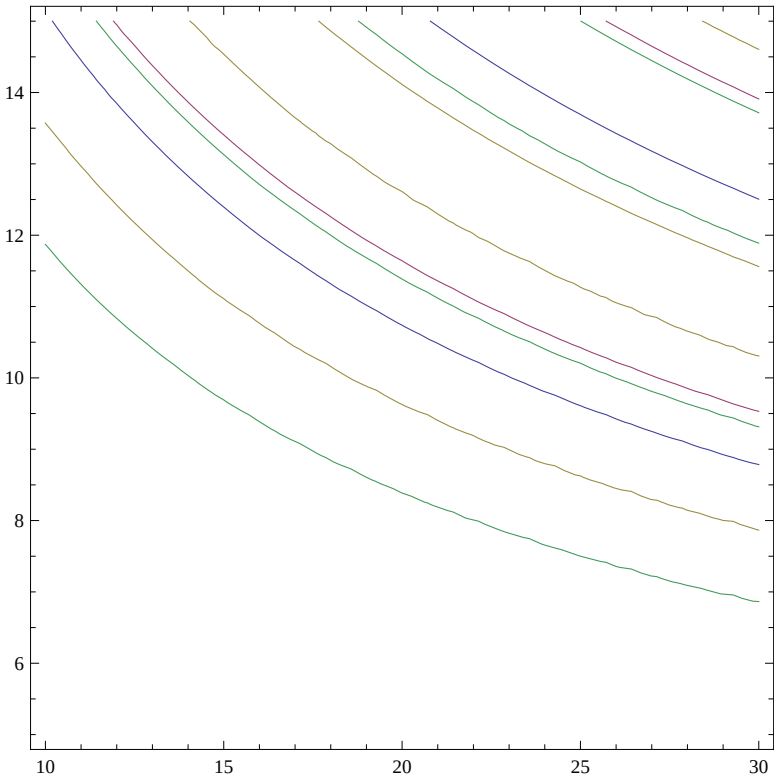


```
e0 = 20; (* Estimated ϵ' *)
(* Calculation of f(HEM111)[GHz], f(TE011)[GHz],
f(HEM211)[GHz], f(TM011)[GHz] for estimated ϵ' *)
FindRoot[ew[fr1, e0, a, h, p, 1] == 0,
  {fr1, 3 / 20 / Pi * Sqrt[2.210997^2 / a^2 + (p * Pi / h)^2] / Sqrt[e0]}];
fr1 = fr1 /. % ;
FindRoot[f2[fr2, e0, a, h, p, 0] == 0,
  {fr2, 3 / 20 / Pi * Sqrt[3.139790^2 / a^2 + (p * Pi / h)^2] / Sqrt[e0]}];
fr2 = fr2 /. % ;
FindRoot[ew[fr3, e0, a, h, p, 2] == 0,
  {fr3, 3 / 20 / Pi * Sqrt[3.604967^2 / a^2 + (p * Pi / h)^2] / Sqrt[e0]}];
fr3 = fr3 /. % ;
FindRoot[f1[fr4, e0, a, h, p, 0] == 0,
  {fr4, 3 / 20 / Pi * Sqrt[3.775222^2 / a^2 + (p * Pi / h)^2] / Sqrt[e0]}];
fr4 = fr4 /. % ;
{fr1, fr2, fr3, fr4}
```

```
(* MODIFIED HAKKI-COLEMAN SCRIPT (FOR HOLLOW CYLINDRICAL SAMPLES) *)

(* Definition of radial wave vectors q(f,h,p) // k(f,e,u,h,p) *)
q = Function[{f, h, p}, Sqrt[(1 / h * p * Pi)^2 - (20 / 3 * Pi * f * 1)^2]];
k = Function[{f, e, u, h, p}, Sqrt[-(1 / h * p * Pi)^2 + (20 / 3 * Pi * f * 1)^2 * e * u]];
(* Definition of eigenvalue equations F1(TM0np), F2(TE0np) *)
f1 = Function[{f, e, u, a, b, h, p},
    (BesselI[1, b * q[f, h, p]] * BesselJ[0, b * k[f, e, u, h, p]] - q[f, h, p] / k[f, e,
          u, h, p] * e * BesselI[0, b * q[f, h, p]] * BesselJ[1, b * k[f, e, u, h, p]]) *
      (BesselK[1, a * q[f, h, p]] * BesselY[0, a * k[f, e, u, h, p]] +
        q[f, h, p] / k[f, e, u, h, p] * e * BesselK[0, a * q[f, h, p]] *
         BesselY[1, a * k[f, e, u, h, p]]) -
     (BesselI[1, b * q[f, h, p]] * BesselY[0, b * k[f, e, u, h, p]] -
        q[f, h, p] / k[f, e, u, h, p] * e * BesselI[0, b * q[f, h, p]] *
         BesselY[1, b * k[f, e, u, h, p]]) *
      (BesselK[1, a * q[f, h, p]] * BesselJ[0, a * k[f, e, u, h, p]] +
        q[f, h, p] / k[f, e, u, h, p] * e * BesselK[0, a * q[f, h, p]] *
         BesselJ[1, a * k[f, e, u, h, p]]) ];
f2 = Function[{f, e, u, a, b, h, p}, (BesselI[1, b * q[f, h, p]] *
         BesselJ[0, b * k[f, e, u, h, p]] - q[f, h, p] / k[f, e, u, h, p] *
         u * BesselI[0, b * q[f, h, p]] * BesselJ[1, b * k[f, e, u, h, p]]) *
      (BesselK[1, a * q[f, h, p]] * BesselY[0, a * k[f, e, u, h, p]] +
        q[f, h, p] / k[f, e, u, h, p] * u * BesselK[0, a * q[f, h, p]] *
         BesselY[1, a * k[f, e, u, h, p]]) -
     (BesselI[1, b * q[f, h, p]] * BesselY[0, b * k[f, e, u, h, p]] -
        q[f, h, p] / k[f, e, u, h, p] * u * BesselI[0, b * q[f, h, p]] *
         BesselY[1, b * k[f, e, u, h, p]]) *
      (BesselK[1, a * q[f, h, p]] * BesselJ[0, a * k[f, e, u, h, p]] +
        q[f, h, p] / k[f, e, u, h, p] * u * BesselK[0, a * q[f, h, p]] *
         BesselJ[1, a * k[f, e, u, h, p]]) ];

(* Definition of W2=Ud, W13=Ua (necessary for A,B) and tanδ = A/Q0 - B *)
W2 = Function[{f, e, u, a, b, h, p},

   1/(2 k[f, e, u, h, p]) (a^2 k[f, e, u, h, p] BesselJ[0, a k[f, e, u, h, p]]^2 -
      b^2 k[f, e, u, h, p] BesselJ[0, b k[f, e, u, h, p]]^2 -
      2 a BesselJ[0, a k[f, e, u, h, p]] BesselJ[1, a k[f, e, u, h, p]] +
      a^2 k[f, e, u, h, p] BesselJ[1, a k[f, e, u, h, p]]^2 +
      2 b BesselJ[0, b k[f, e, u, h, p]] BesselJ[1, b k[f, e, u, h, p]] -
      b^2 k[f, e, u, h, p] BesselJ[1, b k[f, e, u, h, p]]^2 +
      (BesselJ[0, b * k[f, e, u, h, p]] * (BesselI[1, b q[f, h, p]] /
            BesselI[0, b q[f, h, p]] * k[f, e, u, h, p] / q[f, h, p] / u) -
         BesselJ[1, b * k[f, e, u, h, p]]) / (-BesselY[1, b * k[f, e, u, h, p]] *
        (BesselI[1, b q[f, h, p]] / BesselI[0, b q[f, h, p]] *
          k[f, e, u, h, p] / q[f, h, p] / u) + BesselY[1, b * k[f, e, u, h, p]])^2 *
     1/(2 k[f, e, u, h, p]) (a^2 k[f, e, u, h, p] BesselY[0, a k[f, e, u, h, p]]^2 -
      b^2 k[f, e, u, h, p] BesselY[0, b k[f, e, u, h, p]]^2 -
      2 a BesselY[0, a k[f, e, u, h, p]] BesselY[1, a k[f, e, u, h, p]] +
      a^2 k[f, e, u, h, p] BesselY[1, a k[f, e, u, h, p]]^2 +
```

```
        2 b BesselY[0, b k[f, e, u, h, p]] BesselY[1, b k[f, e, u, h, p]] -
        b^2 k[f, e, u, h, p] BesselY[1, b k[f, e, u, h, p]]^2) +
     2 * (BesselJ[0, b * k[f, e, u, h, p]] * (BesselI[1, b q[f, h, p]] /
           BesselI[0, b q[f, h, p]] * k[f, e, u, h, p] / q[f, h, p] / u) -
        BesselJ[1, b * k[f, e, u, h, p]]) / (-BesselY[1, b * k[f, e, u, h, p]] *
         (BesselI[1, b q[f, h, p]] / BesselI[0, b q[f, h, p]] *
           k[f, e, u, h, p] / q[f, h, p] / u) + BesselY[1, b * k[f, e, u, h, p]]) *
     (1 / (2 Sqrt[π]) (a^2 MeijerG[{{{0, 1/2}, {-1/2}}, {{0, 1}, {-1, -1, -1/2}}},
           a k[f, e, u, h, p], 1/2] - b^2 MeijerG[{{{0, 1/2}, {-1/2}}},
           {{0, 1}, {-1, -1, -1/2}}, b k[f, e, u, h, p], 1/2]))];

W13 = Function[{f, e, u, a, b, h, p}, 1 / (2 q[f, h, p]) b
    (-b q[f, h, p] BesselI[0, b q[f, h, p]]^2 + 2 BesselI[0, b q[f, h, p]]
       BesselI[1, b q[f, h, p]] + b q[f, h, p] BesselI[1, b q[f, h, p]]^2) *
    (BesselJ[0, b * k[f, e, u, h, p]] / BesselI[0, b * q[f, h, p]] +
       BesselY[0, b * k[f, e, u, h, p]] / BesselI[0, b * q[f, h, p]] *
        (BesselJ[0, b * k[f, e, u, h, p]] * (BesselI[1, b q[f, h, p]] /
             BesselI[0, b q[f, h, p]] * k[f, e, u, h, p] / q[f, h, p] / u) -
          BesselJ[1, b * k[f, e, u, h, p]]) / (-BesselY[1, b * k[f, e, u, h, p]] *
           (BesselI[1, b q[f, h, p]] / BesselI[0, b q[f, h, p]] * k[f, e, u, h, p] /
             q[f, h, p] / u) + BesselY[1, b * k[f, e, u, h, p]]))^2 +
    Sqrt[π] MeijerG[{{}, {3/2}}, {{0, 0, 2}, {}}, a^2 q[f, h, p]^2] /
     (4 q[f, h, p]^2) *
    (BesselJ[0, a * k[f, e, u, h, p]] / BesselK[0, a * q[f, h, p]] +
       BesselY[0, a * k[f, e, u, h, p]] / BesselK[0, a * q[f, h, p]] *
        (BesselJ[0, b * k[f, e, u, h, p]] * (BesselI[1, b q[f, h, p]] /
             BesselI[0, b q[f, h, p]] * k[f, e, u, h, p] / q[f, h, p] / u) -
          BesselJ[1, b * k[f, e, u, h, p]]) / (-BesselY[1, b * k[f, e, u, h, p]] *
           (BesselI[1, b q[f, h, p]] / BesselI[0, b q[f, h, p]] * k[f, e, u, h, p] /
             q[f, h, p] / u) + BesselY[1, b * k[f, e, u, h, p]]))^2];
aq = Function[{f, e, u, a, b, h, p}, 1 + (k[f, e, u, h, p] / q[f, h, p])^2 / e / u^2 *
     W13[f, e, u, a, b, h, p] / W2[f, e, u, a, b, h, p]];
rs = Function[{f, σ}, (20 * Pi * Sqrt[f / σ])];
bq = Function[{f, e, u, a, b, h, p, σ},
   p^2 * 9 * rs[f, σ] / (8 * 10 000 * Pi^2 * f^3 * h^3 * e * u^2) *
    (1 + (k[f, e, u, h, p] / q[f, h, p])^2 *
       W13[f, e, u, a, b, h, p] / W2[f, e, u, a, b, h, p]) ];
```

```
(* Measurement parameters *)
u = 1 ; (* μ:=1 // Non-magnetic sample *)
a = 0.01000 / 2 ; (* Outer sample radius // a[m], a > b *)
b = 0.00100 / 2 ; (* Inner sample radius // b[m], b > 0 *)
h = 0.00400 ; (* Sample height h[m] *)
σ = 5.8 * 10^7; (* Conductivity of metal plates σ[S/m]: copper: 5.8*10^7 ,
silver: 6.3*10^7 *)
p = 1 (* Node number p (0np-Modes) *) ;

(* Determination of permittivity from measured TE0np resonance frequency
  f0[GHz] //remark: n solutions, start value needs to be adapted *)
f0 = 10 ;
FindRoot[f2[f0, ϵ, u, a, b, h, p] == 0,
  {ϵ, (3 / 20 / Pi / f0)^2 (3.139790^2 / a^2 + (p * Pi / h)^2)}];
ϵ =
 ϵ /.
  %

(* Determination of tanδ from measured Q-
 loaded Qm and insertion loss S21[dB] *)
Qm = 500 ;
S21 = -30.00 ;
tanδ =
 aq[f0, ϵ, u, a, b, h, p] / (Qm / (1 - 10^(S21 / 20))) - bq[f0, ϵ, u, a, b, h, p, σ]
Qf = f0 / tanδ
Qd = 1 / tanδ

(* OPTIONAL: Determination of permittivity
   from measured TM0np resonance frequency fm[GHz] //
 remark: n solutions, start value needs to be adapted *)
fm = 11 ;
FindRoot[f1[fm, ϵ, u, a, b, h, p] == 0,
  {ϵ, (3 / 20 / Pi / f0)^2 (3.775222^2 / a^2 + (p * Pi / h)^2)}];
ϵ =
 ϵ /.
  %

(* OPTIONAL: Estimation of the resonance modes for unknown samples *)
ContourPlot[{f2[f, e, u, a, b, h, 1] == 0, f1[f, e, u, a, b, h, 1] == 0,
  f2[f, e, u, a, b, h, 2] == 0, f1[f, e, u, a, b, h, 2] == 0}, {e, 17, 30}, {f, 4.5, 11}]

e0 = 20; (* Estimated ϵ' *)
(* Calculation of f(TE0np)[GHz], f(TM0np)[GHz] for estimated ϵ' *)
FindRoot[f2[fte, e0, u, a, b, h, p] == 0,
  {fte, 3 / 20 / Pi * Sqrt[3.13979^2 / a^2 + (p * Pi / h)^2] / Sqrt[e0]}];
fte = fte /. % ;
FindRoot[f1[ftm, e0, u, a, b, h, p] == 0,
  {ftm, 3 / 20 / Pi * Sqrt[3.775222^2 / a^2 + (p * Pi / h)^2] / Sqrt[e0]}];
ftm = ftm /. % ;
{fte, ftm}
```

```
(* CYLINDRICAL CAVITY RESONANCE SCRIPT *)

(* Definition of eigenvalue equation cew and cewϕ *)
cew = Function[{k, q, a, b}, BesselJ[0, k * a] / BesselJ[1, k * a] +
    q / k / BesselK[1, q * a] * (BesselK[0, q * a] + BesselK[1, q * b] / (q * a))];
cewϕ = Function[{β, α1, α2, L, L1, L2},
   Tan[β * L] - (α1 * Coth[α1 * L1] + α2 * Coth[α2 * L2]) /
     (β - α1 * α2 * Coth[α1 * L1] * Coth[α2 * L2] / β)] ;

(* Measurement parameters *)
a = 0.010 / 2 ; (* Sample radius a[m] *)
L = 0.004 ; (* Sample height L[m] *)
e1 = 3.8 ; (* permittivity of support e1: Fused Silica: 3.8 *)
e2 = 1 ; (* permittivity of top support e2: air: 1 *)
b = 0.02622 / 2 ; (* Cavity radius b[m] // standard diameter: 26.22 mm *)
h = 0.02025 ; (* Cavity height h[m] // standard height: 20.25 mm *)
L1 = 0.00793 ; (* Support height L1[m] // standard height: 7.93 mm *)
L2 = h - L1 - L ; (* Top support height, determined from h1, h and L *)
f = 7 ; (* Measured TE01δ resonance frequency f[GHz] *)
σ = 6.3 * 10^7 ; (* Conductivity of metal walls σ[S/m]: copper: 5.8*10^7 ,
silver: 6.3*10^7 *)
rs = 20 * Pi * Sqrt[f / σ] ; (* Calculation of RS *)
(* Determination of q from measured fTE01δ *)
q = Pi * Sqrt[(1 / h)^2 - (2 / (3 * 10^8) * f * 10^9)^2] ;
fgr = 0.15 / h (* cut-off frequency fgr[GHz] *)

(* Permittivity determination *)

(* Graphical determination of k to find start value for
 the numerical solution *)Plot[cew[k, q, a, b], {k, 400, 600}]

FindRoot[cew[k, q, a, b], {k, 510}] (* Numerical determination of k *)

k = k /. %
α1 = Sqrt[ k^2 - (2 * Pi / (3 * 10^8) * f * 10^9)^2 * e1] ; (* Calculation of α1 *)
α2 = Sqrt[ k^2 - (2 * Pi / (3 * 10^8) * f * 10^9)^2 * e2] ; (* Calculation of α2 *)

(* Graphical determination of β to find start value for the
 numerical solution *)Plot[cewϕ[β, α1, α2, L, L1, L2], {β, 370, 460}]

FindRoot[cewϕ[β, α1, α2, L, L1, L2], {β, 415}] (* Numerical determination of β *)

β = β /. % ;
ϵ = 9 / 400 / Pi^2 * (β^2 + k^2) / f^2 (* Calculation of ϵ' *)

(* Determination of the necessary volume &
 surface integrals for the tanδ calculation,
E0/H0=2pi f μ0 /ik, all E fields were expressed as E/E0 *)
ϕ = ArcTan[α1 / β * Coth[α1 * L1]] - β * L / 2;
S = Function[{β, L, ϕ}, (β * L + Sin[β * L] Cos[2 * ϕ]) / 2 / β];
Z = Function[{β, L, ϕ, αi, Li}, (Cos[β * L / 2 + ϕ] / Sinh[αi * Li])^2];
P = Function[{αi, Li}, -Li / 2 + Sinh[2 * αi * Li] / 4 / αi];
F = Function[{a, k},
   a^2 / 2 * (BesselJ[1, k * a]^2 - BesselJ[2, k * a] * BesselJ[0, k * a])];
G = Function[{a, b, q}, -a^2 / 2 * (BesselK[1, q * a]^2 -
       BesselK[2, q * a] * BesselK[0, q * a] + BesselK[1, q * b]^2) +
```

```
    b^2 / 2 * (2 * BesselK[1, q * b] ^2 - BesselK[2, q * b] * BesselK[0, q * b]) -
    2 * BesselK[1, q * b] 1/4 (-a^2 MeijerG[{{0}, {}}, {{-1/2, 1/2}, {-1}}, a q/2, 1/2] +
       b^2 MeijerG[{{0}, {}}, {{-1/2, 1/2}, {-1}}, b q/2, 1/2])];
W1 = Function[{ϵ, β, L, ϕ, a, k}, 8.8542 * 10^(-12) ϵ / 2 *
    2 * Pi * F[a, k] * S[β, L, ϕ]];
W23 = Function[{ei, β, L, ϕ, αi, Li, a, k}, 8.8542 * 10^(-12) *
    ei / 2 * 2 * Pi * F[a, k] * Z[β, L, ϕ, αi, Li] * P[αi, Li]];
(* W2=W23[e1,β,L,ϕ,α1,L1,a,k] , W3=W23[e2,β,L,-ϕ,α2,L2,a,k] *)
W45 = Function[{ei, β, L, ϕ, αi, Li, a, b, k, q},
   8.8542 * 10^(-12) * ei / 2 * 2 * Pi * (BesselJ[1, k * a] / BesselK[1, q * a])^2 *
    G[a, b, q] * Z[β, L, ϕ, αi, Li] * P[αi, Li]] ;
 (* W4=W45[e1,β,L,ϕ,α1,L1,a,b,k,q] , W5=W45[e2,β,L,-ϕ,α2,L2,a,b,k,q] *)
W6 = Function[{β, L, ϕ, a, b, k, q}, 8.8542 * 10^(-12) / 2 * 2 * Pi *
    (BesselJ[1, k * a] / BesselK[1, q * a])^2 * G[a, b, q] * S[β, L, ϕ]];
M45 = Function[{rs, f, β, L, ϕ, αi, Li, a, b, k, q}, b * 1 / 2 * 2 * Pi *
    rs / 64 / (10 * Pi)^4 / f^2 * (q * BesselJ[1, k * a] / BesselK[1, q * a])^2 *
    (BesselK[0, q * b] + BesselK[1, q * b] / (q * b))^2 *
    Z[β, L, ϕ, αi, Li] * P[αi, Li]];
(* M4=M45[rs,f,β,L,ϕ,α1,L1,a,b,k,q] , M5=M45[rs,f,β,L,-ϕ,α2,L2,a,b,k,q] *)
M6 = Function[{rs, f, β, L, ϕ, a, b, k, q}, b * 1 / 2 * 2 * Pi *
    rs / 64 / (10 * Pi)^4 / f^2 * (q * BesselJ[1, k * a] / BesselK[1, q * a])^2 *
    (BesselK[0, q * b] + BesselK[1, q * b] / (q * b))^2 * S[β, L, ϕ]];
O23 = Function[{rs, f, β, L, ϕ, αi, Li, a, k},
   1 / 2 * 2 * Pi * rs / 64 / (10 * Pi)^4 / f^2 * αi^2 * F[a, k] * Z[β, L, ϕ, αi, Li]];
(* O2=O23[rs,f,β,L,ϕ,α1,L1,a,k] , O3=O23[rs,f,β,L,-ϕ,α2,L2,a,k] *)
O45 = Function[{rs, f, β, L, ϕ, αi, Li, a, b, k, q},
   1 / 2 * 2 * Pi * rs / 64 / (10 * Pi)^4 / f^2 *
    (αi * BesselJ[1, k * a] / BesselK[1, q * a])^2 G[a, b, q] * Z[β, L, ϕ, αi, Li]];
(* O4=O45[rs,f,β,L,ϕ,α1,L1,a,b,k,q] , O5=O45[rs,f,β,L,-ϕ,α2,L2,a,b,k,q] *)
(* Calculation of A and B *)
Pc = M45[rs, f, β, L, ϕ, α1, L1, a, b, k, q] +
   M45[rs, f, β, L, -ϕ, α2, L2, a, b, k, q] + M6[rs, f, β, L, ϕ, a, b, k, q] +
   O23[rs, f, β, L, ϕ, α1, L1, a, k] + O23[rs, f, β, L, -ϕ, α2, L2, a, k] +
   O45[rs, f, β, L, ϕ, α1, L1, a, b, k, q] + O45[rs, f, β, L, -ϕ, α2, L2, a, b, k, q];
B = Pc / (2 * Pi * 10^9 * f * W1[ϵ, β, L, ϕ, a, k]) ;
A = 1 + (W23[e1, β, L, ϕ, α1, L1, a, k] + W23[e2, β, L, -ϕ, α2, L2, a, k] +
      W45[e1, β, L, ϕ, α1, L1, a, b, k, q] + W45[e2, β, L, -ϕ, α2, L2, a, b, k, q] +
      W6[β, L, ϕ, a, b, k, q]) / W1[ϵ, β, L, ϕ, a, k] ;

(* Determination of tanδ from measured Q-
 loaded Qm and insertion loss S21[dB] *)
Qm = 500 ;
S21 = -30.0 ;
tanδ = A / (Qm / (1 - 10^(S21 / 20))) - B
Qf = f / tanδ
Qd = 1 / tanδ
```

A.4 Publications and conference contributions

A.4.1 Publications

- Patent: "Glass-ceramic as dielectric in the high-frequency range", H. Braun; M. Letz; B. Rüdinger; D. Seiler, *Publication No. (WO 2013076114 A2, DE 102011119804 A1, US20140256530, CN 103958428 A)*
- Publication: "Glass-ceramics as dielectrics for antennas in microwave electronics", H. Braun, Y. Zheng, R. Jakoby, O. Leisten, M. Letz, *European Microwave Conference (EuMC)*, Oct. 2013, 1167-1170, IEEE
- Publication: "Compact dual-band hybrid dielectric resonator antenna based on new glass-ceramic material", A. Mehmood; Y. Sun; Y. Zheng; O.H. Karabey; H. Braun; M. Hovhannisyan; M. Letz; R. Jakoby, *European Microwave Conference (EuMC)*, Oct. 2013, 763-766, IEEE
- Publication: "Liquid crystal based phased array antenna with improved beam scanning capability", O.H. Karabey; A. Mehmood; M. Ayluctarhan; H. Braun; M. Letz; R. Jakoby, *Electronics Letter*, Mar. 2014, 50, 6, 2436-2439, IET
- Publication: "Dual Band Dielectric Resonator Antenna For Hiperlan Based on Transparent Glass Material", A. Mehmood; Y. Zheng; H. Braun; M. Hovhannisyan; M. Letz; R. Jakoby, *German Microwave Conference (GeMIC)*, Mar. 2014, 1, 4, 10-12, VDE (Best Paper Award GeMIC 2014)
- Publication: "Reconfigurable dualband antenna module with integrated high voltage charge pump and digital analog converter", E. Gonzalez-Rodriguez; A. Mehmood; Y. Zheng; H. Maune; L. Shen; J. Ning; H. Braun; M. Hovhannisyan; K. Hofmann; R. Jakoby, *8th European Conference on Antennas and Propagation (EuCAP)*, Apr. 2014, 2749-2753, IEEE
- Publication: "Dielectric resonator antenna phased array with liquid crystal based phase shifters", A. Mehmood; O.H. Karabey; M. Ayluctarhan; Y. Zheng; H. Braun; M. Hovhannisyan; M. Letz; R. Jakoby, *8th European Conference on Antennas and Propagation (EuCAP)*, Apr. 2014, 2436-2439, IEEE
- Publication*: "Titanate-based paraelectric glass-ceramics for applications in GHz electronics", H. Braun; A. Mehmood; M. Hovhannisyan; H. Zhang; D. Sohrabi Baba Heidary; M. Lanagan; I.M. Reaney; M. Letz; H.J. Elmers (*: in preparation)

A.4.2 Conferences, seminars & research visits

- Research visit: 03/15/2014 - 06/15/2014, Penn State University (State College (PA), USA), Department of Materials Science and Engineering (Collaboration with the groups of Michael Lanagan and Clive Randall)

- Conference: 03/25/2012 - 03/30/2012, DPG Frühjahrstagung (Berlin, Germany),
  Talk: "Dielectric pore-free glass-ceramic materials with good metal adhesion properties for GHz applications"

- Conference: 07/23/2012 - 07/27/2012, 2nd Global Congress on Microwave Energy Applications (Long Beach (CA), USA),
  Talk: "Dielectric pore-free Glass-ceramic Materials for mobile Applications in the GHz Frequency range"

- Conference: 03/10/2013 - 03/15/2013, DPG Frühjahrstagung (Regensburg, Germany),
  Talk: "Titanate glass-ceramics for mobile applications in the GHz range"

- Conference: 06/02/2013 - 06/07/2013, 10th Pacific Rim Conference on Ceramic and Glass Technology (San Diego (CA), USA),
  Talk: "Titanate glass-ceramics for mobile applications in the GHz range"

- Conference: 05/12/2014 - 05/16/2014, 2014 Joint IEEE International Symposium on the Applications of Ferroelectric, International Workshop on Acoustic Transduction Materials and Devices & Workshop on Piezoresponse Force Microscopy (ISAF/IWATMD/PFM) (State College (PA), USA),
  Talk: "Titanate Glass-Ceramic Materials for Mobile Applications in the GHz Frequency Range"

- Conference: 06/01/2014 - 06/04/2014, MMA2014: Microwave Materials and their Applications (Boise (ID), USA),
  Talk: "Titanate glass-ceramic materials for mobile applications in the GHz frequency range"

- Conference*: 03/15/2015 - 03/20/2015, DPG Frühjahrstagung (Berlin, Germany),
  Talk: "Titanate-based paraelectric glass-ceramics for applications in GHz electronics" (*: abstract accepted and talk confirmed by the DPG)

- Workshop: 11/08/2011, TICMO (Tunable Integrated Components in Microwave Technology and Optics) workshop on glass ceramics and ceramic antennas (Darmstadt, Germany),
  Talk: "La-Ti-Si glass-ceramics as microwave dielectric materials"

- Workshop: 05/16/2014 - 05/17/2014, Center for Dielectrics and Piezoelectrics - Spring 2014 Meeting (State College (PA), USA),
  Poster: "Dielectric Glass-Ceramic Materials for Microwave Applications"

- Summer school: 07/02/2012 - 07/06/2012, 4th ICG Summer School (Montpellier, France), "Glasses: Formation, Structure and Strength"

- Summer school: 08/17/2013 - 08/25/2013, RACIRI Summer School (St. Petersburg, Russia), "Advanced Design of New Materials at X-Ray and Neutron Facilities: Soft Matter and Nanocomposites"

Bibliography

[83107] Application Note No. 831. Temperature coefficients of dielectric resonators. Technical report, Skyworks, March 2007.

[AB70] S. Arafa, A. Bishay. ESR and optical absorption spectra of irradiated borate glasses containing titanium. *Phys. Chem. Glasses*, 11(3):75–82, June 1970.

[AB77] R. M. A. Azzam, N. M. Bashara. *Ellipsometry and polarized light*. North-Holland personal library. North-Holland Pub. Co., 1977.

[Abr63] S. C. Abrahams. Magnetic and crystal structure of titanium sesquioxide. *Phys. Rev.*, 130:2230–2237, Jun 1963.

[ABW+01] N. McN. Alford, J. Breeze, X. Wang, S. J. Penn, S. Dalla, S. J. Webb, N. Ljepojevic, X. Aupi. Dielectric loss of oxide single crystals and polycrystalline analogues from 10 to 320 K. *Journal of the European Ceramic Society*, 21(15):2605 – 2611, 2001.

[ADP06] P. W. Atkins, J. De Paula. *Physikalische Chemie: Hauptbd.* Wiley-VCH, 2006.

[ALN+08] L. H. C. Andrade, S. M. Lima, A. Novatski, A. M. Neto, A. C. Bento, M. L. Baesso, F. C. G. Gandra, Y. Guyot, G. Boulon. Spectroscopic assignments of Ti^{3+} and Ti^{4+} in titanium-doped OH^{-} free low-silica calcium aluminosilicate glass and role of structural defects on the observed long lifetime and high fluorescence of Ti^{3+} ions. *Phys. Rev. B*, 78:224202, Dec 2008.

[BALGG10] M. Brandily-Anne, J. Lumeau, L. Glebova, L. B. Glebov. Specific absorption spectra of cerium in multicomponent silicate glasses. *Journal of Non-Crystalline Solids*, 356:2337 – 2343, 2010. 12th International Conference on the Physics of Non-Crystalline Solids (PNCS 12).

[Bam77] C. R. Bamford. *Colour Generation and Control in Glass*. Number Bd. 2 in Colour Generation and Control in Glass. Elsevier Scientific Publishing Company : distributors for the U.S. and Canada, Elsevier North-Holland, 1977.

[BB70] H. Böhm, G. Bayer. ESR-spectra of sodium-titanium-silicate glasses and of titanium-containing oxide compounds. *Journal of Physics and Chemistry of Solids*, 31(9):2125 – 2137, 1970.

[BDT+00] D. C. Boyd, P. S. Danielson, D. A. Thompson, M. Velez, S. T. Reis, R. K. Brow. *Glass*. John Wiley and Sons, Inc., 2000.

[BFHS66] G. Bayer, O. Floerke, W. Hoffmann, H. Scheel. Entmischung und Kristallisation in Gläsern des Systems Na_2O-TiO_2-SiO_2. *Glastech. Ber.*, 39(5):242–261, May 1966.

[BGH60] H. Bilz, L. Genzel, H. Happ. Zur Ultrarotdispersion der Alkali-Halogenide. *Zeitschrift für Physik*, 160:535–553, October 1960.

[BH72] L. A. Bursill, B. G. Hyde. Crystallographic shear in the higher titanium oxides: Structure, texture, mechanisms and thermodynamics. *Progress in Solid State Chemistry*, 7(0):177 – 253, 1972.

[BHK04] C. Bernhard, J. Humlicek, B. Keimer. Far-infrared ellipsometry using a synchrotron light source - the dielectric response of the cuprate high Tc superconductors. *Thin Solid Films*, 455-456(0):143 – 149, 2004. The 3rd International Conference on Spectroscopic Ellipsometry.

[BJJR+02] J. Baker-Jarvis, M. D. Janezic, B. Riddle, C. L. Holloway, N. G. Paulter, J. E. Blendell. Dielectric and conductor-loss charaterization and measurements on electronic packaging materials. Technical report, NIST Technical Note 1520, 2002.

[BK99] H. Bach, D. Krause. *Analysis of the Composition and Structure of Glass and Glass Ceramics*. Springer, 1999.

[BKS+09] R. Bechstein, M. Kitta, J. Schütte, H. Onishi, A. Kühnle. The effects of antimony doping on the surface structure of rutile TiO_2 (110). *Nanotechnology*, 20(26):264003, 2009.

[BMT94] D. Benbertal, A. Mosset, J. C. Trombe. Synthese et structure cristalline d'un nouveau silicate de lanthane et de titane. *Materials Research Bulletin*, 29(1):47–54, January 1994.

[BPMA09] J. D. Breeze, J. M. Perkins, D. W. McComb, N. McN. Alford. Do grain boundaries affect microwave dielectric loss in oxides? *Journal of the American Ceramic Society*, 92(3):671–674, 2009.

[BQP74] A. Bishay, C. Quadros, A. Piccini. *Phys. Chem. Glass*, 15(109), 1974.

[Bra11] H. Braun. Glaskeramiken mit paraelektrischen Phasen für mobile Anwendungen im GHz Bereich. *Diploma thesis, University of Mainz*, August 2011.

[BRC66] R. A. Buchanan, H. E. Rast, H. H. Caspers. Infrared absorption of Ce^{3+} in LaF_3 and of CeF_3. *The Journal of Chemical Physics*, 44(11):4063–4065, 1966.

[BRMF10] A. Bartsch, K. Rätzke, A. Meyer, F. Faupel. Dynamic arrest in multicomponent glass-forming alloys. *Phys. Rev. Lett.*, 104:195901, May 2010.

[Brü85] R. Brückner. Effects of modes of formation on the structure of glass. *Journal of Non-Crystalline Solids*, 71(1-3):49–57, 1985.

[BSDN91] L. E. Bausa, J. Garcia Sole, A. Duran, J. M. Fernandez Navarro. Characterization of titanium induced optical absorption bands in phosphate glasses. *Journal of Non-Crystalline Solids*, 127(3):267 – 272, 1991.

[BSMM05] I. N. Bronstein, K. A. Semendjajew, G. Musiol, H. Mühlig. *Taschenbuch der Mathematik*. Harri Deutsch, 6. auflage edition, 2005.

[Bur81] R. G. Burns. Intervalence transitions in mixed valence minerals of iron and titanium. *Annual Review of Earth and Planetary Sciences*, 9(1):345–383, 1981.

[Car07] R. Carl. *Herstellung gerichteter Mullitglaskeramiken durch elektrochemisch induzierte Keimbildung*. PhD thesis, Univ. Jena, 2007.

[CN07] C. B. Carter, M. G. Norton. *Ceramic Materials - Science and Engineering*. Springer Verlag, 2007.

[Coh68] S. B. Cohn. Microwave bandpass filters containing high-Q dielectric resonators. *IEEE Transactions on Microwave Theory and Techniques*, 16(4):218–227, April 1968.

[Cou70] W. E. Courtney. Analysis and evaluation of a method of measuring the complex permittivity and permeability of microwave insulators. *IEEE Transactions on Microwave Theory and Techniques*, MTT-18(8):476–485, August 1970.

[DG02] M. Dressel, G. Grüner. *Electrodynamics of Solids: Optical Properties of Electrons in Matter*. Cambridge University Press, 2002.

[DI71] J. A. Duffy, M. D. Ingram. Establishment of an optical scale for lewis basicity in inorganic oxyacids, molten salts, and glasses. *Journal of the American Chemical Society*, 93(24):6448–6454, 1971.

[DI75] J. A. Duffy, M. D. Ingram. Optical basicity-IV: Influence of electronegativity on the lewis basicity and solvent properties of molten oxyanion salts and glasses. *Journal of Inorganic and Nuclear Chemistry*, 37(5):1203 – 1206, 1975.

[DI76] J. A. Duffy, M. D. Ingram. An interpretation of glass chemistry in terms of the optical basicity concept. *Journal of Non-Crystalline Solids*, 21(3):373 – 410, 1976.

[DKPK04] R. Demirbilek, A. B. Kutsenko, R. Pankrath, S. E. Kapphan. Investigation of far infrared transitions of Ce^{3+} in congruent SBN crystals. *Ferroelectrics*, 303(1):177–180, 2004.

[DS96] V. Dimitrov, S. Sakka. Electronic oxide polarizability and optical basicity of simple oxides. I. *Journal of Applied Physics*, 79(3):1736–1740, 1996.

[Duf89] J. A. Duffy. Optical basicity of titanium(IV) oxide and zirconium(IV) oxide. *Journal of the American Ceramic Society*, 72(10):2012–2013, 1989.

[Duf93] J. A. Duffy. A review of optical basicity and its applications to oxidic systems. *Geochimica et Cosmochimica Acta*, 57(16):3961 – 3970, 1993.

[Duf96] J. A. Duffy. Redox equilibria in glass. *Journal of Non-Crystalline Solids*, 196(0):45 – 50, 1996.

[Dun82] T. Dunn. Oxygen diffusion in three silicate melts along the join diopside-anorthite. *Geochimica et Cosmochimica Acta*, 46(11):2293 – 2299, 1982.

[DZB+97] D. C. Dube, R. Zurmuhlen, A. Bell, N. Setter, W. Wersing. Dielectric measurements on high-Q ceramics in the microwave region. *Journal of the American Ceramic Society*, 80(5):1095–1100, May 1997.

[EE03] D. Ehrt, P. Ebeling. Radiation defects in borosilicate glasses. *Glass Technol.*, 44(2):46–49, 2003.

[EEWW10] G. R. Eaton, S. S. Eaton, D. P. Warr, R. T. Weber. *Quantitative EPR*. Springer, 2010.

[Eic11] R.-A. Eichel. Structural and dynamic properties of oxygen vacancies in perovskite oxides-analysis of defect chemistry by modern multi-frequency and pulsed epr techniques. *Phys. Chem. Chem. Phys.*, 13:368–384, 2011.

[ELM01] D. Ehrt, M. Leister, A. Matthai. Polyvalent elements iron, tin and titanium in silicate, phosphate and fluoride glasses and melts. *Physics and Chemistry of Glasses*, 42(3):231–239, 2001.

[FA08] R. Freer, F. Azough. Microstructural engineering of microwave dielectric ceramics. *Journal of the European Ceramic Society*, 28(7):1433 – 1441, 2008. Developments in Ceramic Science and Engineering: the last 50 years. A meeting in celebration of Professor Sir Richard Brook's 70th Birthday.

[Far96] F. Farges. Coordination of Ti in crystalline and glassy fresnoites: A high-resolution XANES spectroscopy study at the Ti K-edge. *Journal of Non-Crystalline Solids*, 204(1):53 – 64, 1996.

[Far97] F. Farges. Coordination of Ti^{3+} in silicate glasses: A high-resolution XANES spectroscopy study at the Ti K-edge. *American Mineralogist*, 82:36–43, 1997.

[FBS+07] J. Fang, X. Bi, D. Si, Z. Jiang, W. Huang. Spectroscopic studies of interfacial structures of CeO_2-TiO_2 mixed oxides. *Applied Surface Science*, 253(22):8952 – 8961, 2007.

[FJN+96] F. Farges, G. E. Brown Jr., A. Navrotsky, H. Gan, J. J. Rehr. Coordination chemistry of Ti(IV) in silicate glasses and melts: II. glasses at ambient temperature and pressure. *Geochimica et Cosmochimica Acta*, 60(16):3039 – 3053, 1996.

[FJR96] F. Farges, G. E. Brown Jr., J. J. Rehr. Coordination chemistry of Ti(IV) in silicate glasses and melts: I. XAFS study of titanium coordination in oxide model compounds. *Geochimica et Cosmochimica Acta*, 60(16):3023 – 3038, 1996.

[Gan92] F. Gan. *Optical and spectroscopic properties of glass*. Springer, 1992.

[Gol26] V. M. Goldschmidt. Geochemische verteilungsgesetzte der elemente. *Skrifter Norske Videnkasps Akad. - I. Math. Naturwiss. Kl. 8*, 36:7–156, Oslo 1926.

[Göt99] W. Götze. Recent tests of the mode-coupling theory for glassy dynamics. *Journal of Physics: Condensed Matter*, 11(10A):A1, 1999.

[Göt08] W. Götze. *Complex Dynamics of Glass-Forming Liquids : A Mode-Coupling Theory: A Mode-Coupling Theory*. International Series of Monographs on Physics. OUP Oxford, 2008.

[GPT] V. Gottardi, G. Paoletti, M. Tornati. The ratio Ce^{3+}/Ce^{4+} in the melting of different glasses and its influence on their properties. *Physics and Chemistry of Glasses*.

[GT91] V. L. Gurevich, A. K. Tagantsev. Intrinsic dielectric loss in crystals. *Advances in Physics*, 40(6):719–767, 1991.

[GW07] B. Glover, K. W. Whites. Engineering lossy artificial dielectrics using single-walled carbon nanotubes. *2007 IEEE Antennas and Propagation Society International Symposium*, pages 3400–3403, June 2007.

[HBF+02] T. Honma, Y. Benino, T. Fujiwara, T. Komatsu, R. Sato, V. Dimitrov. Electronic polarizability, optical basicity, and interaction parameter of La_2O_3 and related glasses. *Journal of Applied Physics*, 91(5):2942–2950, 2002.

[HC60] B. W. Hakki, P. D. Coleman. A dielectric resonator method of measuring inductive capacities in the millimeter range. *IRE Transactions on Microwave Theory and Techniques*, 8(4):402–410, July 1960.

[HH01] J. H. Hwang, Y. H. Han. Electrical properties of cerium-doped $BaTiO_3$. *Journal of the American Ceramic Society*, 84(8):1750–1754, 2001.

[HJ27] H. Heinrichs, G. Jaeckel. *Das Cer als Rohmaterial und Glasbildner*. Müller & Schmidt, 1927.

[HS95] D. Haarer, H. W. Spiess. *Spektroskopie amorpher und kristalliner Festkörper*. Steinkopff, 1995.

[HT03] Y. Higuchi, H. Tamura. Recent progress on the dielectric properties of dielectric resonator materials with their applications from microwave to optical frequencies. *Journal of the European Ceramic Society*, 23(14):2683 – 2688, 2003. Microwave Materials and Applications.

[Hun09] S. Hunklinger. *Festkörperphysik*. Oldenbourg, 2009.

[IBM92] D. M. Iddles, A. J. Bell, A. J. Moulson. Relationships between dopants, microstructure and the microwave dielectric properties of $\mathrm{ZrO_2}$-$\mathrm{TiO_2}$-$\mathrm{SnO_2}$ ceramics. *Journal of Materials Science*, 27(23):6303–6310, 1992.

[IH78] H. Ihrig, D. Hennings. Electrical transport properties of n-type $\mathrm{BaTiO_3}$. *Phys. Rev. B*, 17:4593–4599, Jun 1978.

[Isa62] J. O. Isard. A study of the migration loss in glass and a generalized method of calculating the rise of dielectric loss with temperature. *Proceedings of the IEE - Part B: Electronic and Communication Engineering*, 109:440–447(7), January 1962.

[ITU14] ITU. Key ict data 2005-2014: Mobile-cellular subscriptions. *World Telecommunication/ICT Indicators database 2014 (18th edition)*, December 2014.

[Jac99] J. D. Jackson. *Klassische Elektrodynamik*. John Wiley, New York 1999.

[Jan03] M. Janezic. *Nondestructive Relative Permittivity and Loss Tangent Measurements Using a Split-Cylinder Resonator*. PhD thesis, University of Colorado, 2003.

[Joh65] W. D. Johnston. Oxidation-reduction equilibria in molten $\mathrm{Na_2O.2SiO_2}$ glass. *Journal of the American Ceramic Society*, 48(4):184–190, 1965.

[Jon77] A. K. Jonscher. The universal dielectric response. *Nature*, 267:673–679, June 1977.

[Jon81] A. K. Jonscher. A new understanding of the dielectric relaxation of solids. *Journal of Materials Science*, 16(8):2037–2060, 1981.

[Jon99] A. K Jonscher. Dielectric relaxation in solids. *Journal of Physics D: Applied Physics*, 32(14):R57, 1999.

[Kaj84] D. Kajfez. Q-factor measurements, analog and digital. *IEEE Transactions on Microwave Theory and Techniques*, MTT-32(7):666–670, July 1984.

[KDA+99] J. Krupka, K. Derzakowski, A. Abramowicz, M. E. Tobar, R. G. Geyer. Use of whispering gallery-modes for complex permittivity determinations of ultra-low-loss dielectric materials. *IEEE Transactions on Microwave Theory and Techniques*, 47(6):752–759, June 1999.

[KG86] D. Kajfez, P. Guillon. *Dielectric Resonators*. Artech House, Inc., Dedham 1986.

[KH84] D. Kajfez, E. J. Hwan. Q-factor measurement with network analyzer. *IEEE Transactions on Microwave Theory and Techniques*, MTT-32(7):666–670, July 1984.

[KK85] Y. Kobayashi, M. Katoh. Microwave measurement of dielectric properties of low-loss materials by the dielectric rod resonator method. *IEEE Transactions on Microwave Theory and Techniques*, 33(7):586–592, July 1985.

[KKZ+95] D. Kivelson, S.A. Kivelson, X. Zhao, Z. Nussinov, G. Tarjus. A thermodynamic theory of supercooled liquids. *Physica A: Statistical Mechanics and its Applications*, 219(1):27–38, 1995.

[KMAR11] L. Kido, M. Müller, I. Avramov, C. Rüssel. Redox freezing temperature and bartenev equation in a 25Na_2O-15B_2O_3-60SiO_2 glass doped with chromium and manganese. *Journal of Non-Crystalline Solids*, 357(18):3307 – 3312, 2011.

[KNP+06] S. Kamba, D. Noujni, A. Pashkin, J. Petzelt, R. C. Pullar, A.-K. Axelsson, N. McN. Alford. Low-temperature microwave and THz dielectric response in novel microwave ceramics. *Journal of the European Ceramic Society*, 26(10-11):1845 – 1851, 2006. Papers Presented at the Third International Conference on Microwave Materials and their Applications - {MMA2004} Inuyama, Japan The Third International Conference on Microwave Materials and their Applications - {MMA2004}.

[KP03] T. Kolodiazhnyi, A. Petric. Analysis of point defects in polycrystalline $BaTiO_3$ by electron paramagnetic resonance. *Journal of Physics and Chemistry of Solids*, 64(6):953–960, 2003.

[KR97] R. Keding, C. Rüssel. Electrochemical nucleation for the preparation of oriented glass ceramics. *Journal of Non-Crystalline Solids*, 219(0):136 – 141, 1997. Glass Crystallization.

[KR00] R. Keding, C. Rüssel. Oriented glass-ceramics containing fresnoite prepared by electrochemical nucleation of a BaO-TiO_2-SiO_2-B_2O_3 melt. *Journal of Non-Crystalline Solids*, 278(1-3):7 – 12, 2000.

[Kru06] J. Krupka. Frequency domain complex permittivity measurements at microwave frequencies. *Measurement Science and Technology*, 17(6):R55, 2006.

[KRW38] C. Kühl, H. Rudow, W. Weyl. Oxidation and reduction equilibria in colored glasses. *Sprechsaal*, 71(7):91–93, 1938.

[KUCS03] M. Kumar, A. Uniyal, A. P. S. Chauhan, S. P. Singh. Optical absorption and fluorescent behaviour of titanium ions in silicate glasses. *Bulletin of Materials Science*, 26(3):335–341, 2003.

[Kuz98] H. Kuzmany. *Solid-State Spectroscopy - An Introduction*. Springer, 1998.

[KV56] F. A. Kröger, H. J. Vink. Relations between the concentrations of imperfections in crystalline solids. volume 3 of *Solid State Physics*, pages 307 – 435. Academic Press, 1956.

[KWW86] D. Kajfez, W. P. Wheless, R. T. Ward. Influence of an airgap on the measurement of dielectric constant by a parallel-plate dielectric resonator. *Microwaves, Antennas and Propagation, IEE Proceedings H*, 133(4):253–258, August 1986.

[Lan36] R. J. Lang. *Can. J. Res.*, 14:127, 1936.

[LB86] J. Lee, R. Brückner. The electrochemical series of the 3d transition metal ions in alkali borate glasses. *Glastech. Ber.*, 59(9):233–251, 1986.

[Lei11] O. Leisten. Private correspondence (Sarantel Ltd.). 2011.

[Li00] Y. Li. Glass formation and glass forming ability of alloys near eutectic composition. In *Symposium L - Supercooled Liquid, Bulk Glassy and Nanocrystalline State of Alloys*, volume 644 of *MRS Proceedings*, 1 2000.

[LL67] L. D. Landau, E. M. Lifshitz. *Lehrbuch der theoretischen Physik VIII - Elektrodynamik der Kontinua*. Akademie-Verlag, 1967.

[LL05] Y. Liu, P. Lin. Effects of glass additions on microwave dielectric properties of $La_4Ti_9O_{24}$ ceramics. *Materials Chemistry and Physics*, 92(1):98–103, July 2005.

[LL06] Y. Liu, P. Lin. Phase formation and microwave dielectric properties of Pb^{2+} and Sr^{2+} doped $La_4Ti_9O_{24}$ ceramics. *Materials Research Bulletin*, 41(10):1845–1853, October 2006.

[LSSR71] G. F. Lynch, M. Sayer, S. L. Segel, G. Rosenblatt. Electron and nuclear magnetic resonance in semiconducting phosphate glasses. *Journal of Applied Physics*, 42(7):2587–2591, 1971.

[MB03] L. Murawski, R. J. Barczynski. Lecture: Electronic and ionic relaxations in oxide glasses (IMSPEMAS WORKSHOP: Impedance spectroscopy for characterisation of materials and structures). 2003.

[McM79a] P. McMillan. *Glass ceramics*. 2nd ed., Academic Press, London 1979.

[MCM79b] L. Murawski, C. H. Chung, J. D. Mackenzie. Electrical properties of semiconducting oxide glasses. *Journal of Non-Crystalline Solids*, 32(1-3):91 – 104, 1979. Electronic Properties and Structure of Amorphous Solids.

[MGSL93] B. A. Maksimov, E. A. Genkina, V. R. Samygina, V. R. Leonyuk. Crystal structure of la-analog of stilvellite. *Kristallografiya*, 38:61 – 65, 1993.

[MH03] A. J. Moulson, J. M. Herbert. *Electroceramics - Materials Properties Applications*. Wiley, 2nd Edition, 2003.

[Mir10] M. Mirsaneh. Internal report (SCHOTT AG). 2010.

[MJN98] M. P. McNeal, S. Jang, R. E. Newnham. The effect of grain and particle size on the microwave properties of barium titanate ($BaTiO_3$). *Journal of Applied Physics*, 83(6):3288–3297, March 1998.

[MLZ08] M. Mirsaneh, O. P. Leisten, B. Zalinska. Circularly polarized dielectric-loaded antennas: Current technology and future challenges. *Advanced Functional Materials*, 18(16):2293–2300, August 2008.

[MMR10] E. Meechoowas, M. Müller, C. Rüssel. Redox relaxation in a sodium borosilicate glass doped with copper and arsenic, antimony, or tin. *Journal of Non-Crystalline Solids*, 356:2528 – 2533, 2010. 12th International Conference on the Physics of Non-Crystalline Solids (PNCS 12).

[MOC95] R. E. Morris, J. J. Owen, A. K. Cheetham. The structure of $La_4Ti_9O_{24}$ from synchrotron X-ray powder diffraction. *Journal of Physics and Chemistry of Solids*, 56(10):1297–1303, October 1995.

[Mot68] N. F. Mott. Conduction in glasses containing transition metal ions. *Journal of Non-Crystalline Solids*, 1(1):1 – 17, 1968.

[MR71] K. D. Möller, W. G. Rothschild. *Far-infrared spectroscopy*. Wiley series in pure and applied optics. Wiley-Interscience, 1971.

[MS62] J. B. MacChesney, H. A. Sauer. The system La_2O_3-TiO_2, phase equilibria and electrical properties. *Journal of the American Ceramic Society*, 45(9):416–422, September 1962.

[Mur82] L. Murawski. Electrical conductivity in iron-containing oxide glasses. *Journal of Materials Science*, 17(8):2155–2163, 1982.

[MYI87] M. Maeda, T. Yamamura, T. Ikeda. Dielectric characteristics of several complex oxide ceramics at microwave frequencies. *Japanese Journal of Applied Physics*, 26(2):76–79, May 1987.

[MYT94] K. Moringa, H. Yoshida, H. Takebe. Compositional dependence of absorption spectra of Ti^{3+} in silicate, borate, and phosphate glasses. *Journal of the American Ceramic Society*, 77(12):3113–3118, 1994.

[NA13] M. Neshat, N. P. Armitage. Developments in THz range ellipsometry. *Journal of Infrared, Millimeter, and Terahertz Waves*, 34(11):682–708, 2013.

[NG46] L. Navias, R. L. Green. Dielectric properties of glasses at ultra-high frequencies and their relation to composition. *The Journal of the American Ceramic Society*, 29(10):267–276, October 1946.

[NOA+06] A. Nakatsuko, O. Ohtaka, H. Arima, N. Nakayama, T. Mizota. Aragonite-type lanthanum orthoborate, $LaBO_3$. *Actra Crystallographica Section E*, 62:103–105, March 2006.

[Noe97] G. Noelle. *Technik der Glasherstellung*. Wiley-VCH, 1997.

[Nol80] D. A. Nolet. Optical absorption and mössbauer spectra of Fe, Ti silicate glasses. *Journal of Non-Crystalline Solids*, 37(1):99 – 110, 1980.

[NYB+93] T. Negas, G. Yeager, S. Bell, N. Coats, I. Minis. $BaTi_4O_9/Ba_2Ti_9O_{20}$-based ceramics resurrected for modern microwave applications. *American Ceramic Society bulletin*, 72(1):80–89, 1993.

[PA99] S. Penn, N. Alford. Chapter 10 - ceramic dielectrics for microwave applications. In Hari Singh Nalwa, editor, *Handbook of Low and High Dielectric Constant Materials and Their Applications*, pages 493–532. Academic Press, Burlington, 1999.

[Pap62] A. Papoulis. *The Fourier Integral and Its Applications*. McGraw-Hill, New York 1962.

[Par12] J. M. Parker. Lecture: Glass colour (ICG Summer School, Montpellier). 2012.

[PAT+97] S. J. Penn, N. McN. Alford, A. Templeton, X. Wang, M. Xu, M. Reece, K. Schrapel. Effect of porosity and grain size on the microwave dielectric properties of sintered alumina. *Journal of the American Ceramic Society*, 80(7):1885–1888, 1997.

[Pau75] A. Paul. Optical and esr spectra of titanium (III) in Na_2O-B_2O_3 and Na_2O-P_2O_5 glasses. *Journal of Materials Science*, 10(4):692–696, 1975.

[Pau76] A. Paul. Cerium - titanium yellow colour in glass. *Physics and Chemistry of Glasses*, 17(1), February 1976.

[Pau82] A. Paul. *Chemistry of glasses*. Springer, 1982.

[Pau85] A. Paul. Effect of thermal stabilization on redox equilibria and colour of glass. *Journal of Non-Crystalline Solids*, 71(1-3):269 – 278, 1985. Effects of Modes of Formation on the Structure of Glass.

[PD65] A. Paul, R. W. Douglas. Cerous-ceric equilibrium in binary alkali borate and alkali silicate glasses. *Physics and Chemistry of Glasses*, 6(6), December 1965.

[PD96] A. Paul, R. W. Douglas. Mutual interaction of different redox pairs in glass. *Physics and Chemistry of Glasses*, 7(1), February 1996.

[Pfe14] T. Pfeiffer. Internal report (SCHOTT AG). 2014.

[PK72] G. E. Peterson, C. R. Kurkjian. Resolution of ^{47}Ti and ^{49}Ti hyperfine lines in glass. *Solid State Communications*, 11(9):1105 – 1107, 1972.

[PK03] J. Petzelt, S. Kamba. Submillimetre and infrared response of microwave materials: extrapolation to microwave properties. *Materials Chemistry*

and Physics, 79(2-3):175 – 180, 2003. APMC-SSMM Asia-pacific Microwave conference: Special session on microwave materials.

[PKKV96] J. Petzelt, S. Kamba, G. V. Kozlov, A. A. Volkov. Dielectric properties of microwave ceramics investigated by infrared and submillimetre spectroscopy. *Ferroelectrics*, 176(1):145–165, 1996.

[PKN+07] Y. V. Pivak, V. V. Kharton, E. N. Naumovich, J. R. Frade, F. M. B. Marques. Ionic and electronic transport in $RE_2Ti_2SiO_9$-based materials. *Journal of Solid State Chemistry*, 180:1259–1271, January 2007.

[PMZ76] A. Paul, M. Mulholland, M. S. Zaman. Ultraviolet absorption of cerium(III) and cerium(IV) in some simple glasses. *Journal of Materials Science*, 11(11):2082–2086, 1976.

[Poz04] D. M. Pozar. *Microwave Engineering*. Wiley, 3rd Edition, 2004.

[PP07] A. Prasad, K. Prasad. Effective permittivity of random composite media a comparative study. *Physica B: Condensed Matter*, 396(1-2):132–137, June 2007.

[PPW+09] R. C. Pullar, S. J. Penn, X. Wang, I. M. Reaney, N. McN. Alford. Dielectric loss caused by oxygen vacancies in titania ceramics. *Journal of the European Ceramic Society*, 29(3):419 – 424, 2009.

[Prö14] D. Pröpper. Private correspondence (MPI für Festkörperforschung). 2014.

[PS93] J. Petzelt, N. Setter. Far infrared spectroscopy and origin of microwave losses in low-loss ceramics far infrared spectroscopy in low loss ceramics. *Ferroelectrics*, 150(1):89–102, 1993.

[Rao64] Bh. V. J. Rao. Properties and structure of glasses in the binary systems alkali-TiO_2. *Journal of the American Ceramic Society*, 47(9):455–463, 1964.

[Rao02] K. J. Rao. *Structural Chemistry of Glasses*. Elsevier Science, 2002.

[RBS61] G. Rupprecht, R. O. Bell, B. D. Silverman. Nonlinearity and microwave losses in cubic strontium-titanate. *Phys. Rev.*, 123:97–98, Jul 1961.

[RI06] I. M. Reaney, D. Iddles. Microwave dielectric ceramics for resonators and filters in mobile phone networks. *Journal of the American Ceramic Society*, 89(7):2063–2072, July 2006.

[Ric39] R. D. Richtmyer. Dielectric resonators. *Journal of Applied Physics*, 10(6):391–398, 1939.

[Rie68] H. M. Rietveld. A profile refinement method for nuclear and magnetic structures. *Journal of Applied Chrystallography*, 2:65–71, November 1968.

[Rie07] P. H. Rieger. *Electron Spin Resonance: Analysis and Interpretation*. Royal Society of Chemistry, 2007.

[RM78] B. S. Rawal, R. K. MacCrone. Electrical conductivity and structure of a barium borosilicate glass containing titanium ions. *Journal of Non-Crystalline Solids*, 28(3):347 – 368, 1978.

[RM91] M. Reece, R. Morrell. Electron microscope study of non-stoichiometric titania. *Journal of Materials Science*, 26(20):5566–5574, 1991.

[RW79] B. S. Rawal, J. T. Warden. EPR in a barium borosilicate glass containing titanium ions. *Journal of Materials Science*, 14(9):2215–2224, 1979.

[RWU+01] I. M. Reaney, P. Wise, R. Ubic, J. Breeze, N. McN. Alford, D. Iddles, D. Cannell, T. Price. On the temperature coefficient of resonant frequency in microwave dielectrics. *Philosophical Magazine A*, 81(2):501–510, 2001.

[SCC+09] J. Sheen, C. Chen, Y. Chen, C. Lai, Z. Hong. Microwave measurements of dielectric properties - a further study to a new theoretical model for a closed cylindrical cavity dielectric resonator. *EuCAP 2009. 3rd European Conference on Antennas and Propagation*, pages 3874–3877, March 2009.

[Sch68] A. P. Schmid. Evidence for the small polaron as the charge carrier in glasses containing transition metal oxides. *Journal of Applied Physics*, 39(7):3140–3149, 1968.

[Sch69] A. P. Schmid. Small polaron as the source of the frequency-dependent conductivity in glasses containing transition metal oxides. *Journal of Applied Physics*, 40(10):4128–4136, 1969.

[Sch87] H. D. Schreiber. An electrochemical series of redox couples in silicate melts: A review and applications to geochemistry. *Journal of Geophysical Research: Solid Earth*, 92(B9):9225–9232, 1987.

[Sch88] H. Scholze. *Glas- Natur, Struktur und Eigenschaften*. Springer Verlag, Berlin 1988.

[Sch04] A. Schütz. *Untersuchung zum Verhalten polyvalenter Ionen in Natriumborosilicatgläsern mit verschiedenen Methoden*. PhD thesis, Univ. Jena, 2004.

[SCH14] SCHOTT AG. *Datasheet - LITHOSIL Synthetic Fused Silica*, January 2014.

[SD65] R. Stolen, K. Dransfeld. Far-infrared lattice absorption in alkali halide crystals. *Phys. Rev.*, 139:A1295–A1303, Aug 1965.

[SD08] J. Shackelford, R. Doremus. *Ceramic and Glass Materials*. Springer, 2008.

[SDN91] M. A. Sainz, A. Duran, J. M. Fernandez Navarro. *Phys. Chem. Glass*, 32(3), June 1991.

[Seb08] M. T. Sebastian. *Dielectric Materials for Wireless Communication*. Elsevier, June 2008.

[Seb15] M. T. Sebastian. Private correspondence. 2015.

[SG91] L. Sjörgen, W. Götze. α-relaxation near the glass transition. *Journal of Non-Crystalline Solids*, 131-133, Part 1(0):153 – 160, 1991. Proceedings of the International Discussion Meeting on Relaxations in Complex Systems.

[Sha76] R. D. Shannon. Revised effective ionic radii and systematic studies of interatomic distances in halides and chalcogenides. *Acta Crystallographica Section A*, 32(5):751–767, Sep 1976.

[She05a] J. Sheen. Study of microwave dielectric properties by various resonance techniques. *Measurement*, 37(2):123–130, march 2005.

[She05b] J. E. Shelby. *Introduction to Glass Science and Technology*. The Royal Society of Chemistry, 2005.

[She07] J. Sheen. Microwave measurements of dielectric properties using a closed cylindrical cavity dielectric resonator. *IEEE Transactions on Dielectrics and Electrical Insulation*, 14(5):1139–1144, October 2007.

[She09] J. Sheen. Comparisons of microwave dielectric property measurements by transmission reflection techniques and resonance techniques. *Measurement Science and Technology*, 20(4):12pp, January 2009.

[Shi03] T. Shimada. Dielectric loss and damping constants of lattice vibrations in $\mathrm{BaMg_{1/3}Ta_{2/3}O_3}$ ceramics. *Journal of the European Ceramic Society*, 23(14):2647 – 2651, 2003. Microwave Materials and Applications.

[Shi04] T. Shimada. Far-infrared reflection and microwave properties of $Ba[Mg_{1-x}Zn_x]_{1/3}Ta_{2/3}O_3$ ceramics. *Journal of the European Ceramic Society*, 24(6):1799 – 1803, 2004. Electroceramics VIII.

[SIM+10] T. Shimada, K. Ichikawa, T. Minemura, H. Yamauchi, W. Utsumi, Y. Ishii, J. Breeze, N. M. Alford. Intrinsic microwave dielectric loss of lanthanum aluminate. *Ultrasonics, Ferroelectrics, and Frequency Control, IEEE Transactions on*, 57(10):2243–2249, October 2010.

[SJT80a] H. D. Schreiber, H. V. Lauer Jr., T. Thanyasiri. Oxidation-reduction equilibria of iron and cerium in silicate glasses: Individual redox potentials and mutual interactions. *Journal of Non-Crystalline Solids*, 38-39, Part 2(0):785 – 790, 1980. International Congress on Glass.

[SJT80b] H. D. Schreiber, H. V. Lauer Jr, T. Thanyasiri. The redox state of cerium in basaltic magmas: an experimental study of iron-cerium interactions in silicate melts. *Geochimica et Cosmochimica Acta*, 44(10):1599 – 1612, 1980.

[SK61] W. G. Spitzer, D. A. Kleinman. Infrared lattice bands of quartz. *Phys. Rev.*, 121:1324–1335, Mar 1961.

[SKM82] M. Sparks, D. F. King, D. L. Mills. Simple theory of microwave absorption in alkali halides. *Phys. Rev. B*, 26:6987–7003, Dec 1982.

[SKS99] S. D. Skapin, D. Kolar, D. Suvorov. Phase stability and equilibira in the La_2O_3-TiO_2 system. *Journal of the European Ceramic Society*, 20:1179–1185, October 1999.

[SM72] M. Sayer, A. Mansingh. Transport properties of semiconducting phosphate glasses. *Phys. Rev. B*, 6:4629–4643, Dec 1972.

[SMKH62a] W. G. Spitzer, Robert C. Miller, D. A. Kleinman, L. E. Howarth. Far infrared dielectric dispersion in $BaTiO_3$, $SrTiO_3$, and TiO_2. *Phys. Rev.*, 126:1710–1721, Jun 1962.

[SMKH62b] W. G. Spitzer, Robert C. Miller, D. A. Kleinman, L. E. Howarth. Far infrared dielectric dispersion in $BaTiO_3$, $SrTiO_3$, and TiO_2. *Phys. Rev.*, 126:1710–1721, Jun 1962.

[SML07] J. Sheen, W. L. Mao, W. Liu. Study on the measurements techniques of microwave dielectric properties. *NST*, pages 349–352, 2007.

[SMMW88] B. Stahlberg, B. D. Mosel, W. Müller-Warmuth. Elektrochemische und Mössbauer-Untersuchungen des Sb^{3+}/Sb^{5+}-Gleichgewichts in einer Silicatglasschmelze. *Journal Glastech. Ber.*, 61(12):335–340, July 1988.

[SMR03] H. Schirmer, M. Möller, C. Rüssel. High-temperature spectroscopic study of redox reactions in iron- and arsenic-doped melts. *Glass Sci. Technol.*, 76(2), 2003.

[SMS+96] R. Scharfschwerdt, A. Mazur, O. F. Schirmer, H. Hesse, S. Mendricks. Oxygen vacancies in $BaTiO_3$. *Phys. Rev. B*, 54:15284–15290, Dec 1996.

[Smy00] D. M. Smyth. *The Defect Chemistry of Metal Oxides*. Oxford University Press, 2000.

[SPBS96a] H. Schreiber, L. Peters, J. Beckman, C. Schreiber. Redox chemistry of iron-manganese and iron-chromium interactions in soda lime silicate glass melts. *Glass science and technology*, 69(9):269–277, 1996.

[SPBS96b] H. Schreiber, L. Peters, J. Beckman, C. Schreiber. Redox chemistry of iron-manganese and iron-chromium interactions in soda lime silicate glass melts. *Glass science and technology*, 69(9):269–277, 1996.

[SRGN+03] A. V. Sidorenko, P. A. Rodnyi, O. Guillot-Noel, D. Gourier, C. W. E. van Eijk. Study of ESR spectra of Ce^{3+} ions in polycrystalline $Sr_2B_5O_9Br$. *Physics of the Solid State*, 45(9):1676–1678, 2003.

[SRKR98] M. Schneider, W. Richter, R. Keding, C. Rüssel. XPS investigations on coordination and valency of Ti in fresnoite glasses and glass ceramics. *Journal of Non-Crystalline Solids*, 226(3):273 – 280, 1998.

[SSL95] R. J. Swope, J. R. Smyth, A. C. Larson. H in rutile-type compounds: I. single-crystal neutron and X-ray diffraction study of H in rutile. *American Mineralogist*, 80:448–453, February 1995.

[SSL+02] N. V. Skorodumova, S. I. Simak, B. I. Lundqvist, I. A. Abrikosov, B. Johansson. Quantum origin of the oxygen storage capability of ceria. *Phys. Rev. Lett.*, 89:166601, Sep 2002.

[Ste57] J. M. Stevels. The electrical properties of glass. In *Electrical Conductivity II / Elektrische Leitungsphänomene II*, volume 4 / 20 of *Handbuch der Physik / Encyclopedia of Physics*, pages 350–391. Springer Berlin Heidelberg, 1957.

[Ste85a] J. M. Stevels. Relaxation phenomena in glass. *J. Phys. Colloques*, 46(C8):613–616, 1985.

[Ste85b] J. M. Stevels. Relaxation phenomena in glass. *Journal of Non-Crystalline Solids*, 73(1-3):165 – 178, 1985. Glass Science and Technology Problems and Prospects for 2004.

[STL+07] T. Shimada, K. Touji, Hsiang-Lin L., Yuan-Tai T., Chih-Ta C., T. Kolodiazhnyi. Signature of lattice defects in far infrared reflectivity of $Ba(Mg_{1/3}Ta_{2/3})O_3$. *Journal of the European Ceramic Society*, 27(8-9):2797 – 2802, 2007. Papers Presented at the Fourth International Conference on Microwave Materials and their Applications - MMA2006, Oulu, Finland {MMA2006} Fourth International Conference on Microwave Materials and their Applications.

[Sto59] S. D. Stookey. *Proceedings of the Fifth International Glass Congress (Glastech. Ber .)*, 32K:1–8, 1959.

[Str61] J. S. Stroud. Photoionization of Ce^{3+} in glass. *The Journal of Chemical Physics*, 35(3):844–850, 1961.

[Tag93] A. K. Tagantsev. Phonon mechanisms of intrinsic dielectric loss in crystals. In N. Setter, E.L. Colla, editors, *Ferroelectric Ceramics*, Monte Verit, pages 127–145. Birkhäuser Basel, 1993.

[Tam33] G. Tammann. *Der Glaszustand*. L. Voss, 1933.

[Tam06] H. Tamura. Microwave dielectric losses caused by lattice defects. *Journal of the European Ceramic Society*, 26:1775 – 1780, 2006. Papers Presented at the Third International Conference on Microwave Materials and their Applications - {MMA2004} Inuyama, Japan The Third International Conference on Microwave Materials and their Applications - {MMA2004}.

[TK05] T. Takada, K. Kageyama. Synthesis and microwave dielectric properties of La_2O_3-xB_2O_3-based melt mixtures for low-temperature cofired ceramics. *Japanese Journal of Applied Physics*, 44(9A):6629–6635, September 2005.

[TKK93] J. Takahashi, K. Kageyama, K. Kodaira. Microwave dielectric properties of lanthanide titanate ceramics. *Japanese Journal of Applied Physics*, 32(9B):4327–4331, September 1993.

[TKNV05] G. Tarjus, S. A. Kivelson, Z. Nussinov, P. Viot. The frustration-based approach of supercooled liquids and the glass transition: a review and critical assessment. *Journal of Physics: Condensed Matter*, 17(50):R1143, 2005.

[TPS93] A. K. Tagantsev, J. Petzelt, N. Setter. Relation between intrinsic microwave and submillimeter losses and permitivity in dielectrics. *Solid State Communications*, 87(12):1117 – 1120, 1993.

[Tre60] H. J. Tress. A thermodynamic approach to redox equilibria in glass. *Physics and Chemistry of Glasses*, 1(6), December 1960.

[TSS11] S. Thomas, B. Sayoojyam, M. T. Sebastian. Microwave dielectric properties of novel rare earth based silicates: $\mathrm{RE_2Ti_2SiO_9}$. *Journal of Materials Science: Materials in Electronics*, 22:1340–1345, January 2011.

[TWP+00] A. Templeton, X. Wang, S. J. Penn, S. J. Webb, L. F. Cohen, N. McN. Alford. Microwave dielectric loss of titanium oxide. *Journal of the American Ceramic Society*, 83(1):95–100, 2000.

[TYK03] T. Takada, H. Yamamoto, K. Kageyama. Synthesis and microwave dielectric properties of $\mathrm{xRe_2O_3}$-$\mathrm{yB_2O_3}$ (Re:La,Nd,Sm,Dy,Ho,Y) compounds. *Japan Society of Applied Physics*, 42(9B):6162–6167, July 2003.

[Vog92] W. Vogel. *Glaschemie*. Springer Verlag, Berlin 1992.

[Vol84] M. B. Volf. *Glass Science and Technology - Chemical Approach to Glass*. Elsevier, Amsterdam 1984.

[WA76] J. Wong, C. A. Angell. *Glass: Structure by Spectroscopy*. Marcel Dekker, 1976.

[Wak89] K. Wakino. Recent development of dielectric resonator materials and filters in japan. *Ferroelectrics*, 91(1):69–86, 1989.

[WBC+89] G. M. Williams, P. C. Becker, J. G. Conway, N. Edelstein, L. A. Boatner, M. M. Abraham. Intensities of electronic raman scattering between crystal-field levels of $\mathrm{Ce^{3+}}$ in $\mathrm{LuPO_4}$: Nonresonant and near-resonant excitation. *Phys. Rev. B*, 40:4132–4142, Aug 1989.

[Web73] M. J. Weber. Optical spectra of $\mathrm{Ce^{3+}}$ and $\mathrm{Ce^{3+}}$-sensitized fluorescence in $\mathrm{YAlO_3}$. *Journal of Applied Physics*, 44(7):3205–3208, 1973.

[WEBA89] G. M. Williams, N. Edelstein, L. A. Boatner, M. M. Abraham. Anomalously small 4f-5d oscillator strengths and 4f-4f electronic raman scattering cross sections for Ce^{3+} in crystals of $LuPO_4$. *Phys. Rev. B*, 40:4143–4152, Aug 1989.

[WEM05] A. R. Weily, K. P. Esselle, A. S. Mohan. *Dielectric Resonators*. John Wiley & Sons, Inc., 2005.

[WF50] W. A. Weyl, T. Förland. Photochemistry of rutile. *Industrial amp; Engineering Chemistry*, 42(2):257–263, 1950.

[WH99] J. M. Wu, H.-L. Huang. Microwave properties of zinc, barium and lead borosilicate glasses. *Journal of Non-Crystalline Solids*, 260:116–124, June 1999.

[WMT84] K. Wakino, K. Minai, H. Tamura. Microwave characteristics of $(Zr, Sn)TiO_4$ and BaO-PbO-Nd_2O_3-TiO_2 dielectric resonators. *Journal of the American Ceramic Society*, 67(4):278–281, 1984.

[WMT86] K. Wakino, M. Murata, H. Tamura. Far infrared reflection spectra of $Ba(Zn, Ta)O_3$-$BaZrO_3$ dielectric resonator material. *Journal of the American Ceramic Society*, 69(1):34–37, 1986.

[WT98] H. Witzke, R. Takke. Luminscence and esr-properties of Ce-/Ti-doped fused quartz. *18th International congress on glass*, July 1998.

[XLYY12] L.-B. Xiong, J.-L. Li, B. Yang, Y. Yu. Ti^{3+} in the surface of titanium dioxide: Generation, properties and photocatalytic application,. *Journal of Nanomaterials*, 2012, 2012.

[XXHQ07] Z. X. Xiong, F. Xiao, J. R. Huang, H. Qiu. Dielectric polarization of $Ba_2Ti_9O_{20}$ ceramics for microwave applications. *Key Engineering Materials Vols. 280-283*, 42(9B):43–46, February 2007.

[YDES08] X. C. Yang, M. Dubiel, D. Ehrt, A. Schütz. X-ray absorption near edge structure analysis of valence state and coordination geometry of Ti ions in borosilicate glasses. *Journal of Non-Crystalline Solids*, 354:1172 – 1174, 2008. Proceedings of the 2005 International Conference on Glass In conjunction with the Annual Meeting of the International Commission on Glass.

[YYM04] M. Yoshino, H. Yukawa, M. Morinaga. Modification of local electronic structures due to phase transition in perovskite-type oxides, $SrBO_3$ (B=Zr, Ru, Hf). *MATERIALS TRANSACTIONS*, 45(7):2056–2061, 2004.

[Zac32] W. H. Zachariasen. The atomic arrangement in glass. *J. Amer. Chem. Soc.*, 54:3841–3851, 1932.

[Zar71] J. Zarzycki. X-ray diffraction study of alkali titanate glasses. *Journal of Materials Science*, 6(2):130–135, 1971.

[Zar91] Jerzy Zarzycki, editor. *Halide Glasses, in: [Materials science and technology]: Glasses and amorphous materials*, volume 9. Glasses and amorphous materials. VCH, Weinheim [u.a.], 1991. Literaturangaben.

[ZB65] O. Zinke, H. Brunswig. *Lehrbuch der Hochfrequenztechnik*. Springer, 1965.

[ZWKU97] C. Zuccaro, M. Winter, N. Klein, K. Urban. Microwave absorption in single crystals of lanthanum aluminate. *Journal of Applied Physics*, 82(11):5695–5704, 1997.

[ZZY+13] S. Zheng, Y. Zhou, D. Yin, X. Xu, Y. Qi, S. Peng. Improvement of 1.53 µm band fluorescence and energy transfer in Er^{3+}/Ce^{3+} codoped tellurite glasses. *Journal of Alloys and Compounds*, 566(0):90 – 97, 2013.

Danksagung

Aus Datenschutzgründen entfernt.

Erklärung

Die vorliegende Arbeit wurde in der Zeit von November 2011 bis Januar 2015 am Institut für Physik im Fachbereich 08 - Physik, Mathematik und Informatik der Johannes Gutenberg-Universität, Mainz in Zusammenarbeit mit der Schott AG in Mainz angefertigt.

Hiermit versichere ich, dass ich die vorliegende Arbeit ohne unzulässige Hilfe Dritter und ohne Benutzung anderer als der angegebenen Hilfsmittel angefertigt habe. Die aus fremden Quellen direkt oder indirekt übernommenen Gedanken sind als solche kenntlich gemacht. Ich habe bisher keinen Promotionsversuch unternommen und die Arbeit wurde bisher weder im In- noch im Ausland in gleicher oder ähnlicher Form einer anderen Prüfungsbehörde vorgelegt.

Hubertus Braun
Mainz, Januar 2015

Lebenslauf

Aus Datenschutzgründen entfernt.